Thèse de doctorat de l'Université Pierre et Marie Curie

Spécialité

Physique Fondamentale

École Doctorale de Physique et Chimie des Matériaux (ED 397)

présentée par

Pascaline Hayoun

pour obtenir le grade de

Docteur de l'Université Pierre et Marie Curie

Partial wetting of thin liquid films in polymer tubes

Soutenue le 20 septembre 2016 devant le jury composé de :

M. Benoit Scheid	TIPs - Université libre de Bruxelles	rapporteur
M^{me} Élisabeth Charlaix	LiPhy - Université Joseph Fourier	rapporteur
M. Laurent Limat	MSC - Université Paris 7	président du jury
M. David Quéré	PMMH - ESPCI ParisTech	examinateur
M. Étienne Barthel	SIMM - ESPCI ParisTech	directeur
M. François Lequeux	SIMM - ESPCI ParisTech	co-directeur
M^{me} Émilie Verneuil	SIMM - ESPCI ParisTech	invité
M. Alban Letailleur	Saint-Gobain Recherche	invité

École doctorale 397
4 place Jussieu
75 005 Paris

SIMM, ESPCI Paris
10, rue Vauquelin
75 005 Paris

Saint-Gobain Recherche
39 quai Lucien Lefranc
93 300 Aubervilliers

“Dans la vie, rien n’est à craindre,
tout est à comprendre.”

Marie Curie

Remerciements

Ce manuscrit de thèse est l'aboutissement de trois années de travail qui ont été très agréables et enrichissantes. Durant ces trois dernières années, j'ai évolué au sein de trois laboratoires : le laboratoire *Sciences et Ingénierie de la Matière Molle* (SIMM) à l'ESPCI, le laboratoire *Surface du Verre et Interfaces* (SVI) à l'unité mixte Saint-Gobain/CNRS et l'équipe *Fluid Systems* (FLS) du département *Produits Composites et Revêtements de Surface* (PCRS) de Saint-Gobain Recherche. L'accomplissement de ce travail est en très grande partie due aux personnes que j'ai pu rencontrer et que j'aimerais remercier ici.

J'aimerais tout d'abord remercier les membres de mon jury, en commençant par Élisabeth Charlaix et Benoit Scheid pour avoir accepté d'être les rapporteurs de ce travail et pour l'intérêt qu'ils y ont porté. Merci également à David Quéré et Laurent Limat pour avoir accepté de faire partie de ce jury et pour leurs remarques très judicieuses.

Ensuite, j'adresse mes remerciements à la société Saint-Gobain qui a lancé et financé cette thèse sous l'impulsion d'Étienne Barthel, Boris Jaffrennou, Hélène Lannibois-Dréan et Mathieu Joanicot.

Mes plus sincères remerciements vont à mes encadrants, Étienne Barthel, François Lequeux et Émilie Verneuil au SIMM, Jérémie Teisseire à SVI et Alban Letailleur à FLS. Chacun à sa manière a su m'apporter soutien et accompagnement quand je les sollicitais, tout en me faisant entièrement confiance.

Étienne, merci pour ton optimisme, ton expérience et ton calme. Ta façon de relativiser les choses m'a souvent aidé à prendre du recul. Merci également pour ta patience, notamment lorsqu'il s'agissait de m'initier au numérique. Enfin, merci pour ta vision scientifique qui m'a beaucoup éclairée durant ma thèse.

François, merci pour les discussions variées que l'on a pu avoir. Ta rapidité d'esprit et ta capacité à synthétiser un problème complexe m'a beaucoup impressionné et inspiré.

Émilie, merci pour ton enthousiasme, ton humour et ta rigueur scientifique. Merci notamment de m'avoir aidé dans la conception de mes dispositifs expérimentaux.

Jérémie, merci pour ta gentillesse et ta disponibilité. C'était toujours un plaisir de discuter avec toi. Quand j'avais la tête dans le guidon tu étais là pour m'aider à reformuler mes interrogations.

Alban, merci pour ton implication, ta disponibilité et ton accompagnement dans le monde de la R&D. Je te suis très reconnaissante de m'avoir complétement intégrée à Saint-Gobain Recherche et en particulier à l'équipe FLS. Je garderai un très bon souvenir de notre passage au salon de l'aéronautique au Bourget, des visites d'usines aux Etats-Unis, des revues R&D...

Merci à vous cinq de m'avoir permis d'effectuer de nombreuses choses en parallèle de mon travail de thèse (permanences au Palais de la Découverte, missions de vulgarisation scientifique, participation aux 24H chrono de l'entreprenariat, organisation de session poster...), de m'avoir donné l'occasion de voyager à travers plusieurs conférences nationales et internationales, et encore merci pour votre disponibilité et la liberté d'action que vous m'avez accordées.

Merci aux stagiaires qui ont eu l'occasion de travailler avec moi et qui ont contribué à ma thèse: Claire BARRAS, Clément LASKAR et Sen LI.

Plus largement, j'ai eu la chance au fil des conférences et écoles d'été de faire la rencontre de chercheurs passionnés. Un grand merci à Marc FERMIGIER, José BICO, Élie RAPHAËL, Christophe CLANET, Marie-Caroline JULLIEN, Terry BLAKE, Joël DE CONINCK, Tomas BOHR, Michel RIEPEN, John BUSH, Jacco SNOEIJER, Philippe BRUNET, Laurent ROYON, Luc LEBON, Adrian DAERR, Henri LHUISSIER, Christophe JOSSERAND, Arnaud ANTKOWIAK, Frédéric RESTAGNO, Benjamin DOLLET, Kristina DAVITT, Xavier NOBLIN, Philippe COUSSOT, Christian RUYER-QUIL, Sophie MERGUI, Georg DIETZE, Nicolas KOFMAN, Valérie BOTTON, Paul GRANDGEORGE, Claude PERDIGOU... pour les discussions très intéressantes que j'ai eu l'occasion d'avoir avec vous.

À Saint-Gobain Recherche, je tiens sincèrement à te remercier Hélène LANNIBOIS-DRÉAN pour ta gentillesse, ta disponibilité et ton regard critique. Merci également pour ton implication au côté d'Alban LETAILLEUR et François CREUZET dans le suivi de ma thèse mais aussi dans mes projets comme ma candidature pour les bourses L'Oréal-Unesco *pour les Femmes et la Science*, mon embauche à Saint-Gobain et ma mobilité aux États-Unis. Merci à vous trois.

Je souhaite remercier aussi l'ensemble de l'équipe FLS Alban LETAILLEUR, Ludovic LEYMARIE, Hadrien HEUCLIN, Siska HAMDANI-DEVARENNES, Harayer CHILINGUIRIAN, Raphaël DANGUILLAUME, Didier ROBERT, Stéphanie VAN NOORT, Julien NALLET, Jim DING... ainsi que les ingénieurs et techniciens du département PCRS pour la très bonne ambiance de travail et les échanges que j'ai pu avoir avec vous. Merci également à mes co-bureaux Romain HIVET et Andrea GIOIA pour votre accueil un jour par semaine et votre bonne humeur.

À SVI, mes remerciements vont à Emmanuelle GOUILLART, Franck PIGEONNEAU, Pierre JOP, Alban SAURET et Iryna GOZHYK pour l'intérêt que vous avez porté à mon

travail. Merci également à Emmanuelle et Alban pour votre soutien lors de ma candidature pour les bourses L'Oréal-Unesco *pour les Femmes et la Science*.

Je remercie tous les membres de SVI (présents et passés) pour votre gentillesse, votre bonne humeur et la bonne ambiance du laboratoire. Je garderai un très bon souvenir des pique-niques annuels, des soirées régulières chez les uns et les autres, des culbitures et de ses fidèles membres Corinne Claireaux, Gautier Lefebvre, Barbara Brudieux, Yann Cohin, Jean-Yvon Faou, William Woelffel, Marine Guémas, Isabelle Tannou, Aymeric Merceron, Paul Jacquet, Ekaterina Chernysheva, Thomas Barrès...

Au SIMM, merci à Christian Frétigny et Guylaine Ducouret pour m'avoir accueilli au laboratoire. Merci à Guylaine pour m'avoir aiguillé pour les aspects de rhéologie des liquides et Hélène Montes pour ceux des solides. Nicolas Sanson pour les conseils en spectroscopie. Ludovic Olanier pour m'avoir aidé à penser et concevoir une partie de mon dispositif expérimental. Mohamed Hanafi pour avoir réalisé des expériences de DSC. Merci également à Freddy Martin, Armand Hakopian et Pierre Christine pour les coups de pouces du quotidien.

Merci à l'ensemble des membres du laboratoire SIMM (présent et passé) pour avoir fait de ces trois dernières années un moment très agréable. Je vais regretter les discussions de nos déjeuners escalier C avec entre autres Marc Yonger, Charles Barrand, Tom Saint Martin, Corentin Trégouët, Julien Dupré de Baubigny, Guillaume Chatté, Alice Boursier, Cécile Monteux, Guylaine Ducouret, Flore Lasaone, anciennement Rémi Deleurence, Pauline Valois, Eric Lintingre, Solenn Moro. Les bières du lundi avec en plus Davide Colombo, Paul Elzière, Pierre Millereau, Pierre Gélineau, Robert Gurney, Jingwen Zhao, Francisco Cedano, anciennement Benjamin Chollet, Yannick Nziakou, Robin Masurel, Jennifer Macron... Les soirées jeux de sociétés et aussi les week-ends de labo vertigineux organisés par notre cher David Martina. Un remerciement spécial à mes co-bureaux, les tous premiers Rémi Deleurence et Solenn Moro, remplacés par Marc Yonger, Marine Protat et Menghua Zhao, pour m'avoir supporté pendant ces années. Également à Corentin Trégouët, Bruno Bresson et Matteo Ciccotti mes compagnons de clarinette.

Hors du cadre professionnel, il y a aussi des amis qui m'ont épaulée et soutenue depuis déjà de nombreuses années. Un grand merci à mes amis d'école d'ingénieur (l'ESPCI) Marianne, Célia, Fanny, Bénédicte, Pauline, Maya, François, Marine, Claire, Pierre, Rémi, Nicolas, Jean, Lauriane, Perrine, Samy, Maëlle, Maxime L., Romain D. ... Mes amis de classe préparatoire à Michelet Agathe, Gautier, Thibault, Arthur, Jérémy, Maxime, Lamya, Maxence, Claire, Alexandre et Vincent. Mais aussi mes professeurs qui ont joué un rôle majeur dans mon devenir en sciences Pierre Robin, Florence Vidal, Sandrine Chevy et Anne Teillet. Mais encore Fleur, Cécile, Marion, Flavien & Co de Mennecy. Et la team Suisse Amélie, Anna, Alice M., Laura, Virginie, Alice P., Elsa. Mes amies du handball au PUC qui m'ont permis de me vider la tête régulièrement après de longues

journées de travail Isabelle, Julie, Manon, Hélène, Lison, Barbara, Nelly, Marion, Carole, Claire, Géraldine, Lucie, Camille & Co, et mes entraineurs Vincent et Alex.

Enfin, mes derniers remerciements vont à ma famille (oncles, tantes et cousin(e)s), mes frères Florent et Charley, ma mère Christiane et son compagnon Bernard qui m'ont toujours encouragée et soutenue depuis toujours.

Un remerciement tout particulier à ma tante Martine, ma grande tante Marie, ma mère Christiane et mon frère Florent pour avoir géré avec brio mon pot de thèse.

Résumé en français

Mouillage partiel de films liquides dans des tubes polymères

Les tubes polymères, de PDMS ou de PVC, sont des matériaux hydrophobes polyvalents et peu couteux. Ils sont très largement utilisés dans l'industrie pour transférer des fluides plus ou moins complexes tels que de l'eau potable, des émulsions (*e.g* lait), des suspensions (*e.g* café), ou encore des solutions de molécules actives (*e.g* médicament). La plupart de ces applications mettent en jeux des écoulements intermittents répétés de liquide qui peuvent contaminer le matériau. Cette étude a pour but de mieux comprendre comment ces écoulements de fluides complexes entraînent la contamination des tubes.

Nous étudions expérimentalement et théoriquement les régimes d'un segment de liquide de faible viscosité s'écoulant dans un tube en conditions de mouillage partiel. Nous avons fait varier la viscosité du liquide ainsi que l'interaction liquide/solide près de la ligne triple. Étonnamment la géométrie cylindrique est moins étudiée expérimentalement dans la littérature que la géométrie plane. En effet, la visualisation de l'écoulement est plus compliquée dans des tubes bien que cette géométrie présente l'avantage de ne pas avoir d'effet de bords. Nous avons conçu un dispositif expérimental polyvalent permettant d'accéder à des vitesses élevées du segment liquide sur une large gamme, avec une bonne reproductibilité et une bonne qualité de la visualisation permettant ainsi de mesurer la cinématique du segment liquide et la morphologie du film liquide. Une méthode de mesure d'épaisseur basée sur l'absorption de la lumière a été mise au point.

Nous montrons dans un premier temps que le nombre capillaire Ca est le paramètre pertinent pour rendre compte de nos observations. Dans une perspective classique pour des surfaces hydrophobes, on s'attendrait à observer des transitions dynamiques de mouillage forcé à des nombres capillaires très élevés. Pour le PVC par exemple, la transition est attendue à environ $Ca = 3.5\ 10^{-3}$, à savoir 26 cm.s^{-1} pour de l'eau pure. Expérimentalement, ce n'est pas ce que l'on observe. Un film de liquide peut être entrainé à des nombres capillaires bien plus faibles $Ca = 1.8\ 10^{-4}$, correspondant à une vitesse de 1.4 cm.s^{-1}. Des résultats similaires sont également observés avec le PDMS (Chapter 6). Nous montrons qu'il y a deux raisons pour cette différence de comportements par rapport au cas classique. La première est que l'angle de contact à la reculée pertinent θ_e n'est pas l'angle de contact à la reculée en quasi-statique θ_r^0. La seconde est que même si l'on corrige l'angle de contact de référence, la transition dynamique de mouillage se produit à des vitesses bien plus faibles d'un ordre de grandeur.

Le comportement phénoménologique observé dans notre étude est représenté de manière schématique dans la Figure 1 : *(i)* ménisque dynamique stationnaire et déstabilisation du ménisque (Chapitre 3) ; *(ii)* formation d'un film épais (Chapitre 4) ; *(iii)* coexistence de deux films (Chapitre 5) ; et est en accord avec les modèles numériques bien que les transitions ne soient pas aux valeurs de nombres capillaires prédites.

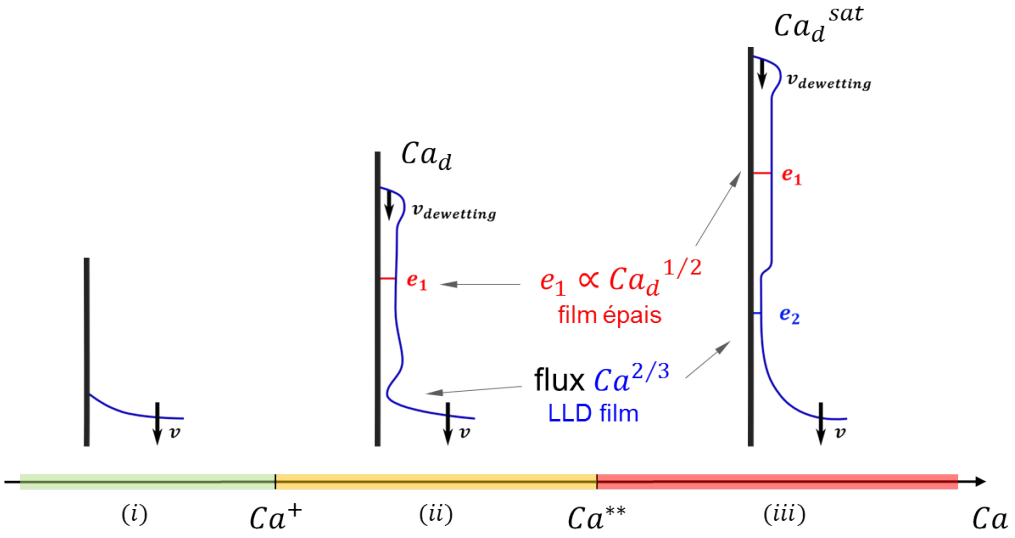

FIGURE 1: *Schéma récapitulatif des différents régimes et des morphologies de films observés en faisant varier le nombre capillaire.*

Dans le *régime (i)*, la forme du ménisque évolue en temps pour atteindre une forme stationnaire avec un angle de contact fini. À faibles nombres capillaires Ca, il y a une forte dépendance de l'angle de contact à la fois en avancée et en reculée avec le nombre capillaire (zone a dans la Figure 2). Les modèles hydrodynamiques ne rendent pas compte de cet aspect. Cette variation inattendue peut être attribuée au couplage entre la rugosité de la surface et le piégeage de la ligne triple. Pour des nombres capillaire plus élevés Ca (zone b), un plateau visqueux de type Cox-Voinov est observé, mais il se termine prématurément par rapport aux prédictions hydrodynamiques. Ce plateau se termine à $Ca^+ = 1.8\ 10^{-4}$ où l'on trouve une forte chute à environ zéro sur la gamme Ca^+ et $Ca^* = 4\ 10^{-4}$ (zone c). Entre ces deux nombres capillaires, Ca^+ et Ca^*, la transition vers la formation d'un film dépend de l'échelle de temps de la mesure. Il y a un ralentissement critique autour de la transition. Tous ces aspects sont inclus dans nos simulations numériques. Ca^* définit la transition de mouillage dynamique instantanée, correspondant à la transition entre *régime (i)* and *(ii)*. Dans notre système expérimental la dissipation visqueuse dans le coin de liquide est négligeable, en remplacement un mécanisme de dissipation de type friction permet d'expliquer qualitativement à la fois la valeur de l'angle de contact à la reculée en quasi-statique et le nombre capillaire critique Ca^+ auquel on observe la transition d'un ménisque à un film (ou Ca^* pour la transition dynamique instantanée). Cette dernière valeur est bien plus faible que celle obtenue dans la littérature en utilisant les modèles hydrodynamiques classiques, couramment notée Ca_c (mais Ca_c^{Cox} dans ce manuscrit).

Dans ces cas, la transition est définie quand la solution stationnaire du ménisque cesse d'exister ($z_{cl} = \sqrt{2}$) [1]. Dans notre étude, Ca^* est un ordre de grandeur plus faible que Ca_c^{Cox}. Expérimentalement la transition est non seulement décalée mais aussi élargie. Ce résultat remarquable est une opportunité pour observer en détail la phénoménologie autour de la transition.

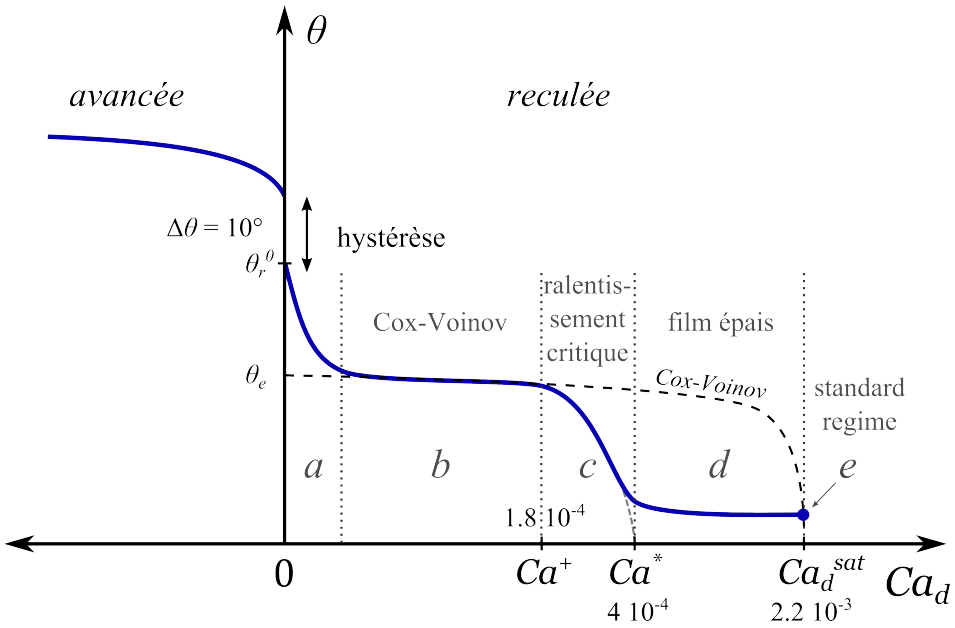

FIGURE 2: *Schéma de l'évolution de l'angle de contact dynamique θ en fonction du nombre capillaire basé sur la vitesse de la ligne triple Ca_d. Les lignes de contact en avancée correspondent à des vitesses négatives. Les valeurs sont données pour des tubes de PVC.*

Au-delà de ce nombre capillaire, on observe expérimentalement l'existence d'un film épais sur une large gamme de nombre capillaire $Ca^+ < Ca < Ca^{**}$ (zone d dans la Figure 2). Ce film épais démouille à une vitesse Ca_d légèrement inférieure à la vitesse du segment de fluide Ca. De plus, contrairement à la littérature (Chapitre 1), l'épaisseur du film épais n'est pas unique et dépend de la vitesse de la ligne triple : $e_1 = l_c\sqrt{3Ca_d}$. La vitesse Ca_d augmente avec la vitesse du segment liquide mais reste légèrement inférieure. On observe des films épais avec une variété d'épaisseurs allant d'environ 50 à 200 μm. La différence $Ca - Ca_d$ est de plus en plus prononcée jusqu'à une certaine valeur, où la vitesse de démouillage sature à Ca_d^{sat}. La saturation de la vitesse de la ligne triple a été identifié à $Ca^{**} = 2.2\ 10^{-3}$ et définie la transition entre *régime (ii)* et *(iii)* et correspond à la valeur de Ca prédite par Cox-Voinov pour la transition de mouillage forcé.

Dans le *régime (iii)* un film plus mince croît entre le précédent film épais et le ménisque (zone e). Nous retrouvons une épaisseur indépendante de la vitesse $e_1^{sat} = l_c\sqrt{3Ca_d^{sat}}$ pour le film épais du haut, tout comme d'autres auteurs Snoeijer *et al.* [2, 3] (expérimentalement) et Hocking [4], Snoeijer *et al.* [1], Gao *et al.* [5] (numériquement). La transition vers deux films liquides est associée à la saturation du flux descendant généré par le démouil-

lage et la gravité. Ce flux devient plus faible que le flux de liquide montant éjecté par le segment liquide par forçage visqueux, ce qui sélectionne une seconde épaisseur : deux épaisseurs de films coexistent et sont reliées par un ressaut capillaire formé à la transition. Le film du bas correspond à un film de Landau-Levich-Derjaguin/Bretherton, usuellement observé pour des conditions de mouillage total, et présente une épaisseur variant en $Ca^{2/3}$. Dans les *régimes (ii)* et *(iii)*, les profils de films obtenus numériquement en stationnaire rendent compte de nos observations expérimentales en terme d'évolution de l'épaisseur du film avec Ca, à l'exception du bourrelet observé près de la ligne triple. L'existence du *régime (iii)* peut être obtenue en prenant en compte les dérivées temporelles. Ainsi, on trouve les différents régimes obtenus par Gao *et al.* [5]. Ainsi, on trouve les différents régimes obtenus par Gao *et al.* [5]. Néanmoins, on obtient une épaisseur du film épais constante indépendamment de la vitesse, ce qui est en accord avec $e_1 = l_c\sqrt{3Ca^*}$ mais pas avec notre résultat expérimental $e_1 = l_c\sqrt{3Ca_d}$. De plus, la différence entre Ca^* et Ca^{**} est bien plus marquée expérimentalement ($\Delta Ca = 1.8\ 10^{-3}$) que numériquement ($\Delta Ca = 10^{-4}$).

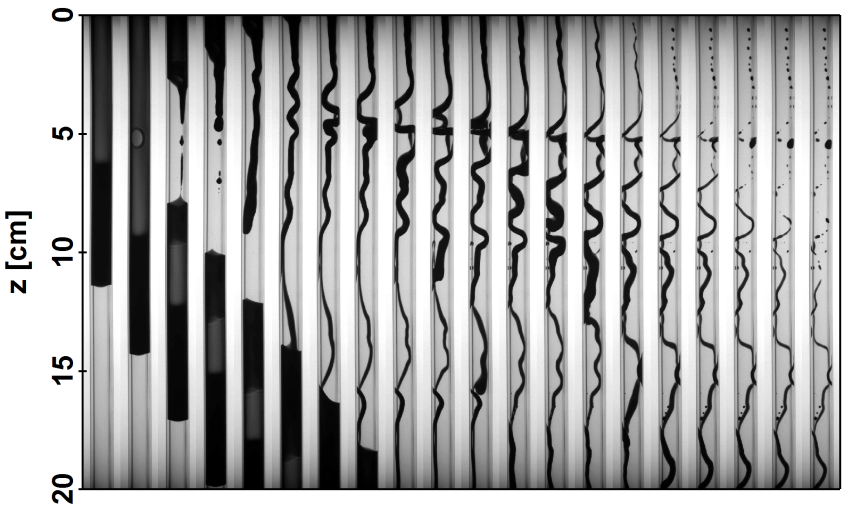

(a)

(b)

FIGURE 3: *(a) Séquence d'images obtenue pour une expérince typique où le film liquide se rompt ($\Delta t = 100$ ms). Une zone sèche se forme et croît laissant un ruisselet qui se déstabilise lui-même en gouttelettes qui restent piégées à la surface. (b) Zoom sur la zone de nucléation ($\Delta t = 4$ ms).*

Lorsque le nombre capillaire est suffisamment important, le second film devient plus épais que le premier film. Dans le même temps, des oscillations d'épaisseurs localisées près du ressaut capillaire apparaissent. Un dernier scenario est occasionnellement observé où le film liquide se déstabilise soit dans la zone mince, soit au niveau des oscillations. Une zone sèche se forme et croît laissant seulement un ruisselet connectant la partie haute du film au segment liquide ou au nouveau film formé plus bas (Figure 3). Une fois que le film a drainé complétement à travers le ruisselet, ce dernier se déstabilise en gouttelettes (instabilité de Rayleigh-Plateau). Ces gouttelettes sont sujettes à l'évaporation et laissent des résidus, générant la contamination du substrat.

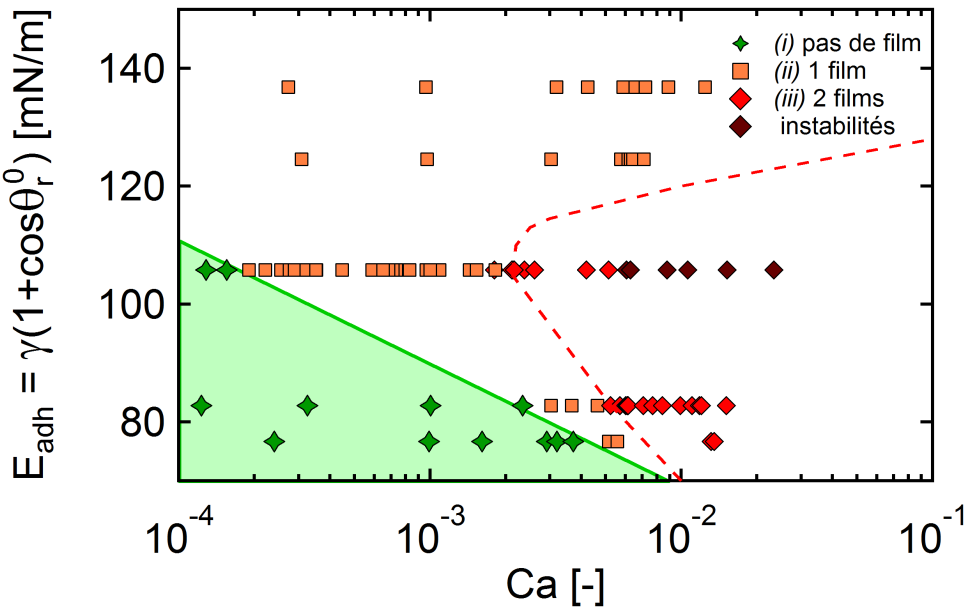

FIGURE 4: *Diagramme de phase pour de l'eau pure : énergie d'adhésion* $E_{adh} = \gamma\,(1+\cos\theta_r^0)$ *en fonction du nombre capillaire* Ca*. Les courbes verte et rouge correspondent respectivement à la limite qualitative entre régime (i) et (ii), et régime (ii) et (iii).*

Notre étude apporte un aperçu fondamental du problème classique d'une ligne de contact mobile en géométrie cylindrique et de la déposition d'un film sur des substrats partiellement mouillants. En outre, ces résultats trouvent une application pratique pour les fabricants de tubes, tel que Saint-Gobain, ou leurs clients. En effet, comme expliqué précédemment, un point crucial est de réduire la contamination du tube causée par le transfert de liquide. Cela nécessite d'une part la réduction du temps de contact entre le liquide et le tube, et d'autre part la stabilisation de l'écoulement pour éviter la formation et le piégeage de gouttes. Dans les deux cas il est préférable d'éviter le dépôt d'un film liquide et de restreindre l'écoulement à une zone stable : *régime (i)*. Nous montrons que l'ajustement des paramètres (propriétés du liquide et du matériau) permettent soit d'empêcher, soit d'induire la formation d'un film liquide. Cette vue globale du problème

permet d'aider le fabriquant à conseiller leur clients en terme de propriétés du tube à utiliser pour un liquide donné (η, γ, débit de l'écoulement via Ca, chimie du tube via θ_r).

Un diagramme de phase E_{adh} en fonction de Ca peut ainsi être construit, comme le montre la Figure 4. L'énergie d'adhésion E_{adh} correspond aux interactions liquide/solide à travers la chimie du tube θ_r^0 et à travers la tension de surface du liquide γ. En utilisant ce diagramme de phase, la chimie du tube pour une tension de surface donnée et un débit donné peut être ajustée afin de placer le système dans un régime stable, à savoir *régime (i)*.

Table of Contents

Introduction

0.1 Industrial context

Polymer tubes, made of poly(dimethylsiloxane) (PDMS) or poly(vinyl chloride) (PVC), are versatile, low cost, hydrophobic materials. They are heavily used for tubing in Food & Beverage markets. The Fluid Systems division of Saint-Gobain has a strong market share for these activities. These applications involve repeated, intermittent flows of liquid. In addition the liquids at stake are more or less complex fluids such as drinkable water, emulsions (*e.g* milk), suspensions (*e.g* coffee), or solution of active molecules (*e.g* pharmaceutics). However, polymer material presents some drawbacks such as large permeability, easy adsorption/adhesion at the surface, possible heterogeneity, leading to unwanted contamination, and making the cleaning difficult. In order to improve product quality and strengthen the marketing process, the Fluid Systems division of Saint-Gobain is interested in a better understanding of how intermittent flows of complex fluids in polymer tubes result in contamination.

PDMS exhibits an hydrophobic surface with low surface energy (around 20 $\mathrm{mN.m^{-1}}$). As mentioned previously, while tubes are in use, aqueous solutions are flowing and contaminants can accumulate at the inner wall. Moreover, because of the high contact angle hysteresis for the couple water/PDMS, the triple line can be pinned. To solve the fouling problem, it is important to properly identify and understand the mechanisms which lead to deposition/pinning of a fraction of the liquid and to find ways to decrease the contamination by technically viable surface modifications of the PDMS tubes.

0.2 Scientific problem

In this context, we are interested in the coupling between macroscopic flow and more local effects at the triple line. Two main phenomena could explain tube contamination after a fluid segment (slug) has passed through (see Figure 5): chemical interaction and liquid deposition.

The first one is the chemical interaction between the liquid and the substrate which may lead to chemical or physical adsorption at the tube surface while a slug is flowing (Figure 5a). Another possibility is the deformation of the meniscus at the rear which may

lead to triple line destabilization and, even worse, liquid deposition at the back of a slug. This liquid deposition can either be a continuous film or droplets which can evaporate and leave contaminants. This case is depicted in Figure 5b.

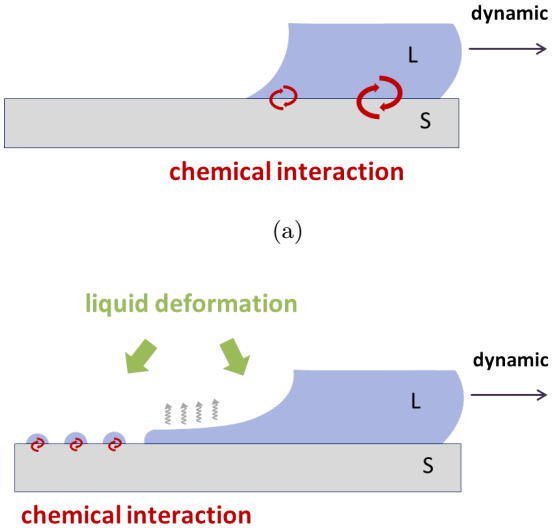

FIGURE 5: *Contamination mechanisms: (a) chemical interaction liquid/substrate leading to adsorption, (b) deformation of the liquid meniscus leading to film deposition and/or droplets.*

To probe the relative importance of the adsorption mechanism and of the film/droplet deposition scenario, a side experiment was carried out where we artificially contaminate tubes. For that purpose, we flow a dilute solution of hot milk in a PDMS tube (Sanitech® ULTRA). Milk proteins are the contamination agent that will be characterized. In a first case (#1), the flow is running for 55 min. In this situation, called "continuous flow": one single long slug will go through the tube. In a second case (#2), the flow is stopped every 20 secs, for 1.5 mins. To get the same contact time as for case #1 (55 min), 163 cycles are run. In this situation, the flow is intermittent and multiple slugs will flow on the surface. After flowing the liquid, we cut a length of 5 cm of the tube to extract and quantify the milk proteins adsorbed on the surface. Protein concentrations in both cases are gathered in Figure 6. It shows that the contamination is ten times larger in the case of intermittent flow. Indeed, in our study, flows are gravity-driven in tubes (tens of centimeters long), and velocities are of the order of several centimeters per second. At this time scale (a few seconds), only elements a few micrometers away from the wall can diffuse towards the surface and be adsorbed. Therefore, it can be concluded that diffusion and/or adsorption from the bulk are not relevant for contamination. Instead, the precise behavior of the contact line between liquid meniscus and tube seems to control the contamination (Figure 5b).

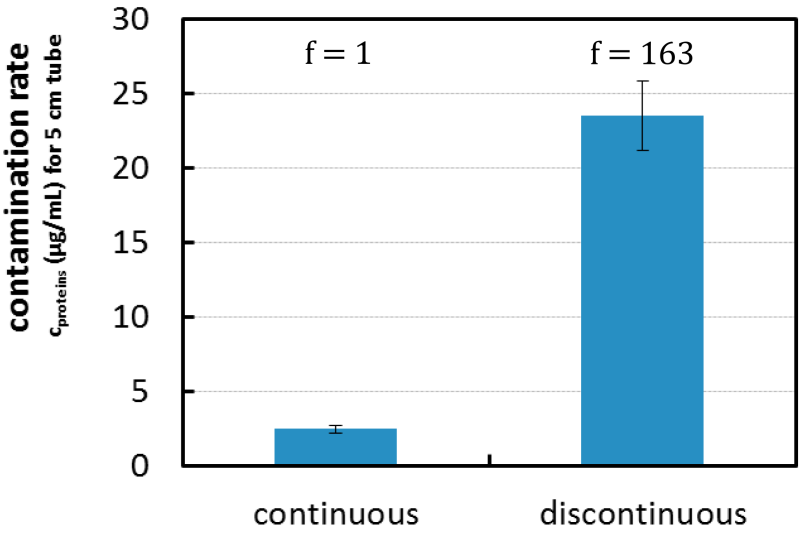

Figure 6: *Artificial contamination of PDMS tube by milk.*

To better understand the mechanisms of contamination for intermittent flows, we have developed a model experiment. We consider flows in vertical cylindrical tubes under partial wetting condition, such that two processes are in competition. On the one hand, because of the large slug velocity, a liquid film tends to be created at the back of the rear meniscus. On the other hand, because of the partial wetting condition, the liquid film dewets. We will investigate how this competition controls film deposition in hydrophobic tubes and propose theoretical approaches of the problem to explain and rationalize the experimental observations and identify the dominant effects.

Notations

γ	Surface tension of the fluid
η	Viscosity of the fluid
κ	Interface curvature
θ	Dynamic contact angle
θ_e	Equilibrium or static contact angle
θ_a	Advancing contact angle
θ_r	Receding contact angle
θ_r^0	Quasi-static receding contact angle measured with pure water displaced at a velocity $v = 0.3$ cm.s^{-1}
$\Delta\theta$	Contact angle hysteresis
ρ	Density of the fluid
Ψ	Dimensionless triple line friction coefficient
Ca	Capillary number of the rear of the slug
Ca_f	Capillary number of the front of the slug
Ca_d	Capillary number of the dewetting film
Ca_d^{sat}	Saturation capillary number of the dewetting film
Ca_j	Capillary number of the *jump*
Ca^*	First threshold in capillary number describing qualitatively the transition between *regime (i)* and *regime (ii)* (instantaneous wetting transition)
Ca^+	Critical capillary number at the dynamic wetting transition delimiting the transition between *regime (i)* and *regime (ii)*
Ca^{**}	Second threshold in capillary number of the slug delimiting the transition between *regime (ii)* and *regime (iii)*

Ca_c^{Cox}	Capillary number threshold found by the Cox-Voinov model
d_{in}	Inner diameter of the tube
d_{out}	Outer diameter of the tube
e_1	Thickness of the *first film*
e_1^{sat}	Maximal thickness of the *first film*
e_2	Thickness of the *second film*
g	Gravitational acceleration constant
$h(z)$ or e	Thickness profile of the liquid/air interface along the $z-$ direction
H	Normalized meniscus profile by the capillary length l_c
$\tilde{h}$	Normalized meniscus profile by $l_c Ca^{1/2}$
l_c	Capillary length
l_s	Slip length
L_{slug}	Length of the slug
L_{film}	Length of the film
L_{film1}	Length of the *first film*
L_{film2}	Length of the *second film*
P	Pressure
Q_c	Convected upward flux
Q_g	Gravitational downward flux
Q_d	Dewetting downward flux
R	Radius of the tube
t	Time
T	Time normalized by the capillary length l_c
$\tilde{t}$	Time normalized by $l_c Ca^{1/6}/v$
v	Velocity of the rear of the slug
v_d	Velocity of the dewetting film
v_d^{sat}	Saturation velocity of the dewetting film

v_j	Velocity of the *jump*
v_c^{Cox}	Velocity threshold found by the Cox-Voinov model
v^*	First threshold in velocity describing qualitatively the transition between *regime (i)* and *regime (ii)*
v^{**}	Second threshold in velocity of the slug delimiting the transition between *regime (ii)* and *regime (iii)*
v_{liq}	Characteristic velocity of the fluid
z	Vertical position
Z	Vertical position normalized by the capillary length l_c
$\tilde{z}$	Vertical position normalized by $l_c Ca^{1/6}$
z_{cl}	Contact line elevation

Chapter 1

State of the art

1.1 Introduction

In this chapter, we provide a panorama of the state of the art on two main aspects. The first one concerns thin liquid films entrained by moving surface. The main concern is predicting the thickness of the film as a function of the velocity of the surfaces. The second aspect is about moving contact lines: a liquid/solid contact line is displaced on a horizontal surface. Authors mainly focus on the evolution of the dynamic contact angle at the triple line as a function of the relative velocity of the contact line on the surface. In a third part of this chapter, we will see that looking deeper into the literature very few examples can be found where authors investigate simultaneously thin liquid films and moving contact lines. The last part will detail the scope of the manuscript.

1.2 Flow in thin liquid films

The deposition of a liquid layer on a solid substrate is widely encountered in a variety of industrial or natural situations involving the motion of liquid menisci on a dry solid. It is realized by imposing a relative motion between the solid and the triple line. Common applications are coating (*e.g.* dip-coating) and painting; enhanced oil recovery, or soil remediation, where liquid foams are pushed into porous media to displace oil or pollutants [6, 7]; in the bronchial tubes of the lung where surfactant lamellae are produced and moved [8]; in the throat and the esophagus where alimentary boluses are propelled during swallowing [9]; in microfluidics to control bubble motion in innovative setups [10].

1.2.1 Landau-Levich-Derjaguin film

One of the simplest setups for liquid film deposition is the so-called dip coating, in which a solid surface is withdrawn from a liquid reservoir with a velocity v, giving rise to a thin film of controlled thickness. For a Newtonian liquid with a dynamic viscosity η and a surface tension γ, the dip-coating process, as illustrated in Figure 1.1, is governed by the balance between the viscous and capillary forces, which is measured by the capillary

number $Ca = \eta v/\gamma$. The capillary number can be written as a ratio of two velocities: $Ca = v/v_{liq}$, highlighting a characteristic velocity of the fluid defined as $v_{liq} = \gamma/\eta$. For water, this velocity is very large (70 m.s^{-1}). In most cases, because of the comparatively small value of v, the associated capillary number is small, typically $Ca < 0.01$.

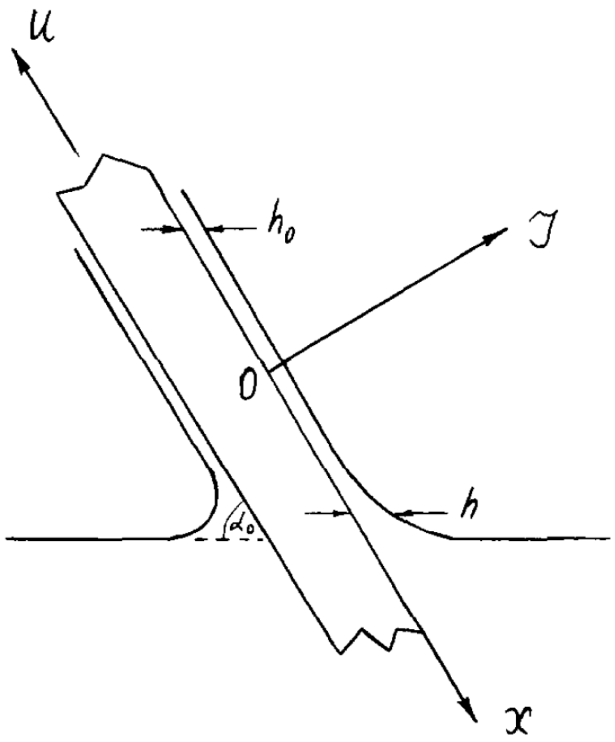

FIGURE 1.1: *A Landau-Levich-Derjaguin (LLD) film in a dip coating experiment (from [11]).*

Specifically, Landau, Levich and Derjaguin (LLD), motivated by the problem of the coating of cine films, proposed a well-know relation, referred to as the LLD law in the following [11, 12], which gives the film thickness e_{LLD} as a function of the capillary number Ca (Equation (1.1)).

$$e_{LLD} = 0.95\ l_c\ Ca^{2/3} \tag{1.1}$$

where $l_c = \sqrt{\gamma/\rho g}$ is the capillary length, which compares surface tension and gravity effects. Below the length scale l_c the gravity can be neglected. For water, the capillary length is about 2.7 mm. It sets the curvature of the connection between the film and the liquid bath.

The LLD law corresponds to the small capillary number limit of the film deposition, and is generally believed to be valid for $Ca \leq 0.01$ according to a series of experimental and numerical tests (see Ruschak [13] and references therein). For a bath of water and a plate velocity $v = 7$ m.s^{-1} corresponding to a capillary number $Ca = 1\ 10^{-4}$, the thickness of the remaining film is $e_{LLD} = 6\ \mu$m.

Later, Bretherton [14] developed a similar model for the case of an air bubble displaced in a capillary tube filled with liquid. In the absence of gravitational and inertial forces, the motion of elongated bubbles within a liquid is expected to be mainly governed by the competition between viscous and surface tension forces, *i.e* by the capillary number Ca. In this configuration the relevant length scale for the calculation of the film thickness e_B is no longer the capillary length l_c but the tube radius $R << l_c$ (Equation (1.2)), and the thickness is given by:

$$e_B = 1.34\ R\ Ca^{2/3} \tag{1.2}$$

We provide in Appendix A a simple scaling approach and the complete calculation of the Bretherton problem to obtain Equation (1.2). For an easy to follow derivation see also Cantat [15]. For small tube radius $R << l_c$, the thickness of the entrained film is smaller than LLD film.

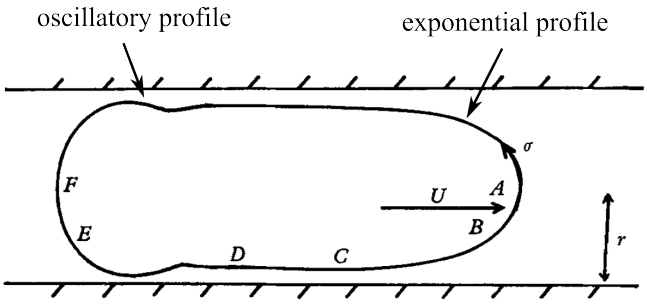

Figure 1.2: *Section of a bubble in a horizontal tube where U represents the bubble velocity [14].*

Contrary to the LLD film, the Bretherton bubble has two ends. An interesting point is the dissymmetrical shape of the bubble (Figure 1.2). The front of the bubble (on the right side) presents an exponential profile while the back end of the bubble (on the left) exhibits an oscillating profile.

In fact, in the reference frame of the bubble at the right of the bubble (Figure 1.2) the wall of the tube can be considered as translating at the velocity $-v$ (in the left direction) compared to the static liquid reservoir. Similarly to the LLD case, where a plate is withdrawn out of a bath, the corresponding profile of the liquid film is exponential. On the left side of the bubble, the wall of the tube is entering the static liquid reservoir located to the left and a soft buckling of the surface results.

Similarly to Fairbrother & Stubbs [16] in 1935, twenty five years later Taylor [17] experimentally investigated the bubble motion for the range of $Ca < 2$ in glycerine and concentrated sucrose solutions in glass tubes of diameters $2R = 1.5$, 2 and 3 mm. The sketch of the setup is given in Figure 1.3b. The tube is horizontal.

As a result, he found that the relation presented in Equation (1.2) provides a good approximation up to $Ca = 0.09$. The same relation was observed to over-predict his measurements in highly viscous liquids at $Ca > 0.09$. Taylor's experimental results are

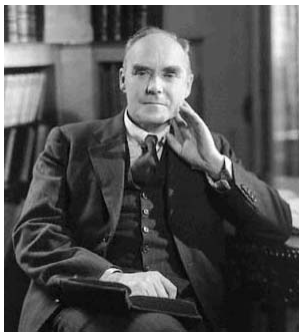

(a)

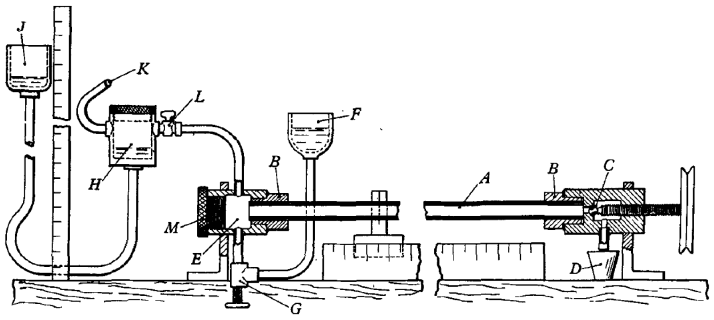

(b)

FIGURE 1.3: *(a) Taylor's portrait. (b) Sketch of Taylors's apparatus [17].*

well described by the following expression, which is referred to as the empirical Taylor's law in the literature in the range of $Ca < 10^{-2}$:

$$\frac{e_T}{R} = \frac{0.67\ Ca^{2/3}}{1 + 3.35\ Ca^{2/3}} \tag{1.3}$$

More recently, the effect of inertia on the motion of confined elongated bubbles was investigated in numerical and experimental studies [18, 19, 20, 21]. In general, this effect was found to increase the thickness of the liquid film around the gas bubbles, which caused notable deviations from Taylor's law for larger capillary numbers. Aussillous & Quéré [18] performed experimental measurements with low viscosity liquids for a large range of capillary numbers and reported significant under-estimation of their results by the relations proposed by Taylor [17] and Bretherton [14]. They found a systematic deviation for capillary numbers larger than $Ca \sim \left(\eta^2/\gamma\rho R\right)^{3/4}$. Finally, they concluded that the modification of the film thickness can be captured by the following relation:

$$\frac{e}{R} \sim \frac{Ca^{2/3}}{1 + Ca^{2/3} - We} \tag{1.4}$$

where $We = \rho v^2(R-e)/\gamma$ is the Weber number that describes the ratio of inertia to capillary effects.

Callegari *et al.* [22] experimentally investigated the dewetting of liquid films using slugs of water-glycerol solutions in PVC cylindrical tubes. Tubes of radius $R = 1$ mm were placed horizontally. They noted that it was difficult to measure the thickness of the film in a cylindrical geometry, so that they chose to measure it indirectly considering the volume conservation and assuming a homogenous film. Doing so, they found that the variation of the film thickness e is well fitted by the relation:

$$\frac{e}{R} \sim 0.95\ {Ca_f}^{0.6} \tag{1.5}$$

Here, contrary to the LLD prediction which uses the velocity of the slug rear, Callegari *et al.* [22] define the capillary number Ca_f based on the velocity of the front of the slug v_f. They noticed that the two variations in $Ca^{2/3}$ and $Ca^{0.6}$ are quite similar.

Despite the large number of numerical and experimental studies devoted to such flows, most of these investigations were mainly focused on quantifying the film to mean flow velocity ratio and the average film thickness. Other aspects of film flow such as the profile of the free surface and the length of the film, or the onset of the transitions to axisymmetric and time-dependent flows were usually overlooked in the literature, especially in the experimental studies, due to the limitations in the measurement techniques. In addition, whenever a liquid/solid/gas triple line exists, the liquid is assumed to be completely wetting and there is no relative velocity between contact line and solid wall.

1.2.2 Thick film

Looking deeper in the literature, we can find other types of liquid films (Figure 1.4), that have only been calculated theoretically or numerically. These films are commonly named "thick films".

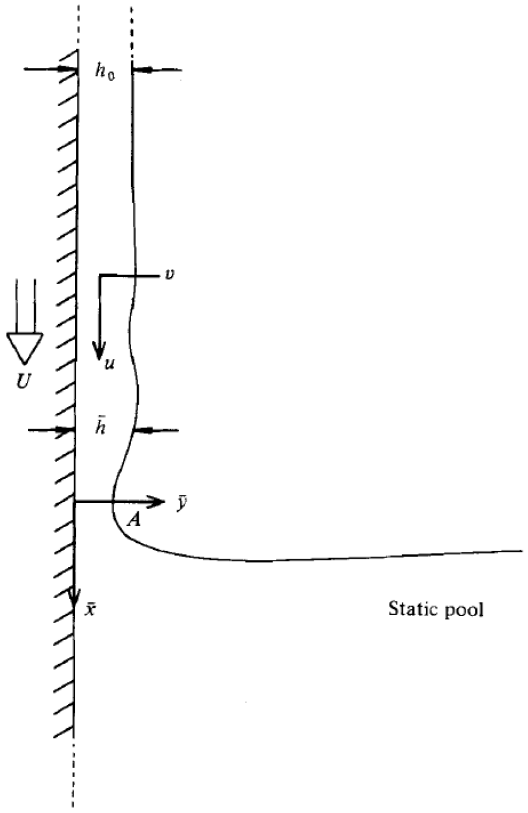

Figure 1.4: *Film flowing down a plate with mean velocity U and thickness h, connected to a liquid bath. A denotes the final wave trough, or dimple (from [23]).*

Derjaguin is the first author to mention the existence of such thick film solutions, through a theoretical derivation [12]. He considered the steady state obtained when pulling an infinite plate oriented at an angle α with the horizontal line from a liquid at a constant velocity v (Figure 1.1). He found that when the time is sufficiently large, the thickness of the film at a considerable distance above the liquid bath will be constant and approximately

equal to e_D, according to:

$$e_D \sim \sqrt{\frac{\eta v}{\rho g \sin \alpha}} \tag{1.6}$$

Later, the reverse problem has been studied: a liquid film running down a vertical plate and entering a large bath (Cook & Clarke [24], Cullen & Davidson [25]). It was found that the free liquid surface does not simply match into the bath but exhibits several stationary ripples near the point of entry (Figure 1.4). The explanation, in terms of the interplay between gravity, viscosity and capillarity, was given in essence by Ruschak [26], and has been further investigated by Wilson & Jones [23] using the method of matched expansions. They both investigated the case of a static wall and the case of a vertical wall moving downwards. These oscillations are similar in nature to the back side of Bretherton's bubble. An experimental study by Maleki *et al.* [27] confirms the existence of a stationary wavy shape when plunging a coated plate with a liquid film into a bath.

Whether in the LLD or in the thick film cases, the finite vertical extent of the film is not taken into account, so that there may actually exist a triple line at the end of the film. All the phenomena are considered to happen close to the meniscus. On the other hand, a large part of the literature is dedicated to the description of moving contact lines out of the context of film deposition. This is the focus of the next section.

1.3 Moving contact line and dynamic contact angle

When a drop is deposited on a surface, the droplet interface takes an equilibrium shape. The static or equilibrium contact angle θ_e is the angle, conventionally measured in the liquid, where the liquid-vapor interface meets the solid (static conditions: $v = 0$ in Figure 1.5).

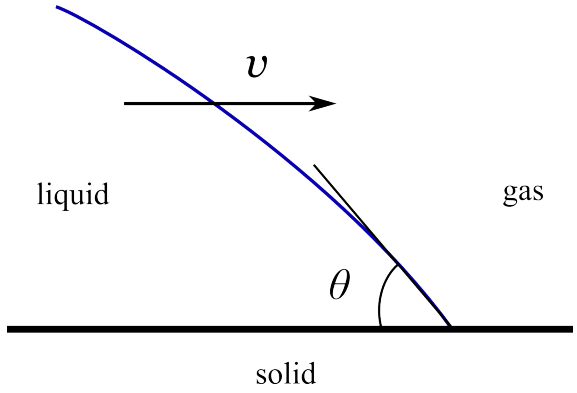

FIGURE 1.5: *Schematic of a moving contact line with a dynamic contact angle.*

θ_e quantifies the wettability of a solid surface by a liquid via the Young equation [28]:

$$\gamma \cos \theta_e = \gamma_{sg} - \gamma_{sl} \tag{1.7}$$

where γ, γ_{sg} and γ_{sl} are the liquid/gas, solid/gas and solid/liquid surface tensions respectively. A given system of solid, liquid, and gas at a given temperature and pressure has a unique equilibrium contact angle θ_e.

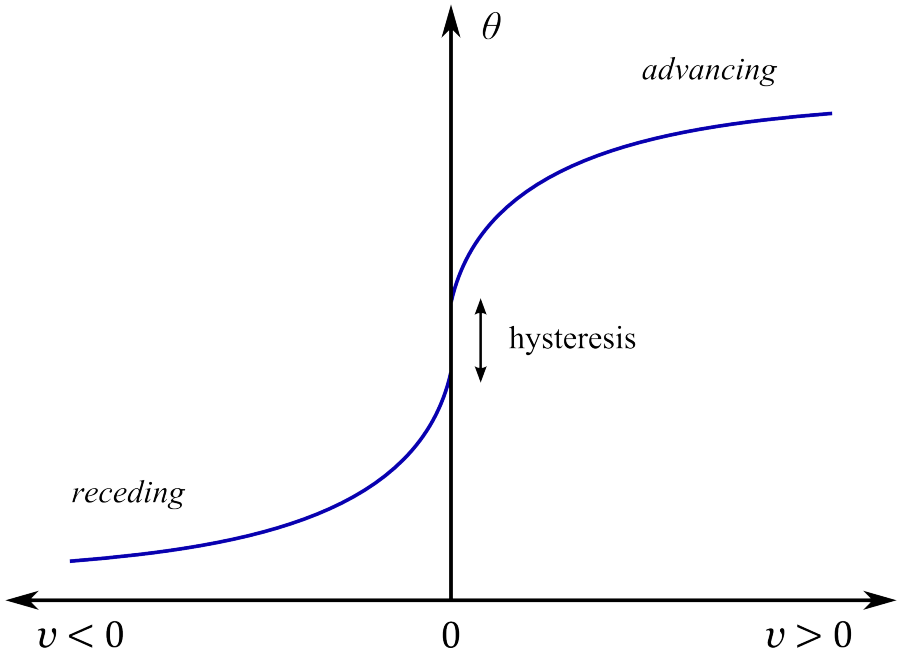

Figure 1.6: *Velocity-dependence of the contact angle for a partially wetting liquid.*

However, in practice solid surfaces are not perfect and often present a roughness or chemical heterogeneity. It results in the non uniqueness of the equilibrium contact angle. The contact angle value will depend on whether the interface has been advancing or receding, ranging from the so-called advancing (wetting) contact angle θ_a to the receding (dewetting) contact angle θ_r. This phenomenon is known as contact angle hysteresis [29, 30, 31] and can be quantified by the difference between the cosines of advancing contact angle and the receding contact angle $\Delta\cos\theta = \cos\theta_r - \cos\theta_a$, or by $\Delta\theta = \theta_a - \theta_r$. On such surfaces, wetting lines tend to pin and depin in an unsteady way. Such factors complicate both the measurement and the interpretation of contact angles. When we consider a contact line moving at velocity v in the reference frame of the substrate (Figure 1.5), the dynamic contact angle $\theta = f(v)$ differs from its equilibrium value θ_e because of dissipation. When the contact line advances the dynamic contact angle increases with velocity v whereas it decreases when the contact line recedes (Figure 1.6). In all the models presented below, the contact angle hysteresis is neglected even though this phenomenon is almost always observed experimentally.

1.3.1 Wetting dynamics - models and dissipation

Despite a huge amount of work, dissipation mechanisms close to the dynamic contact line are still a controversial issue. The most obvious source of dissipation is the flow of the viscous liquid near the triple line. Due to the decreasing liquid thickness towards the contact

line, the shear rate increases. In fact one difficulty comes from the well-known contact line singularity of the shear rate that arises when the Navier-Stokes equation together with the no-slip boundary condition are used to model the problem. This singularity is non-physical since it leads to infinite energy dissipation rate. Apart from the mathematical complication, this highlights the complex physical processes occurring in the vicinity of the contact line. A number of researchers including Ablett [32], Huh & Scriven [33], Dussan & Davis [34] and Dussan [35] have studied flow conditions near moving contact lines, pointing out difficulties in avoiding singularities and suggesting ways to overcome them. For this viscosity dominated case, standard theories were given by Cox [36] and Voinov [37] on one side and de Gennes *et al.* [38, 39] and Eggers [40] on the other side.

Another approach considers the dissipation at the triple line as essentially localized at the microscopic scale. Mechanisms such as molecular displacement by adsorption/desorption have been considered by Blake *et al.* [41, 42] or numerical techniques by the diffuse interface method [43]. Some other models combine the two main approaches using molecular-hydrodynamic models [44, 42, 45]. Below we detail the main models commonly discussed in the literature and of interest to our study. These models are established for small capillary numbers Ca ($Ca < 0.01$) and small dynamic contact angles θ. Note that although they are derived for small contact angles, these models are considered to be valid up to angles of 135° [37].

Hydrodynamic theories: Cox-Voinov model

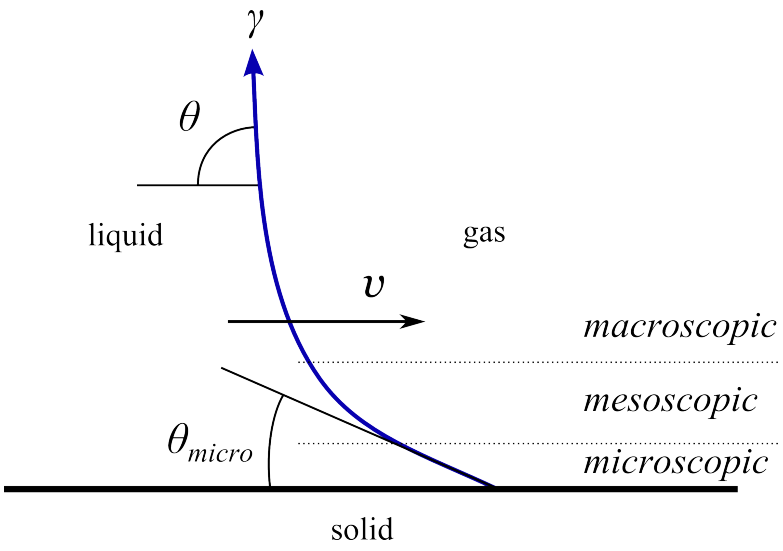

FIGURE 1.7: *Viscous bending at the meso-scale for an advancing meniscus.*

Many efforts have been dedicated to modifying the hydrodynamic model in order to remove the triple line singularity. In most of these modified models, slip is postulated to occur at the liquid/solid interface near the contact line. This is modeled either by assuming that the tangential stress vanishes near the contact line [36], or by the Navier boundary condition in which the shear stress is assumed to be proportional to the slip

velocity [37]. In the hydrodynamic models the dynamic contact angle is calculated. As the capillary number is assumed to be small, far from the triple line the liquid/gas interface adopts its static shape (Figure 1.7). By matching the local dynamic solution to the static macroscopic solution, the dynamic contact angle can be determined (asymptotic matching [36]).

A simplified version of the Cox-Voinov calculation is presented below. We consider a moving contact line at constant velocity v in the $z-$direction in the reference frame of the substrate (Figure 1.8). The liquid is in partial wetting condition. Invariance in the $x-$direction is assumed and inertial and gravitational effects are neglected. The velocity in the $z-$direction is denoted $v_z(y)$, the thickness profile of the meniscus is $h(z)$.

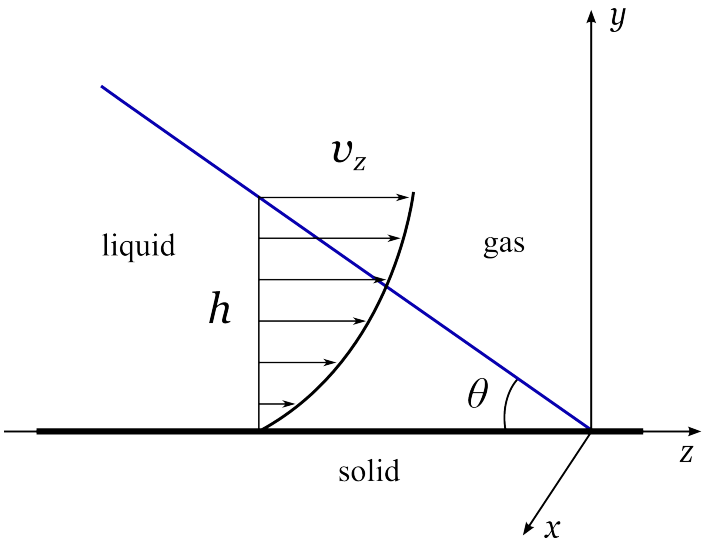

Figure 1.8: *Moving contact drawing and notation for the the Cox-Voinov calculation.*

The pressure in the liquid phase is set by the Laplace equation: $P(z) = -\gamma\partial_{zz}h$, for small angles [46]. A small contact angle at equilibrium θ_e is considered, so that the liquid wedge is nearly parallel to the wall and complies with the lubrication hypothesis. Under these assumptions, the Stokes equation writes:

$$\eta\partial_{yy}v_z = -\gamma\partial_{zzz}h \tag{1.8}$$

where η is the fluid viscosity and γ the surface tension.

Considering a no slip condition at the liquid/solid interface $v_z = 0$ in $y = 0$ and a stress free condition at the liquid/gas interface $\partial_y v_z|_{y=h} = 0$, Equation (1.8) can be integrated to obtain the velocity field. The resulting flux per unit length in the $x-$direction is given by

$$q(h) = \int_0^h v_z(y)\mathrm{d}y = -\frac{\gamma}{\eta}\frac{h^3}{3}\partial_{zzz}h \tag{1.9}$$

Using the mean velocity v, the flux writes $q = vh$. Therefore, flux conservation implies

$$\partial_{zzz} h = -\frac{3\eta v}{\gamma}\frac{1}{h^2} \tag{1.10}$$

Exact solution to the previous equation can be expressed in terms of Airy functions [47]. To obtain the Cox-Voinov result, a trick is to consider $h(z) \simeq -z\theta(z)$ where θ is roughly constant, because $\theta(z)$ varies slowly with z. Equation (1.10) becomes

$$-\partial_{zz}\theta \simeq -\frac{3\eta v}{\gamma}\frac{1}{z^2\theta^2} \tag{1.11}$$

The previous equation is integrated as follows:

$$\partial_z \theta \simeq -\frac{3\eta v}{\gamma}\frac{1}{z\theta^2} \tag{1.12}$$

After variable separation and integration, the simplified resulting relation, known as the Cox-Voinov law [36, 37], is obtained:

$$\theta(z)^3 - {\theta_e}^3 = 9Ca \ln\left(\frac{z}{a}\right) \tag{1.13}$$

where θ_e is the equilibrium contact angle and a is a lower cut-off distance of z: atomic length, used to truncate the divergence of the logarithm at small z. This equation describes the variation of the dynamic contact angle θ due to viscous bending of the liquid/gas interface in terms of the capillary number Ca at the position z attached to the line end.

Equation (1.13) shows that the divergence is very slow since it is included in a logarithm, confirming *a posteriori* the hypothesis considering liquid wedges as nearly parallel to the wall. Moreover, this equation highlights that a measure of the contact angle is dependent on the scale at which the measurement is done. Considering a macroscopic contact angle, a typical macroscopic length scale of the problem like the capillary length l_c can be used for z.

The Cox-Voinov law predicts a zero value of the contact angle for a finite value of velocity Ca. For $\theta = \theta_c = 0°$, the Cox-Voinov equation (1.13) exhibits a threshold velocity Ca_c^{Cox} above which there is no longer a solution for a dynamic meniscus and a liquid film will be entrained. This threshold formally defines a forced wetting transition and is given by:

$$Ca_c^{Cox} \simeq \frac{{\theta_e}^3}{9\ln\left(l_c/a\right)} \tag{1.14}$$

For example, for water in a hydrophobic tube, taking $\ln(l_c/a) \simeq 15$ and $\theta_e = 45°$ the corresponding threshold velocity is $Ca_c^{Cox} \simeq 3.6\ 10^{-3}$. This value is supposed to provide the maximal dewetting velocity of the triple line: $v_c^{Cox} \simeq 25$ cm.s^{-1} for water ($\gamma/\eta \simeq 70$ m.s^{-1}).

Hydrodynamic theories: de Gennes model

In their model, de Gennes *et al.* [38, 39] carried out an energy balance for a liquid wedge of height h moving at velocity v. The viscous stress $3\eta v/h$ is balanced by the capillary forces due to the unbalanced Young stress F given by:

$$F = \gamma \left(\cos\theta - \cos\theta_e\right) \tag{1.15}$$

The elementary work of the capillary forces during a time δt is $\delta W_{cap} = Fv\delta t$. On the other side, the infinitesimal work of the viscous dissipation forces can be written as follows:

$$\delta W_{vis} = \int \frac{3\eta v^2}{h} \delta t \delta y \tag{1.16}$$

The previous equation shows a divergent integral which signals the contact line singularity. Similarly to the Cox-Voinov model, a macroscopic (L) and microscopic (a) length scales are introduced to regularize the problem. Assuming the liquid/gas interface is locally planar, we finally obtain

$$\delta W_{vis} = \frac{3\eta v^2}{\tan\theta} \ln\left(\frac{L}{a}\right) \delta t \tag{1.17}$$

Balancing those two works, and expanding at small θ, we finally obtain the so-called de Gennes relation providing the variation of the dynamic contact angle θ with the capillary number Ca:

$$\theta\left(\theta^2 - {\theta_e}^2\right) = 6Ca \ln\left(\frac{L}{a}\right) \tag{1.18}$$

The main difference with the Cox-Voinov model can be found in the critical value of the contact angle at which the wetting transition occurs. As seen previously, the wetting transition occurs for a zero receding contact angle in the Cox-Voinov model. In the de Gennes model, the critical contact angle is non-zero since the wetting transition is defined when $\partial_\theta v = 0$ corresponding to a minimum in the variations of Ca with θ. According to Equation (1.18), the receding dynamic contact angle cannot be smaller than:

$$\theta_c = \frac{\theta_e}{\sqrt{3}} \tag{1.19}$$

Another option for the lower dimension cut-off a is to introduce Van der Waals forces acting to maintain a finite thickness in place of the slip length [48, 30]. The van der Waals interaction very close to the contact line leads to a precursor film. Whatever the nature of the lower size cut-off, the physics at the larger length scales remains the same.

These modified hydrodynamic models do succeed in removing the singularity, but they are often quite *ad hoc*. In particular, they assume that viscous dissipation is dominant even at small length scales. This is probably not the case and others types of dissipation mechanisms can take place near the triple line.

Molecular kinetic theory

A different type of approach to describe the contact line dynamics is the molecular kinetic theory as proposed by Blake & Haynes [41]. Similar to de Gennes' model, it is driven by the unbalanced Young stress given by Equation (1.15). However, instead of viscous flow, it is an Eyring process at the triple line that gives rise to dissipation [49].

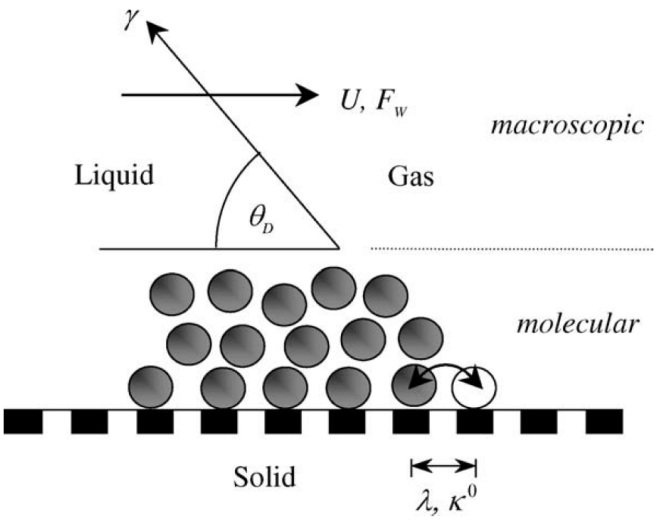

FIGURE 1.9: *Dynamic wetting according to the molecular-kinetic theory [50].*

At equilibrium, the contact line jumps back and forth from one adsorption site to another with the same frequency (Figure 1.9). In a dynamic situation where the system is out of equilibrium, the force F given in Equation (1.15) introduces an unbalance between forward and backward jump frequencies from which motion results. The difference of the two frequencies multiplied by the characteristic length between adsorptions sites gives the contact line speed v. From Eyring's rate theory, the contact line speed is related to the force F by the formula:

$$v = 2\kappa^0 \lambda \sinh\left(\frac{\gamma\left(\cos\theta - \cos\theta_e\right)\lambda^2}{2k_bT}\right) \tag{1.20}$$

where κ^0 and λ are molecular parameters that depend on the characteristics of the solid surface.

Equation (1.20) is the main result of the molecular kinetic theory for contact line dynamics; it provides a relation between the dynamic contact angle θ and the contact line velocity v. For small angles, Equation (1.20) can be approximated by:

$$\theta^2 - {\theta_e}^2 = \frac{2k_bT}{\gamma\kappa^0\lambda^3}v \tag{1.21}$$

Similarly to the Cox-Voinov model, the molecular kinetic theory predicts a zero-value contact angle at the wetting transition (second order transition). In contrast, de Gennes' model predicts a first order wetting transition. Note that Golestanian & Raphaël [51, 31]

and later Eggers [40] suggest that the wetting transition is of second order at the macroscopic scale while the transition may be of first order when looking at the microscopic scale. Maleki *et al.* [52] have shown experimentally using large tubes (compared to the capillary length) that the macroscopic contact angle might be discontinuous at the transition to forced wetting.

Combined models

Alternatively, other models can be found in the literature where hydrodynamic approaches are combined with the molecular kinetic theory. The first authors to propose a combined model were Petrov & Petrov [44]. They take advantage of the molecular kinetic theory to get a microscopic contact angle (using Equation (1.20)) to substitute the equilibrium contact angle θ_e in the Cox-Voinov equation (1.13). The resulting equation presents three adjustable parameters to fit experimental data. It was found that this kind of models accounts for the experimental data and results in physically acceptable values of the adjustable parameters. Similar results were obtain by other authors [42, 45].

A similar model developed by Brochard-Wyart & de Gennes [53] introduced a contact line friction which accounts for additional dissipation at low velocity. This contact line friction can be interpreted in term of molecular kinetic theory. They show that viscous dissipation in bulk dominates at small angles (larger velocity). Additional work by Ruijter *et al.* [54] or very recently by Perrin *et al.* [55] confirms the previous statement, since they found that the wetting-line friction regime precedes the viscous regime, which becomes dominant only as the contact angle becomes small.

An alternative approach proposed by Ren *et al.* [56, 57] consists in deriving continuum models using basic principles of non-equilibrium thermodynamics. Their model combines both the viscous dissipation in the bulk and non-hydrodynamic dissipation at the solid surface and at the contact line. They show that the microscopic contact angle actually deviates from its static value during the motion of the contact line. This accounts for the energy dissipation at the contact line. The regularized hydrodynamic models all contain more than one relevant length scale: an inner region near the contact line and an outer region away from the contact line. This is reflected in the different contact angles one sees at different scales as depicted in Figure 1.7.

1.3.2 Experimental investigation of the wetting dynamics

There is a fundamental difference between the hydrodynamic theory and the molecular kinetic theory, which is the origin of the energy dissipation. The hydrodynamic theory emphasizes energy loss in the bulk due to viscous flow while molecular kinetic theory focuses on the non-hydrodynamic dissipation near the contact line. Out of the two models one obtains two different relations between the dynamic contact angle θ and the contact line speed v (Equation (1.13) and (1.20)). When considering the spreading of a droplet in the case of small contact angles, a standard experiment in the literature, these two

relations lead to two different scaling laws for the droplet radius: $R(t) \sim t^{1/10}$ (Hoffman-Tanner law) for the hydrodynamic theory and $R(t) \sim t^{1/7}$ for the molecular kinetic theory. Discrepancies between these theoretical predictions and the experimental data have been found by various authors [58, 53, 59]. For instance Davitt *et al.* [60] show that the region of validity of the molecular kinetic theory on mesoscopically rough surfaces typically corresponds to velocities of less than 1 mm.s^{-1}. Their observations suggest that neither model is comprehensive in the description of the energy dissipation.

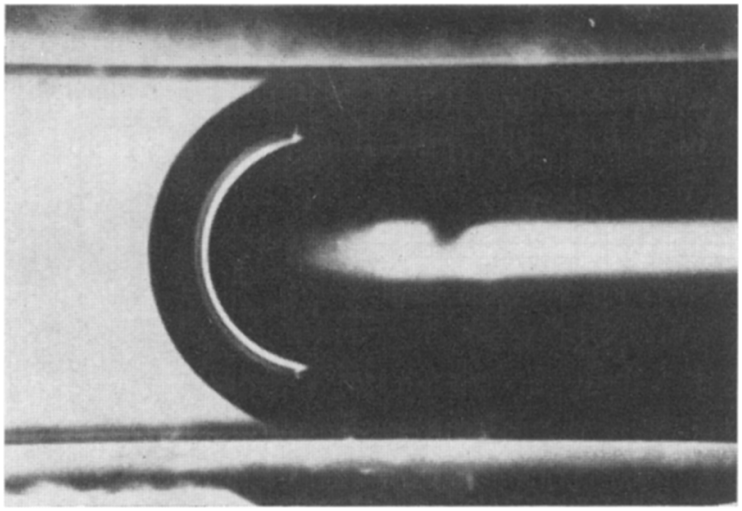

FIGURE 1.10: *Photograph of the advancing liquid/gas interface in a glass capillary tube. The liquid is left of the interface (from [61]).*

Most of the experimental studies found in the literature concern planar configurations. In particular, very few have investigated dynamic contact angle in tubes. We may cite three studies where capillary tubes are employed.

The first one is due to Hoffman [61] who investigated the shape of an advancing interface in a liquid/gas system in glass capillaries (Figure 1.10). The interface velocity was varied from roughly 0.8 μm.s^{-1} to 0.6 mm.s^{-1} assessing the complete range of contact angles from 0 to 180°. Note that velocities are small compared to our own study. He found that the apparent contact angle θ can be correlated to a function of the capillary number Ca plus a shift factor $F(\theta_e)$ when interfacial and viscous forces are the dominant effects controlling the system. The shift factor $F(\theta_e)$ was found to be fully determined by the static contact angle θ_e between the liquid and the solid substrate, when interfacial forces do not change during the flow. In a review paper [50] Blake shows that both the conventional hydrodynamic theory and the molecular-kinetic theory are able to represent the data reasonably well, with acceptable values of the fitting parameters.

The second one was carried out by Fermigier & Jenffer [62] who measured dynamic contact angles during the displacement of silicone oil/gas interfaces in capillary glass tubes. Their data were in good agreement with the so-called Hoffman-Tanner law ($R(t) \sim t^{1/10}$), and with the Cox model (Equation (1.13)).

The third example is experiments by Quéré [63] for a variety of liquids and contact angles, with alcanes in Teflon capillaries. The velocity of the segment of liquid was varied from 10 μm.s^{-1} to 10 mm.s^{-1}. He shows that the critical speed is proportional to the cube of the contact angle as suggested by the Cox-Voinov model and also by the hydrodynamic model (Equation (1.14)) [36, 37], and the thickness of the liquid film is proportional to the two-thirds power of the speed as for a LLD-Bretherton film (Equation (1.1) and (1.2)).

A last example also of interest for us, that is not with a tube but with a horizontal plate, is an experimental study carried out by Redon *et al.* [64] on the viscous dewetting process by nucleation. Their experiment consists in creating a hole in a uniform film of liquid by blowing air. The metastable film dewets from the partially wetting surface. The liquid accumulates into a visible rim. The width of the rim increases with time. This work validates the scaling given by Equation (1.13): θ versus Ca. Surprisingly this law does not include the thickness of the macroscopic film as a parameter, suggesting that there is a limit dewetting velocity.

The different studies reported previously suggest that a coupling seems to occur between the microscopic and macroscopic scales. The necessity to combine the two scales is crucial to predict the velocity dependance of the contact angle and the shape of the interface. Progress was made by Eggers [65, 66], who elucidated quantitatively how the contact line displacement depends on the withdrawal speed when coating an inclined plate. He derived an analytical expression of the critical speed Ca_c, which is related to both the microscopic behavior of the contact line and the macroscopic geometry. However, numerically the threshold is not very different from the Cox-Voinov prediction Ca_c^{Cox} (Equation (1.14)). Another limitation is that what happens above the threshold has not been considered.

1.4 Thin films with moving contact line

The film deposition process on a partially wetting plate can exhibit much more complicated behaviors, mostly due to the presence of moving contact lines. This time, the velocity v of the dip coated plate, for example, has to be large enough to observe the deposition of a liquid film.

As numerically shown by Snoeijer *et al.* [1], the critical behavior of the film deposition is avoided and is associated with a saddle-point bifurcation of stable and unstable meniscus solutions, and the film that can be physically realized is actually one stable branch of a wider family of solutions. Interestingly, Snoeijer *et al.* [1] also identified a series of bifurcations around a capillary number Ca^* smaller than the critical one Ca_c. The behavior of the unstable solutions was analytically interpreted by Chan *et al.* [67], who also presented an explicit expression for the critical point of a vertical plate by extending the work of Eggers [66]. Details of the bifurcation curves for inclined plate were recently studied by Galvagno *et al.* [68] and Tseluiko *et al.* [69], who also found discontinuous transitions of the film solutions.

Moreover, the entrained film can present instabilities beyond another critical capillary number. The first kind of particular feature that can be observed is that the film is not completely distributed over the entire plate [70, 71, 2, 3]. The film admits a trapezoidal or triangular shape, which is characterized by the presence of inclined contact lines as illustrated in Figure 1.11.

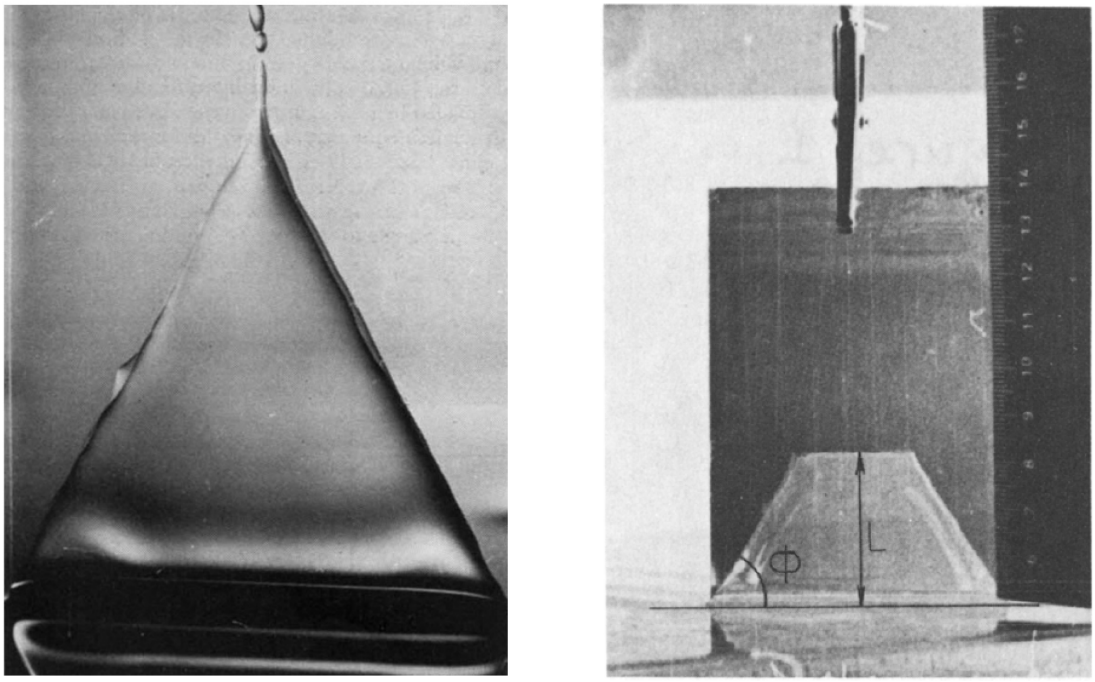

(a) (b)

FIGURE 1.11: *Examples of unusual film shapes. (a) Triangular film obtained by Blake & Ruschak [70]. (b) Trapezoidal film observed by Petrov & Sedev [71].*

Similar contact-line inclination was observed in the context of sliding drops [72, 73, 74]. The inclination is an effective way to reduce the normal speed of the contact line relative to the plate, which is believed to be constrained by a maximum. Blake & Ruschak [70] postulated that this normal speed remains a constant, irrespective of the inclination angle. As demonstrated in a recent work by Gao *et al.* [75], the constant-speed assumption was only valid up to a logarithmic correction, and a significant reduction of the contact-line speed was predicted for large inclination angles.

The second kind of particular feature found is that the film is not of uniform thickness. As predicted by Hocking [4], in addition to the LLD film, there exists a region close to the contact line that displays a jump, whose thickness does not follow the LLD law (Equation (1.1)). Hocking's predictions were confirmed experimentally by Snoeijer *et al.* [2]: the thickness of this part of the film is fully determined by the physics of the contact line (Figure 1.12). In a later work, Snoeijer *et al.* [76] showed that the LLD film may be absent at the early stages of the motion, when the capillary number is close to the critical value for film entrainment. The plate was instead coated by a temporary thick

film, which is again determined by the contact line. In fact this film solution is directly connected to the bifurcations at $Ca = Ca^*$. The measurement of the thickness of this thick film provides one single value, independently of the capillary number Ca and depending only on Ca^*. The thick film is connected to the liquid bath via a dimple similar to the Wilson thick film (Section 1.2.2). The dimple disappears when the LLD film grows. The behavior of the dimple-LLD film transition remains to be further studied.

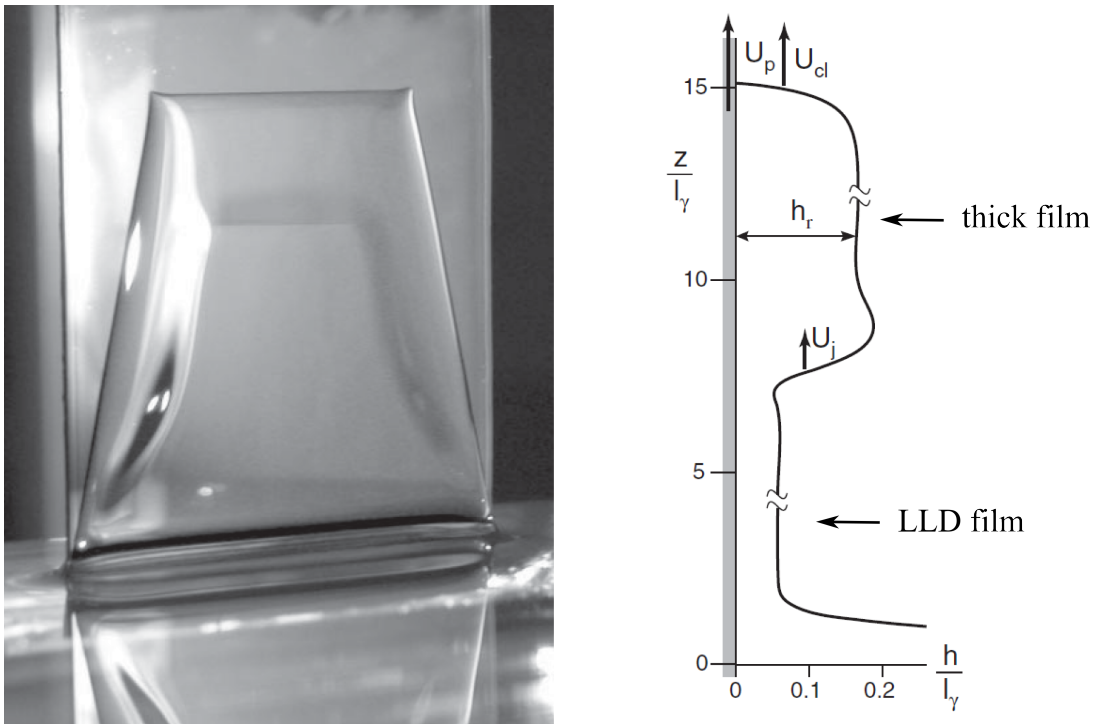

(a) (b)

FIGURE 1.12: *(a) picture and (b) profile of the two films thickness coexistence observed by Snoeijer et al. [2].*

Very recently, Gao *et al.* [5] have solved the full Stokes equations considering a dip coating configuration in the presence of a moving contact lines. They found very similar results and numerically identified four different regimes corresponding to different film morphologies, when increasing the plate velocity. The first one corresponds to a stationary meniscus where the triple line velocity is equal to the meniscus velocity Ca, without film (Figure 1.13). The second regime for $Ca > Ca_c$ is a speed-independent thick film connected to the liquid bath through a stationary dimple.

In Figure 1.13, we note that the triple line velocity is constant in this regime (regime II in Gao's notations) and defines Ca^*. In the third one, there is coexistence of a thick film and of the classical Landau-Levich-Derjaguin (LLD) film connected by a propagating capillary shock. In their regime II and III, the velocity of the triple line has one unique value Ca^* which is smaller than the threshold of regime II Ca_c: there is velocity discontinuity. Finally, they report a regime IV where a film with a monotonically varying thickness is

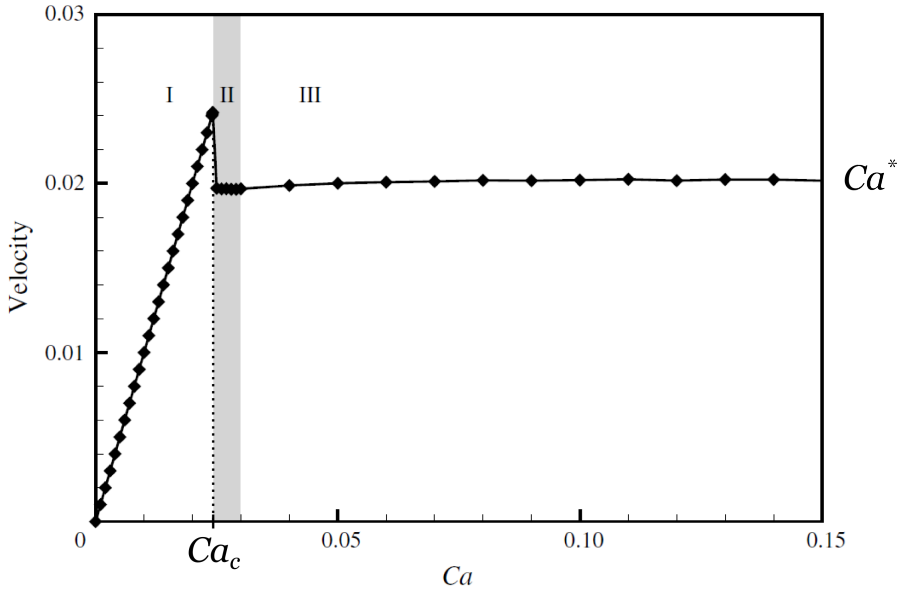

FIGURE 1.13: *Numerical resolution of the contact line velocity with respect to the plate (rescaled by $v_{liq} = \gamma/\eta$) versus Ca. The grey bar marks the flow regimes II (from Gao et al. [5]).*

obtained (not represented in Figure 1.13). They found that the onset of film deposition occurs at a vanishing apparent contact angle, consistent with the predictions of lubrication theory.

1.5 Summary and scope of the manuscript

The current understanding of the problem in the literature is summarized in Figure 1.14. On horizontal surfaces, moving contact lines can destabilize into a film when the velocity reaches a critical capillary number Ca^*. Above the wetting transition, the entrained liquid film is assumed to be a LLD or Bretherton film. On vertical surfaces where gravity come into play, the phenomena are similar except that the morphology of the entrained liquid film is more complex: there is coexistence of a thick film, with thickness independent of the velocity and given by $e = l_c\sqrt{3Ca^*}$, and of a classical LLD film.

As mentioned in the introduction, our work addresses the practical problem of surface contamination due to the intermittent flow of low viscosity fluids through a polymer tube at large flow rate. This contamination is essentially due to liquid film deposition behind the segment of liquid. The current state of the art shows that there is no accurate picture of the problem of film coating with moving contact lines in a partially hydrophobic tube. The predictions of the available literature are quite clear for plates and high viscosity liquids. Since the tube is hydrophobic, films should not form below a high threshold velocity close to Ca^* and given by Cox-Voinov. Above that threshold a two film regime should be observed. The thick film should have constant thickness and dewetting velocity

Ca^* independent of slug velocities. At threshold a temporary thick film may form, with the same thickness and dewetting velocity.

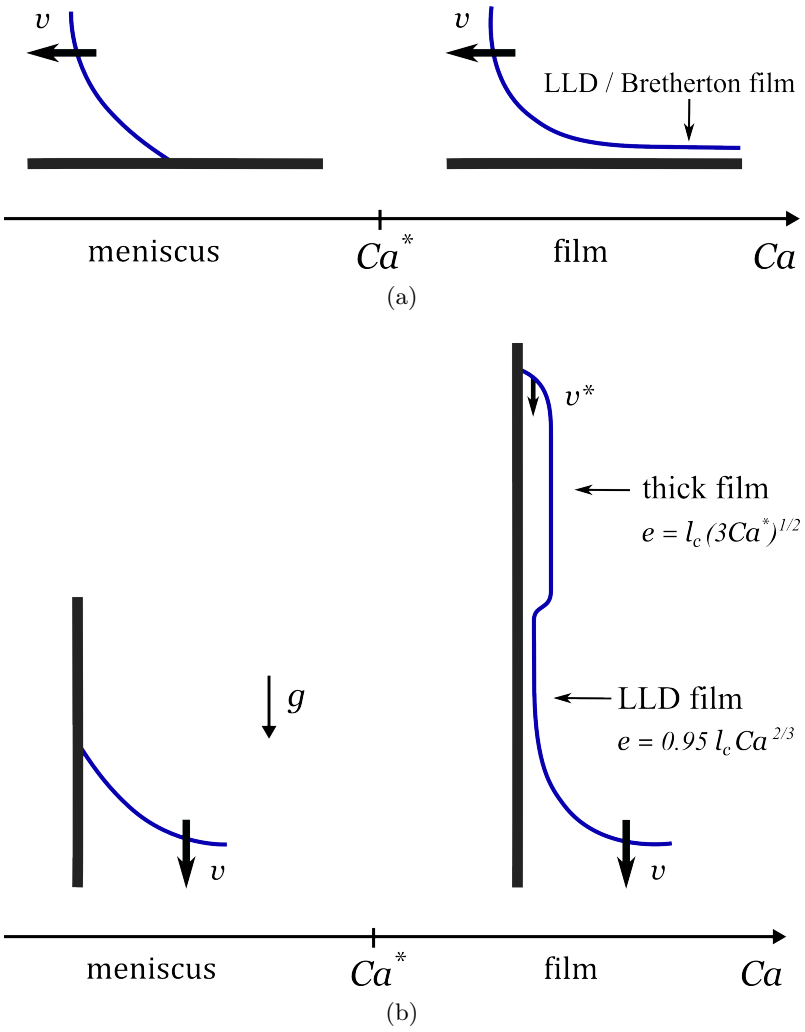

FIGURE 1.14: *(a) Literature on the dynamics wetting on horizontal solid surface. (b) Literature on the dynamics wetting on vertical solid surface.*

In Chapter 2, we will describe the experimental and numerical tools developed to investigate these questions. Chapter 3 will be devoted to the low velocity range using various liquid viscosities in order to determine the characteristics of the dynamic wetting transition. We will present experimental data and theoretical predictions on the evolution of the receding contact angle as a function of Ca for various liquid viscosities η. In Chapter 4 and 5, we will focus on the film aspects. We will prove experimentally and theoretically the existence of a thick film which does not behave as expected from the literature, in addition to the two film morphology and show that in our systems there are two very distinct thresholds in Ca. Finally in the last chapter, we will investigate the influence of the tube surface chemistry, and see how it impacts the meniscus instability and film formation.

Chapter 2

Experimental description

To investigate liquid flow in tubes, we have developed a setup which is described in the following. We also give details on the materials and liquids we used and on the numerical methods we have resorted to.

2.1 Experimental setup and measurement techniques

In this work, we have built an experimental setup allowing to visualize a liquid segment flowing in a tube at high velocity. In the following, this setup will be denoted "large velocity setup". We want to investigate what happens at the front and rear menisci of the liquid slug (segment); in particular if liquid deposition occurs behind the liquid segment, but also under which conditions and if it is as a film or as drops. We also aim at measuring the film thickness whenever it formed.

2.1.1 Observation of the liquid film

The experimental setup developed consists in imaging the flow of a fluid segment, or slug, in a vertical tube, as shown in Figure 2.1. To start an experiment, a slug of controlled volume is taken to its initial position at the top of the vertical tube by means of a syringe pump. Initially, the top part of the tube is kept closed and the slug is thus at rest. Then, the slug is brought to the desired velocity by opening the upper part of the setup, to the ambient atmosphere or to a pressurized chamber. The flow observed at high velocities requires a large setup: here the tube is 1.5 m high. Slug motion is monitored in transmission with a high speed camera and a LED backlight, at a frame rate ranging between 5 and 1000 frames per second. An example of observation is shown in Figure 2.2. The motion of the slug can be controlled in two different manners:

- The top of the tube can be directly connected to atmospheric pressure using an adjustable valve. In this case the flow is driven by gravity and pressure drop at the valve, and the slug presents an accelerated motion at the early stage of the experiment, which is non negligible. The velocity directly depends on the weight of the liquid segment and to the size of the valve opening. Therefore, if part of

the liquid is deposited behind the slug during the experiment, the slug velocity will decrease. For this type of velocity control, flow observations and measurements are restricted to a limited zone of the tube.

- Alternatively, the tube can be connected to pressurized nitrogen gas. The gas flow-rate is controlled at the top of the setup allowing a fine control of the slug velocity. The start of the slug motion is close to instantaneous. Small glitches are observed but the velocity is stabilized within 0.4 s. This method provides constant speed of the fluid segment along the whole length of the tube. Flow observations and measurements can be achieved on the whole length of the tube.

In both configurations, the slug can reach a large range of velocities, from 1 μm.s^{-1} up to 1 m.s^{-1}, and the same phenomena are observed. The second option, with the advantage of constant speed, is the one used in the following. In our setup gas admissions controlled by a solenoid valve, and camera recordings are synchronized using a Labview script that we have developed.

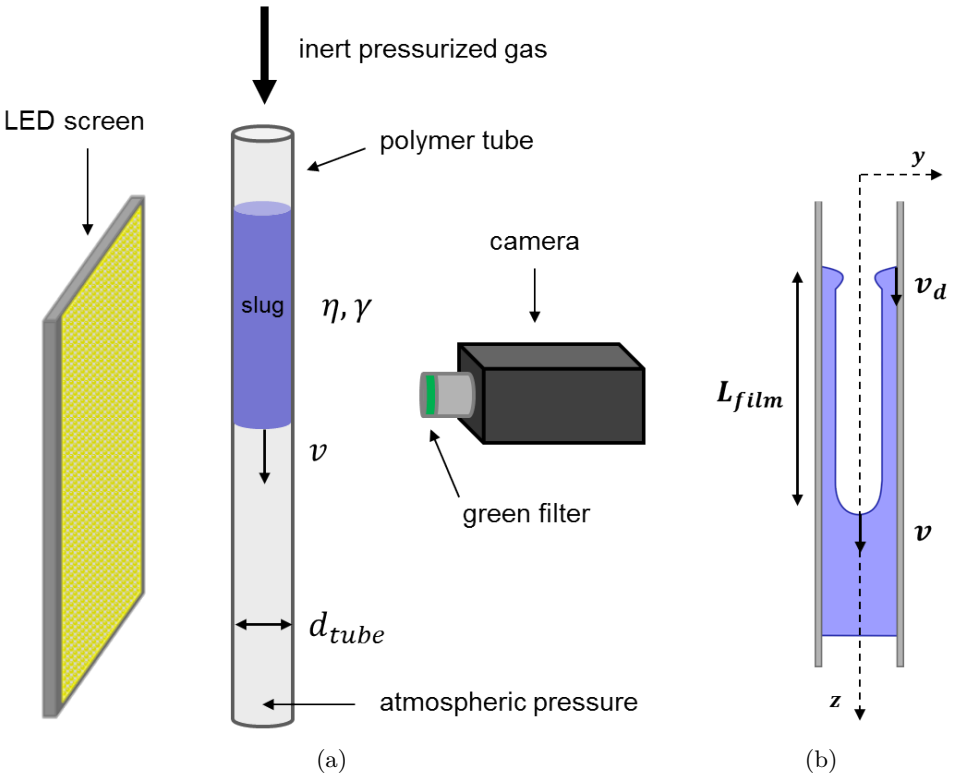

FIGURE 2.1: *(a) "Large velocity setup" for liquid film visualization. (b) Schematic representation of a flowing slug with liquid film deposition.*

The tube is polymer based (PVC) and quite transparent. Typical inner and outer diameters are $d_{in} = 6.4$ mm, $d_{out} = 9.5$ mm. The inner radius is larger than the capillary length of water $l_c = 2.7$ mm. Consequently, a liquid slug does not hold in the tube if not retained by an external force. This makes the experimental manipulation harder, and we have to close the tube to hold a slug at rest. Tube length is about $L_{tube} = 1.5$ m. Details

on the tube materials will be given in Section 2.2 as well as a characterization of the inner tube surfaces.

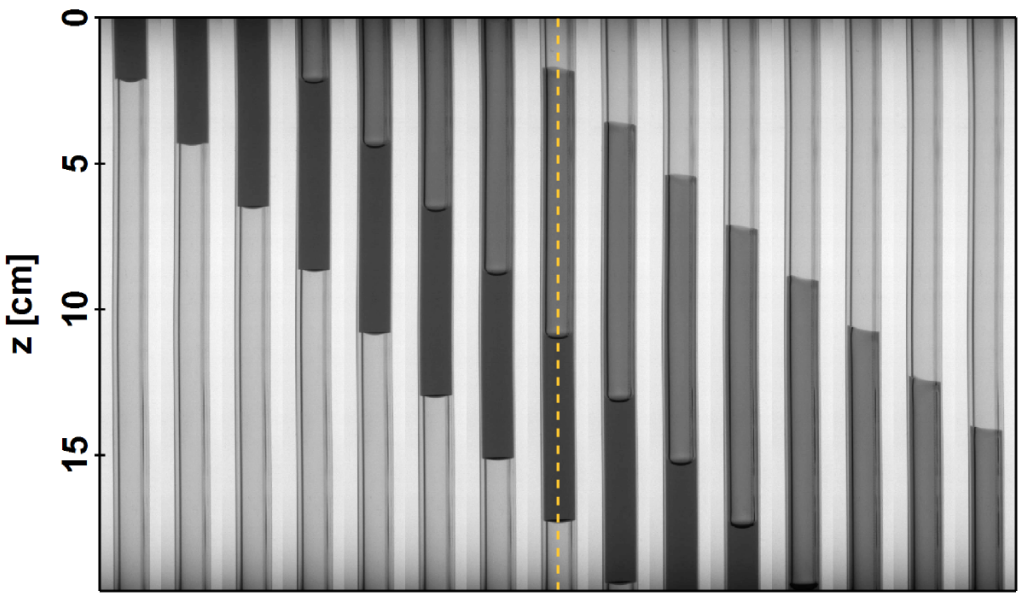

Figure 2.2: *Image sequence of a typical experiment where a liquid film is deposited at the rear of the liquid slug (light grey). The slug appears in dark grey, $V = 2$ mL of dyed water. The inner diameter of the polymer tube (PVC) is $d_{in} = 6.4$ mm. The images are separated by a time step of $\Delta t = 0.8$ s.*

The tube curvature and material makes the visualization of the inside of the tube difficult. The choice of lighting, camera and optics were therefore critical. Moreover, we wanted to assess two, *a priori*, incompatible elements at the same time: a wide range of velocity requiring high frequency and a long observation window to catch a long part of the tube. To overcome this difficulty, we have chosen a CMOS Sentech Black & White (STC-CMB2MCL 2MP), with a 2 Megapixels rectangular sensor (2048×1088). With a good choice of the optics, we were able to record a tube length ranging from 1 cm up to 1 m at a frequency going up to 1000 Hz on the 2048 pixels. A long LED backlight provided a uniform and steady illumination over the observation area.

The liquid slug was first carefully injected at the top of the tube using a syringe pump, allowing to control the initial volume from $V = 0.1$ mL up to $V = 60$ mL. In a typical experiment, initial slug volume was $V = 2$ mL.

2.1.2 Velocity measurement

Thanks to dye addition, liquid/air interfaces are optically outlined and can be tracked directly on the images recorded by the camera. Video analysis is based on the extraction of the transmitted light intensity along the center line of the tube (line width = 1 pixel), to build a spatio-temporal diagram. As an example, Figure 2.3 presents the spatio-temporal

diagram extracted from the image sequence given in Figure 2.2. In the example of Figure 2.2 and Figure 2.3, a liquid film is deposited at the rear of the slug. The slug appears in dark grey and the film in light grey. Interfaces correspond to changes in the intensity of the recorded images. Their velocities are measured as the slopes formed by these intensity steps in the spatio-temporal diagrams (Figure 2.3).

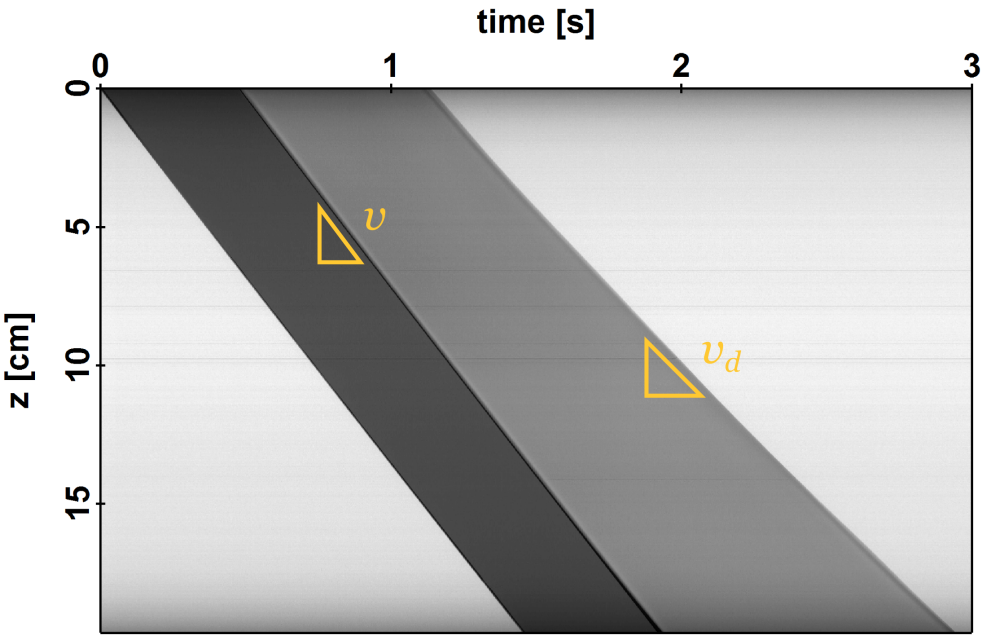

FIGURE 2.3: *Spatio-temporal diagram extracted from the central zone of the tube (Figure 2.2). Velocities of the different interfaces (v and v_d) are given by the slopes formed by intensity steps.*

The different velocities are defined as v the velocity of the slug and v_d for the velocity associated to the dewetting triple line at the film end (Figure 2.1b). Note that the velocity of the slug at the front is slightly smaller than the velocity at the rear of the slug, since the volume ejected by the slug to form the film is small but non zero. The problem can be considered as quasi-static, since velocities during an experiment are constant along the tube.

2.1.3 Film thickness measurement

Film thickness measurement by mass conservation

The film thickness is usually evaluated in the literature using mass conservation under the assumption of constant film thickness e [18, 22]. Indeed, the mass conservation of the system slug of volume V_{slug} and film of volume V_{film} writes:

$$\frac{\mathrm{d}V_{film}}{\mathrm{d}t} = -\frac{\mathrm{d}V_{slug}}{\mathrm{d}t} \tag{2.1}$$

Here, the considered section of the slug is the disc of radius $R = 3.2$ mm, while the section of the film is an annulus of external radius R and thickness e. Equation (2.1) rewrites as follows:

$$\pi \left(R^2 - (R-e)^2 \right) \frac{\mathrm{d}L_{film}}{\mathrm{d}t} = -\pi R^2 \frac{\mathrm{d}L_{slug}}{\mathrm{d}t} \tag{2.2}$$

which leads to

$$e = R \left(1 - \sqrt{1 - \frac{\mathrm{d}L_{slug}}{\mathrm{d}L_{film}}} \right) \tag{2.3}$$

This method does not provide the instantaneous film thickness profile, so that we have developed an optical measurement method, described in the next section, to assess the liquid film profile. We found that the optical method is also more accurate in our experimental conditions.

Optical measurement of the film thickness

A light absorption measurement method has been implemented in order to extract the film thickness profile. The liquid film thickness is obtained directly from the intensity I measured by the camera, using the Beer-Lambert law:

$$A = -\ln \left(\frac{I}{I_0} \right) = \varepsilon_m l c \tag{2.4}$$

where A is the absorbance, I and I_0 are the transmitted intensity through the solution sample and through the reference respectively, ε_m the molar extinction coefficient in L.mol^{-1}.cm^{-1}, l the thickness of the sample in cm and c is the solution concentration in mol.L^{-1}. This law relates the absorption of light to the properties of the medium through which the light is traveling. The thickness of the sample will be two times the thickness of the liquid film, $l = 2e$.

The choice of the dye was critical. We first used Rhodamine B, but this dye was adsorbed and even absorbed at the inner wall of the tube which resulted in contamination of the tube. As a result, the tube was darker and darker with time, and the reference I_0 was therefore no longer valid. We then tried Congo Red dye, which does not diffuse into the tube but impacts the surface tension of our aqueous solution. Finally we tested New Coccine, which does not contaminate the tube nor change the interfacial properties of our liquid phase. This dye, New Coccine, absorbs in the whole visible spectrum: the extinction coefficient $\varepsilon_m(\lambda)$ is a function of the wave length λ. As the setup is back lighted with a white LED screen, the Beer Lambert law has to be integrated on the whole spectrum to get the film thickness. To avoid this complication, the objective of the camera was equipped with a bandpass green filter of narrow width (10 nm) whose wavelength was chosen to be at the maximum of absorption of the dye $\lambda = 508$ nm, and ε_m was considered constant in this narrow window.

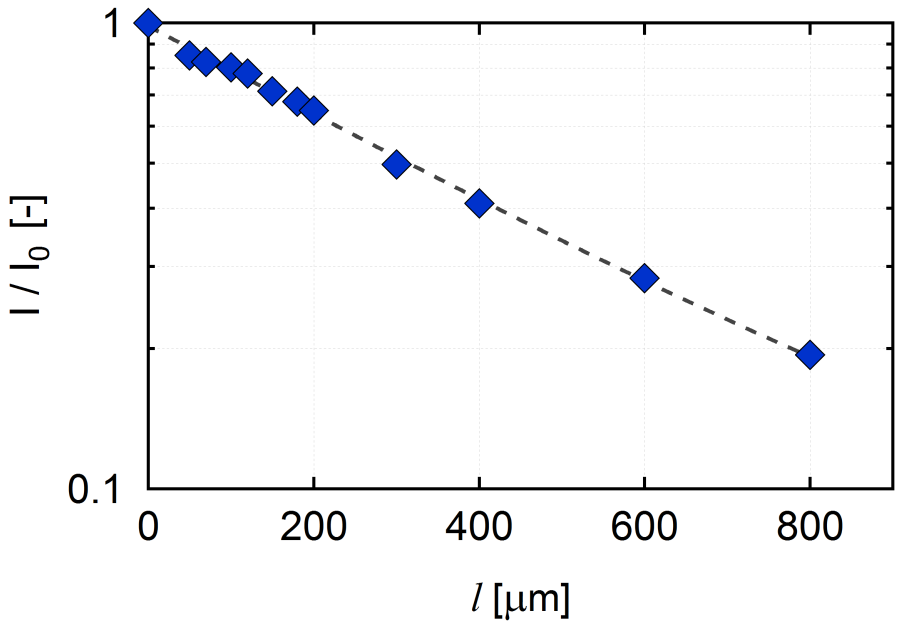

FIGURE 2.4: *Calibration curve $I/I_0 = f(l)$ carried out with glass capillary tubes with various rectangular cross section.*

To ensure a quantitative measurement of film thickness versus absorbance, a calibration was carried out for each dye solution (see Section 2.2.1). Glass capillary tubes with rectangular cross section, of inner thickness l filled with the solution containing a concentration $c = 4.9\ 10^{-4}$ mol.L^{-1} of the dye ($M = 604.47$ g.mol^{-1}). Intensity I was measured and normalized intensity I/I_0 was computed as a function of capillary thickness l, allowing to assess the constant $\tau = \varepsilon_m c$ (Equation (2.4)). Here, the reference is measured by filling the capillary with pure deionized water. The results are plotted in Figure 2.4 in a log-linear plot in which the thickness l of the capillary tube was varied between 10 and 800 μm. The data can be fitted to a line with a slope $\tau = 22.02 \pm 0.02$ cm^{-1}. This gives an effective extinction coefficient of the solution $\varepsilon_m^{eff} = 44945 \pm 40$ L.mol^{-1}.cm^{-1}.

In the case of a liquid film, the reference $\widetilde{I}_0$ is taken as the intensity of the transmitted light through a pure water film in the same tube. This allows to avoid any effect of optical diffusion from the roughness of the tube walls. The calibrated value of τ holds in this configuration. In a tube where two films are in the light path, the film thickness e is estimated as:

$$e = -\frac{1}{2\tau} \ln\left(\frac{\widetilde{I}}{\widetilde{I}_0}\right) \tag{2.5}$$

where $\widetilde{I}$ is the transmitted intensity through the tube and the film.

Finally spatio-temporal diagrams of the thickness, as represented in Figure 2.5, are obtained. Uncertainty on the film thickness measurement is typically $\pm$ 5 μm.

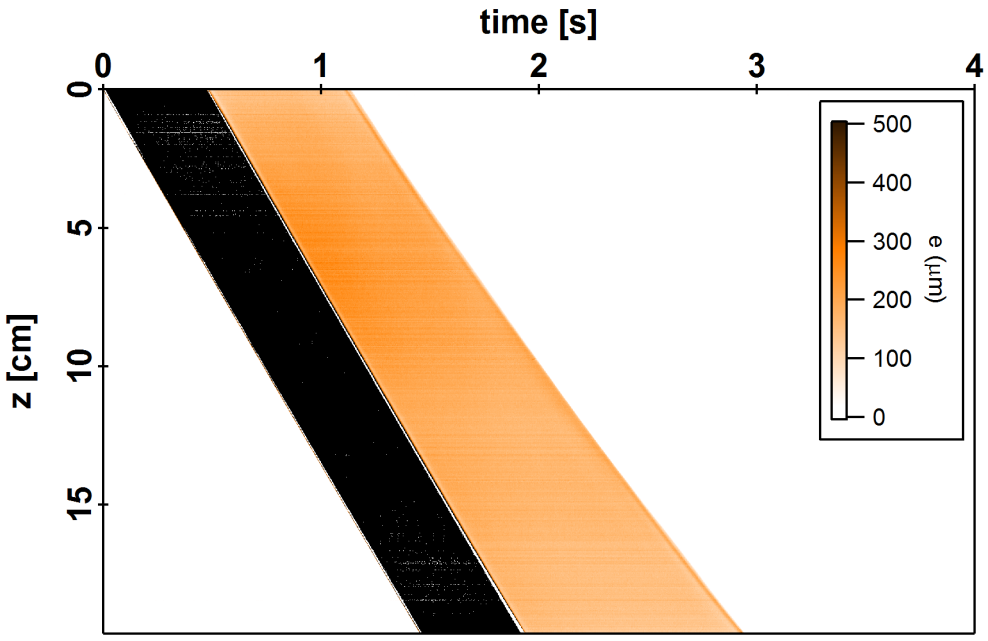

Figure 2.5: *Converted spatio-temporal diagram, giving a thickness map of the film for a typical experiment. The corresponding spatio-temporal diagram is represented in Figure 2.3.*

2.1.4 Contact angle measurement

As we are dealing with a wetting problem, it is of interest to measure the contact angles at the triple line. Thanks to the slug geometry it is possible to measure simultaneously advancing contact angles at the front of the slug and receding contact angles at the rear of the slug. It is also interesting to get access to the contact angle at the dewetting triple line, *i.e* the top of the liquid film. Different methods have been implemented to measure these angles.

Direct contact angle measurement in a tube

For low velocity displacements, typically below 5 cm.s^{-1}, a smaller setup shown in Figure 2.6a has been designed. In the following, this setup is denoted "low velocity setup".

To minimize the optical distortion of the meniscus shape due to the curvature of the tube walls, the outer tube/air interface is optically erased by immersing the tube in a rectangular cell with index matching liquid. The liquid used is dimethyl phthalate. The fluid is now introduced from the lower part of the tube with a syringe pump, as shown in Figure 2.6b. Then we inject the liquid and measure the advancing contact angle at a given velocity. The velocity of the meniscus that can be achieved using the syringe pump is typically between $v = 1$ μm.s^{-1} and $v = 5$ cm.s^{-1}. To measure receding contact angles, we pull the liquid and direct measurement is made by evaluating optically the shape of the meniscus (Figure 2.6b). Contact angle values are given in Section 2.2.

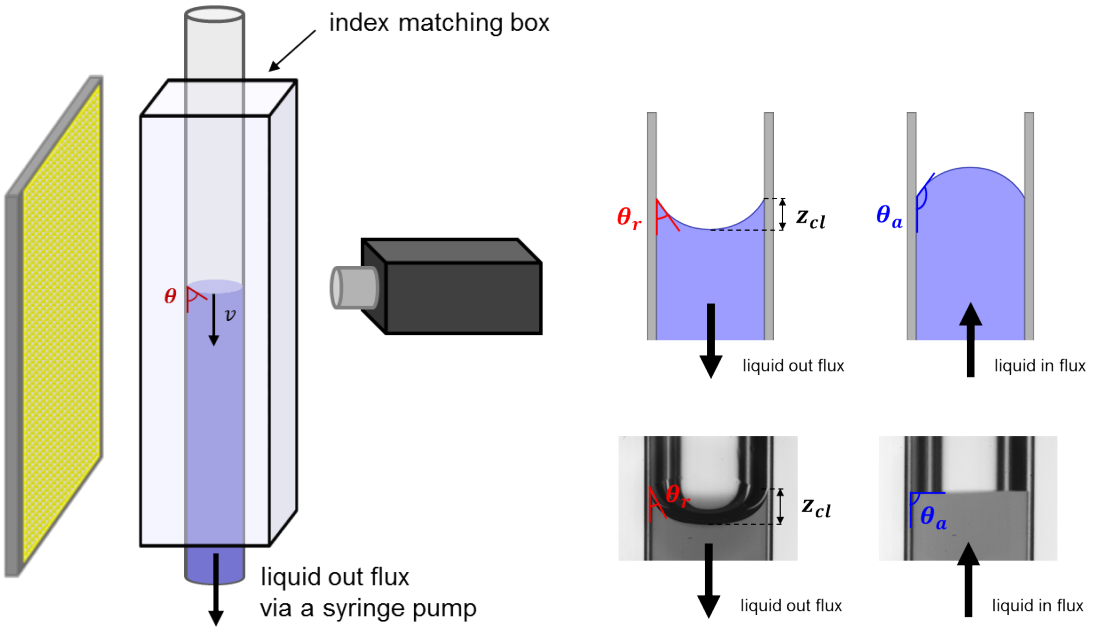

FIGURE 2.6: *(a) "Low velocity setup" using an index matching box to measure contact angle. (b) Parameters measured when pushing or pulling liquid using the "low velocity setup": schematics and images.*

This method has been compared to the classical method of drop deposition on a planar surface. To do so, tubes are opened and maintained flat. Or alternatively, tubes are recast as plates by molding. Similar results are obtained within the uncertainties.

Measurement from the film profile

With the previous method, we can measure the contact angles of a moving meniscus. Once a film is entrained at the tube wall, this method is not accurate enough to evaluate the angle at the triple line of the film. This is why another method has been used.

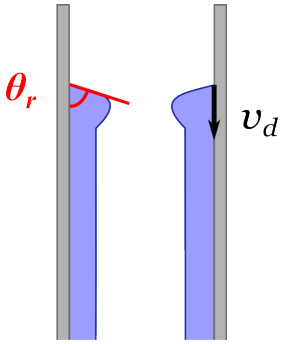

FIGURE 2.7: *Measurement of the receding contact angle from the profile: the measurement is achieved at the end of the film.*

In that case we use the "large velocity setup" Figure 2.1. From the spatio-temporal diagram converted into thickness (Figure 2.3), we can extract the profile of the liquid film. Taking the first-derivative of this profile close to the end of the film, we get an evaluation of the contact angle at the triple line as schematically represented in Figure 2.7.

2.2 Materials

2.2.1 Liquid solutions

To study the impact of viscous dissipation, aqueous glycerol solutions with varied concentrations have been used to adjust the viscosity η. Solutions are prepared with distilled water.

%wt glycerol	η (mPa.s)	γ (mN.m^{-1})	$v_{liq} = \gamma/\eta$ (m.s^{-1})	l_c (mm)
0	0.94	70.3	75	2.66
5	1.06	70	66	2.63
10	1.26	69.5	55	2.61
15	1.32	68	51.5	2.56
20	1.66	65.8	39.6	2.52
30	2.17	64	29.5	2.45
40	3.25	61.8	19	2.37
50	6	60	10	2.34
75	30	59	2	2.25

Table 2.1: *Characteristics of glycerol solutions: viscosity η, surface tension γ, liquid characteristic velocity v_{liq} and capillary length l_c. Solutions are prepared with distilled water. Viscosity and surface tension are measured at* 28° *C.*

The viscosity of the aqueous glycerol solutions was characterized using a low shear rheometer under simple shear in a Couette geometry. This kind of rheometer is well adapted for measurements on low viscosity fluids.

Surface tension was measured with a tensiometer (TECLIS), using a pendant drop method. This method is based on the numerical fit of the shape taken by a pendant drop inflated at the end of a needle [77]. The shape of the drop results from a balance between hydrostatic pressure and Laplace pressure, including surface tension. Note that the resulting equation is similar to the one corresponding to a static meniscus in the inside of a tube, apart from the fact that the liquid phase and the gas phase are inverted. The liquid characteristics were measured at 28° C, which is the temperature of the other experiments.

The glycerol concentration was varied in the range $0 - 75$%wt, to obtain a viscosity range $\eta = 0.94 - 30$ mPa.s covering more than one decade while the surface tension does

not vary much ($\gamma = 59 - 70.3$ mN.m^{-1} at 28° C). See Table 2.1 for more details on the characteristics of the glycerol solutions. The capillary length $l_c = \sqrt{\gamma/\rho g}$ is calculated based on the fluid density ρ taken from the literature [78, 79, 80].

In situations where the effect of surface tension was studied, it was varied over a larger range by using aqueous solutions of ethanol (see Chapter 6). The concentration of ethanol has been varied in the range $0 - 15$%wt, to obtain a viscosity range of $0.94 - 1.7$ mPa.s and a surface tension range of $37 - 70.3$ mN.m^{-1}at 28° C. The physical properties of the ethanol solutions are reported in Table 2.2.

%wt ethanol	η (mPa.s)	γ (mN.m^{-1})	$v_{liq} = \gamma/\eta$ (m.s^{-1})	l_c (mm)
0	0.94	70.3	75	2.66
5	1.15	56	48.7	2.40
10	1.22	49	40.2	2.24
15	1.7	37	21.8	1.95

Table 2.2: *Characteristics of ethanol solutions: viscosity η, surface tension γ, liquid characteristic velocity v_{liq} and capillary length l_c. Solutions are prepared with distilled water. Viscosity and surface tension are measured at 28° C.*

As mentioned earlier a red dye powder, New Coccine from Sigma-Aldrich, was added to enhance the contrast in the images and allow the measurement of film thickness. We have ensured that the dye has no impact on the rheological properties nor on the surface tension of the liquids at the concentration used $c_m = 300$ mg.L^{-1}.

2.2.2 Commercial polymer tubes

Commercial polymer tubes were plasticized polyvinyl chloride PVC Tygon S3^{TM} E-3603 from Saint-Gobain. Typical inner and outer diameters are $d_{in} = 6.4$ mm, $d_{out} = 9.5$ mm. This type of tube is hydrophobic. The determination of contact angles is a simple and direct method to characterize the hydrophobicity of surfaces. Contact angle measurements were performed by liquid meniscus displacement at a velocity $v = 0.3$ cm.s^{-1} in the tube, as explained in section 2.1.4. The quasi-static receding contact angle does not present significant variations with the glycerol concentration in the range investigated and is around $\theta_r^0 = 60°$, ensuring partial wetting condition. The measurement has not been carried out for water-ethanol mixture, but we expect a variation due to the strong change in the surface tension γ. The surface tension is supposed to be included in the theoretical determination of the equilibrium contact angle (Young's law).

The roughness of the inside of the tube is set by the industrial manufacturing process (extrusion). Looking closer at the surface, we found that the surfaces have roughnesses at two different scales: (1) a micrometric roughness shown on the profilometer image in Figure 2.8a, with typical height of few microns and lateral extension of about 0.2 mm.

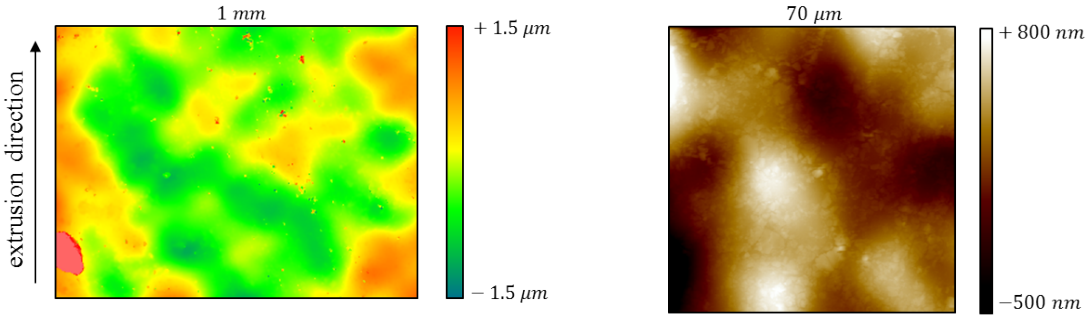

(a) (b)

FIGURE 2.8: *(a) Profilometer image from the inside of a PVC tube. (b) AFM image from the inside of a PVC tube.*

The roughness slope is low, typically within about 1/100; (2) a nanometric roughness observed on the AFM picture in Figure 2.8b with typical height of about 100 nm and a lateral extension in the 10 μm range. No particular orientation in the roughness was found, meaning that the extrusion process does not create anisotropic patterns in the extrusion direction.

To extend the hydrophobicity scales, we have also worked with Polydimethylsiloxane PDMS Sanitech® ULTRA 50 tubes, which is more hydrophobic than PVC. The quasi-static receding contact angle has only been measured for water at $v = 0.3$ cm.s^{-1} and is around $\theta_r^0 = 80°$. We can assume that as for PVC this angle should not present significant variations with the glycerol concentration in the range investigated, but should with the ethanol concentration. Typical inner and outer diameters are $d_{in} = 6.4$ mm, $d_{out} = 9.5$ mm. Other tube diameters have also been investigated (Table 2.3), and results are discussed in Appendix C.

Commercial Name	Type	d_{in} (mm)	d_{out} (mm)	θ_r^0 (°)
Tygon S3™ E-3603 ACF00017	PVC	6.4	9.5	60
Tygon S3™ E-3603 ACF00012	PVC	4.8	7.9	60
Tygon S3™ E-3603 ACF00007	PVC	3.2	6.4	60
Sanitech® ULTRA-C-250-2	PDMS	6.4	9.5	80
Sanitech® ULTRA-C-125-2	PDMS	3.2	6.4	80

Table 2.3: *Commercial tubes: name, type, internal diameter d_{in}, outer diameter d_{out} and quasi-static receding contact angle θ_r^0. This angle is measured with pure water at $v = 0.3$ cm.s^{-1}.*

2.2.3 Surface modified tubes

To extend the range of surface energy even further, we have chemically modified the inside of PDMS tubes by oxidation of the inner tube surface and adsorption of hydrophilic polymers. Briefly, right after a plasma treatment, different functional polymer solutions were introduced in the tube. By physical adsorption and formation of hydrogen bonds between polymer chains and activated PDMS surface, a stable and homogeneous surface of given hydrophilicity could be produced similarly to Papra *et al.* [81].

Plasma treatment

In order to create reactive sites on the silicone (PDMS) for subsequent attachment of hydrophilic polymers, PDMS tubes were treated with a plasma of air. This activation step produces free oxygen radicals to oxidize the first molecular layer, in particular to change $SiCH_3$ sites into SiOH [82]. To do so, one side of the tube was connected to a primary vacuum. As a result, plasma could be generated inside the tube with a high frequency generator (also named Tesla coil, by Electro-Technic Products, Inc., 50/60 Hz, 300 W). The plasma propagates along the tube length $L_{tube} = 1.5$ m. However, the plasma generation needs to be under low pressure condition, which leads to a limit on the diameter of the tube for a given wall thickness. Indeed, the tube collapses under vacuum as soon as the wall thickness to inner radius ratio is below 2. For that purpose, we have used PDMS tubes of inner diameter $d_{in} = 3.2$ mm to carry out the surface modification.

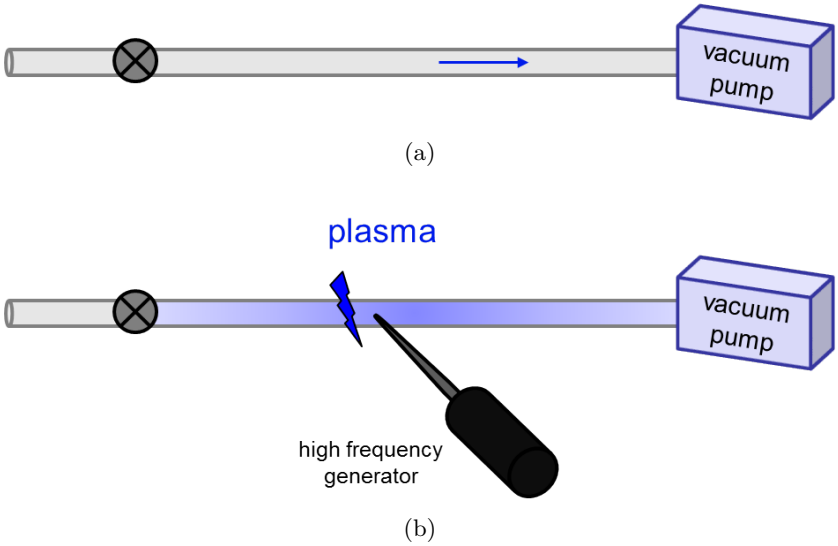

FIGURE 2.9: *Schematic representation of the plasma treatment: (a) first step vacuum, (b) second step plasma ignition. The plasma propagates along the tube* $L_{tube} = 1.5$ *m.*

Figure 2.9 shows the system and process of the plasma treatment for the modification of PDMS surface. The operational conditions were 1.5 minutes to reduce air pressure in the tube with primary vacuum pump and 15 seconds for the plasma treatment.

Hydrophobic recovery

The hydrophilicity of PDMS surfaces treated by a plasma is reported to be unstable. These surfaces gradually regain their hydrophobic properties upon exposure to air [83, 84]. This phenomenon, known as hydrophobic recovery, is caused by the migration of low molecular weight chains to the surface [85, 86, 87].

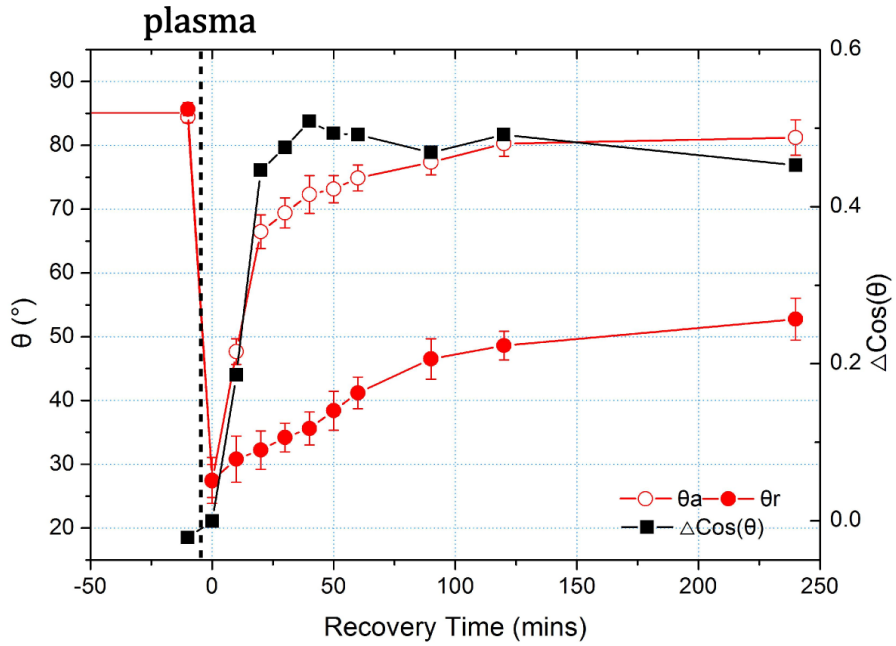

FIGURE 2.10: *Typical hydrophobic recovery curve: variation of the quasi-static advancing θ_a and receding θ_r contact angle (in red circle) as a function of time, and contact angle hysteresis $\Delta\cos\theta$ (in black square), where $\Delta\cos\theta = \cos\theta_r - \cos\theta_a$. Measurement are performed with water meniscus displaced at velocity $v = 0.3$ $cm.s^{-1}$.*

Contact angle measurements were performed by meniscus displacement at a velocity $v = 0.3$ cm.s^{-1} of water in the modified tube. For experimental convenience, the tube of smaller diameter were used and placed horizontally in that case. Measured quasi-static contact angles are plotted in Figure 2.10 as a function of time. The very first data points (at negative times) corresponds to untreated tubes. After plasma treatment, contact angles drop from $85° \pm 3°$ to $25° \pm 5°$ degrees. The produced surface is hydrophilic, which shows that plasma treatment is an effective technique for the modification of the inner surface of a tube. Nevertheless, the modified PDMS surface loses gradually its hydrophilic properties over time.

Polymers adsorption

In order to stabilize this hydrophilic property, a series of hydrophilic polymer solutions was introduced during 1 hour on the active surface by physical absorption. Polymers having oxygen atoms able to engage in hydrogen bonds were chosen: poly(ethylene glycol) (PEG)

and poly(dimethylacrylamide) (PDMA). Indeed, we found that the quasi-static contact angle decreases, and is stable over time (several weeks). This effect was attributed to the physical adsorption of the polymers onto the oxidized SiO groups of the silicone. We tested a wide range of molecular weight for PEG, $M_n = 1,000 - 2,000,000$ g.mol^{-1}, prepared at the concentration 1%wt. The use of a large molecular weight ($M_n = 2,000,000$ g.mol^{-1}) was key to stabilize the polymer adsorption. As the molecular weight of polymers increases, the hydrophobic recovery rate decreases. The global process to produce modified surfaces is summarized in Figure 2.11.

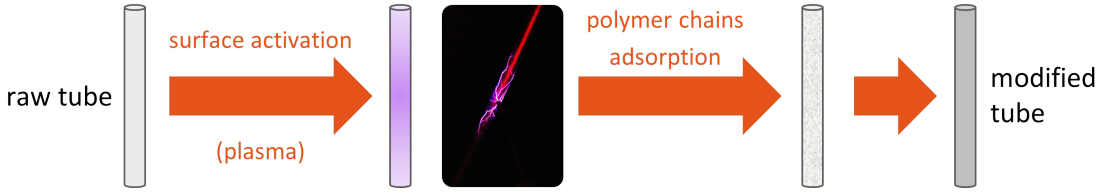

FIGURE 2.11: *Surface modification steps.*

The choice of the adsorbed polymer can provide tubes of controlled hydrophobicity (tube A and B), as summarized in Figure 2.12.

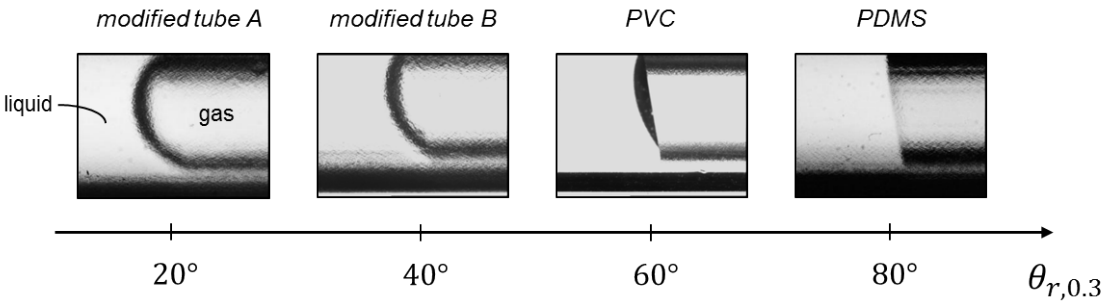

FIGURE 2.12: *Hydrophobic scale. Quasi-static receding contact angles θ_r^0 are given for pure water menisci displaced at a velocity $v = 0.3$ cm.s^{-1} in different tubes. (a) modified tube A is a PDMS tube with PEG 2,000,000 chains, (b) modified tube B is a PDMS tube with PEG 1,000,000 chains, (c) and (d) are PVC and PDMS commercial tubes see Section 2.2.2.*

2.3 Numerical methods

In this section, we provide general equations of the lubrication approximation theory applied to a liquid film. We also explain how we solve these equations to get the meniscus or the liquid film profiles.

2.3.1 Governing equations

Dynamic equations

We consider a liquid segment moving at a velocity $-v$ down a vertical tube of radius R. The liquid has a viscosity η, surface tension γ and density ρ and is in the gravity field g directed downward. The problem is described in cylindrical geometry in the reference frame of the slug centered in the tube (O, r, z) and is considered axisymmetric (Figure 2.13). We define the normal at the interface pointing towards the center of the tube, such that the interface curvature κ is positive.

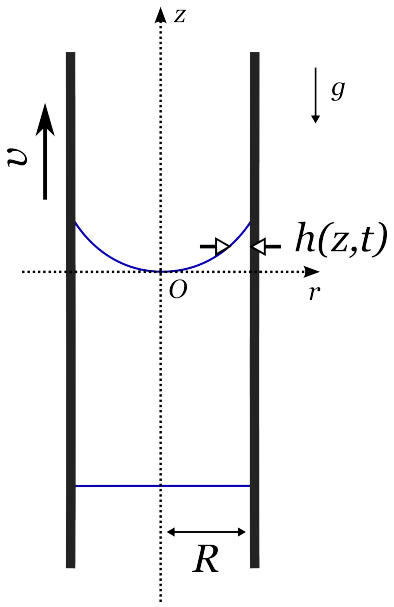

FIGURE 2.13: *In the reference frame of the liquid meniscus, our problem is equivalent to a static meniscus with a cylindrical tube moving up at velocity $+v$. The reference frame is the center of the liquid meniscus. The thickness profile is denoted $h(z,t)$.*

The liquid is in partial wetting condition. Inertial effects are neglected but gravitational effects are of importance. The velocity in the $z-$direction is denoted $v(z)$, the film thickness $h(z,t)$ where t is the time. Considering the Navier-Stokes equation in the lubrication approximation for a dynamic meniscus, mass conservation leads to the equation:

$$\partial_t h + \partial_z \left(\frac{h^3}{3\eta} \left(\gamma \partial_z \kappa - \rho g \right) + vh \right) = 0 \tag{2.6}$$

where κ is the curvature, so that $\gamma\partial_z\kappa$ is the capillary pressure gradient, ρg is the gravitational driving force, $\left(h^3/3\eta\right)^{-1}$ is the hydrodynamic impedance and vh is the convected flux.
For a steady state, $\partial_t h = 0$, Equation (2.6) can be integrated once to get:

$$\partial_z\kappa = \frac{1}{{l_c}^2} - \frac{3Ca}{h^2} + \frac{3qCa}{v_{liq}h^3} \tag{2.7}$$

where q is an integration constant.

This equation can also be seen as a force balance between viscosity η, surface tension γ and gravity ρg considering a flow-rate q. As already discussed in Section 1.3.1, Equation (2.7) presents a singularity when we get closer to the triple line ($h \to 0$). This singularity can be regularized in different manners: in this work we have chosen the Navier-slip condition, *i.e*, $h^2 \to h(h + 3l_s)$ where l_s is a slip length.

The problem can be reduced with appropriate dimensionless quantities:

$$\tilde{h} = Ca^{-1/2}\frac{h}{l_c} \tag{2.8}$$

$$\tilde{z} = Ca^{-1/6}\frac{z}{l_c} \tag{2.9}$$

$$\tilde{t} = Ca^{-1/6}\frac{vt}{l_c} \tag{2.10}$$

So that Equation (2.6) writes as:

$$\partial_{\tilde{t}}\tilde{h} + \partial_{\tilde{z}}\left(\frac{\tilde{h}^3}{3}\left(\partial_{\tilde{z}}\tilde{\kappa} - 1\right) + \tilde{h}\right) = 0 \tag{2.11}$$

In a cylinder the curvature of the interface has two components, one radial and one longitudinal:

$$\kappa = \frac{1}{R\sqrt{1+\partial_z h^2}} - \partial_z\left(\frac{\partial_z h}{\sqrt{1+\partial_z h^2}}\right) \tag{2.12}$$

We can define a dimensionless parameter $\Pi = l_c/(RCa^{1/6}) = Bo^{-1/2}Ca^{-1/6}$, to write the reduced curvature of the interface $\tilde{\kappa}$ so that $\partial_z\tilde{\kappa} = l_c^2\partial_{\tilde{z}}\kappa$. This number depends on the capillary number and on the Bond number. The Bond number $Bo = \rho g R^2/\gamma = (R/l_c)^2$ is defined as the dimensionless number measuring the importance of surface tension forces compared to gravitational forces.

$$\tilde{\kappa} = \Pi\tilde{\kappa}_r + \tilde{\kappa}_l \tag{2.13}$$

The capillary number is always lower than one. Moreover, tube radii are of the order of few millimeters, providing a Bond number of order 1. Consequently, gravitational forces are as important as surface tension forces. In the calculations below, we have neglected the radial curvature. Preliminary results including the tube curvature shows that the results are marginally affected for our large radius values, so that we effectively solve the flat plate problem.

Flat film

The solution for a free flat film flowing down a wall is obtained when taking $\partial_z \kappa = 0$ and $q = 0$ (external flux) in Equation (2.7) so that the flux is:

$$q_g = \frac{\rho g}{3\eta} h^3 \tag{2.14}$$

Static equation

The static meniscus case is obtained from Equation (2.7) taking $Ca = 0$ and $q = 0$. Surface tension balanced by gravity imposes $\partial_{\tilde{z}} \tilde{\kappa} = 1$. For the planar case (very large Bond number), an analytic expression of the static meniscus can be obtained. The exact solution can be found in Batchelor [88]:

$$\tilde{h} = \text{acosh}^{-1}\left(\frac{2}{\tilde{z}}\right) - \text{acosh}^{-1}\left(\frac{2}{\tilde{z}_1}\right) + \sqrt{4 - \tilde{z}_1^2} - \sqrt{4 - \tilde{z}^2} \tag{2.15}$$

with $\tilde{z}_1 = \sqrt{2\,(1 - \sin\theta)}$, where θ is the triple line contact angle.

In dimensional form it gives the equation used in Appendix B to get the contact angle out of the meniscus elevation $z_{cl} = z_1$. Contrary to the planar situation, there is no exact analytical solution for the shape of the interface in a cylinder.

2.3.2 Equation solving method

In order to get the numerical meniscus or film profile for steady state configurations, we integrate Equation (2.7) using a numerical method. A Runge-Kutta algorithm available in the software Igor is used via the function *IntegrateODE*. Our third-order equation is recast as three first order equations. The numerical solution is obtained by integrating derivatives from this set of coupled ordinary differential equations (ODE). The algorithms used calculate results at intervals that vary according to the characteristics of the ODE system and the required accuracy. It is possible to either record the output $\tilde{h}$ at given values of $\tilde{z}$ or $\tilde{t}$, or to run the integration in free-run mode. In the latter case, output $\tilde{h}$ records all steps regardless of the spacing of the $\tilde{z}$ or $\tilde{t}$ values.

To solve our third-order equation three boundary conditions are required. These conditions will vary according to the situation that we want to solve, and will be detailed where needed.

Some of the results actually reflect transient effects. To calculate these transients, Equation (2.11) is integrated with a finite difference scheme based on Bertozzi [89].

Chapter 3

Dynamic contact angle and wetting transition

3.1 Introduction

As already mentioned in Section 1.3, an external driving of the triple line can push the system sufficiently far from equilibrium such that it enhances the energy dissipated by viscous shear and undergoes a dynamical wetting transition forming a liquid film with a moving contact line. As a result, solid objects can be coated by a partially wetting liquid when withdrawn fast enough from a liquid bath as illustrated in Figure 3.1 [70, 63, 90]. However, the lack of understanding of the fundamental processes involved in the formation of dynamic contact angle makes any prediction very difficult in practice.

This chapter aims at better understanding this dynamic wetting transition in a cylindrical geometry using a low viscosity fluid. We address the following questions: what are the physical processes at play at the contact line and at which length scale? Are these processes induced only by non-equilibrium contact angles (Young's law) or by the concentrated friction force as assumed in the molecular kinetics theory or both or may be something else?

The tube used throughout this chapter is a PVC tubing of inner diameter $d_{in} = 6.4$ mm. For more details see Section 2.2.2. For capillary numbers Ca lower than a threshold value Ca^*, the free surface of the fluid is steady and is raised by a finite height z_{cl} above the level of the fluid free surface at the center of the tube. This height depends on the capillary number. In this regime, the contact line slips on the wall of the tube and the velocity v at the liquid/air interface is uniform along the liquid meniscus. In this chapter, we will investigate the evolution of the contact angle and show that this threshold is not so easily defined, reflecting the critical nature of the dynamic wetting transition. Then a comparison with the models available in the literature and presented in Chapter 1.3 will be performed. Finally, we will present experimental and numerical results concerning a time dependence of the film formation.

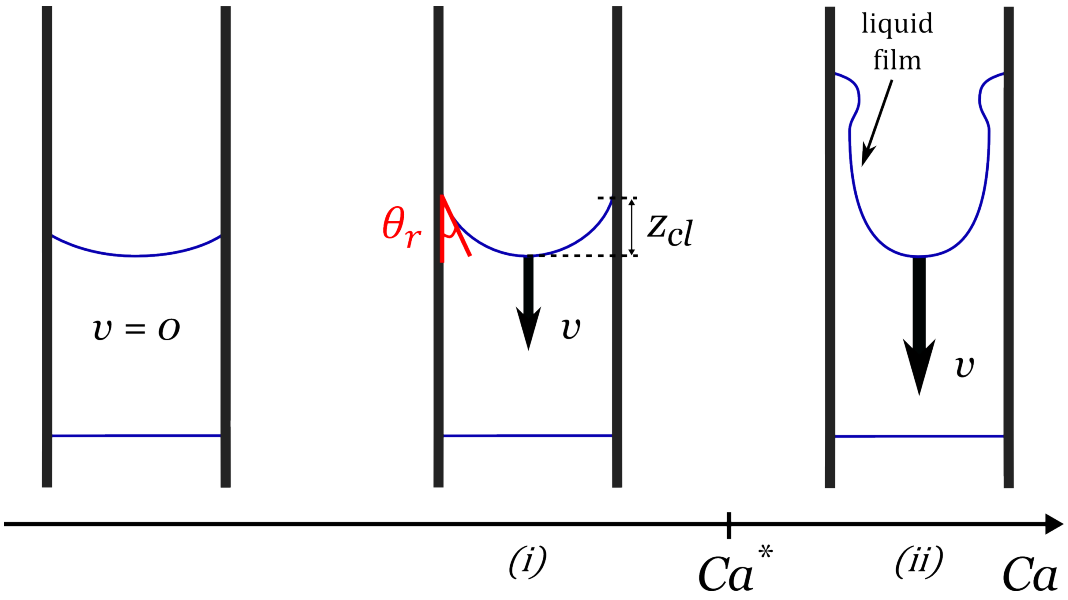

FIGURE 3.1: *Schematic of the evolution of a meniscus when increasing its velocity v, and consequently its capillary number Ca. Two parameters are mainly of interest: the receding contact angle θ_r at the contact line, and the meniscus elevation z_{cl}. Below Ca^*, the meniscus has a stationary shape (regime (i)). At some point a liquid film is entrained and the parameters θ_r and z_{cl} cannot be defined anymore (regime (ii)).*

3.2 Evolution of contact angle with slug velocity

We investigate in detail the contact angle evolution in the vicinity of the dynamic wetting transition. We use here the "low velocity setup" (below 5 cm.s^{-1}) presented in Section 2.1.4 to measure contact angles with a fine resolution. The fluid is pushed or pulled using a syringe pump connected to the lower part of the tube to induce the motion of the meniscus. For each experiment, both advancing and receding contact angles are measured at a given position in the tube using the direct measurement method. Initially, the meniscus is static and placed at a distance of $z = 3.4$ cm away from the measurement position in order to be in a quasi-stationnary state at the measurement position. The meniscus velocity v varies in the range 4.10^{-3} cm.s^{-1} to 5 cm.s^{-1}. The duration of the measurement is $\tau_m = 3.4$ cm$/v$ corresponding to the elapsed time after the beginning of the meniscus motion.

A typical series of experiments is showed in Figure 3.2 for receding menisci at various velocities v obtained with a 5wt% glycerol solution ($\eta = 1.06$ mPa.s). Each image corresponds to one experiment. Receding velocity varies from $v = 45$ μm.s^{-1} to $v = 3.3$ cm.s^{-1} (from left to right). We observe that the meniscus curvature and the elevation z_{cl} both increase with receding velocity. In the meantime, the receding contact angle θ_r decreases. Above a threshold velocity, a liquid film is entrained as observed on the last image. In the following, the regime where the meniscus is stationary will be denoted *regime (i)*,

and the state with a liquid film entrained behind the slug *regime (ii)*. The contact angle measurements are reported in Figure 3.3: by convention, the velocity is taken as positive for receding contact lines and negative for advancing ones.

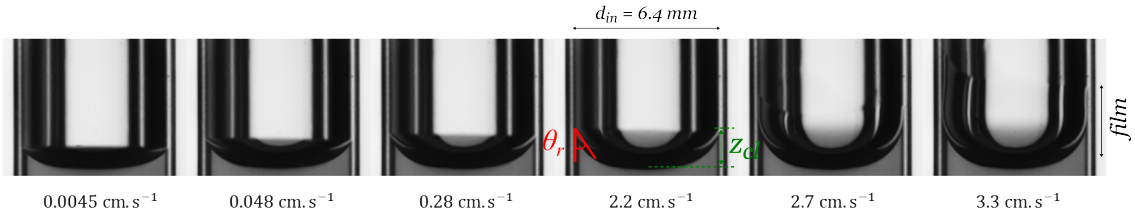

Figure 3.2: *Images of a receding meniscus for various meniscus velocity v as indicated below each image. The tube diameter is 6.4 mm. The liquid used is 5wt% glycerol solution, $\eta = 1.06$ mPa.s. The meniscus elevation z_{cl} and receding contact angle θ_r are measured for each value of v. z_{cl} increases and θ_r decreases with increasing v. Above a threshold velocity v^*, a liquid film is entrained as observed on the last image.*

We first focus on the receding contact lines (red symbols in Figure 3.3b). We observe that the receding contact angle decreases with increasing capillary number Ca. At very small capillary number (zone (2)), from 0 to 5 10^{-5}, a first strong decrease from 75° down to 45° is observed. Then, in zone (3), the receding contact angle decreases more slowly and is even almost constant on a significant range of capillary number ($Ca = 5\ 10^{-5}$ to $2.8\ 10^{-4}$). Region (4) corresponds to a second sharp decrease of the contact angle from 45° to 15°, down to the threshold value where a liquid film is entrained. This dynamic wetting transition, from *regime (i)* to *regime (ii)*, is indicated by the black vertical dashed line at $Ca^* = 4\ 10^{-4}$. It corresponds to the experimental observation of a film of length equal or larger than 6 pixels (limit of the measurement) after a time corresponding to a displacement of 0.08 mm in our observation window in Figure 3.2 where speed are indicated. Above Ca^*, the contact angle is measured at the end of the dewetting film using the method explained in Section 2.1.4. This contact angle is small but remains non zero (about $5 \pm 2°$).

We now examine the advancing contact angle measurements (blue symbols in Figure 3.3a). At very small capillary number (below 5 10^{-5}), in absolute value, the contact angle slightly increases from $\theta_a = 78°$ to 90°. Then, the advancing contact angle becomes independent of the capillary number. Up to $Ca = -2\ 10^{-2}$, we measure an advancing contact angle of 90°. The dotted-dashed lines in Figure 3.3 shows the Cox-Voinov prediction (Equation (1.13)): the equilibrium contact angle θ_e was chosen to fit the flat portions of the advancing and receding curves (zone (3)): $\theta_e = 45°$ for receding contact lines and 90° for advancing ones. From Figure 3.3b, it is clear that the sharp decrease in receding contact angle in zone (4) cannot be described by the Cox-Voinov model. We will analyze this point in more detail in Section 3.4.

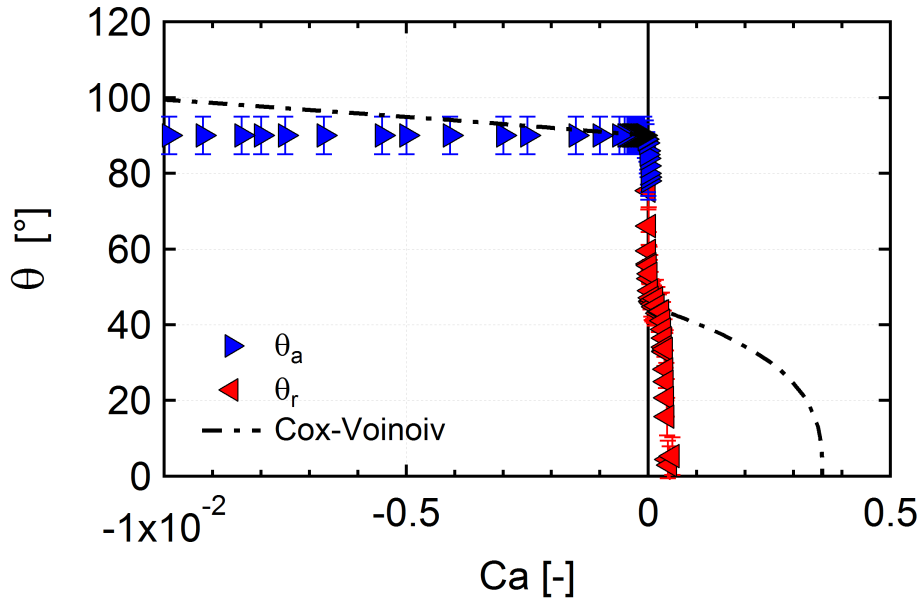

(a)

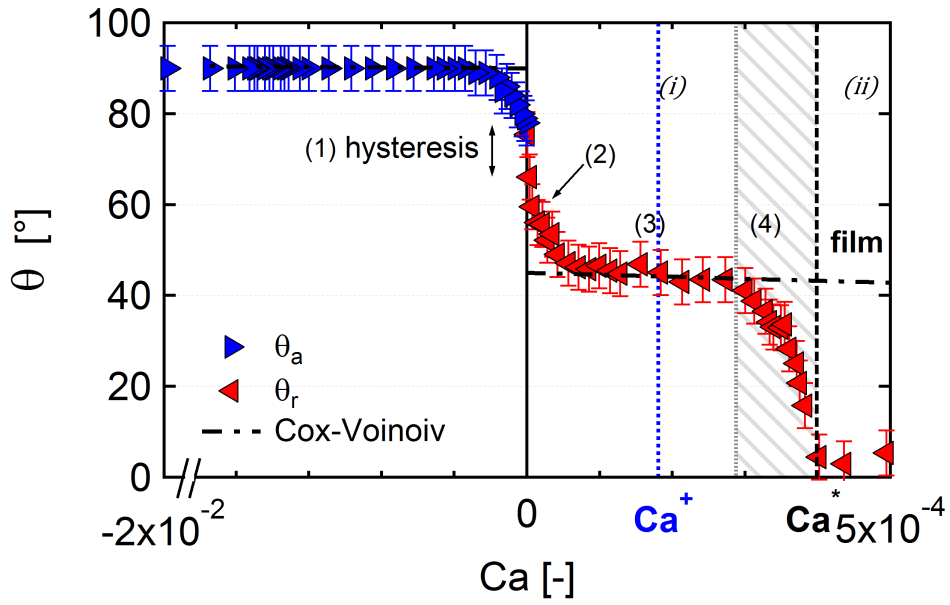

(b)

FIGURE 3.3: *Advancing θ_a and receding θ_r contact angles as a function of the capillary number Ca for a 5%wt glycerol solution ($\eta = 1.06$ mPa.s). (a) Full Ca scale (b) zoom in. By convention, receding contact lines have a positive velocity. The dotted-dashed curve represents the Cox-Voinov prediction for $\theta_e = 45°$ for receding and $\theta_e = 90°$ for advancing triple line (Equation (1.13)). The black dashed vertical line indicates our measurement of the dynamic wetting transition (Ca^*). The blue vertical dotted line indicates Ca^+ as defined in Section 3.5.*

For completeness, an additional zone must be defined at the zero velocity limit: zone (1). As mentioned earlier in Section 1.3, this contact angle hysteresis is defined as $\Delta\theta = \theta_a - \theta_r$. In Figure 3.3b, we measure experimentally $\Delta\theta = 10°$.

In the following, we focus on the dynamic wetting transition at the receding contact line, from a regime where the meniscus has a non zero contact angle and a steady shape, to the regime of film entrainment, at a capillary number Ca^*.

3.3 Threshold capillary number for the dynamic wetting transition

In order to broaden the set of data, liquids with various viscosities are used in this section. We investigate the effect of viscosity on both $\theta_r(Ca)$ and Ca^* with different glycerol concentrations. Sets of dewetting experiments are carried out.

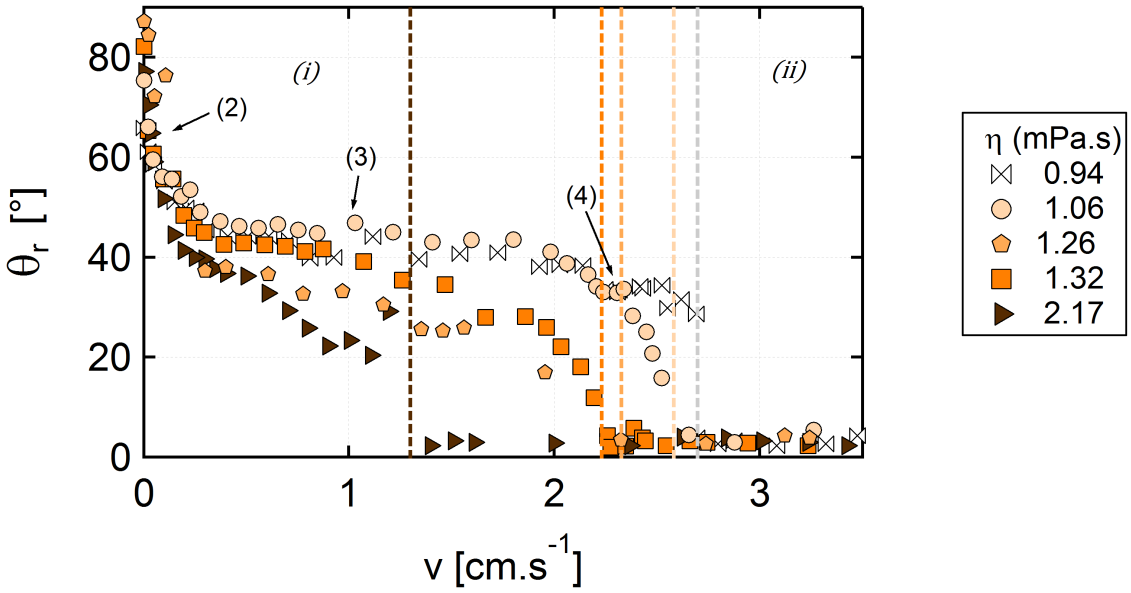

Figure 3.4: *Receding contact angle θ_r as a function of slug velocity v for different viscosities of the water-glycerol mixture. The brownish color index indicates the glycerol percentage. The darker the index, the larger the concentration. The dashed vertical lines indicate the dynamic wetting transition v^* for each liquid.*

The evolution of the receding contact angle θ_r is reported as a function of the velocity of the slug v in Figure 3.4. Each marker corresponds to one experiment performed at a given velocity. The same trend is observed for all mixtures. θ_r decreases with the velocity of the slug v. Furthermore, the same zones as previously defined and described in Figure 3.3b are observed when varying the viscosity of the liquid. When the viscosity increases, the threshold velocity v^* of the meniscus at which we observe the dynamic wetting transition decreases, as represented by the dashed vertical lines. As a result, the range of the plateau

regime (zone (3)), where the receding contact angle is approximately constant, decreases and even disappears for larger viscosities (above $\eta = 1.32$ mPa.s). When a plateau is observed (for $\eta = 0.94$, 1.06 and 1.26 mPa.s) the contact angle in the plateau regime is independent of viscosity and equal to $45 \pm 2°$.

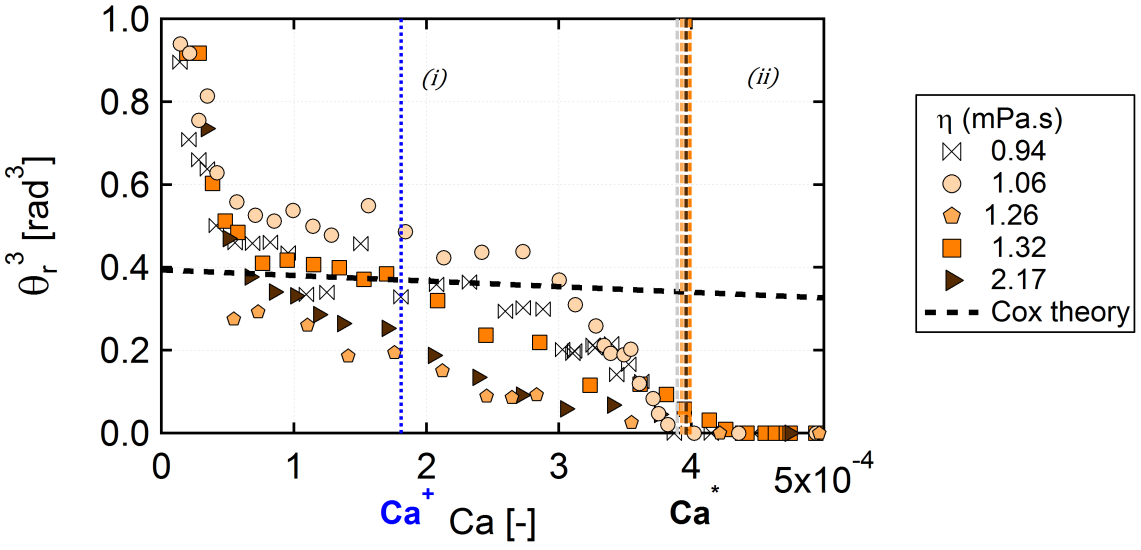

(a)

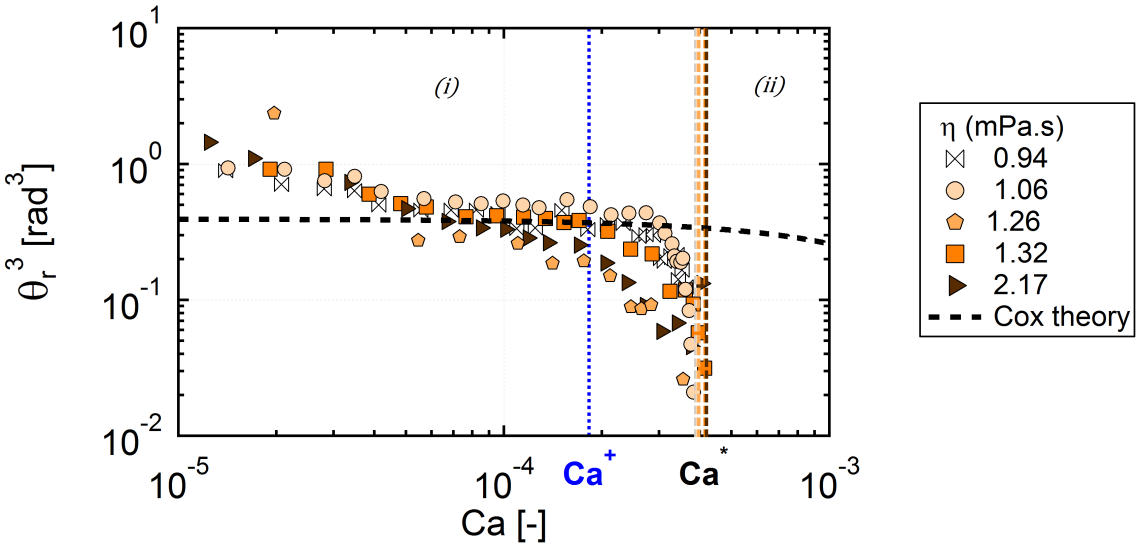

(b)

FIGURE 3.5: *$\theta_r{}^3$ as a function of the capillary number Ca for different concentrations in glycerol. (a) Linear and (b) logarithmic scales. The brownish color index indicates the glycerol percentage. The dashed curve represents the Cox-Voinov prediction. The dashed vertical lines indicate the dynamic wetting transition.*

The meniscus velocity v can be rescaled by the characteristic velocity $v_{liq} = \gamma/\eta$ for each liquid to get the capillary number $Ca = \eta v/\gamma$. Figure 3.5 presents the resulting curves, where the receding contact angle $\theta_r{}^3$ is reported as a function of the capillary

number of the meniscus Ca, as suggested by the Cox-Voinov law (Equation (1.13)).

We find that this scaling collapses the experimental curves partially. Indeed, for all the liquids considered in our experiments, the dynamic wetting transition occurs around $Ca^* = 4 \pm 0.1\ 10^{-4}$. Therefore the capillary number is the appropriate quantity to define the dynamic wetting transition. Note that the threshold capillary number Ca^* depends on the static contact angle θ_e. Other experiments with different values of static contact angle θ_e will be presented in Chapter 6.

3.4 Comparison with models and discussion

In this part, we compare the experimental evolution of the receding contact angles with existing models. We are looking for a general law for $\theta = f(Ca)$ and a prediction of the threshold capillary number for the dynamic wetting transition Ca^*.

As shown in Section 1.3, the Cox-Voinov law reads:

$$\theta^3 = {\theta_e}^3 \pm 9Ca \ln\left(\frac{l_c}{l_s}\right) \tag{3.1}$$

where θ_e is the equilibrium contact angle, l_c (capillary length) and l_s (slip length) are a macroscopic and microscopic cutoff length scales respectively.

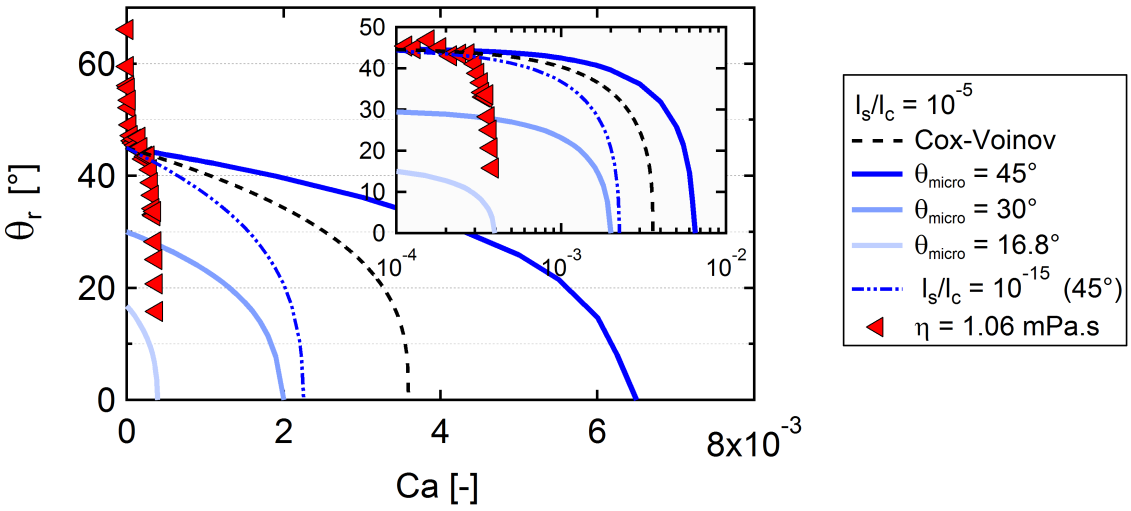

Figure 3.6: *Experimental contact angle for 5%wt glycerol solution ($\eta = 1.06$ mPa.s red triangles), Cox-Voinov model (dashed lines) and model assuming a constant microscopic contact angle θ_{micro} (solid lines). Logarithmic scale in inset.*

We first consider this model with an equilibrium contact angle $\theta_e = \theta_e^{exp} = 45°$ and a ratio $l_s/l_c = 10^{-5}$ corresponding to a slip length $l_s = 26$ nm for the liquid considered (5%wt glycerol solution). In Figure 3.6, we plot the Cox-Voinov model (black dashed line) given by Equation (3.1), and we report our experimental receding contact angles (red triangles) measured for 5%wt glycerol solution ($\eta = 1.06$ mPa.s). For the sake of

clarity, both linear and logarithmic representations in Ca are given in Figure 3.6. We see that the Cox-Voinov model first predicts a slight decrease of the contact angle below $Ca = 4\ 10^{-4}$, and then a sharp fall of the contact angle around $Ca_c^{Cox} = 3.5\ 10^{-3}$. The model can thus account for the experimental data in the plateau region (zone (3)), but strongly overestimates the capillary number at the dynamic wetting transition Ca^*.

In most models, the solid surface is considered as smooth and the problem is considered as a multiscales problem. In most theoretical works (see Snoeijer *et al.* [1] for example) a microscopic contact angle is introduced, providing a continuous description. As shown in Figure 3.7, this microscopic contact angle θ_{micro} is kept constant and independent of the capillary number, while the macroscopic contact angle θ_r varies with the capillary number of the meniscus.

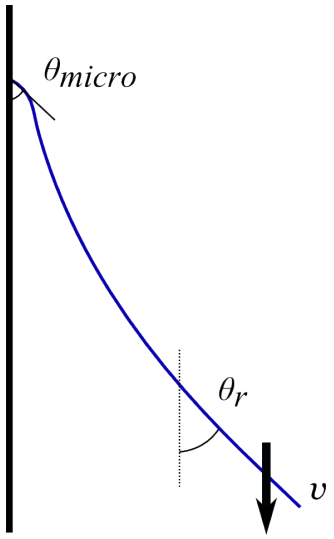

FIGURE 3.7: *Schematic of the meniscus shape exhibiting the two scales at which a contact angle can be defined. The microscopic contact angle θ_{micro} is defined at micrometric length scale from the contact line. The apparent receding contact θ_r, which is measured here, is a macroscopic measurement.*

Following Snoeijer [1] and Eggers [40], we have carried out the numerical integration of Equation (2.7) with $q = 0$ using a constant microscopic contact angle, and the full expression of the meniscus curvature. Initial boundary conditions were a static meniscus with macroscopic contact angle θ_r. In this model, we can vary the value of the microscopic contact θ_{micro}. Similarly to what has been done for the Cox-Voinov prediction, we take $\theta_{micro} = 45°$ and $l_s/l_c = 10^{-5}$. In the same figure, we represent this new prediction as solid lines (dark blue). This constant microscopic contact angle model provides a variation similar to the Cox-Voinov law. This is not surprising, since the physical ingredients are the same. Nevertheless, we note that the dynamic wetting transition occurs at en even larger Ca than for the Cox-Voinov model: $Ca^*_{\theta_{micro}=45°} = 6.5\ 10^{-3} > Ca_c^{Cox} >> Ca^*_{exp}$.

With a model with a constant $\theta_{micro} = 45°$, we can try to adjust the value of the ratio l_s/l_c in order to decrease the value of Ca^*. Nevertheless we end up with non physical value

without reaching our experimental Ca^*. An example is given in Figure 3.6 for $l_s/l_c = 10^{-15}$ (dashed dotted line). For 5%wt glycerol solution, $l_s/l_c = 10^{-15}$ would corresponds to a slip length $l_s \sim 10^{-18}$ m which is 8 decades lower than atomic scale and therefore not acceptable.

Alternatively, we can decrease the value of θ_{micro}. Two examples are given Figure 3.6 for $\theta_{micro} = 30°$ (middle blue) and 16.8° (light blue). Doing so, we reduce the value Ca^* at the dynamic wetting transition, but we loose the match with the experimental data at the plateau. We cannot render simultaneously the evolution of the contact angle and the Ca^* at the dynamic wetting transition.

None of the standard hydrodynamic contact angle theories or molecular kinetic theory can describe our experimental trend. Experimentally, the dynamic wetting transition occurs much earlier than predicted by hydrodynamic models. In these models, the flow imposes the curvature of the meniscus. Consequently, the variation of the receding contact angle cannot be explained by the hydrodynamic pressure close to the triple line. Another option is to consider alternative sources of dissipation. Indeed, in addition to the viscous dissipation at the triple line, another source of dissipation is induced by the friction at the triple line for example due to surface roughness. This assumption is relevant for two reasons. First, because we have experimentally measured the surface roughness of the PVC tubes by AFM and profilometer and we have found a micrometric and nanometric roughness (see Section 2.2.2). The second reason is that we found experimentally a static contact angle hysteresis $\Delta\theta = \theta_a - \theta_r$ at vanishing velocities of order 10° (zone (1) in Figure 3.3b). This phenomenon proves that our surfaces are not perfectly smooth, and present roughness and/or chemical heterogeneity.

Concerning the advancing contact angle we have shown that there is very limited influence of the capillary number contrary to the Cox-Voinov model, which predicts a small increase of the advancing contact angle in the range of capillary number studied here, from $Ca = -1\ 10^{-4}$ to $-2\ 10^{-2}$ (Figure 3.3a). This observation has also been made by Blake when coating polyester plates with water at very high velocities [91]. To the best of our knowledge, the earliest published study of dynamic wetting by Ablett [32] shows a similar independence of both the advancing and receding angles with Ca. Much larger capillary numbers are needed to see a significant change. It is also likely that the rough surface of the tubing would tend to mask more subtle effects.

The strong decrease of the receding contact angle in zone (2), shown in Figure 3.3b, can be attributed to a thermal activation process (molecular kinetic theory), since this mechanism was validated by Davitt *et al.* [60] on mesoscopically rough surfaces for low velocity of the triple line. This explanation also holds for the strong increase observed for the advancing contact angle θ_a at small velocity Ca.

3.5 Time to film formation: transient profiles

Another important question is the role of the transients. In our experiments and in the industrial applications, the liquid is initially at rest and subsequently moves at constant velocity. This implies that there is a transient state in which the slug evolves into its steady state configuration. Here we inquire into the duration of this transient.

3.5.1 Experimental observations of film formation delay

In this section, we present a set of experiments performed using the "large velocity setup" presented in Section 2.1.1. Here, the fluid used is dyed water and the volume of the slug is $V = 4$ mL. The fluid segment is initially in the camera frame and we visualize the flow along the tube over 45 cm. In that case, $\tau_m = 45$ cm$/v$ is larger than previously, but the spatial resolution is lower. An image sequence of a typical experiment is shown in Figure 3.8.

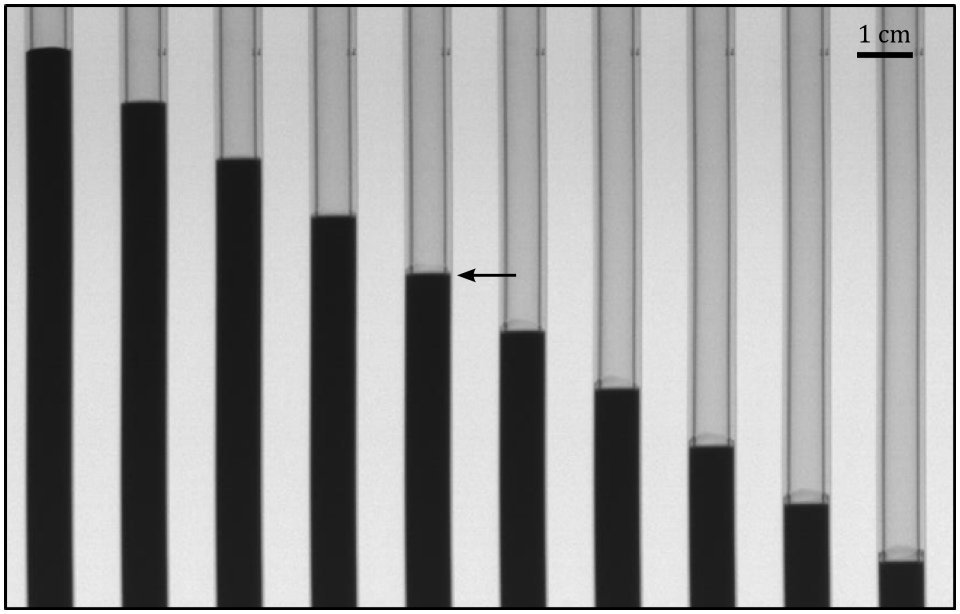

FIGURE 3.8: *Image sequence of a low velocity experiment illustrating the delay to the dynamic wetting transition. $V = 4$ mL of dyed water, $\Delta t = 0.8$ s. The height of the image corresponds to the first 12 cm of the full visualization window. The arrow indicates when the liquid film starts to be observed macroscopically. Initial time is taken when the slug motion is induced.*

In Figure 3.8, images are zoomed in to have a good accuracy on the back of the slug. Time step between images is $\Delta t = 0.8$ s. Initially the slug is at rest (first image in the image sequence) then the motion is induced at $t = 0$ by applying the gas pressure behind the fluid segment (top of the tube). The velocity of the rear of the slug $v = 1.4$ cm.s^{-1} is constant. The corresponding capillary number is $Ca = \eta v/\gamma = 1.89\ 10^{-4}$. The measurement duration is $\tau_m = 32$ s. In Figure 3.8, we see that a liquid film is entrained

behind the slug after a given time, denoted τ_{film}. While the slug reaches constant velocity instantaneously within our time resolution, film formation suffers a significant delay. In the present case, this phenomenon occurs between the fourth and the fifth images. This characteristic time for film formation is here $\tau_{film} = 2.5$ s$< \tau_m$.

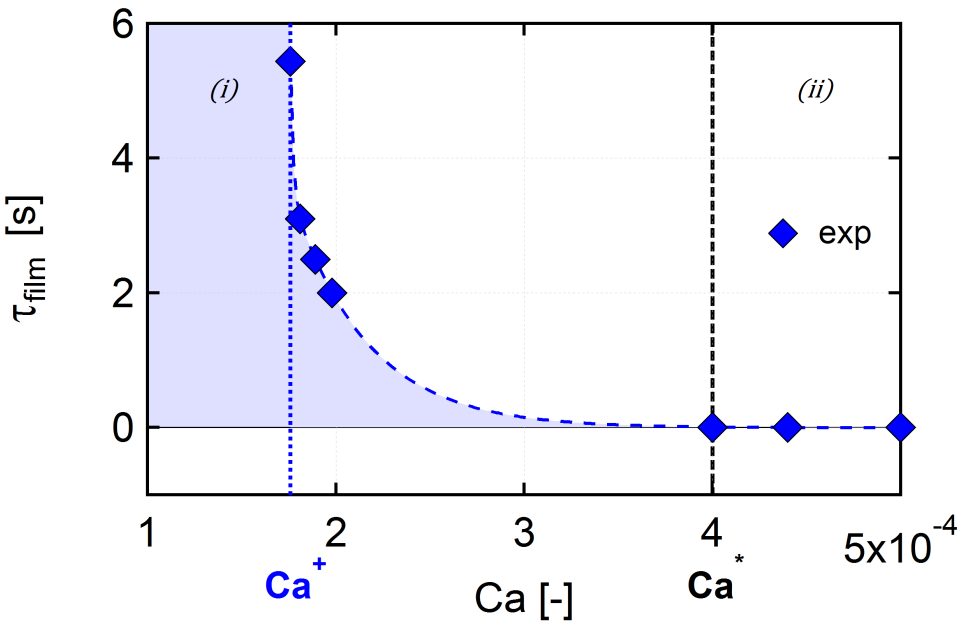

FIGURE 3.9: *Delay to the dynamic wetting transition: time for film formation τ_{film} as a function of capillary number Ca. The dashed blue curve is given as a guide to the eyes. The time to film formation diverges at Ca^+. Above a given capillary number Ca^* the transition towards the film is instantaneous.*

The characteristic time for film formation τ_{film} can be systematically measured when varying the slug velocity v and therefore the capillary number Ca. The corresponding results are gathered in Figure 3.9. We also find a film for $Ca > Ca^+ = 1.8\ 10^{-4}$ (vertical blue dotted line). We observe that the time to film formation decreases with the capillary number. The dashed blue curve is given as a guide to the eyes, but seems to follow a power law $(Ca - Ca^+)^{-\alpha}$. Above a threshold in capillary number $Ca^* > Ca^+$, denoted by the vertical black dashed line, film formation is instantaneous within experimental resolution: $\tau_{film} \simeq 0$ s. We emphasize that the position in the tube at which the film is entrained varied from one experiment to another as required by the dependance upon velocity and time. We can therefore conclude that film entrainment is not related to a particular defect on the inner tube surface.

In this experimental configuration, we cannot consider that the dynamic wetting transition is simply controlled by the slug velocity, because the time to film formation, and the distances traveled, may be significant between Ca^+ and Ca^*. In fact, the dynamic wetting transition does not occur at a given capillary number, as it is always stated in the literature [70, 63, 92, 5], and first suggested by our experiments in the previous section.

In fact, it appears that the second decrease of the receding contact angle, as shown in zone (4) in Figure 3.3b, corresponds to the range of capillary number from $Ca = 2.8\ 10^{-4}$ to $4\ 10^{-4}$ where τ_{film} is smaller than the experiment duration τ_m. The dynamic wetting transition is time dependent and Ca^+ provides a better definition of this transition that occurs when the time to film formation diverges.

3.5.2 Numerical investigation of the time-dependency of the film formation

The existence of a possibly large "induction time" for film formation around the threshold velocity is surprising. Here we want to investigate the origin of this phenomenon using a numerical approach. We use the governing equation (Equation (2.11)) and a finite difference scheme (Section 2.3). We use a constitutive relation $f(v) = \gamma\,(\cos\theta - \cos\theta_e) = \Psi\eta v_d$ where Ψ is a dimensionless friction coefficient to account for the dissipation at the triple line [57].

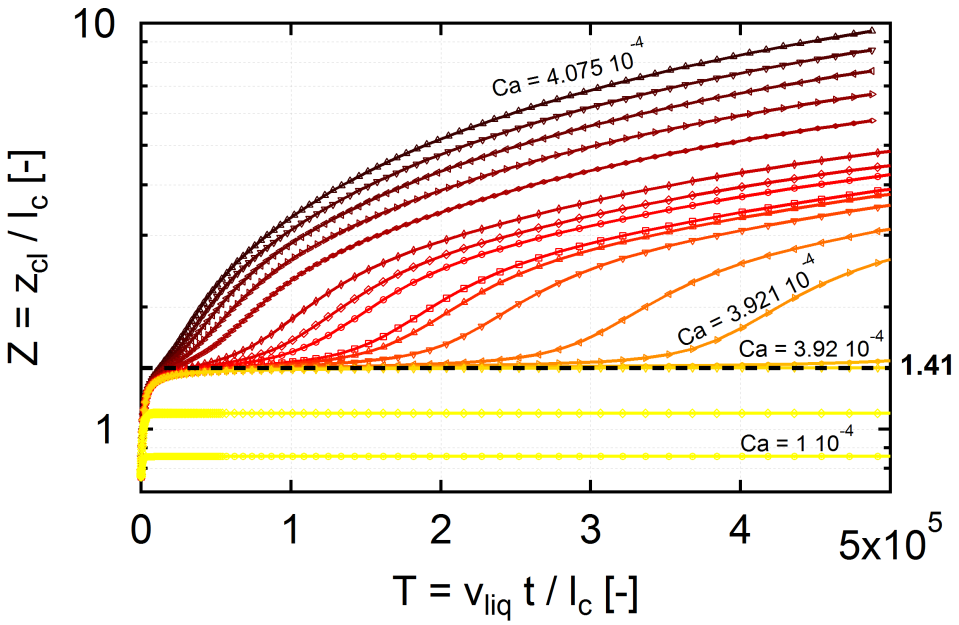

FIGURE 3.10: *Normalized contact line elevation $Z = z_{cl}/l_c$ represented as a function of the normalized time $T = v_{liq}t/l_c$ obtained by numerical integration when varying the capillary number Ca. Darker curves account for larger Ca. Initially the liquid meniscus is at rest. At $T = 0^+$, the motion is induced at fixed capillary number Ca. Below a threshold in Ca, the meniscus stabilizes at an equilibrium elevation. Above a critical capillary number $Ca^+ = 3.919\ 10^{-4}$, the contact line is entrained suddenly to form a liquid film after a certain time T_{film}. The horizontal black dashed line at $Z = \sqrt{2} = 1.41$ corresponds to the maximal contact elevation for a static meniscus.*

There are three free parameters in this model: the capillary number Ca, the friction coefficient Ψ and the equilibrium contact angle θ_e. The equilibrium contact angle was

taken constant equal to 45°. The friction coefficient was increased to $\Psi = 650$ to match an instantaneous transition at $Ca = 4\ 10^{-4}$ and fit with our experimental value. In the following, dimensionless quantities are used and denoted with capital letter.

Figure 3.10 presents the normalized contact line elevation $Z = z_{cl}/l_c$ versus the normalized time $T = v_{liq}t/l_c$. Each curve corresponds to the temporal evolution of the contact line position at given capillary number Ca. Initially the liquid meniscus is at rest $Ca = 0$. Then, at $T = 0^+$, the motion is induced at fixed capillary number Ca. The darker the color index, the larger the capillary number. The maximal numerical time, in the given example, is $T_{num} = 5\ 10^5$ and corresponds to a dimensional time $\tau_{num} = 25$ s (for pure water). Below a threshold in Ca, the meniscus elevation z_{cl} increases progressively and then stabilizes at an equilibrium elevation (yellow curves). Above a critical capillary number, which is $Ca^+ = 3.919\ 10^{-4}$ in the numerical example, the contact line first elevates progressively up to a quasi-stable value of z_{cl} as previously. This value is independent of the capillary number and is $z_{cl} \simeq 1.41 l_c$. Interestingly, this value $z_{cl} = \sqrt{2} l_c$ corresponds to the maximal contact line elevation for a static meniscus for a perfectly wetting liquid (see also Section 2.3.1). But after a certain characteristic time T_{film}, Z becomes larger than $\sqrt{2}$ and a transition into another regime is observed: the position of the triple line increases again and the meniscus is entrained suddenly leading to film formation. As an example $T = 2\ 10^5$ for $Ca = 3.921\ 10^{-4}$. There is a critical slowing down around the transition.

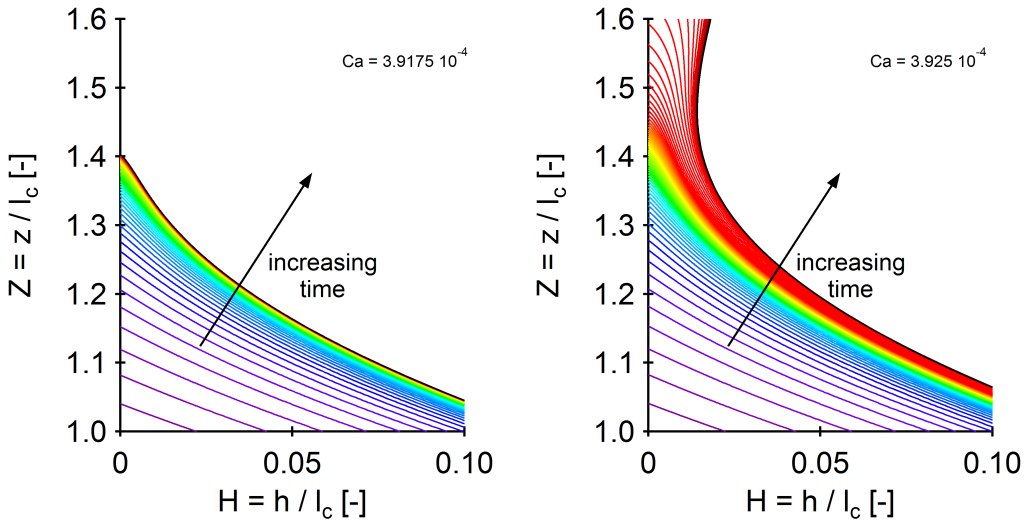

FIGURE 3.11: *Normalized meniscus profile $H(Z)$ as a function of time in the moving frame of the meniscus, (a) below the dynamic wetting transition $Ca = 3.9175\ 10^{-4}$, (b) above the dynamic wetting transition $Ca = 3.925\ 10^{-4}$. $H = h/l_c$ is the thickness of the meniscus profile or of the film, and $Z = z/l_c$ the vertical position along the tube. The time step between each profile is kept constant equal to 25 ms. In (b), the critical slowing down around the transition is manifest.*

To obtain a better visualization of this critical transition, profile evolution of the meniscus with time around the transition are represented in Figure 3.11. Left $Z-$axis corresponds to the vertical position along the surface, and the horizontal axis is the thickness profile H in the orthogonal direction. $H = 0$ corresponds to the wall position. Each curve is a profile at a given time. The time step between each profile is roughly constant. In Figure 3.11a, typical evolution below the transition is represented for $Ca = 3.9175\ 10^{-4} < Ca^{+}$. It corresponds to the yellow family of curves from Figure 3.10. We can note the gradual build up of the viscous bending with time, close to the wall. The local curvature is consequently increasing. The dynamics slows down progressively and the meniscus takes a stationary shape (the curves agglomerate). The meniscus reaches an equilibrium shape, and triple line elevation $Z \leq \sqrt{2} \simeq 1.41$. Above the transition, typical evolution for $Ca = 3.925\ 10^{-4} > Ca^{+}$ is given in Figure 3.11b (orange family curves from Figure 3.10). The meniscus first seems to reach a similar equilibrium shape and position at $Z = \sqrt{2}$ but then, after an "induction time" it undergoes a transition leading to film entrainment. As illustrated in Figure 3.11b, we notice the critical slowing down around the transition. The profile close to the triple line then grows in both directions (length Z and thickness H) with time and a liquid film is formed. In both graphs, the last meniscus profile corresponds to the same time limit: $T_{num} = 5\ 10^{5}$.

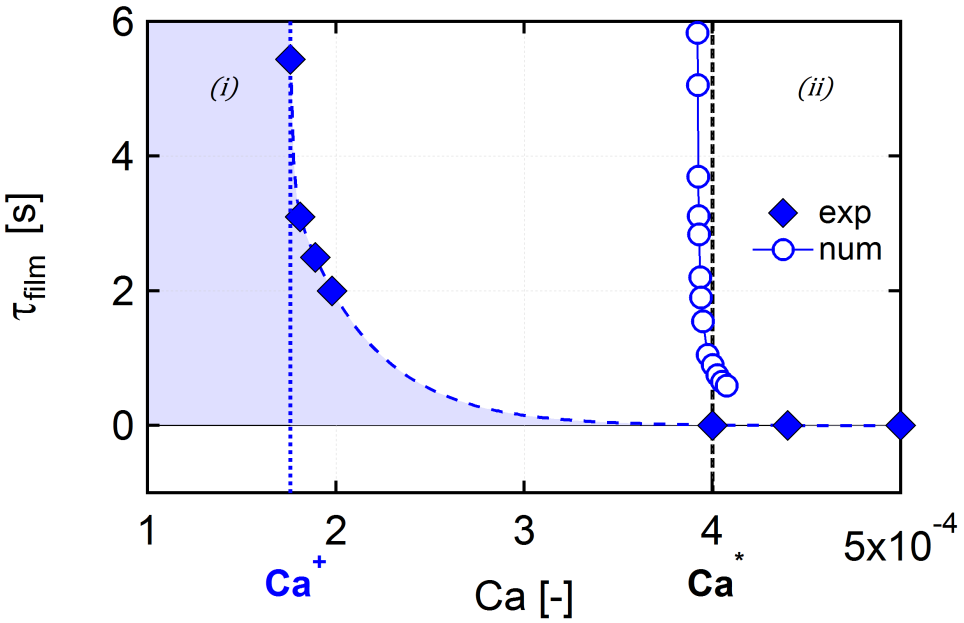

FIGURE 3.12: *Same data as in Figure 3.9 with numerical time for film formation τ_{film} as a function of the capillary number Ca (blue open circles).*

From the simulation we can systematically extract the "induction time" (time for film formation) τ_{film}. This time is taken when Z becomes larger than $\sqrt{2}$. In Figure 3.12 we plot this time as a function of the capillary number (blue open circles). Experimental times for film formation already presented in the previous section is represented by the

blue full diamonds. Experimental and numerical times are both decreasing with Ca. In the present simulations, the adimensional time for film formation can be as large as $T_{film} = \tau_{film}/\tau_0 = 1.5\ 10^5$ obtained for $Ca = 3.92\ 10^{-4}$ ($\tau_0 = l_c/v_{liq}$). The corresponding dimensional time is $\tau_{film} = 7.5$ s, which is comparable to the time we found experimentally. However, we found numerically $Ca^+ = 3.919\ 10^{-4}$ and $Ca^* = 4.1\ 10^{-4}$. The width of the transition is quite narrow: the window in capillary number is of the order of 10^{-5} compared to 10^{-4} experimentally.

3.5.3 Concluding remarks

The liquid film detection actually depends on the experimental window. A film can be observed only if $\tau_{film} < \tau_m$. We will denote as instantaneous film formation the detection of a liquid film (limited by our experimental resolution: film of length 6 pixels) right after the beginning of the experiment. This instantaneous transition corresponds to a threshold $Ca^* = 4\ 10^{-4}$. There is another threshold $Ca^+ = 1.8\ 10^{-4}$, for which the velocity of the film can be very similar to the slug velocity, consequently $Ca^+ \neq Ca^*$. Thus the receding contact angle θ_r measured for $Ca^+ < Ca < Ca^*$ corresponds to an unstationary shape of the meniscus where the transient condition of partial wetting holds while viscous bending builds up. We have seen that the threshold in capillary number Ca^* was independent of the liquid characteristics. Numerical simulations prove that we have to consider transient effects for a better definition of the transition. Finally, we note that the calculation involves a flat surface. However, preliminary calculations with finite tube diameter suggest no qualitative changes. In the following, the dynamic wetting transition will be defined at the critical capillary number Ca^+.

3.6 Conclusion

There is a strong dependence of both advancing and receding contact angles with velocity at low capillary numbers (below 10^{-4} zone (2)). This strong dependence is unexpected in the standard hydrodynamic model and is ascribed to the coupling with surface roughness and pinning. Then, we observe a plateau for advancing triple lines. For receding triple lines, a very slow decrease with velocity is found, which is reminiscent of hydrodynamic models. However, this plateau ends rather unexpectedly, for capillary numbers much lower than predicted by these theories. Instead we find a rather sharp decrease to about zero over the capillary number range $Ca = 3-4\ 10^{-4}$. Above Ca^*, a film forms instantaneously which means that we have completed the forced wetting transition. This decrease has no identified parallel in the literature. More precisely we find that there is a range over which the transition occurs. As a result, in this range, the results strongly depend upon the observation protocol. At the lower end of the range, the film can also form, but only within seconds.

To better understand these observations, we have modeled the transition numerically within the lubrication approximation. We have noted that compared to the standard hy-

drodynamic models, the experimental value of the transition velocity is strongly depressed. Therefore, we cannot simultaneously account for the contact angle plateau and the wetting transition threshold. In fact, in these viscous dissipation models, the microscopic contact angle is usually assumed constant. This perspective must clearly be abandoned here. It is therefore fruitful to add to the model a friction like dissipation mechanism at the triple line with which we can qualitatively render both the quasi-static receding contact angle and the threshold capillary number consistently. We again ascribe this additional friction to the effect of surface roughness. We also find that the complex dynamic behavior observed experimentally is qualitatively consistent with the predictions of this augmented hydrodynamic model. In both experiments and numerics we find that the time to film formation diverges at the critical capillary number Ca^+ and sharply decreases as the velocity departs from the threshold. In practice, we have defined the transition Ca^* as the velocity for which film formation is instantaneous at the measurement space resolution. Similarly, in the dynamic transition velocity range, the contact angles are measured from transient meniscus profiles, and are therefore strongly dependent upon measurement protocols. However, in the calculations, the velocity range over which similar dynamic effects are found is very narrow, of the order of 1% of the transition velocity itself. This range contrasts sharply with the 25% range found in the experiments, suggesting that the additional dissipation does not account for the full response of the triple line.

Chapter 4

An unusual liquid film

4.1 Introduction

In the previous chapter, we have seen that above a critical capillary number Ca^+, a liquid film is entrained behind the slug. The system comes from a regime denoted *regime (i)* to a *regime (ii)* (Figure 4.1). This chapter focuses on the second regime where a film is deposited. It is important to keep in mind that the entrained film is not static at the surface of the tube. Indeed, the film dewets due to partial wetting condition. This is the particularity of the system studied here compared to LLD films.

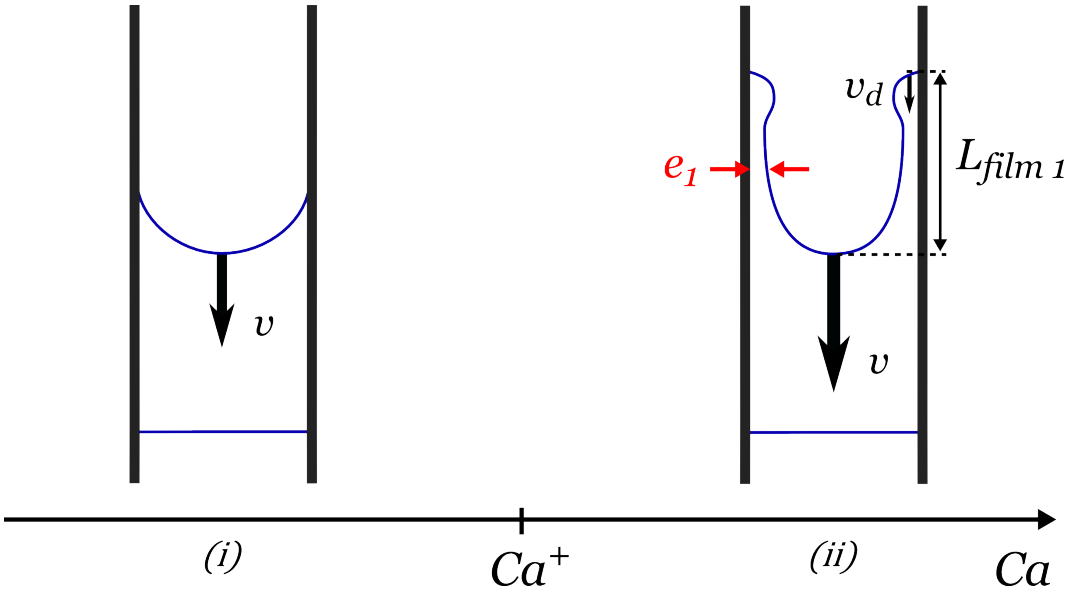

FIGURE 4.1: *Schematic of the evolution of a meniscus when increasing its velocity v, and therefore capillary number Ca. Above the critical capillary number Ca^+ a liquid film of length L_{film1}, thickness e_1 and dewetting velocity v_d is entrained.*

The objective of this chapter is to understand the physical mechanisms at the origin of the formation of the film represented in Figure 4.1. In the continuity of Chapter 3, we investigate the morphology of the film entrained after the dynamic wetting transition

Ca^+, and how it depends on the flow velocity and liquid viscosity. Is there a specific thickness selected? Also an interesting point that we will raise in this chapter and further discuss in Chapter 5 and Chapter 6, is the dynamics of the dewetting film. In particular, what happens at the triple line once the liquid film is formed? What sets the velocity of the triple line and what is the thickness of the film close to the contact line?

In the first part of this chapter, we study the overall properties of the liquid film: velocity, length and morphology. Our experiments highlight the existence of an unexpected thick liquid film in a significant range of capillary numbers. In the second part, we propose a numerical model providing explanations on the nature of the liquid film. The last part of this chapter is devoted to the study of unstationary films and their description using the numerical model.

4.2 Results

4.2.1 Experimental observations

We investigate the film entrainment of solutions with a low concentration of glycerol ($0 - 40\%$wt) in a PVC tube of diameter $d_{in} = 6.4$ mm. We use the "large velocity setup" and techniques described in Chapter 2 to visualize and measure the velocities of the different interfaces and the film thicknesses.

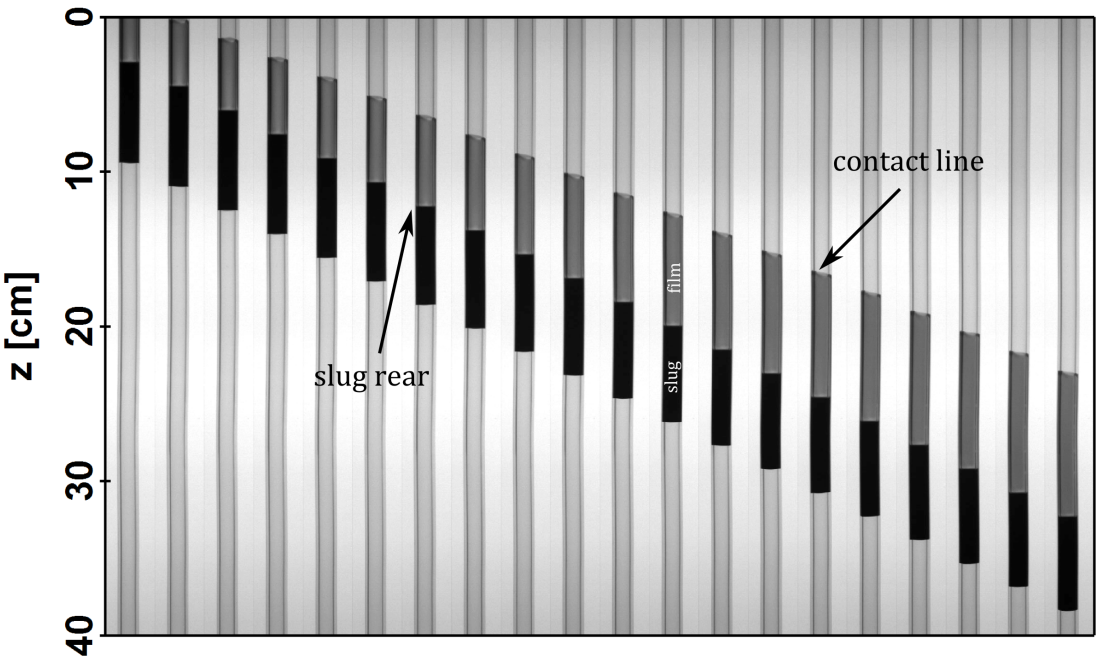

FIGURE 4.2: *Image sequence for a typical experiment in regime (ii), after the critical transition where a thick film is formed. Experimental parameters are: 20%wt glycerol solution* $\eta = 1.66$ *mPa.s,* $v = 7.7$ *cm.s*$^{-1}$ *(*$Ca = 1.9\ 10^{-3}$*),* $v_d = 6.3$ *cm.s*$^{-1}$*,* $\Delta t = 0.2$ *s.*

We vary the velocity of the slug from $v = 1$ up to 20 cm.s^{-1}. We also vary the liquid viscosity, so that we assess a capillary number range $Ca = 4\ 10^{-4} - 2.2\ 10^{-3}$. We focus here on *regime (ii)*, where a dewetting film is entrained behind the slug, for $Ca > Ca^{+}$. We measure two kinds of quantities: the velocities of interfaces (v and v_d) corresponding to a film length L_{film1} and the film morphology, notably its thickness e_1.

One typical image sequence obtained with 20%wt glycerol solution ($\eta = 1.66$ mPa.s) and $v = 7.7$ cm.s^{-1} is given in Figure 4.2. The camera window captures 40 cm of the tube. The time step between each image is $\Delta t = 0.2$ s. Contrary to *regime (i)*, presented in Chapter 3, we observe a liquid film (light grey) entrained behind the slug (in dark grey). We can note that the end of the film is not pinned at the interface and is moving. We denote as v_d the velocity at the triple line of the film in the reference frame of the laboratory. The film has a finite length denoted L_{film1}. We observe a moderate growth of the film length, at constant thickness and that the dewetting film and the slug seem to move at nearly the same velocity.

Kinematics: film lengths and interface velocities

In Figure 4.3, we show the time evolution of the film and slug lengths. These lengths are directly measured from the image sequence in Figure 4.2. The $z-$position of the different interfaces are measured in time, such that $L_{slug} = |z_{front} - z_{rear}|$ and $L_{film1} = |z_{rear} - z_{dewetting}|$.

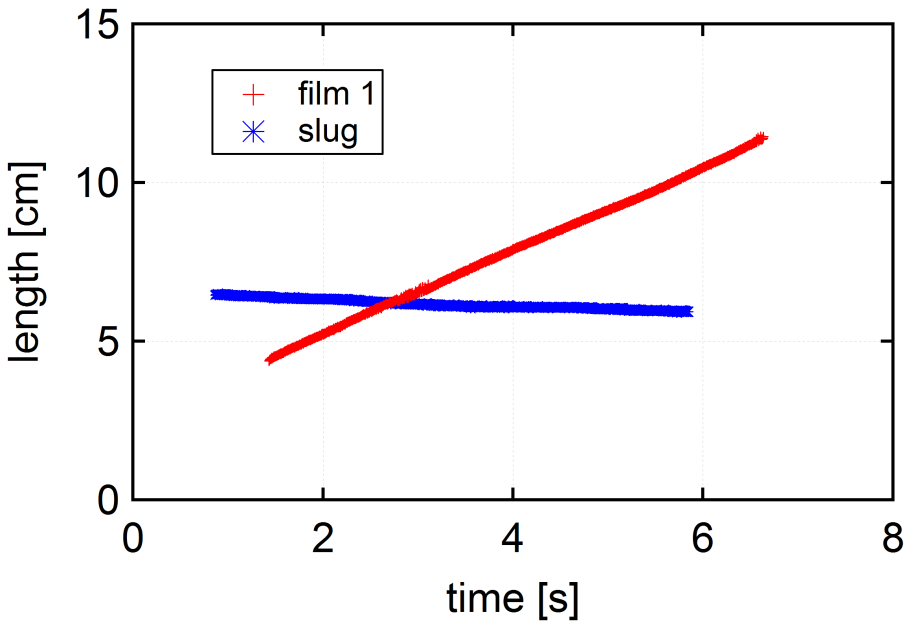

FIGURE 4.3: *Slug (blue) and film length (red) as a function of time, measured from the image sequence Figure 4.2. Experimental parameters are: 20%wt glycerol solution $\eta = 1.66$ mPa.s, $v = 7.7$ cm.s^{-1}, $v_d = 6.3$ cm.s^{-1}. The slug decreases in length while the film grows.*

The liquid film, represented by the red symbols, is growing in time. The growth rate is constant since the slope of the red curve is constant in time. At the same time, the slug length decreases, but very slowly compared to the film length. This decrease is due to the fact that the slug slowly feeds the film. Since the tube diameter is much larger than the film thickness, it is normal to observe a stronger variation of the length for the liquid film. Note that the film length L_{film1} can be measured only when the two extremities of the film are in the visualization window. This is why the film curve in Figure 4.3 does not start from zero, and the slug curve ends earlier than the film. The growth of the film is due to the velocity difference between the slug and the dewetting triple line. In Figure 4.3, the slope of the film length gives $v - v_d = 1.32$ cm.s^{-1}.

We can also measure the interface velocities based on a spatio-temporal diagram (Figure 4.4a). This plot corresponds to the extraction from the image sequence given in Figure 4.2, along the center line of the tube. As explained, in the Experimental description (Section 2.1.2), the slopes directly provide the velocities of the different interfaces (rear of the slug v and dewetting of the film v_d). Using this method, we found for the present example that the velocity of the slug is $v = 7.7$ cm.s^{-1} and the velocity of the dewetting film is $v_d = 6.3$ cm.s^{-1}. Thus, $v - v_d = 1.4$ cm.s^{-1}. The two methods provide roughly the same value for the velocity difference. But the second method is more accurate and provides independently the two interface velocities.

Film morphology

From the spatio-temporal diagram we also extract the film thickness, using the method of Section 2.1.3 (Figure 4.4a). We observe the slug in black and the film in orange. This measurement confirms that the thickness is homogeneous and constant with time.

In order to better describe the film morphology, we extract the profiles from the spatio-temporal diagram (vertical dotted lines in Figure 4.4a). Figure 4.4b presents successive typical profiles of the film in *regime (ii)* for 20%wt glycerol solution at $Ca_d = 1.5\ 10^{-3}$ where $Ca_d = \eta v_d/\gamma$ is the capillary number calculated with the dewetting velocity v_d. The blue color index stands for the elapsed time, and shows the correspondence between spatio-temporal diagram and profiles. The time lapse between each profile is $\Delta t = 0.5$ s. The profiles are given in the reference frame of the rear of the slug. The film length is about 7 cm. We observe again that the film is growing in length over time, with a flat central part of constant thickness. We will denote as e_1 the thickness of the film in this *regime (ii)*. In the present example we have $e_1 = 132 \pm 5$ μm. On the profile we observe that the top part of the film where the triple line is dewetting, forms a rim. This rim is connected to the flat film. A strong variation of the thickness is observed close to the rear of the slug where the profile also exhibits a dimple.

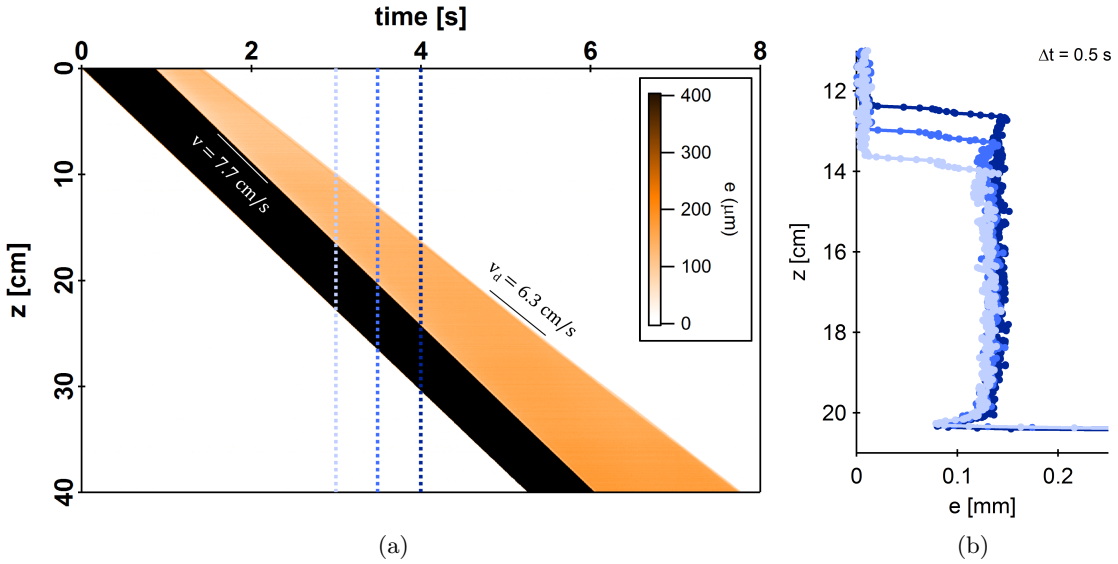

(a) (b)

FIGURE 4.4: *(a) Spatio-temporal diagram of thickness from the image sequence represented in Figure 4.2. (b) Successive experimental thickness profiles ($\Delta t = 0.5$ s) for 20%wt glycerol solution ($\eta = 1.66$ mPa.s), $Ca = 1.9\ 10^{-3}$, $Ca_d = 1.5\ 10^{-3}$. The slug meniscus is linked to the homogeneous film of thickness $e_1 = 132 \pm 5\ \mu m$ by a dimple. And the film, which is about 7 cm long, ends with a rim.*

4.2.2 Kinematic evolution with slug velocity

We reproduce similar experiments with varying slug velocity v and with different concentrations of glycerol in water to vary the liquid viscosity. The velocities v are measured via the spatio-temporal diagram slopes. Image sequences are similar to Figure 4.2, and we also find that the velocities are constant along the tube.

We represent the dewetting velocity v_d as a function of slug velocity v in Figure 4.5. The brownish color index indicates the glycerol percentage: the darker, the larger the concentration, the larger the viscosity. Each marker corresponds to one experiment of given velocity. The typical curve $v_d = f(v)$ shows first a dewetting velocity v_d equal to the slug velocity v before the dynamic wetting transition ($v < v^*$, *regime (i)* described in Chapter 3). Then, in *regime (ii)* for $v > v^*$, the dewetting velocity v_d and the slug velocity are very close but not equal since a film is growing: $v_d \simeq \alpha v$ with $\alpha \simeq 0.8$. Above a second threshold denoted v^{**}, the dewetting velocity reaches a maximum value denoted v_d^{sat} and becomes independent of the velocity of the slug v (*regime (iii)*). This value of the dewetting film at saturation v_d^{sat} increases when the fluid viscosity decreases. In the following sections of this chapter, we focus on the case where $v_d \simeq \alpha v$, before the saturation. *Regime (iii)*, where the dewetting velocity saturates, will be considered in Chapter 5.

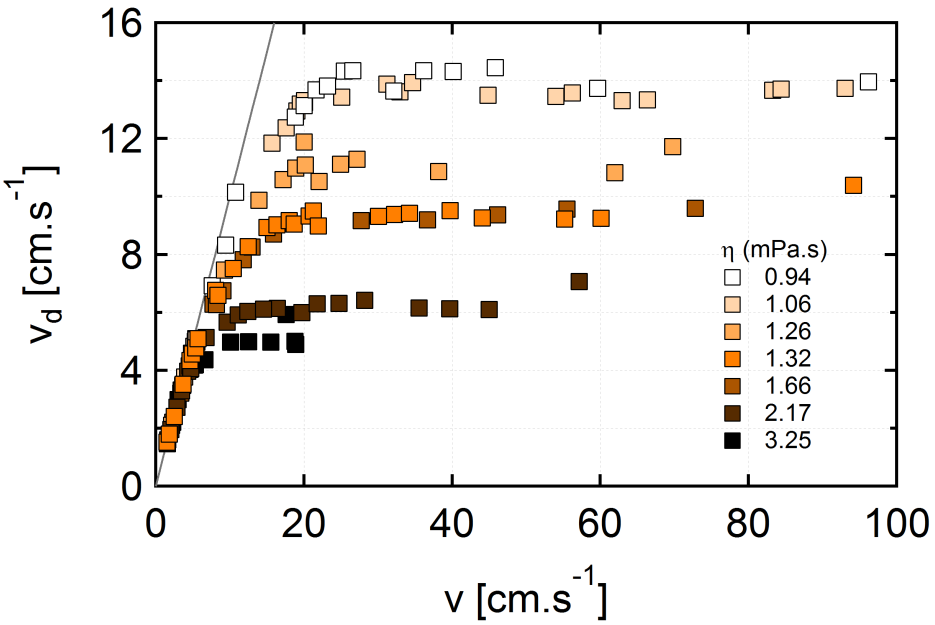

FIGURE 4.5: *Dewetting velocity of the film end v_d as a function of the slug velocity v for different concentrations of glycerol. The brownish color index indicates the glycerol percentage. The grey line corresponds to $v_d = v$. v_d first increases with v, with v_d slightly lower than v. Then, v_d saturates at a maximal value which increases when decreasing the fluid viscosity.*

4.2.3 Thickness of the film as a function of slug velocity

The film morphology has been systematically measured as a function of slug velocity for different glycerol concentrations. It remains identical with a rim at the end and a dimple close to the meniscus. Figure 4.6 gathers film thicknesses e_1 averaged over the flat part of the film as a function of the velocity of the dewetting film v_d for various glycerol concentrations. Note that in this regime v is approximately proportional to v_d, so that the variations of the thickness with v_d are similar to the variations with v.

Take as an example $\eta = 1.66$ mPa.s (20%wt glycerol solution, light brown), e_1 increases with the dewetting velocity v_d. We have seen in the previous section that the velocity of the triple line v_d reaches a saturation value at some point. The curve $e_1 = f(v_d)$ is restricted along the v_d axis by this saturation dewetting velocity $v_d^{sat} = 9.2$ cm.s^{-1}. Moreover, there is also a maximal film thickness limiting the curve along the left axis that is reached at the same time as v_d^{sat}. We denote this value e_1^{sat} (horizontal dotted line in Figure 4.6). For the considered liquid series $e_1^{sat} = 185$ μm.

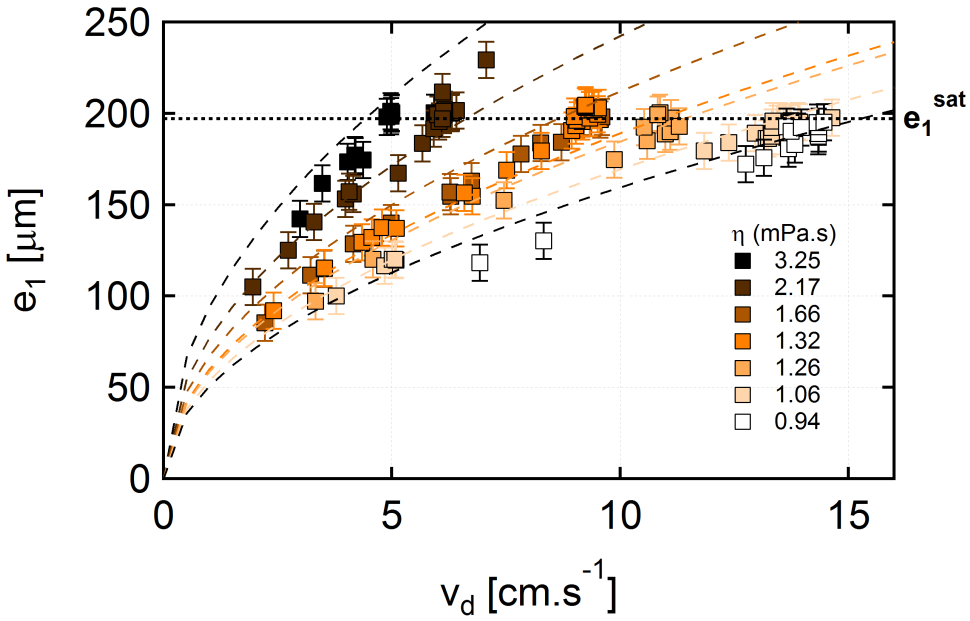

FIGURE 4.6: *Average film thickness e_1 as a function of the velocity of the dewetting film v_d for various glycerol concentrations. e_1 increases with v_d, then saturates at a maximal value independent of fluid viscosity. Predictive model considering a gravitational drainage at constant film thickness is given by the dashed line for each liquid without fitting parameter (Equation (4.7)).*

Moreover the profile of the liquid film changes slightly at the extremities of the film. Figure 4.7 presents the profiles obtained for $\eta = 1.66$ mPa.s (20%wt glycerol solution), when increasing the capillary number from $Ca = 9.6\ 10^{-4}$ to $Ca = 2.3\ 10^{-3}$ (red color scale). The darker the color, the larger the capillary number Ca. Alternatively, the thickness profile $e(z)$ can be rescaled by the average thickness in the flat region e_1 and the vertical dimension z by the capillary length $l_c = 2.52$ mm. In order to compare the shape of the rim and of the dimple, we superimpose the profiles at the triple line (Figure 4.7b) or at the rear of the slug (Figure 4.7c). The dimple gets deeper and its length increases in the $z-$direction for larger velocities. We note that the rim is also more pronounced for lower capillary number Ca. But the length of the rim in the $z-$direction is independent of the capillary number Ca. The receding contact angle, measured at the film end, is small, about 5° and is independent of the capillary number within experimental accuracy.

The same evolution is observed for all the liquids. e_1 first increases with v_d and consequently with v. But the larger the viscosity, the faster the film thickens with velocity (Figure 4.6). At a certain velocity v_d, the film thickness saturates at a maximal value e_1^{sat}. Remarkably e_1^{sat} seems independent of the fluid viscosity, whereas we have seen previously that the saturation dewetting value was larger for lower viscosity fluid. Also, the saturation velocity v_d^{sat} at which the thickness saturates depends on the fluid viscosity. This point will be discussed in the next chapter in Section 5.3.1.

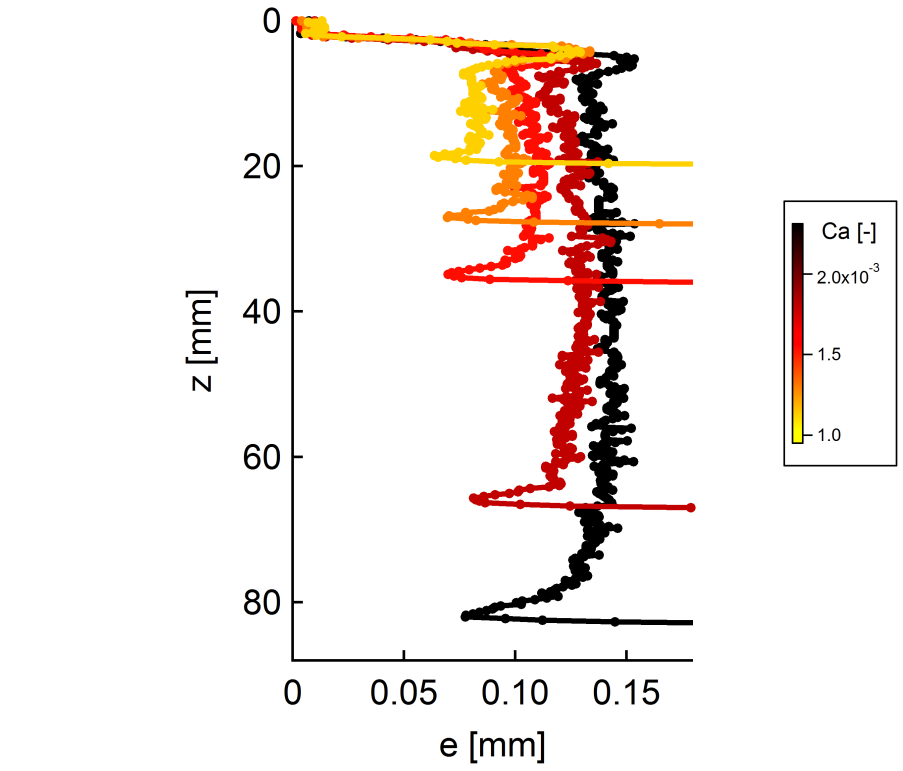

(a)

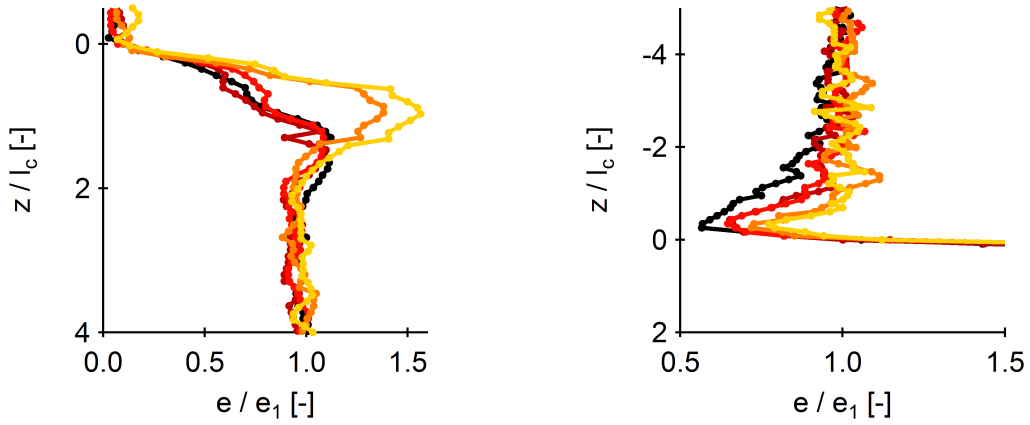

(b) (c)

FIGURE 4.7: *(a) Experimental thickness profile $e(z)$ for 20%wt glycerol solution ($\eta = 1.66$ mPa.s) and capillary numbers from $Ca = 9.6\ 10^{-4}$ to $Ca = 2.3\ 10^{-3}$. The color scale stands for the capillary number Ca. The darker the color, the larger the Ca. Experimental thickness profile from (a) are normalized $e/e_1 = f(z/l_c)$ and zoomed in on the rim (b) and on the dimple (c). The vertical dimension z is normalized by the capillary length $l_c = 2.52$ mm, and the horizontal dimension e is normalized by the thickness of the film in the flat region e_1. The rim grows when decreasing the capillary number Ca. The dimple gets deeper when increasing Ca.*

4.3 Comparison with theory

4.3.1 Kinematics and thickness as a function of capillary number

Figure 4.8 presents the plot of the rescaled velocities ($Ca = \eta v/\gamma = v/v_{liq}$ and $Ca_d = v_d/v_{liq}$). The data collapse on a single master curve. Three regimes are clearly identified. The *regime (i)* without film for $Ca < Ca^+$ discussed in Chapter 3. For $Ca^+ < Ca < Ca^{**}$, there is a *regime (ii)* with a single film of interest in this chapter. For Ca larger than a second threshold denoted Ca^{**}, the dewetting capillary number saturates at Ca_d^{sat} and *regime (iii)* represented by the grey zone is obtained. This regime will be investigated in Chapter 5. In *regime (ii)*, we observe that the two capillary numbers are approximately proportional: $Ca_d \propto Ca$, but as Ca increases, the deviation from slope 1 is more and more pronounced, which means that the difference $Ca - Ca_d$ increases when Ca increases.

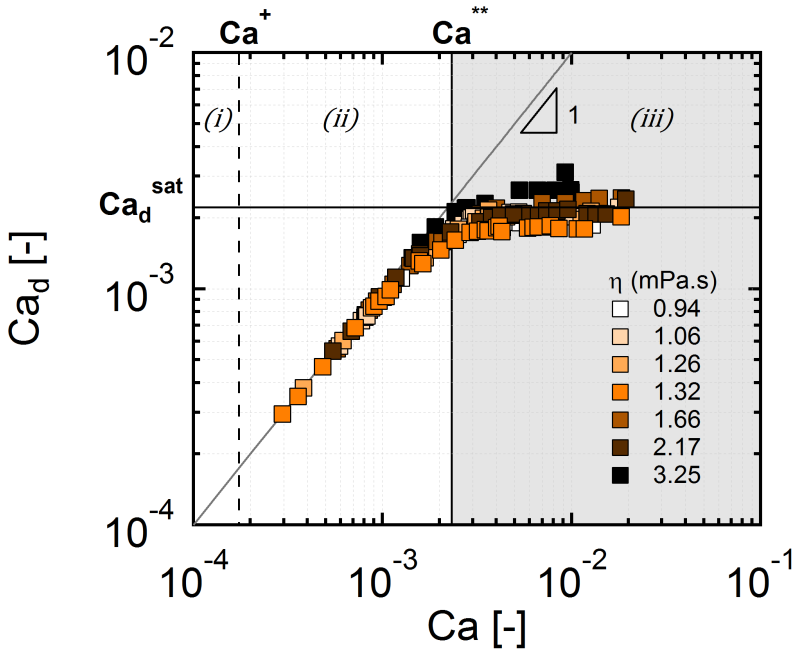

FIGURE 4.8: *Dewetting capillary number Ca_d versus meniscus capillary number Ca for various glycerol concentration. Three different zones are observed: regime (i) $Ca < Ca^+$ below the dynamic wetting transition, meniscus state $Ca_d = Ca$. In regime (ii) $Ca^+ < Ca < Ca^{**}$ a film is entrained but dewets $Ca_d \propto Ca$. In regime (iii) $Ca > Ca^{**}$ dewetting capillary number saturates (grey zone).*

Similarly, the film thickness e_1 rescaled by the capillary length l_c is shown as a function of capillary number Ca in Figure 4.9a. The data collapse and we obtain a single master curve with the same three regimes and especially the saturation of film thickness at e_1^{sat} is observed at the transition between *regime (ii)* and *(iii)*. As seen previously, the capillary number Ca is a good characterization of the limit between physical regimes. In *regime (ii)*, the thickness of the film e_1 roughly scales as $Ca^{1/2}$, but then deviates from this scaling to reach a saturation value e_1^{sat}.

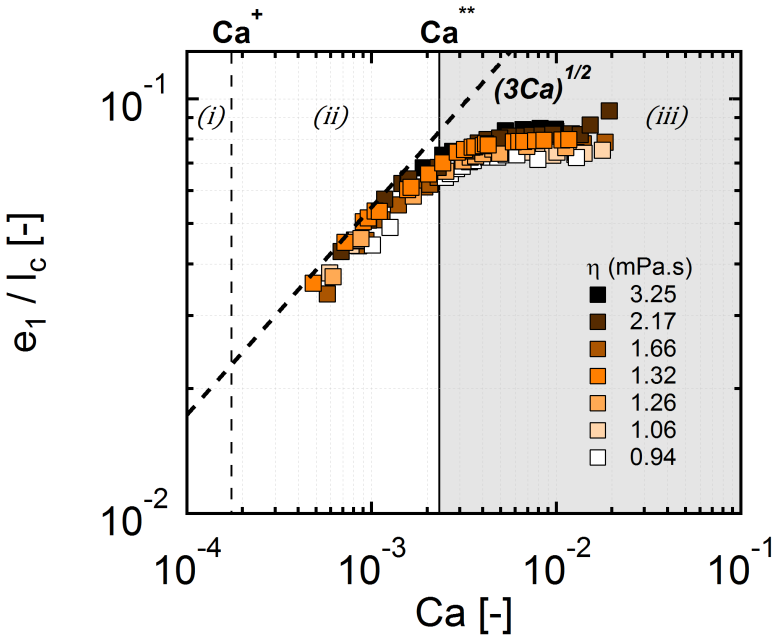

(a)

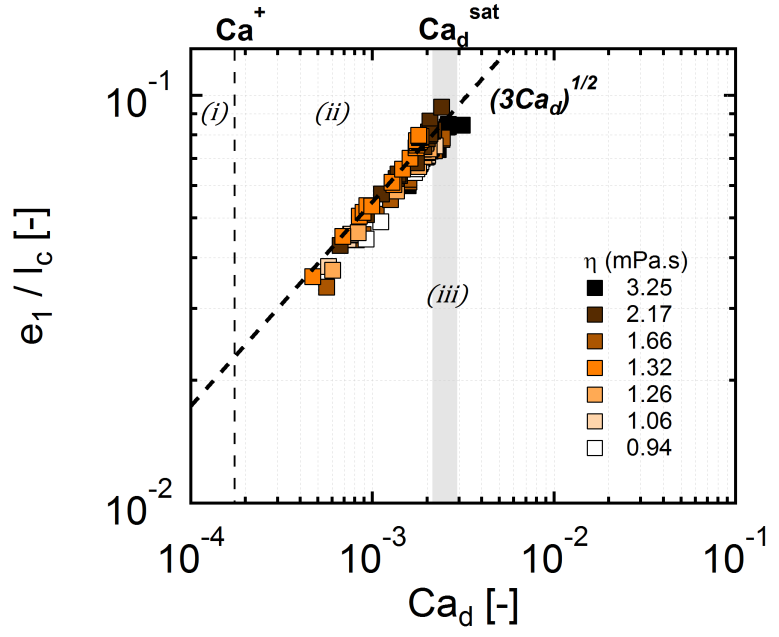

(b)

FIGURE 4.9: *Average film thickness e_1 normalized by the capillary length l_c as a function of (a) the capillary number of the slug Ca, (b) the capillary number of the dewetting film Ca_d. The dashed black line is the predictive model with no adjustable parameter considering a gravitational drainage at constant film thickness.*

Alternatively, the film thickness can be plotted as a function of dewetting capillary number Ca_d (Figure 4.9b). This time, the thickness of the film e_1 clearly scales as $Ca_d^{1/2}$ in the entire *regime (ii)*. This relation will be described in the next section. The film

thickness saturates at a given capillary number. This saturation value of the capillary number is denoted Ca_d^{sat} and announces the beginning of *regime (iii)*. Saturation of film thickness and of dewetting capillary number occur simultaneously: $e_1 = e_1^{sat}$ when $Ca_d = Ca_d^{sat}$.

4.3.2 Matching a film with a meniscus

In this section, we aim at understanding the problem numerically by looking at the existence of film solutions matching with the meniscus to find a prediction of the film thickness profiles. For that purpose we use the stationary equations and the numerical methods established in Section 2.3.

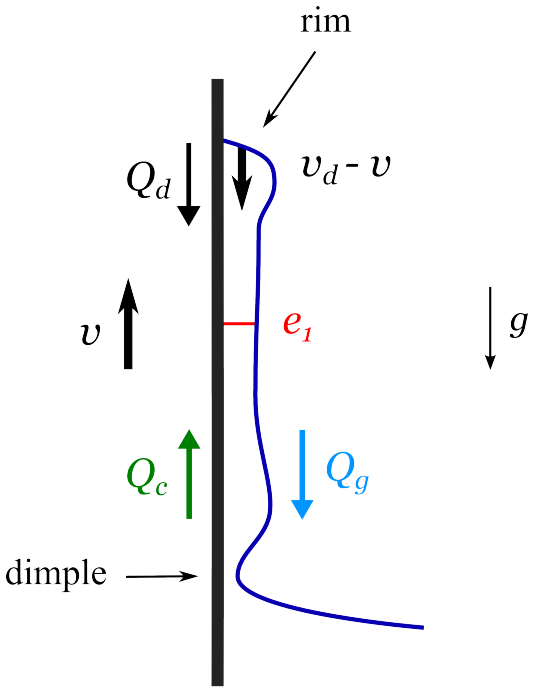

Figure 4.10: *Schematic of the gravitational film, regime (ii), which makes explicit the details of the profile. The film thickness is denoted e_1 in the flat part. In the reference frame of the meniscus, Q_g denotes a gravitational downward flux entering the slug. Q_c denotes the convected upward flux. Q_d is the flux due to dewetting.*

In the reference frame of the meniscus, we define two fluxes of liquid which include the essential features of the physics at stake (Figure 4.10): on the one hand Q_c the flux convected upward by the entrainment velocity v; on the other hand the downward flux Q_g caused by gravity. Q_g is in the opposite direction to Q_c, such that we define the flux ejected by the slug $Q = Q_c - Q_g$ where the fluxes are positives quantities.

Equation (2.7) for a flat surface is integrated starting from the flat film solution (point D in Figure 4.11) towards the static meniscus (direction 1 in red). We look for solutions that match the shape of the static meniscus represented by the dashed black curve. To set the initial values, an analytical expression of the flat film solution is required.

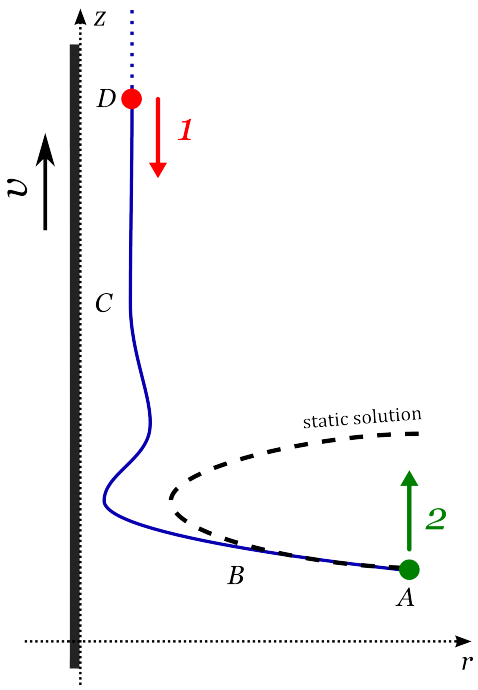

FIGURE 4.11: *Schematic explaining the integration scenarios. The liquid film profile and the static meniscus are represented in blue and in dashed black respectively. The zone $A-B$ corresponds to the matching between the static meniscus and the film solution; zone $B-C$ is a transition zone; zone $C-D$ is the flat film part. Numerical integration can be achieved starting from the flat film in D using the direction 1 (red), or starting from the static meniscus in A using the direction 2 (green).*

Equation (2.7) reduces to:

$$\partial_{\tilde{z}}\tilde{\kappa}_l = 1 - \frac{3}{\tilde{h}^2} + \frac{3\tilde{q}}{\tilde{h}^3} \tag{4.1}$$

where the flux is not restricted to $\tilde{q} = 0$: $\tilde{q} = \tilde{e}_0 - \tilde{e}_0^3/3 = \tilde{q}_c - \tilde{q}_g$.

This equation has been analysed by Snoeijer *et al.* [76]. The normalized thickness of the film far from the meniscus is $E_0 = e_0/l_c$. To calculate initial values for integration, in the limit where the film thickness is nearly constant (flat film) $\tilde{h} \to \tilde{e}_0$, we linearize this equation with $\varepsilon = \tilde{h}/\tilde{e}_0 - 1$. Then, we have

$$\varepsilon''' = -\Omega\varepsilon \tag{4.2}$$

with $\Omega = 3\left(1 - \tilde{e}_0^2\right)/\tilde{e}_0^3$ and $\tilde{e}_0 = Ca^{-1/2}e_0/l_c$.

Ω can be written in terms of flux as follows:

$$\Omega = \frac{3}{{e_0}^4}\left(Q_c - 3Q_g\right) \tag{4.3}$$

Two asymptotic solutions for the flat film are thus obtained from Equation (4.2), according to the sign of Ω:

$$\varepsilon = \beta e^{-\Omega^{1/3}\tilde{z}} \tag{4.4}$$

$$\varepsilon = \beta e^{\frac{(-\Omega)^{1/3}}{2}\tilde{z}} \cos\left(\frac{\sqrt{3}}{2}(-\Omega)^{1/3}\tilde{z} + \phi\right) \tag{4.5}$$

If $\Omega > 0$, the solution is purely exponential and given by Equation (4.4). In terms of flux it corresponds to $Q_c > 3Q_g$. If $\Omega < 0$ ($Q_c < 3Q_g$), the solution is exponential oscillatory, given by Equation (4.5). β and ϕ are respectively the amplitude and the phase of the asymptotic solution. These are the two types of solutions found at the front and back of Bretherton's bubble [14]. The limit $\Omega = 0$: $Q_c = 3Q_g$, implies a film thickness $e_0 = l_c\sqrt{Ca}$.

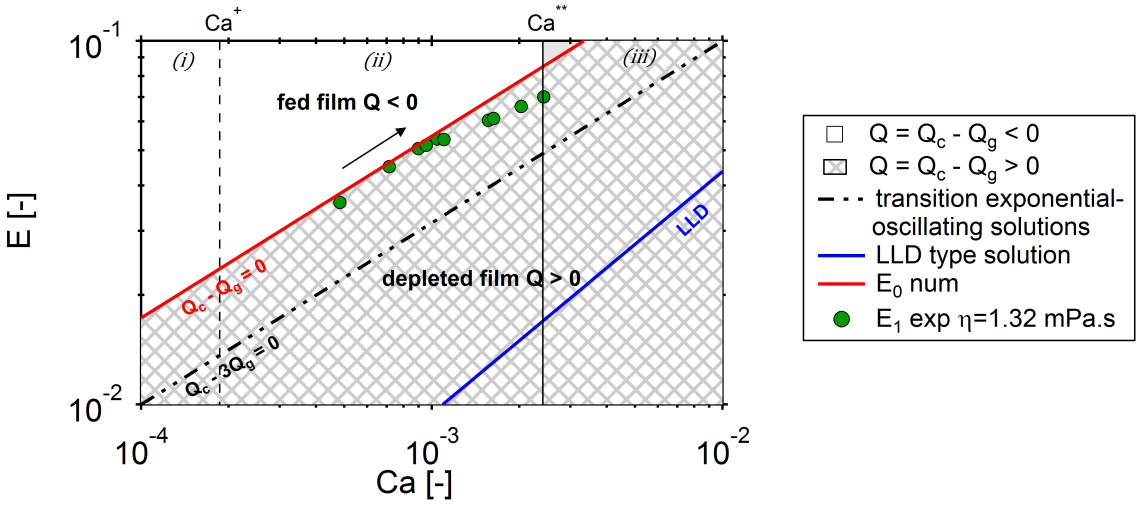

Figure 4.12: *Phase diagram of the profiles: $E = e/l_c$ versus capillary number Ca. The asymptotic limit ($Q_c - 3Q_g = 0$) is given by the black dotted-dashed line (limit between exponential and oscillating solutions). The numerical limit E_0 is the red line ($Q_c - Q_g = 0$). A domain of solutions exists above a minimal value given by $E_0 \geq \sqrt{3Ca}$. Hatched part of the diagram corresponds to a domain without thick film solution, see profile Figure 4.13b. The experimental film thickness E_1 is the green circles. The LLD law is depicted in blue.*

Figure 4.12 presents a phase diagram with the dimensionless film thickness $E = e/l_c$ and Ca. The asymptotic limit between exponential and oscillating solutions obtained for $\Omega = 0$ ($Q_c - 3Q_g = 0$) is the black dotted-dashed line. It corresponds to a thickness $E = \sqrt{Ca}$. Our experimental points $E_1 = e_1/l_c$, depicted by the green circles, lie in oscillatory solution region, but definitely not at the transition: the observed films are much thicker. To better understand this observation, we integrate numerically Equation (4.1)

from the flat film using the direction 1 (red) in Figure 4.11 and evaluate whether or not the profile can be matched to the static meniscus. Doing so, we find a numerical limit plotted in red in Figure 4.12 that divides the space into two regions. The first one (white space) admits solutions: this means that there is a matching between the flat film and the static meniscus. In the second one, there is no flat film solution (hatched zone): this is where the matching is not possible. Of course there is the LLD solution (blue line) but for much thinner films.

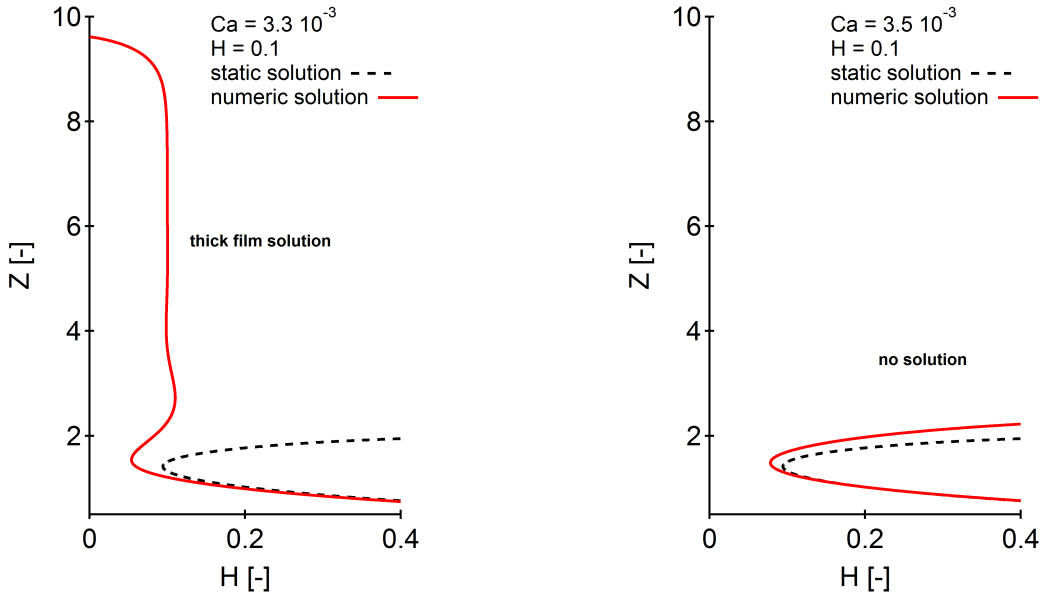

FIGURE 4.13: *(a) Typical numerical profile obtained for $E_0 \geq \sqrt{3Ca}$ ($Q < 0$), when starting from the static meniscus (direction 2 in green). (b) For $E_0 < \sqrt{3Ca}$ ($Q > 0$) no thick film solution is found, the numerical profile diverges from the surface.*

Alternatively, the equation can be integrated starting from the meniscus (point A in Figure 4.11), towards point D (direction 2 in green). In this case, the integration is very sensitive to the initial values of the input parameters. Full profiles can be obtained, as shown in Figure 4.13a, and the same results are recovered: no flat film solution is found for $E_0 < \sqrt{3Ca}$ (Figure 4.13b).

The numerical limit (red curve) is a factor $\sqrt{3}$ larger than the asymptotic limit (black dotted-dashed line). Interestingly, this numerical limit between the two regions fits our experimental data. At larger velocities, some experimental points are observed below this limit possibly because we are in an unstationary state contrary to the numerical calculations and/or because the thick film could be metastable. Altogether, we find that matching is possible only for a sufficiently thick film *i.e* $Q_g \geq Q_c$. There are solutions for $Q_g > Q_c$, but these are not observed experimentally (yet).

4.3.3 Matching a film with a triple line

We look here for an analytical solution of a flat liquid film matched to a triple line using Equation (2.7). As shown in the schematic representation in Figure 4.14, for a flat film solution, *i.e* $\partial_{\tilde{z}}\tilde{\kappa} = 0$. We define Q_d the downward flux due to dewetting (Figure 4.10).

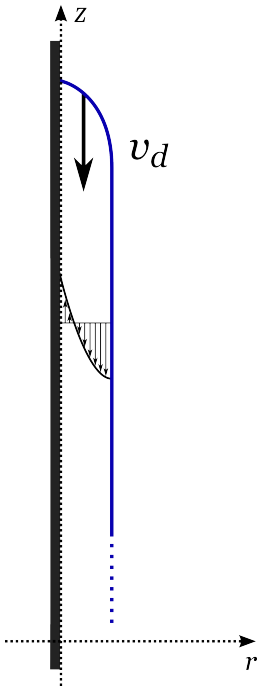

Figure 4.14: *Schematic representation of a flat film solution with a triple line moving down a cylindrical tube up at the velocity $-v_d$ in the reference frame of the triple line. The flow is upward close to the wall and downward close to the free surface.*

Equation (2.7) can be integrated as follows:

$$\tilde{h} - \frac{\tilde{h}^3}{3} = \text{cste} \tag{4.6}$$

Since the flat film ends with a triple line, the flux in the film is null, we obtain cste = 0 so that $Q_d = Q_g$ which translates into:

$$e_1 = l_c\sqrt{3Ca_d} \tag{4.7}$$

Equation (4.7) can be written differently to highlight the physical origin of the film. $e_1 = \sqrt{3\eta v_d/\rho g}$ presents the thickness as the square root of the ratio between viscous resistance and gravitational drainage. This is why we will name this film a gravitational film. This relation has been plotted in Figure 4.6. Each dashed line corresponds to the prediction taking the viscosity of one liquid. There is good agreement between the experiments and the prediction with no adjustable parameter.

The analytical prediction given by Equation (4.7) is represented by the dashed black line in Figure 4.9b. We recover this prediction exactly when writing the capillary number

as the dewetting capillary number Ca_d. Then, the question of the scaling with Ca arises. We note that the 1/2 scaling is also roughly observed with Ca, but deviations appear as Ca increases (Figure 4.9a).

We can conclude that the film thickness e_1 is directly coupled to the dynamics at the dewetting triple line Ca_d. As long as $Ca_d \sim Ca$, a thick film solution exists because the condition close to the meniscus defined in the previous section by the sign of Ω in the asymptotic solution is fulfilled.

4.3.4 Transition from *regime (i)* towards *regime (ii)* and rim formation

As emphasized in Chapter 3, below the threshold Ca^+, the slug keeps a cylindrical shape with slight deformation of the rear meniscus due to viscous bending (Figure 4.15).

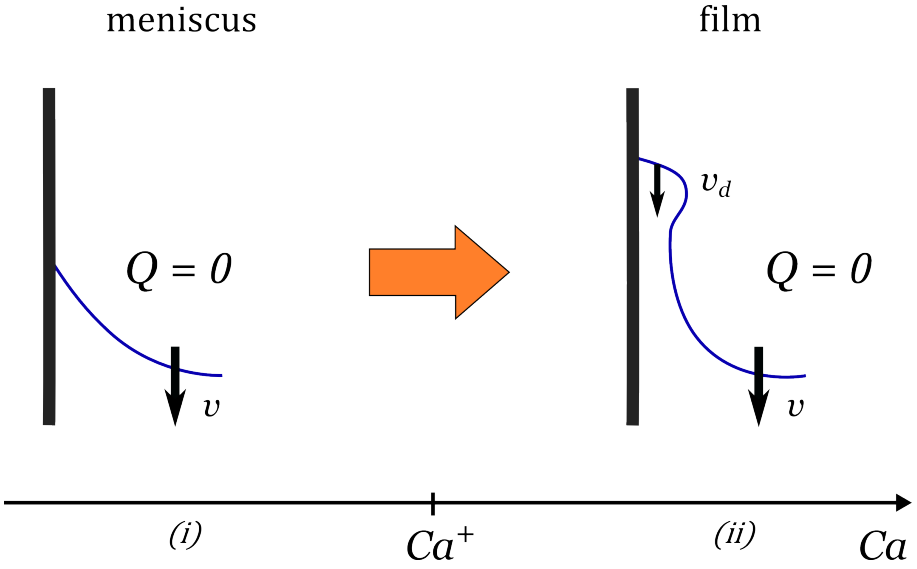

FIGURE 4.15: *Schematic of the transition between a meniscus state and a film state. The dynamic wetting transition occurs at null overall flux.*

The contact line velocity is identical to the slug velocity, $v_d = v$. The overall flux of the meniscus is null $Q = Q_c - Q_g = 0$ and $Q_d = Q_g$. At the transition Ca^+, the previous statement is also fulfilled, meaning that the dynamic wetting transition occurs at an overall flux null. Above Ca^+ the liquid film develops at the rear of the slug (Figure 4.15). The liquid film dewets from the tube wall because of the hydrophobic property of the tube. We have shown earlier that the condition $Q_d = Q_g$ was always fulfilled, therefore after the dynamic wetting transition $Q = Q_c - Q_g > 0$ since $Q_d < Q_c$.

We now look for an explanation for the rim formation. This type of rim is not modeled in the literature, and has not been observed by Snoeijer *et al.* [2, 76]. The typical numerical profile obtained in Figure 4.13a does not present a rim at the dewetting triple line. This is possibly due to the steady state approximation. Indeed, the rim formation may be due to a transient regime observed at the very beginning of film formation. This may explain also why the rim does not grow. To test this hypothesis, the temporal derivative of the

thickness has to be taken into account, *i.e* $\partial_t h \neq 0$, as in Chapter 3.

We numerically investigate the temporal evolution of the thick film formation in order to see whether or not a rim is formed. In Section 3.5.2, we have presented profiles of the meniscus before and slightly after the dynamic wetting transition. We now report in Figure 4.16 profiles evolution with time for a larger capillary number $Ca = 4.075\ 10^{-4}$. After a certain time (a few milliseconds) the triple line moves up and a liquid film is entrained on the surface.

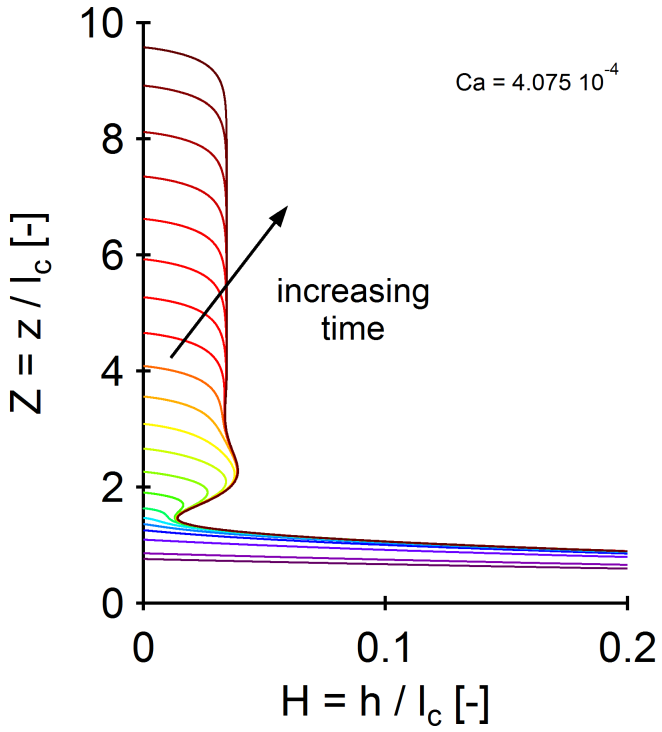

Figure 4.16: *Normalized meniscus profile $H(Z)$ as a function of time after the dynamic wetting transition $Ca = 4.075\ 10^{-4}$. A growing liquid film is entrained at the wall. We observe the formation of a dimple between the meniscus and the film that takes a stationary shape at long times.*

At short time scales, the shape of the profile is a bump which grows both in thickness and along the $Z-$direction. We could think that this bump will be at the origin of the rim at the film end. But after some times, the thickness of the bump reaches a maximal value and stops propagating in the vertical direction. The triple line is continuously moving up forming a homogeneous film, both spatially and temporally. The bump becomes in fact the dimple and there is no rim at the film end on the numerical profiles. Unstationary state alone cannot account for the rim that we observe experimentally close to the triple line. This phenomenon is robust in our experiments but we have no model that neither explains the rim formation nor predicts its shape. We can assume that it may be due to additional dissipation occurring only at an early stage of the film formation, because for longer timescale, the rim is stationary. One possible explanation can be found in the

surface roughness leading to a dependency of the contact angle with the capillary number $\theta = f(Ca)$ or an effect of the axisymmetry of the tube or maybe both.

Previously, we noticed that the rim was more pronounced in thickness for lower capillary number Ca whereas its length was independent of Ca. For smaller capillary number Ca the film is thinner, so the pressure drop is larger leading to a liquid accumulation at at the triple line and consequently to a thicker rim. Note that this rim is not the type of rim observed by Redon *et al.* [64] in their dewetting film experiments. Indeed, in our case the rim is not growing in the vertical dimension over time (it does not collect liquid), and the velocity of the triple line depends on the film thickness.

Besides, these simulated profiles are in good agreement with our experimental results and confirm the quasi-stationary assumption made earlier. Indeed, the dimple takes a stationary shape even when taking into account the time-dependency. The film is homogeneous in time. Nevertheless the thickness selected is independent of Ca: $E_1 \simeq \sqrt{3Ca^+}$. This is not what we found experimentaly but this is in good agreement with Snoeijer *et al.* [2] (experiments) and Hocking [4], Snoeijer *et al.* [1], Gao *et al.* [5] (numerics).

4.4 Discussion

In the previous sections we have demonstrated the existence of a flow *regime (ii)* where a short thick film is generated at the rear of a liquid segment. This type of liquid film differs from the classical film generally observed when displacing a liquid over a plate or in a tube. Most of the experiments found in the literature consider complete wetting conditions [11, 17, 63]. In these classical LLD-Bretherton cases, the triple line is static: $Q_d = 0$ (Figure 4.10). If the triple line is fixed, Q_g is strongly reduced compared to the flux convecting liquid upward Q_c, leading to the deposition of the liquid film. Except at larger $Ca \sim 1$ The thick film regime cannot develop and the LLD-Bretherton film appears. This type of film comes from a visco-capillary balance where the thickness scales as $Ca^{2/3}$. In our work, due to the partial wetting condition, dewetting occurs and the contact line at the end of the deposited film is mobile ($Q_d \neq 0$). This is required to generate thick film solutions. Dewetting and gravity induce downward fluxes Q_d and Q_g which are equal to the convecting flux Q_c at low capillary number, and therefore selects a different, thicker solution.

The general theory of the problem has been first presented by Derjaguin, in the planar geometry [12]. For the case of thick films, he provides a formula without strict derivation, showing that the thickness of the coated layer on a plate is independent of the surface tension of the liquid. The proposed prediction, $e_D = \sqrt{\eta U/\rho g \sin\alpha}$ (Equation (1.6)), where α is the plate inclination, was obtained without considering the moving contact line. Later Wilson and Jones have pursued this problem further, considering fixed and moving plates entering a liquid bath [93, 23]. They have shown that the solution for the thickness of the film is not unique above a threshold capillary number. They have also stated that, above this threshold value, larger values of the film thickness with a wavy

shape are obtained numerically. They explained that such film solutions have not been observed experimentally probably because of their unstable character. We prove here that it is possible to observe the stationary thick film solution. In our case Q_g is fixed by Q_d. In fact the analytical prediction ($Q_d = Q_g$) of a capillary/gravity film and our experiments are in good agreement. The system selects the condition $Q_d = Q_g$ corresponding to an overall flux equal to zero close to the triple line. We found a very good agreement between numerical and experimental results both for the threshold in Ca and for the film profiles, leading to the conclusion that the film observed in *regime (ii)* is a gravitational thick film with a dimple.

In addition, we have shown that the velocity of the slug Ca increasingly differs from the dewetting velocity Ca_d when Ca increases. This is connected to the fact that the flux from the slug to the film $Q = Q_c - Q_g$ is not zero when Ca is sufficiently large. We have also shown that the thickness scaling is obtained for the capillary number relative to the dewetting velocity of the contact line and not the one relative to the slug velocity (or plate in the case of the experiments of Snoeijer *et al.* [2]). Indeed, as we varied the capillary number of the dewetting triple line, we were able to observe various thick film thicknesses.

Moreover, we note in Figure 4.12 that the numerical limit extends over the entire Ca scale, contrary to our experiments that are concentrated between $Ca^+ < Ca < Ca^{**}$. We therefore expect something new to happen in the numerics when Ca reaches Ca^{**}.

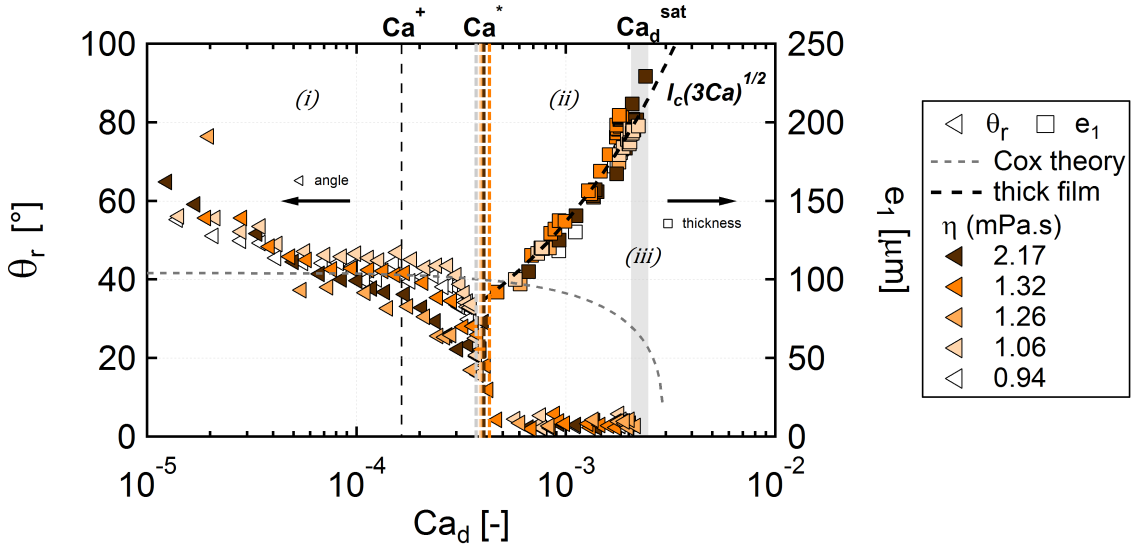

FIGURE 4.17: *Receding contact angle θ_r (left axis - triangles) and thick film thickness e_1 (right axis - squares) as a function of the capillary number of the dewetting film for various mixtures.*

Figure 4.17 gathers the main features of the results obtained in Chapter 3 and 4. The receding contact angle, θ_r, and the thickness of the thick film e_1 are plotted as a function of the dewetting capillary number Ca_d. Before the dynamic wetting transition the only macroscopic quantity is the receding contact angle which decreases with the capillary number. Above the transition $Ca > Ca^+$, the receding contact angle first decreases

sharply, then, above Ca^*, θ_r becomes roughly constant and independent of the capillary number and is equal to $\theta_r = 5 \pm 2°$. The physical quantity of interest is now the film thickness e_1. In our study, we have shown the existence of thick film solutions with a $Ca_d^{1/2}$ scaling for thickness versus capillary numbers in a significant range of capillary number ($1.8\ 10^{-4} < Ca < 22\ 10^{-4}$). We have seen earlier that we observe a dewetting rim close to the triple line, whose shape is stationary and modified when increasing the capillary number Ca. The rim is more pronounced for lower capillary number Ca.

4.5 Playing with transients

To better prove our understanding of film formation, we now experimentally investigate the transient between two well controlled steady state regimes. We start an experiment at a given slug velocity, then we suddenly vary the velocity of the slug by applying a step change to the gas pressure behind the slug. We observe the subsequent variations of the interface velocities, film thickness, film and slug lengths. An example for pure water ($\eta = 0.94$ mPa.s) is given in Figure 4.18.

In the first part of the experiment, the slug velocity is chosen as the upper limit of *regime (ii)*, $v = 19.5$ cm.s^{-1} and the dewetting velocity is $v_d = 14.7$ cm.s^{-1} (zone A in Figure 4.18a). As shown by Figure 4.18b, the slug length decreases while the film grows. Then the velocity of the slug is decreased abruptly down to a value just above Ca^+, $v = 2.8$ cm.s^{-1}. This velocity change corresponds to the limit between zone A and zone B in Figure 4.18. We can observe on the spatio-temporal diagram that the dewetting velocity remains initially unchanged after the transition A−B: $v_d = 14.7$ cm.s^{-1}. It takes about 0.6 s before the dewetting velocity starts to decrease noticeably. At the arrow, the dewetting velocity progressively decreases from $v_d = 14.7$ cm.s^{-1} to $v_d = 2.8$ cm.s^{-1}. Zone B is a transition zone of about 1 s, where the film length decreases to feed the slug which increases in length. In zone C, a second stable state is obtained. The slug velocity and the dewetting velocity are equal at 2.8 cm.s^{-1}, with no significant change in the film and slug lengths.

To summarize, the velocity perturbation brings the system from a state A towards a state C, via a transition zone B.

In fact, if we get a closer look to zone B, we can see that the velocity of the rear of the slug is even reaching values below $v = 2.8$ cm.s^{-1}, the one imposed by the gas pressure. Indeed, in zone B, the liquid film feeds the slug with a larger flux than the upward flux from the slug into the film: $Q_c < Q_g$. As shown earlier, these solutions are perfectly valid. Also, after the transition A−B but before the arrow (Figure 4.18a), the film thickness is constant in time. This observation confirms the close dependence between the dewetting velocity v_d and the thickness of the film e_1.

A remaining question is the mechanism that triggers the change of dewetting velocity, since the triple line adapts its velocity once it gets close enough to the rear of the slug.

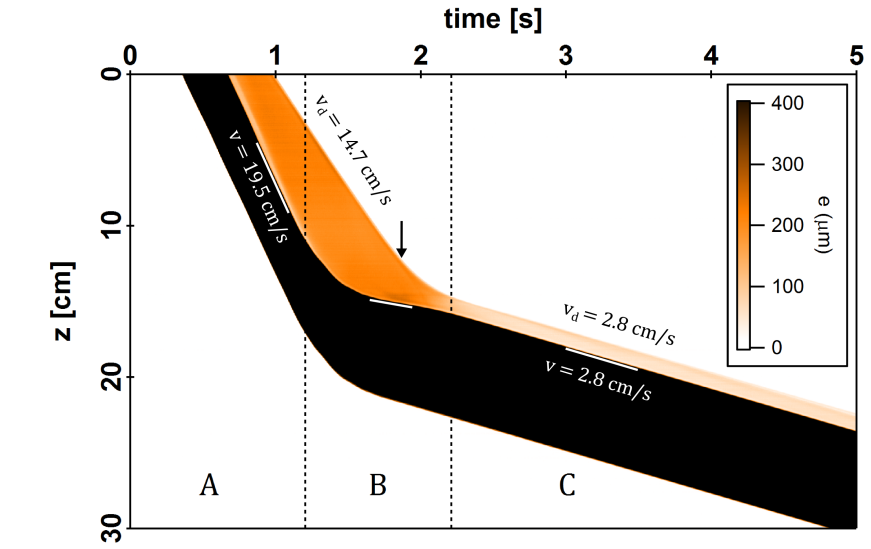

(a)

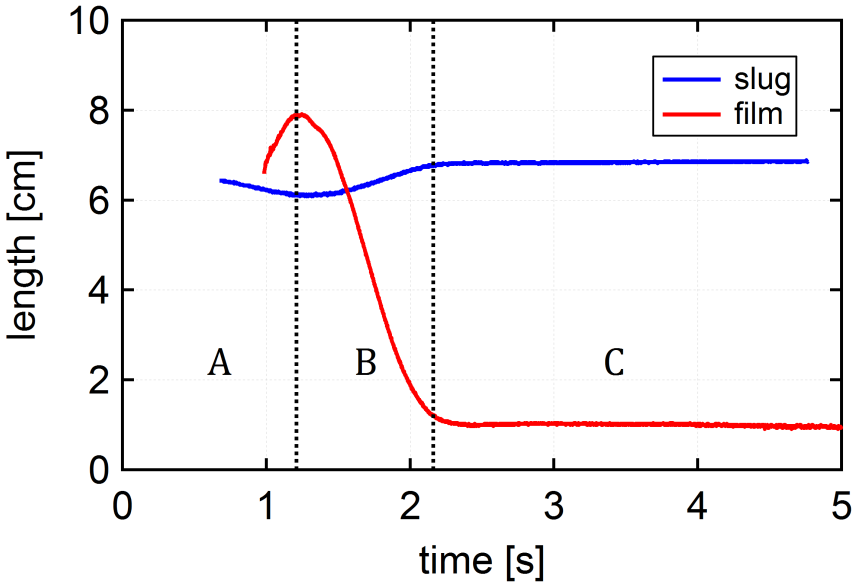

(b)

FIGURE 4.18: *(a) Spatio-temporal diagram of film thickness for an experiment with water ($\eta = 0.94$ mPa.s), where we have suddenly decreased the velocity of the slug during the flow. The velocity goes from 19.5 cm.s^{-1} to 2.8 cm.s^{-1}. (b) Corresponding slug and film length evolution with time.*

Thanks to the phase diagram built in Section 4.3.2, we can get an understanding and a predictive approach of the thickness of the film. For the same experimental example provided in Figure 4.18, we can place the initial state A in the phase diagram Figure 4.19. As seen previously, at given capillary number the system selects the thickness corresponding to $Q_g = Q_d$ (numerical limit, red line in Figure 4.19).

When perturbation of the velocity is induced, the slug velocity and thus the capillary number Ca decreases along the horizontal arrow, from right to left in Figure 4.19. This decrease of Ca occurs at a constant dewetting capillary number Ca_d (in the example $v_d = 14.7$ cm.s^{-1}) and constant film thickness e_1. These two quantities follow the law $e_1 = l_c\,(3Ca_d)^{1/2}$. Along this arrow, we temporarily have a strong flux from the film towards the meniscus ($Q = Q_c - Q_g < 0$) and assess even thicker film solutions that can be matched to the meniscus. The rear meniscus adapts its shape. Note that these solutions are not accessible when starting from a zero velocity (static case).

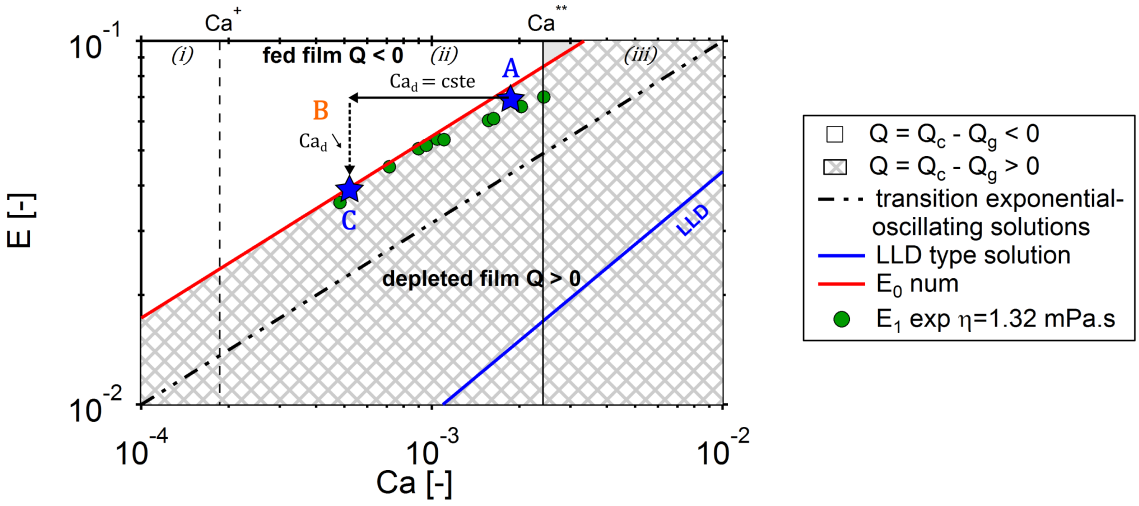

FIGURE 4.19: *Pathway of the experiment from Figure 4.18 represented in the phase diagram $E = e/l_c$ and Ca.*

Once the dewetting triple line reaches the $z-$position of the slug around the transition A$-$B in Figure 4.18, the dewetting capillary number Ca_d starts to decrease. Consequently, the film thickness e_1 is progressively thinning ($e_1 = l_c\sqrt{3Ca_d}$). The liquid flux coming from the film towards the slug decreases. It induces a progressive increase of the velocity of the slug and a stabilization at $v = 2.8$ cm.s^{-1}. The system is in state C, where $e_1 = l_c\,(3Ca_d)^{1/2}$.

We also studied the other case where the slug velocity is increased suddenly. However to understand the results, we first need to investigate *regime (iii)* in more detail.

4.6 Conclusion

In conclusion, we are able to generate and observe thick films, first described theoretically by Derjaguin [12] and later by Wilson [93], Hocking [4] and Snoeijer *et al.* [2, 76]. In our work, we observe the existence of gravity/capillary films in partial wetting condition. Very few experiments exhibit this type of film solution. Indeed, only one example is given in a planar geometry by Snoeijer *et al.* [2, 76].

This kind of thick film is flat with a significant thickness (a few hundred microns), typically larger than the LLD film at the same velocity. It is linked to the meniscus

by a dimple. Typically, once entrained at the wall of the tube, this film is constantly elongating in time, since the dewetting velocity is smaller than the slug velocity $v_d < v$. This velocity difference is more pronounced when the velocity of the slug becomes larger. Then, the dewetting velocity saturates at v_d^{sat} and a transition towards a third flow regime (*regime (iii)*) is observed. The film thickness scales as the triple line velocity $e_1 = l_c\sqrt{3Ca_d}$ rather than meniscus velocity, which shows that there is a strong connection between film thickness and dewetting velocity. This dependency of the dewetting velocity v_d with film thickness far from the contact line e_1 has been predicted analytically by Buckingham *et al.* [94].

Numerically, we are able to account for our experimental observations with an approach similar to the theory of Wilson and Jones [93, 23]. The domain of the solutions is limited by an overall flux equal to zero ($Q = Q_c - Q_g = 0$ or $e_1/l_c = \sqrt{3Ca}$), *i.e* an expanding film. This threshold is a more stringent condition than the limit between exponential and oscillating solutions. Most of our experimental data lie on the numerical lower limit of this solution domain. Indeed, the system selects the condition $Q_c = Q_g$. Experimentally, we can also generate transiently thick film where $Q < 0$ at the meniscus (fed film). Finally, experimental and numerical profiles are in good agreement, apart from the triple line region where we observe experimentally an additional rim.

The rim morphology is independent of the liquid viscosity in the range used, and the contact angle at the triple line is always very low (a few degrees). Such a rim is not modeled in the literature, and has not been observed by Snoeijer *et al.* [2, 76]. We assume that its formation may be due to additional dissipation occurring only at early stage of the film formation. One possible explanation can be found in the surface roughness leading to a dependency of the contact angle with the capillary number $\theta = f(Ca)$ or an effect of the axisymmetry of the tube or maybe both.

In other words, it has been possible to experimentally observe thick film solutions thanks to the presence of downward fluxes of liquid Q_d and Q_g generated by the moving contact line and gravity. But playing with the slug velocity, their behavior has been probed.

Chapter 5

Two films: gravitational and viscous

5.1 Introduction

Above a second threshold capillary number Ca^{**} of the slug, the dewetting capillary number saturates at Ca_d^{sat} and a new regime is obtained: *regime (iii)*. As already mentioned in Chapter 1, experiments in the literature demonstrated that the film thickness entrained on a plate in a dip coating experiment may not be unique [2, 5]. In these experiments it is found that Ca_d is constant and independent of Ca. The entrained film presents a so called ridge structure that divides the film into two regions. The region close to the bath is a LLD film while the region close to the contact line does not follow the classical LLD law. It is stated that instead the non classical film thickness is fully determined by the physics of the contact line, namely the velocity Ca_d. In their experiments, the thick film previously described in Chapter 4 is thought to be a transient state. At the later stage of liquid entrainment, the thick film connected to the liquid bath via a dimple disappears, leading to the emergence of the LLD film. Several questions emerge as to the role of this ridge structure in the transition.

In fact, when deposited on a plate under partial wetting condition, a film takes a trapezoidal or triangular shape, which is characterized by the presence of inclined contact lines [70, 71, 2, 3] (Chapter 1). Similar contact-line inclination was observed in the context of sliding drops [72, 73, 74]. These shapes are typically due to edge effects and can be avoided using a cylindrical geometry.

Taking benefit of the axisymmetric properties of the tube geometry, which stabilizes the liquid film (no edge effect), this chapter aims at understanding the physical mechanisms at the origin of *regime (iii)*. We will address the question of the transition between *regime (ii)* and *(iii)*. What are the criteria to observe this transition, in particular in term of threshold velocity? What is the film morphology in *regime (iii)* and what selects the film thickness? In the first part of this chapter, we study the overall kinematic fields (velocities and thicknesses) of the liquid film. In the second part, we propose a numerical

model providing explanations on the nature of the film morphology. The last part of this chapter is devoted to the study of unstationary films and their description using the numerical model.

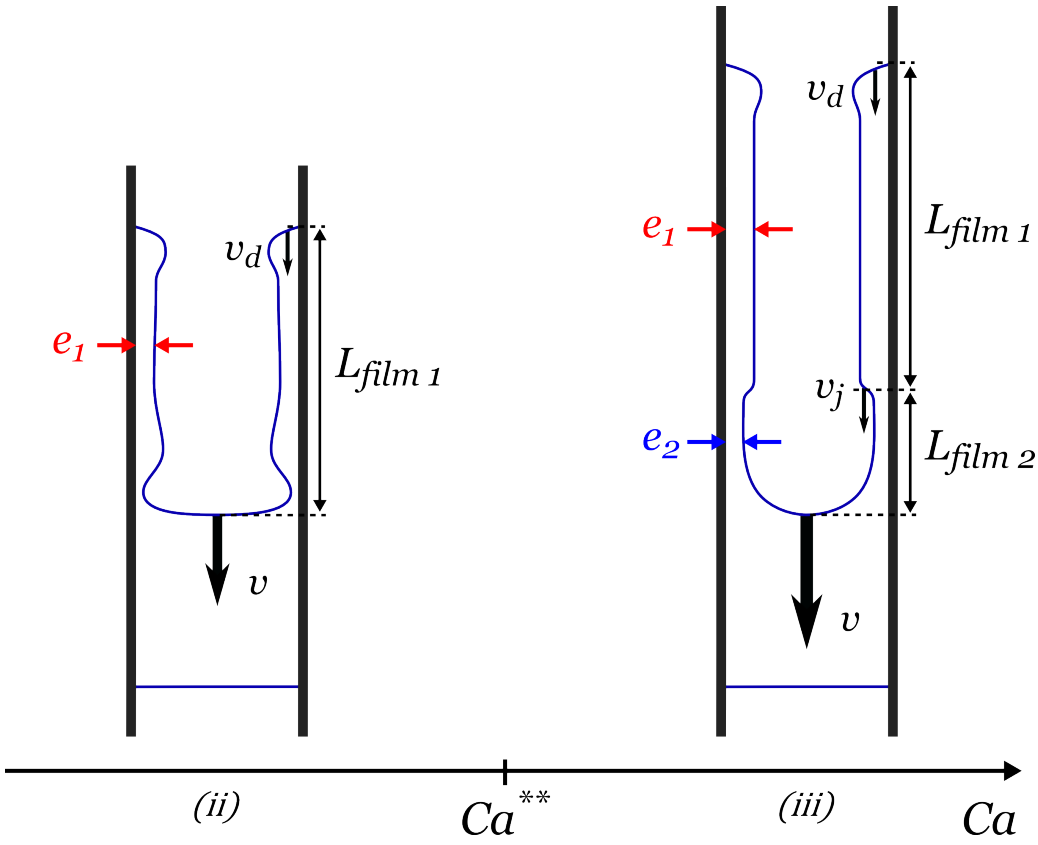

FIGURE 5.1: *Schematic of the evolution of a meniscus when increasing its velocity v, and therefore its capillary number Ca. Above a second threshold capillary number Ca^{**} a second liquid film of length L_{film2} and thickness e_2 is entrained. The velocity of the jump in thickness is v_j.*

5.2 Results

5.2.1 Experimental observations

Similarly to experiments presented in Chapter 4 concerning *regime (ii)*, we investigate the film entrainment of low concentration solutions of water and glycerol ($0-40\%$wt) in a PVC tube of diameter $d_{in} = 6.4$ mm. We use the "large velocity setup" and techniques presented in Chapter 2 to visualize and measure the velocities of the different interfaces and the film thickness. In this chapter, we vary the velocity of the slug to reach a capillary number from $Ca = 2.2\ 10^{-3}$ up to $2\ 10^{-2}$ for different liquid viscosities. These capillary numbers correspond to a wide velocity range $v = 4.5-100$ cm.s^{-1} depending on the liquid viscosity. Two quantities are particularly of interest: the velocities of the interfaces and the film morphology, especially its thickness.

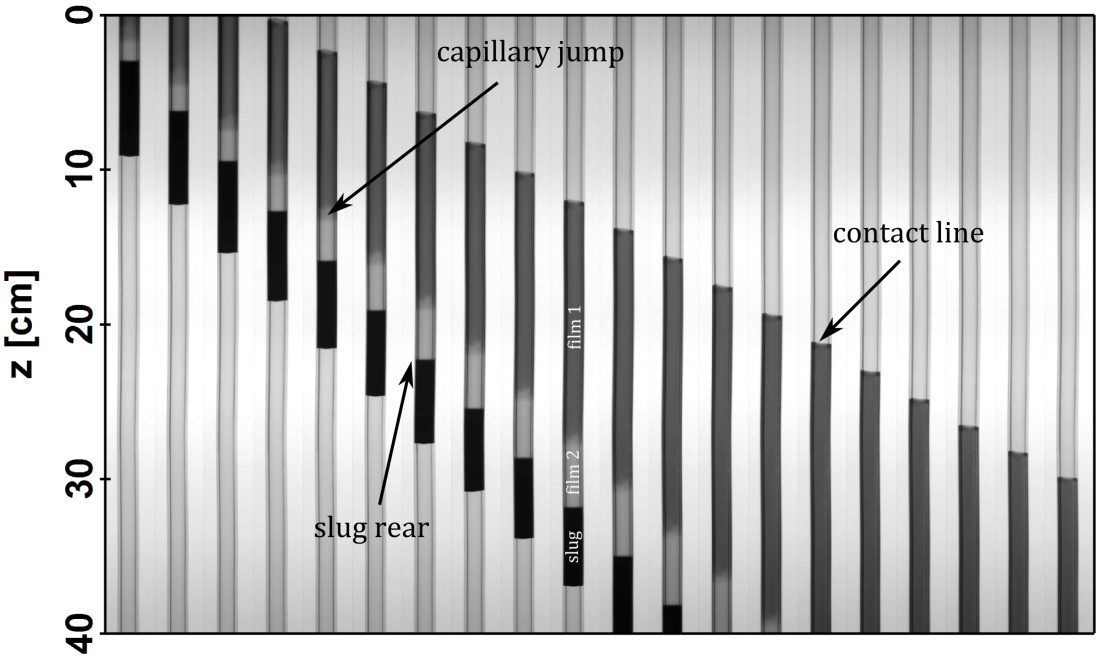

FIGURE 5.2: *Image sequence for a typical experiment in regime (iii), i.e for* $Ca > Ca^{**}$*, where two films are formed. Experimental parameters are: 20%wt glycerol solution* ($\eta = 1.66$ *mPa.s),* $v = 15.8$ $cm.s^{-1}$, $Ca = 4\ 10^{-3}$, $\Delta t = 0.2$ *s.*

In this velocity range, we observe a liquid film entrained behind the slug which dewets at a velocity v_d along the tube, as in *regime (ii)* (Chapter 4). The film has a finite length denoted L_{film}, which increases rapidly with time, suggesting that, in contrast to *regime (ii)*, the velocity of the dewetting film is significantly different from the velocity of the slug. But in this regime, which we call *regime (iii)*, the liquid film is subdivided into two parts along the vertical direction. A typical example of film morphology is shown in Figure 5.2 for 20%wt glycerol solution ($\eta = 1.66$ mPa.s) and slug velocity $v = 15.8$ cm.s^{-1}. The camera window still captures 40 cm of the tube. The time step between each frame is $\Delta t = 0.2$ s. The slug appears as black and right behind the slug, we can notice a short liquid film in light grey. We will name this film the second film with L_{film2} (Figure 5.1). This lower part is connected to an upper part in middle grey, denoted first film with a length L_{film1}. There is a sharp edge between the two films, named jump, with velocity v_j.

Kinematics: film lengths and interface velocities

In Figure 5.3, we show the time evolution of the total film length L_{film} and the slug length L_{slug}. These lengths are directly measured by extracting the $z-$position of the different interfaces from the image sequence in Figure 5.2. We see that the liquid film length (orange) grows with time. The growth rate is constant since the slope of the orange curve is constant in time. Simultaneously, the slug length (blue) decreases. Furthermore, as for

regime (ii), the growth rate of the film is much faster in absolute value than the shrink rate of the slug, since the radius of the tube is large compared to the thickness of the film. We monitor the length of the first film (upper part) L_{film1} and the length of the second film (bottom part) L_{film2} as shown in Figure 5.1. In the observation window, the first film (red in Figure 5.3) is always longer than the second film (green), and grows in length much faster. Moreover the length of the second film L_{film2} seems to saturate in time.

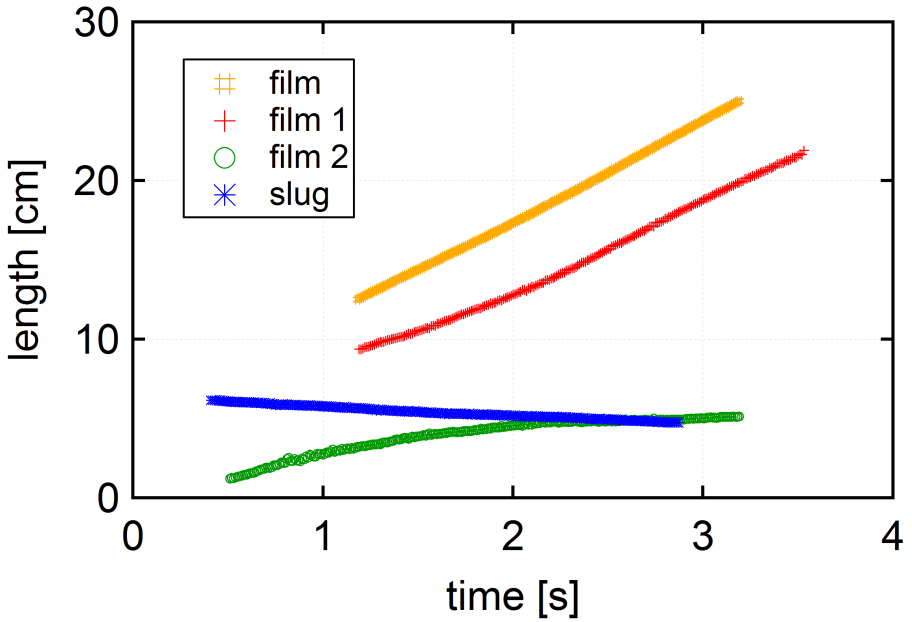

FIGURE 5.3: *Slug (blue) and total film length (orange) as a function of time, measured from the image sequence shown in Figure 5.2. The film is segmented in two parts, the first film in the upper part (red) and the second film in the lower part (green). Experimental parameters are: 20%wt glycerol solution ($\eta = 1.66$ mPa.s), $v = 15.8$ cm.s^{-1} ($Ca = 4\ 10^{-3}$). The slug decreases in length while the film grows.*

Instead of measuring the time evolution of the length of the liquid films, we can measure the interface velocities based on a spatio-temporal diagram (Figure 5.4a). This plot corresponds to the extraction from the image sequence given in Figure 5.2, along the center line of the tube. As explained in the Experimental description (Section 2.1.2), the slopes directly provide the velocity of the different interfaces: rear of the slug v, dewetting of the film v_d and in addition the jump v_j. Using this method, we find that in Figure 5.3 the contact line at the film end dewets at a velocity $v_d = 8.8$ cm.s^{-1} roughly twice slower than the velocity of the slug imposed in the experiment $v = 15.8$ cm.s^{-1}. This is a strong difference with *regime (ii)*. The velocity of the jump is constant in time and $v_j = 14.3$ cm.s^{-1}. The jump is only slightly slower than the slug but faster than the dewetting film. This is why the elongation of the second film $L_{film2} \propto v - v_j$ is slower than that of the first film $L_{film1} \propto v_j - v_d$.

Film morphology

The greyscale spatio-temporal diagram can also be converted into thickness (Figure 5.4a). In this representation, the slug is in black, the second film is in light orange and the first film is in dark orange. We observe that the color of each film is homogenous which means that each film has a uniform thickness. There is a sharp difference between these two thicknesses.

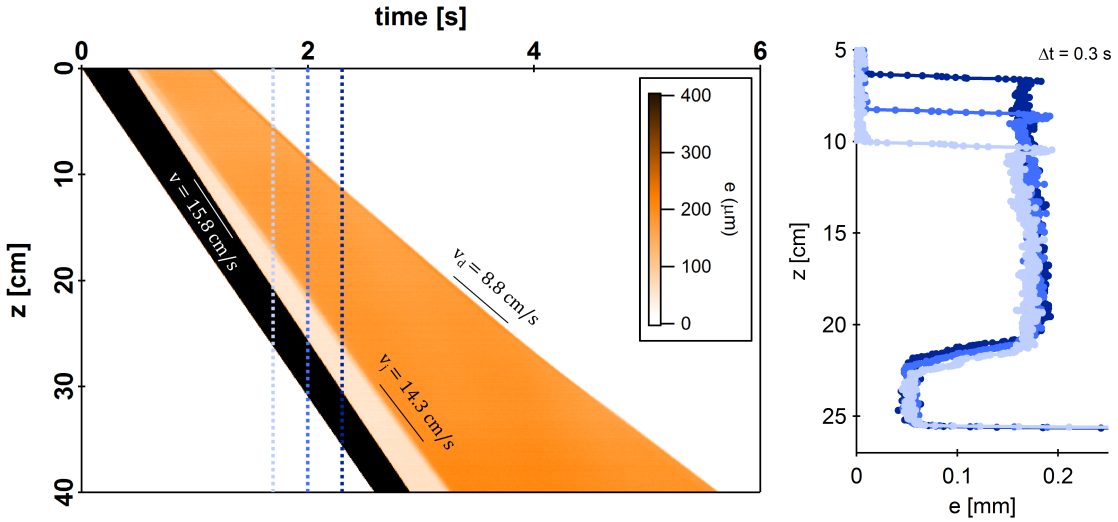

(a) (b)

FIGURE 5.4: *(a) Spatio-temporal diagram of thickness from the image sequence represented in Figure 5.2. (b) Successive experimental thickness profiles ($\Delta t = 0.3$ s) for 20%wt glycerol solution ($\eta = 1.66$ mPa.s), $Ca = 4\ 10^{-3}$, $Ca_d = 2.2\ 10^{-3}$. The slug is linked to a second homogeneous film of thickness $e_2 = 52\ \mu$m, this time without dimple (viscous film). This second film is connected to the first film of thickness $e_1 = 184\ \mu$m (gravitational film). The first film is about 15 cm long and ends with a rim.*

We can extract three profiles from the spatio-temporal diagram to get a clearer view of the film morphology. Typical successive profiles in *regime (iii)* are given in Figure 5.4b for 20%wt glycerol solution at $Ca = 4\ 10^{-3}$. The time lapse between each profile is $\Delta t = 0.3$ s as represented by vertical dotted lines in Figure 5.4a. The profile are given in the reference frame of the rear of the slug. The film length is about 15 cm. The profiles confirm the presence of a thin flat film right behind the rear meniscus of the slug. We will denote as e_2 the thickness of this second film. In the example, the second film thickness is $e_2 = 52 \pm 5\ \mu$m. Contrary to the profile of the gravitational film in Chapter 4, there is no dimple between the rear of the slug and the flat second film. The upper film is also flat but thicker, in the present example $e_1 = 184\ \mu$m. Finally the top part of the film forms a rim, as in *regime (ii)*. Its shape is steady over time even though the triple line is dewetting. These growing films maintain constant thickness over time.

5.2.2 Kinematic evolution with slug velocity

We now focus on the velocities, and especially on the relation between the slug velocity and the two film velocities. We iterate similar experiments as before, and vary the velocity of the slug v by imposing different gas pressures. The slug velocity v, measured using the slopes of the position in the spatio-temporal diagram, is constant in the experimental window. Image sequences obtained in *regime (iii)* are similar to those presented in Figure 5.2.

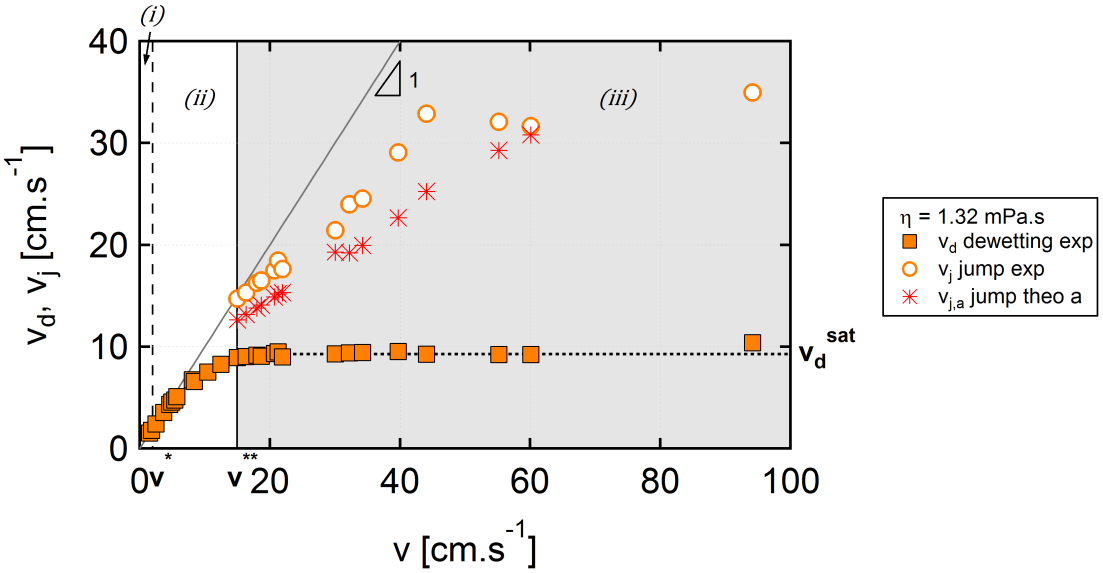

FIGURE 5.5: *Interface velocity variations (v_d and v_j) as a function of slug velocity v for 15%wt glycerol solution, $\eta = 1.32$ mPa.s. The velocity of the jump v_j increases with v. Predicted velocity of the jump $v_{j,a}$ (red stars), considering flux conservation at the capillary jump (Equation (5.6)).*

Typical evolution of interface velocity v_d and v_j as a function of slug velocity v for 15%wt glycerol solution ($\eta = 1.32$ mPa.s) are shown in Figure 5.5. As already seen in Chapter 4, before the transition towards *regime (ii)*, the dewetting velocity v_d is initially very close to the slug velocity, but a significant difference gradually builds up as v increases. Here in *regime (iii)*, for slug velocities $v > v^{**}$ (grey zone), the dewetting velocity v_d saturates at (v_d^{sat} here is 9.2 cm.s^{-1}) and the two film morphology with a jump is observed. The velocity of the jump v_j (open symbols) increases with the slug velocity v and the difference $v - v_j$ increases with v.

The same trends, $v_j = f(v)$, are observed for other viscosities. We have seen in Chapter 4 that v_d^{sat} depends on the fluid characteristics. We will discuss this point in Section 5.3.1. For a comprehensive description of v_d with v for various viscosities, refer to Figure 4.5.

One of the key results is that the jump starts to be observed simultaneously with the saturation of the dewetting velocity.

5.2.3 Thickness evolution of the liquid films with slug velocity

For each viscosity, we define the threshold velocity v^{**} as the slug velocity above which a second film develops over time. The film thickness e_2 can be systematically measured, for a given liquid when varying the slug velocity. The thickness of the first film has been discussed in Chapter 4. Figure 5.6 gathers average film thicknesses e_2 as a function of slug velocity v for various glycerol concentrations and for velocities larger than the threshold v^{**}.

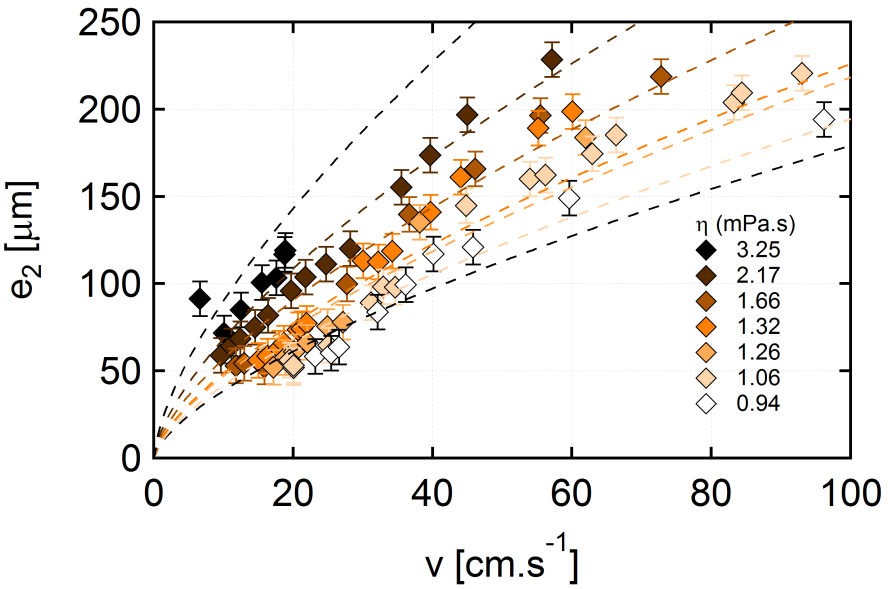

FIGURE 5.6: *Average film thickness e_2 as a function of slug velocity v for various glycerol concentrations. The model considering a visco-capillary entrainment of a flat film is given by the dashed line for each liquid (Equation (1.1) with no fitting parameter).*

The same evolution is observed for all the liquids: e_2 increases with v, but the larger the viscosity the faster the film thickens with velocity. As shown in Section 4.3, we find that the threshold velocity v^{**} decreases with liquid viscosity. For the largest viscosity ($\eta =$ 3.252 mPa.s) we find $v^{**} \simeq 5$ cm.s^{-1}, whereas for the lowest viscosity ($\eta = 0.94$ mPa.s) the second film appears around $v^{**} \simeq 20$ cm.s^{-1}. We can note that at low capillary number e_2 is close to the thickness of the dimple described in Figure 4.7, suggesting that the dimple becomes the second film.

Furthermore, using the thickness profiles at the rim close to the triple line, we observe that the rim morphology, namely its width and height, and the contact angle at the triple line, are independent of v and v_d in *regime (iii)*. This is not surprising because v_d, e_1 and θ_r are fixed close to the triple line in this regime (Figure 4.17).

5.3 Discussion

5.3.1 Dewetting velocity at saturation

In *regime (iii)*, *i.e* for slug velocities $v > v^{**}$, the dewetting velocity saturates at $v_d = v_d^{sat}$ (Figure 4.5). In Figure 5.7, we plot this saturation value v_d^{sat} as a function of the characteristic velocity of the liquid $v_{liq} = \gamma/\eta$. We find that this velocity increases with v_{liq}.

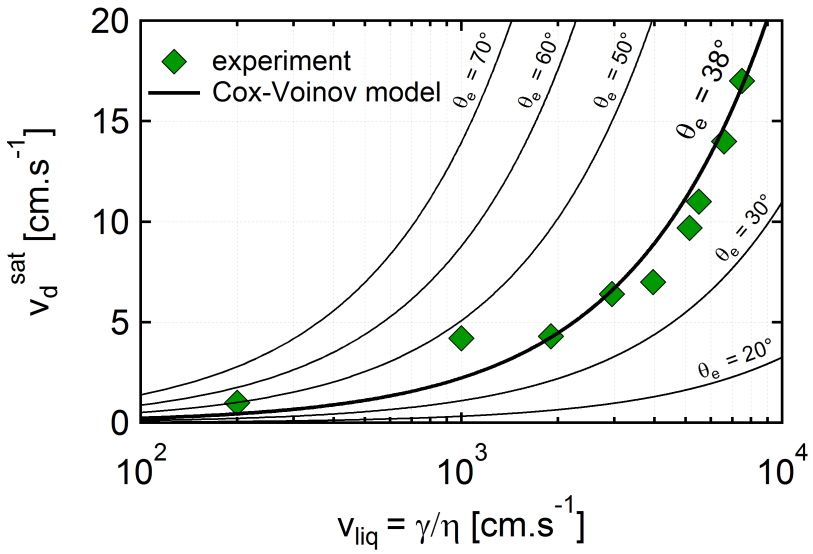

FIGURE 5.7: *Dewetting velocity at saturation v_d^{sat} as a function of the characteristic velocity of the liquid $v_{liq} = \gamma/\eta$. The black solid lines are the analytical predictions given by Equation (5.2) (Cox-Voinov model), taking various values of the equilibrium contact angle θ_e and $L = 200$ μm for the thickness of the film.*

As already mentioned in previous chapters, the Cox-Voinov relation describes variations of the dynamic receding contact angle θ_r due to the viscous bending of the liquid/gas interface as a function of the capillary number Ca:

$$\theta_r{}^3 = \theta_e{}^3 - 9Ca \ln\left(\frac{L}{a}\right) \tag{5.1}$$

where θ_e is the equilibrium contact angle, L and a are a macroscopic and microscopic length scales respectively.

In Section 1.3.1, we have seen that the Cox-Voinov model predicts a threshold velocity v_c^{Cox} for $\theta_r = 0$ given by:

$$v_c^{Cox} \simeq \frac{\theta_e{}^3}{9 \ln\left(\frac{L}{a}\right)} v_{liq} \tag{5.2}$$

This relation states that above v_c^{Cox} a liquid film should be entrained from a meniscus. We have shown in Chapter 3 that our experimental dynamic wetting transition occurs at

much lower v. Nevertheless, the dewetting velocity v_d still increases after the dynamic wetting transition when v increases. The velocity maximum given by Equation (5.2) can be seen as a maximum dewetting velocity of the triple line.

In Figure 5.7, we represent this maximum velocity v_c^{Cox} by the black solid lines. We have chosen $L = e_1^{sat} = 200$ μm since we already have a liquid film entrained, and $a = 10^{-10}$m for the atomic scale. We find a reasonable fit of our experimental data by Equation (5.2) with $\theta_e = 38°$. Interestingly, this value of the equilibrium contact angle is much smaller than the quasi-static receding contact angle $\theta_r^0 = 60°$ and is approximately the one measured on the viscous plateau (zone (3)) in Chapter 3. Note that choosing $L = l_c$ does not change significantly the adjusted value of the equilibrium contact angle as the length scale is in a logarithm. The difference in θ_e is only of a few degrees.

In fact, in *regime (iii)*, we recover the common statement from the literature which is that the motion of a contact line is ultimately determined by the physico-chemical interactions with the substrate [76], meaning that for a given liquid and substrate, namely θ_e, there is a maximum velocity for the triple line [71, 64, 92]. Whereas hydrodynamic models (Cox-Voinov) fail at describing the behavior of the triple line when connected to a meniscus, they succeed in predicting the triple line behavior when connected to a flat film. Therefore, while Ca^+ and Ca^* could not be accounted for by the forced wetting transition calculated via Cox-Voinov, Ca^{**} can be modeled within this framework ($Ca^{**} = {\theta_e}^3/9 \ln(L/a)$).

We will show also in Chapter 6 that this saturation value depends on the tube chemistry and liquid surface tension via θ_e.

5.3.2 Film thickness as a function of capillary number

We have shown that the first film thickness is determined by $e_1 = l_c\sqrt{3Ca_d}$. As a result, in this regime the first film thickness saturates, and the saturation thickness writes $e_1^{sat} = l_c\sqrt{3Ca_d^{sat}}$.

Figure 5.8 gathers the average film thicknesses e_1 and e_2 normalized by the capillary length l_c as a function of the slug capillary number Ca for various glycerol concentrations.

The data for various liquids collapse onto two master curves, for e_1 and e_2 respectively. The second film develops above a threshold in capillary number $Ca^{**} = 2.2\ 10^{-3}$: thus *regime (iii)* corresponds to $Ca > Ca^{**}$. The second film thickness e_2 increases with Ca sharply. Once the capillary number is large enough, the second film can possibly become thicker than the first film. Nevertheless, in the meantime, oscillations of the film thickness located close to the capillary jump appear reducing accuracy of the measurement of the average film thickness e_2. In contrast to the numerical predictions by Gao *et al.* [5], we do not experimentally recover their regime IV where a film with a monotonically varying thickness is obtained.

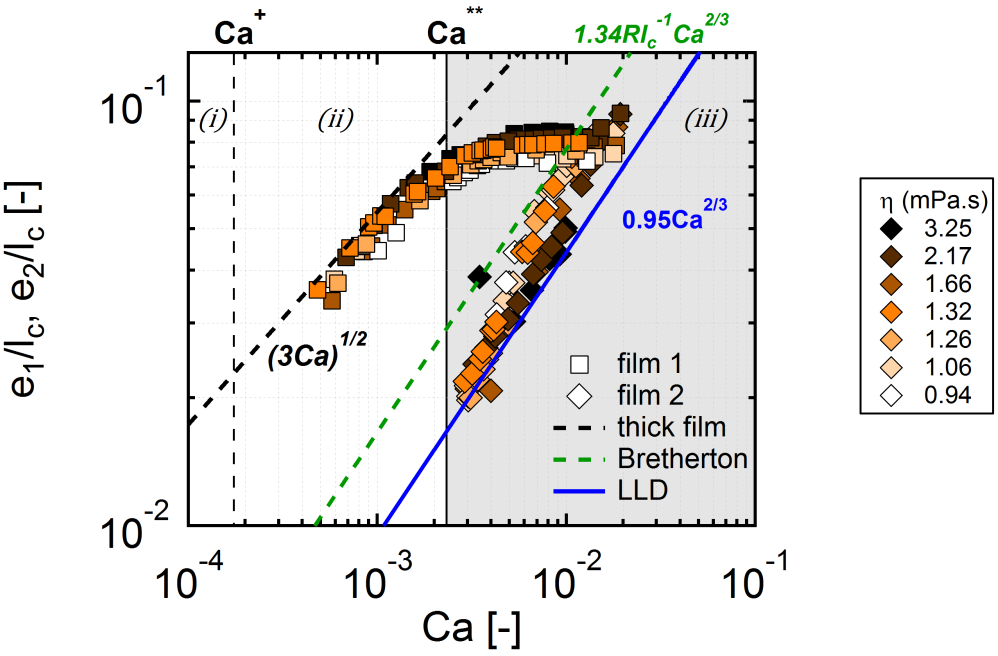

FIGURE 5.8: *Average film thickness of the first e_1 and second e_2 film normalized by the capillary length l_c as a function of the capillary number relative to the slug Ca. e_2 starts above Ca^{**} at a non-zero value and increases with Ca. Predictive model considering a gravitational drainage at constant film thickness (black dashed line). Plot of the Bretherton (green dashed line) and Landau-Levich (blue solid line) laws.*

5.3.3 Matching with a meniscus

As already mentioned in Chapter 1, Landau, Levich and Derjaguin (LLD) [11, 12] proposed a model to predict the thickness of the entrained liquid film when withdrawing a plate out of a bath. In this model, film thickness is given by Equation (1.1).

The same problem has been investigated by Bretherton [14] in cylindrical geometry for the case of an air bubble traveling in a cylinder of radius R filled with a liquid (Equation (1.2)).

These two models can be plotted on our experimental measurements in Figure 5.8, in green the Bretherton model and in blue the LLD model. The $Ca^{2/3}$ power law describes the data reasonably well and the measured film thickness e_2 lies in between these models and seems to span the range from LLD to Bretherton. In fact, in our case the radius of the tube (3.2 mm) and the capillary length (2.6 mm) are of the same order of magnitude, $R \simeq l_c$. It is not easy to discriminate between the two models, nevertheless, the second film is either a Bretherton or LLD-like film and, as such, is of visco-capillary origin. The film seems to be in a transition regime between LLD at low velocity and Bretherton at high velocity. This observation can be explained by inertial effects close to the meniscus that is strongly deformed due to large velocities.

5.3.4 Capillary jump velocity

In the following, we aim at describing the variations of the jump velocity v_j. Considering flux conservation at the capillary jump, we can predict the velocity of the jump v_j similarly to Hocking [4] and Snoeijer *et al.* [2].

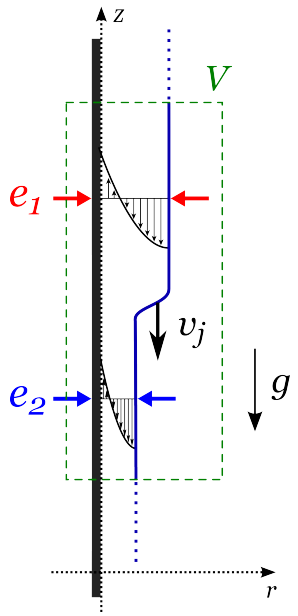

Figure 5.9: *Schematic representation around the thickness jump between the first film (thickness e_1) and the second film (thickness e_2). The green rectangle represents a volume of control V around the capillary jump.*

We consider the thickness jump between the first film (thickness e_1), and a thinner second film (thickness e_2). In the reference frame of the laboratory, we define a volume of control V surrounding the capillary jump. This volume is represented by the green rectangle in Figure 5.9. The volumetric increase dV during a time dt of the liquid enclosed in the control volume V writes:

$$dV = (e_1 - e_2)v_{j,a}dt \tag{5.3}$$

This volumetric increase rewrites as $dV = qdt$, where q is the flux difference between the in and out fluxes through the volume of control. As shown in Chapter 2, Equation (2.14) provides an analytical expression of the liquid flux in a flat lubricated film. In the first film, the flux writes as $e_1^3\rho g/3\eta$, and $e_2^3\rho g/3\eta$ in the second film. Therefore we can write the flux q as follows:

$$q_g = e_1^3\frac{\rho g}{3\eta} - e_2^3\frac{\rho g}{3\eta} \tag{5.4}$$

And finally the jump velocity writes:

$$v_{j,a} = \frac{\rho g}{3\eta}\left({e_1}^2 + e_1e_2 + {e_2}^2\right) \tag{5.5}$$

The prediction given by Equation (5.5) is shown by the red stars in Figure 5.5 using the experimental values of the thicknesses e_1 and e_2. This estimate accounts for our experimental values of the capillary jump velocity for velocities v_j smaller than 35 cm.s^{-1} ($Ca \sim 6\ 10^{-3}$) with a systematic down shift of about 3 cm.s^{-1} between experiments and theory. Note that in *regime (iii)*, $e_1 = e_1^{sat}$ is constant and that consequently v_j only depends on the velocity of the slug via the second film thickness e_2: $v_j = f(v)$.

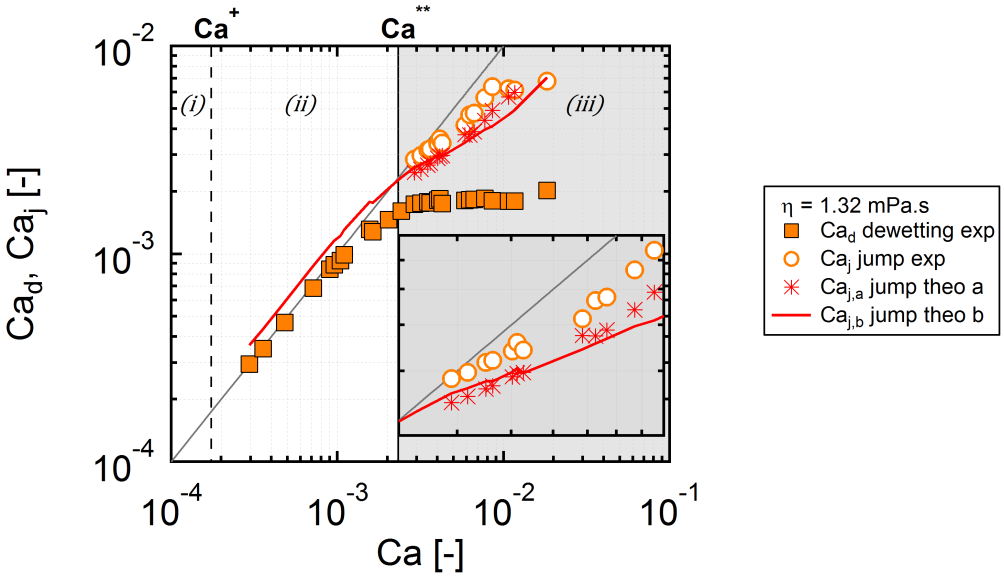

FIGURE 5.10: *Interface capillary numbers (Ca_d and Ca_j) as a function of the capillary number Ca for 15%wt glycerol solution, $\eta = 1.32$ mPa.s. Predicted capillary number of the jump $Ca_{j,a}$ according to Equation (5.6) (red stars) and $Ca_{j,b}$ according to Equation (5.7) taking into account a LLD-Bretherton model with $\beta = 1.3$ (red line).*

Alternatively, velocity can be rescaled to get the capillary number of the interfaces $Ca = \eta v/\gamma$. Equation (5.5) becomes:

$$Ca_{j,a} = \frac{{e_1}^2 + e_1 e_2 + {e_2}^2}{3l_c^2} \tag{5.6}$$

Figure 5.10 is the counterpart of Figure 5.5 with rescaled velocity. The red stars stand for the prediction given in Equation (5.6). Going even further, we can use the LLD-Bretherton model $e_2 = \beta l_c Ca^{2/3}$ to predict the capillary number of the jump if it existed below Ca^{**}. We define β as the prefactor in the models: for the LLD model $\beta = 0.95$ and for the Bretherton model $\beta = 1.34R/l_c = 1.65$. The resulting equation is:

$$Ca_{j,b} = \frac{\beta^2}{3} Ca^{4/3} + \frac{\beta}{\sqrt{3}} Ca_d^{1/2} Ca^{2/3} + Ca_d \tag{5.7}$$

In Section 5.2.3, we have shown that the second film thickness was in between a LLD-Bretherton model. For the red solid line prediction, in Figure 5.10, we have chosen a median value for the prefactor $\beta = 1.3$.

Thanks to this second prediction, we observe that in *regime (ii)* $Ca_j > Ca$. Once Ca is larger enough to allow a LLD film to appear, the transition occurs towards *regime (iii)*, the capillary jump starts to propagate and we observe the appearance of the capillary jump. This is implicitly determined by the saturation of Ca_d since Ca_j is calculated thanks to Ca_d in Equation (5.7).

5.3.5 The flux point of view

From the film thickness that we assess experimentally, we can have an approximate flux description to get the same explanation for the transition toward the capillary jump. We now work in the slug reference frame. As already defined earlier, Q_d is a downward flux from dewetting and can be approximated by the thickness of the first film e_1 times the dewetting velocity v_d. The upstream flux coming due to meniscus motion is Q_c, and can be estimated similarly as the thickness of the second film e_2 times the velocity of the slug v. Nevertheless, before the second transition (below Ca^{**}), we have no experimental measurement for e_2, because the second film does not develop. Alternatively, since we have shown that the thickness of the second film is given by the Bretherton law, we can build Q_c on the calculated Bretherton thickness $e_B = 1.34\ R\ Ca^{2/3}$ multiplied by the velocity of the slug v.

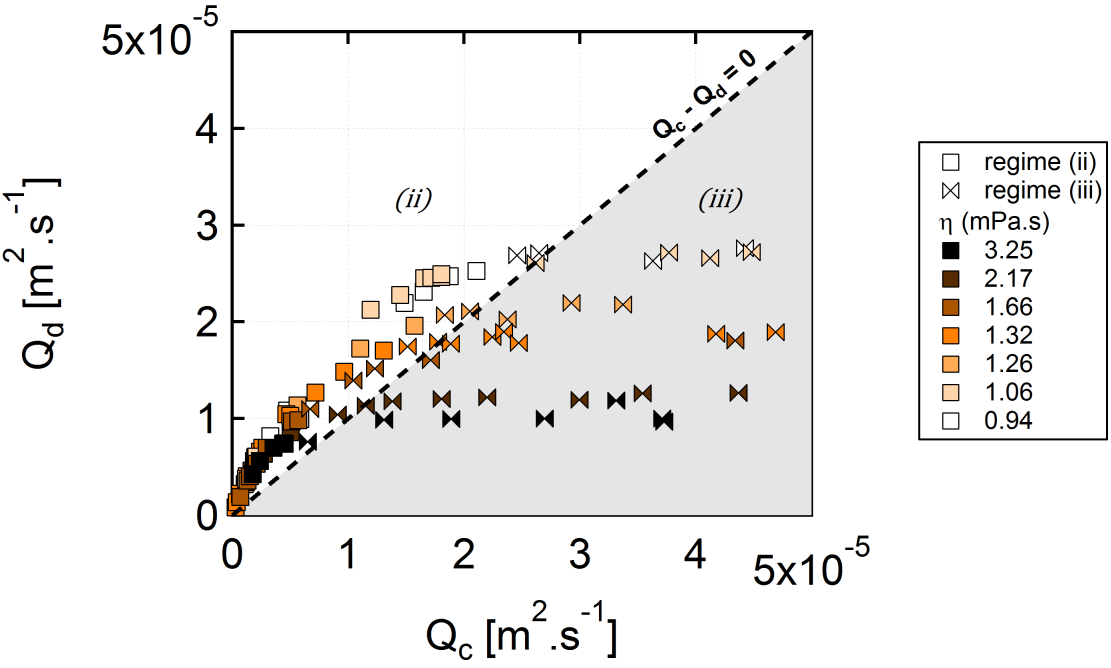

Figure 5.11: *Experimental downward flux coming from the dewetting $Q_d = e_1 v_d$ as a function of the upward flux ejected by the meniscus $Q_c = e_B v$. The squares corresponds to the experimental observation of regime (ii) and the bow ties to regime (iii). For $Q_d > Q_c$, the regime selected is a single gravitational film (regime (ii)). For $Q_d < Q_c$, the regime is the two films: gravitational and viscous (regime (iii)).*

In Figure 5.11 we plot $Q_d = e_1 v_d$ versus $Q_c = e_B v$. The squares correspond to *regime (ii)* with one unique film, the bow ties correspond to the *regime (iii)* with the capillary jump. The dotted line is the line of slope 1. We approximately observe a separation of the two regimes *(ii)* and *(iii)* on both sides of the slope 1 line. Thus, as long as the dewetting flux is close to the flux ejected by the meniscus, we are in the *regime (ii)* with a single film. When the flux ejected by the meniscus becomes larger $Q_c > Q_d$, because of the saturation of the dewetting velocity, then we get the capillary jump and the two films.

5.3.6 Comparison with numerics

Similarly to Section 4.3.2, in this section we aim at numerically understanding the transition between *regime (ii)* and *(iii)* by looking at the existence of stationary and unstationary solutions. As seen earlier, the reduced governing equation (Equation (4.1)) can be linearized considering a stationary state (Equation (4.2)) to provide two types of asymptotic solutions. A purely exponential solution given by Equation (4.4), corresponding to $Q_c > 3Q_g$, and an exponential oscillatory solution (Equation (4.5)) for $Q_c < 3Q_g$. The exponential solution corresponds in fact to the LLD-Bretherton solution.

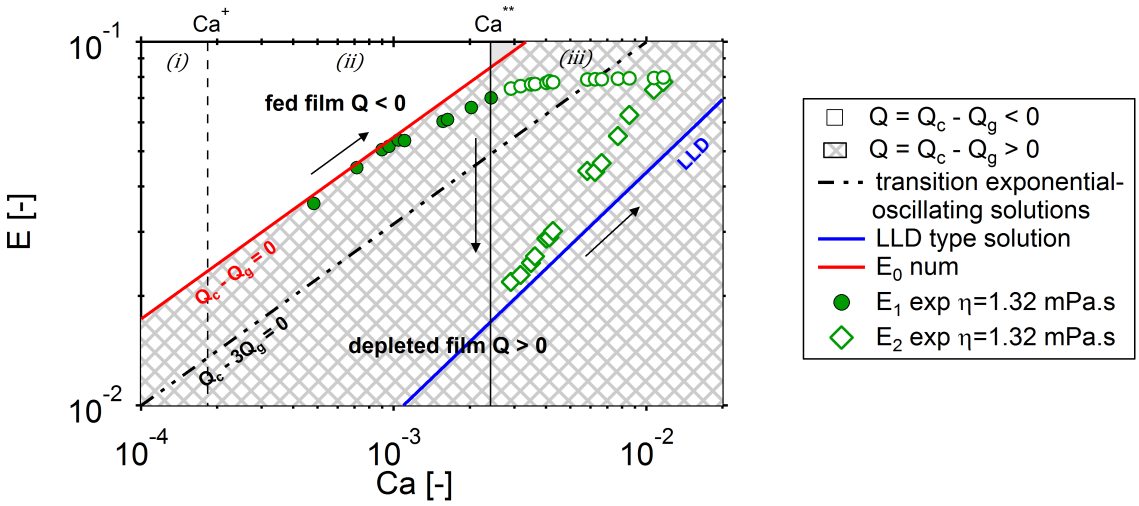

FIGURE 5.12: *Phase diagram of the profiles: $E = e/l_c$ versus capillary number Ca. The asymptotic limit ($Q_c - 3Q_g = 0$) is given by the black dotted-dashed line (limit between exponential and oscillating solutions). The numerical limit E_0 is the red line ($Q_c - Q_g = 0$). A domain of solutions exists above a minimal value given by $E_0 \geq \sqrt{3Ca}$. The hatched part of the diagram corresponds to a domain without solution ($Q > 0$), see profile Figure 4.13b. The experimental first film thickness E_1 is the green circles and the second film thickness E_2 is the green diamonds. The LLD law is depicted in blue.*

We build a numerical phase diagram with $E = e/l_c$ and Ca in Figure 5.12. As for Chapter 4, the space is divided into two regions. The first one (white) admits solutions

because the matching between the flat film and the static meniscus is possible ($Q < 0$). In the second one (hatched zone), there is no solution ($Q > 0$) apart of the LLD-Bretherton solution. The numerical limit between the two regions (red line) and our experiments $E_1 = e_1/l_c$ (green circles) are in good agreement in *regime (ii)*. In *regime (iii)*, the two experimental thicknesses are shown: E_1 (white circles) and E_2 (white diamond). In the same plot we depict the second limit between exponential/oscillatory asymptotic solutions $Q_c - 3Q_g = 0$ (black dotted-dashed line) that is set by the meniscus. The region between the numerical limit (red) and the asymptotic limit (black dotted-dashed line) corresponds to a domain between the two flux limits where no thick film solutions are admitted but where oscillatory solution should be possible ($Q_g < Q_c < 3Q_g$). When Ca_d saturates, the downward flux Q_d saturates as well inducing a saturation of Q_g since $Q_g = Q_d$ as shown in Section 4.3.3. This induces a change of sign of the overall flux $Q = Q_c - Q_g$ leading to numerical and experimental film profiles of LLD-Bretherton (exponential solution) when $Q_c \geq 3Q_g$. Our experimental data E_1 cross the second limit after Ca^{**} because of the increasing difference between Ca and Ca_d. In other words, the first limit $Q_c - Q_g = 0$ is set by the dewetting, thus by Ca_d, while the second limit $Q_c - 3Q_g = 0$ is set by the meniscus, and thus by Ca.

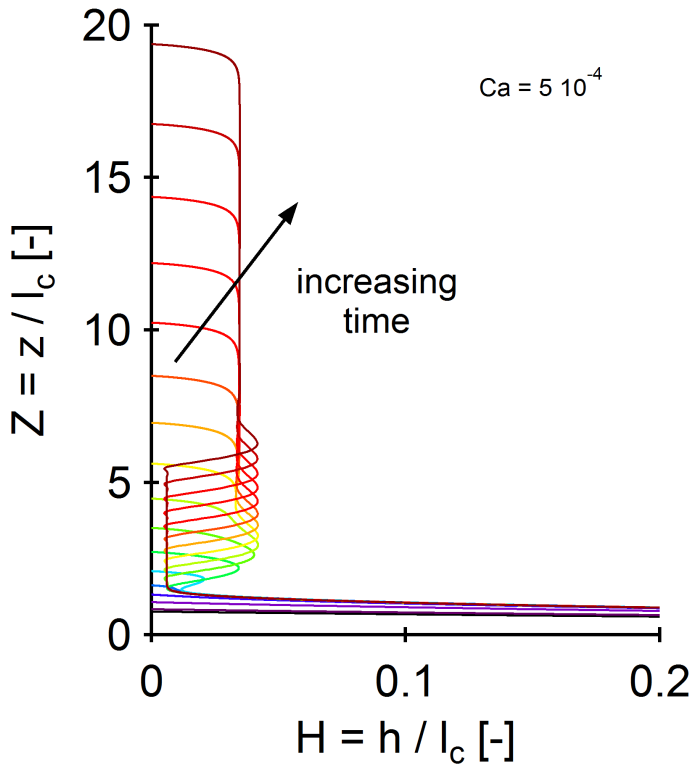

Figure 5.13: *Normalized meniscus profile $H(Z)$ as a function of time after the dynamic wetting transition $Ca = 5\ 10^{-4}$. The profiles prove the formation of two uniform films of constant thicknesses in time. The capillary jump takes a stationary shape with a capillary jump while the two films elongate.*

The stationary solutions provide explanations about the mechanism of the jump formation by separating the problem into two. But we cannot obtain the full profile of the film at once. This is why we now numerically investigate the time evolution of film formation in order to see whether or not a jump is formed. Similarly to the profiles obtained for the thick film formation (Chapter 4), we show in Figure 5.13 profile evolution with time for a larger capillary number $Ca = 5\ 10^{-4}$. After a certain time the triple line elevates and a liquid film is entrained on the surface. As for the first film formation, the shape of the profile is a bump at short time scales. This bump grows both in thickness and along the $Z-$direction. At some point we observe a shoulder. After some time, the thickness of the bump reaches a maximal value, but contrary to *regime (ii)* (Chapter 4) the bump propagates upward. A thinner uniform film lays between the thick film and the meniscus. The bump is in fact our capillary jump and has a stationary shape. The thickness of the first film is independent of Ca ($E_1 = \sqrt{3Ca_d^{sat}}$) as in Chapter 4. The second film thickness is given by the LLD-Bretherton law. It illustrates the transition between the thick gravity/capillary film with a dimple and the LLD film. Note also that *regime (ii)* corresponds numerically to the range of capillary number from $Ca = 4\ 10^{-4}$ to about $4.5\ 10^{-4}$ which is much smaller than the experimental range $Ca = 1.8\ -\ 22\ 10^{-4}$.

At the beginning of the experiment, the slug is at rest, then when the motion is induced the slug assesses the range of velocity up to the final prescribed velocity. In this transient regime, dynamics proceeds through a succession of steady states, which can be referred to as a quasi-steady behavior. The presence of two films show that the unsteady motion of the interface during the very first stage of liquid deposition can lead first to the entrainment of the thick film and then entrainment of the thinner LLD-Bretherton film. Indeed, viscous bending builds up and the first instability is for thick film formation. Subsequently the thin film forms and flows into the thick film which grows.

5.4 Playing with transients

In this section, we study the case of unstationary liquid films to further confirm our understanding of the formation of the two films and the transition between regimes. We start an experiment at a given velocity, then we suddenly vary the velocity of the slug by varying the gas pressure behind the slug. We can adjust the amplitude of the velocity change to either stay in the same regime or switch from one regime to another. We observe the consequences of these velocity changes on the interface velocities, film thickness and film and slug lengths.

5.4.1 From one to two films

To better understand the transition between one and two films we first consider the case of an accelerated slug. An example for pure water ($\eta = 0.94$ mPa.s) is given in Figure 5.14. In the first part of the experiment, the slug velocity is $v = 12.6$ cm.s^{-1} (smaller than Ca^{**}) and the dewetting velocity is $v_d = 10.5$ cm.s^{-1} (zone A).

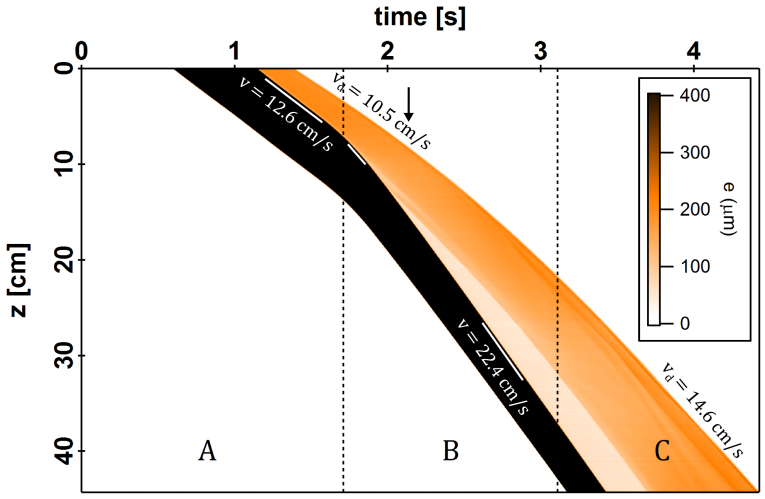

(a)

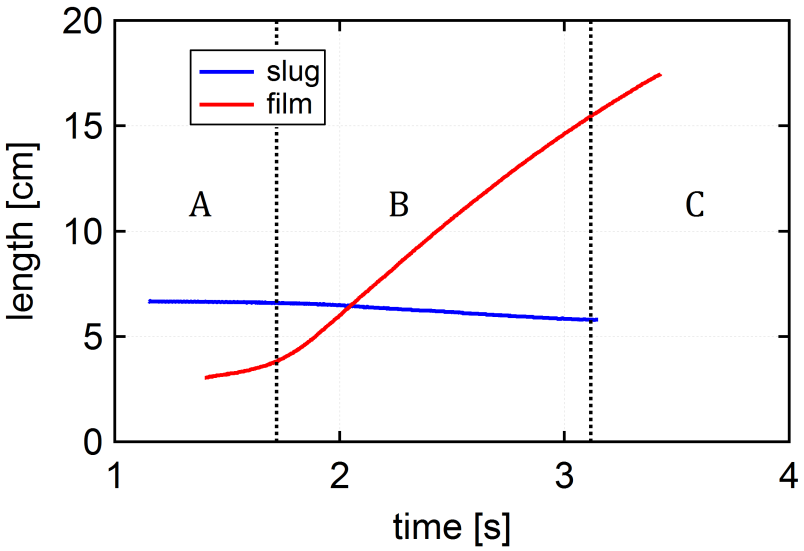

(b)

FIGURE 5.14: *(a) Spatio-temporal diagram of film thickness for an experiment with water ($\eta = 0.94$ mPa.s), where we have increased sharply the velocity of the slug during the flow. The velocity goes from 12.6 cm.s^{-1} to 22.4 cm.s^{-1}. (b) Corresponding slug and film length evolution with time.*

As shown in Figure 5.14b, the slug length decreases while the film grows. Then the velocity of the slug is increased up to $v = 22.4$ cm.s^{-1}, about twice the initial velocity in state A, and above Ca^{**}. On the spatio-temporal diagram we observe that the dewetting velocity remains unchanged for 0.4 s after the transition A−B: $v_d = 10.5$ cm.s^{-1}. At the arrow, the dewetting velocity progressively increases from $v_d = 10.5$ cm.s^{-1} to $v_d = 14.6$ cm.s^{-1}. Zone B is a transition zone of about 1.4 s, where the film length increases mainly due to the formation of the second thinner film. In zone C, the high velocity steady

state regime with two films is obtained.

To summarize, the velocity perturbation brings the system from a state A in *regime (ii)* towards a state C in *regime (iii)*, via a transition zone B.

In fact, looking closer at zone B, we can see that the velocity of the rear of the slug is increasing and stabilizing quite rapidly, within 0.2 s (at the end of the white slope line). Then 0.1 s later, the second film and the capillary jump appear macroscopically. And 0.1 s later, the dewetting line velocity starts to increase (at the arrow).

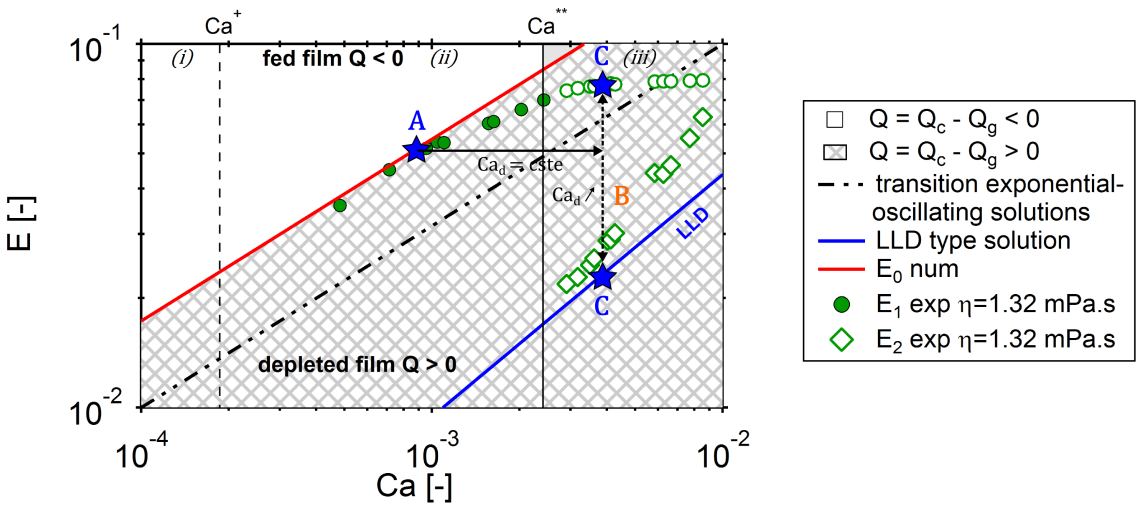

FIGURE 5.15: *Pathway of the experiment from Figure 5.14 represented in the phase diagram $E = e/l_c$ and Ca.*

Thanks to the phase diagram built in Figure 5.12, we can get an understanding of the transition zone B and a predictive approach of the thickness of the film. For the same experimental example provided in Figure 5.14, we can place the initial state A in the phase diagram Figure 5.15. Initially, we are in *regime (ii)* and as seen previously, at a given capillary number the system selects the minimal thickness (dotted line).

When the velocity perturbation is induced, the slug velocity and thus the capillary number Ca increases along the horizontal arrow, from left to right in Figure 5.15. This increase occurs at constant dewetting capillary number Ca_d (in the example $v_d = 10.5$ cm.s^{-1}) and constant film thickness e_1. The two previous quantities follow the law $e_1 = l_c\,(3Ca_d)^{1/2}$. Along this arrow the dewetting flux in the first thick film Q_g is constant and becomes smaller than the upward flux Q_c ejected by the slug ($Q > 0$). We go through a domain where no solutions are admitted numerically and where the sign of $Q_c - Q_g$, jumping from the single thick film solution to the LLD-Bretherton solution type. Once the triple line feels the acceleration of the slug, it tends to accelerate as well. But this phenomenon is limited by the saturation capillary number Ca_d^{sat} of the contact line.

The final state C corresponds to *regime (iii)* with two films where ${e_1}^{sat} = l_c\,(3{Ca_d}^{sat})^{1/2}$ and $e_2 = 0.95 l_c Ca^{2/3}$. In other words the macroscopic observation of the first film in state C is a footprint of state A. Transient states explain the coexistence of two films of different physical origins.

5.4.2 Brief incursion in the two film regime

Now we consider the case of an accelerated slug where we remain in *regime (ii)*. Figure 5.16 shows an example for pure water ($\eta = 0.94$ mPa.s).

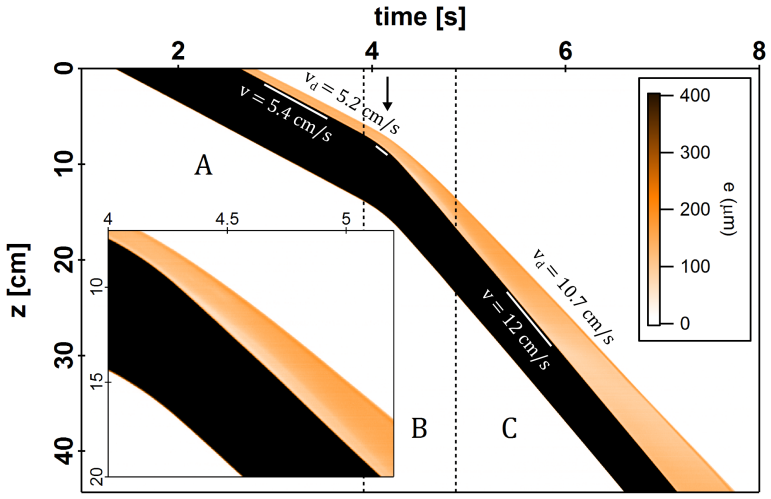

(a)

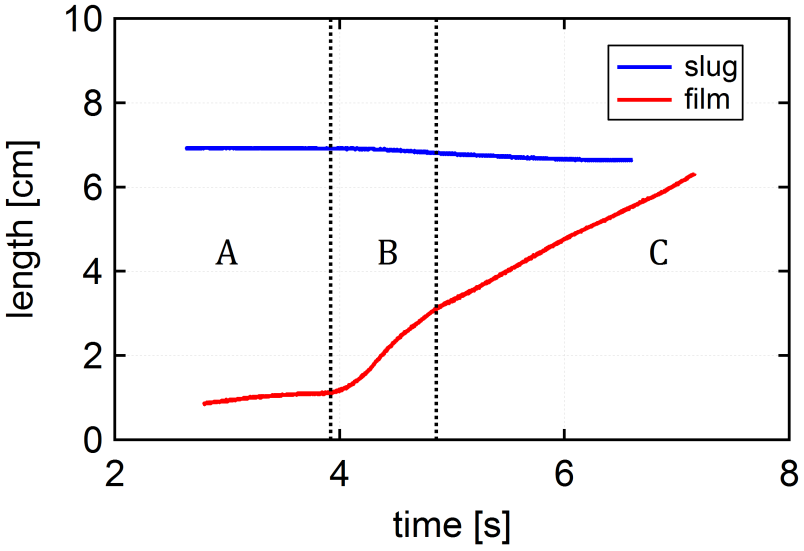

(b)

FIGURE 5.16: *(a) Spatio-temporal diagram of film thickness for an experiment with water ($\eta = 0.94$ mPa.s), where we have increased sharply the velocity of the slug during the flow. The velocity goes from 5.4 cm.s^{-1} to 12 cm.s^{-1}. (b) Corresponding slug and film length evolution with time.*

In the first part of the experiment, the slug velocity is $v = 5.4$ cm.s^{-1} and the dewetting velocity is $v_d = 5.2$ cm.s^{-1}, zone A. The slug length slowly decreases in time while the film grows, as shown by Figure 5.16b. Then, as the beginning of zone B, the velocity of the slug is increased up to $v = 12$ cm.s^{-1}, twice the initial velocity, but still below Ca^{**}.

The dewetting velocity remains unchanged on the spatio-temporal diagram right after the transition A−B: $v_d = 5.2$ cm.s^{-1}. It takes about 0.3 s before having a variation in the dewetting velocity. At the arrow, the dewetting velocity progressively increases from $v_d = 5.2$ cm.s^{-1} to $v_d = 10.7$ cm.s^{-1}. Zone B is a transition zone of about 1 s, where the film length increases. The length increases faster in zone B than in zone C, since the velocity difference between v and v_d is larger. In zone C, a second stable state is obtained with $v = 12$ cm.s^{-1} and $v_d = 10.7$ cm.s^{-1}. To summarize, the velocity perturbation brings the system from a state A in *regime (ii)* towards a state C in *regime (ii)*, via a transition zone B.

In fact, if we get a closer look at zone B, we can see that a thinner film tends to develop behind the slug (lighter zone) while we are below the threshold velocity Ca^{**}. Indeed, the liquid film is filling the slug faster compared to the out flux generated by the slug to feed the liquid film. Also, after the transition A−B but before the arrow, the film thickness is constant in time. This confirms the dependence between the dewetting velocity v_d and the thickness of the film e_1.

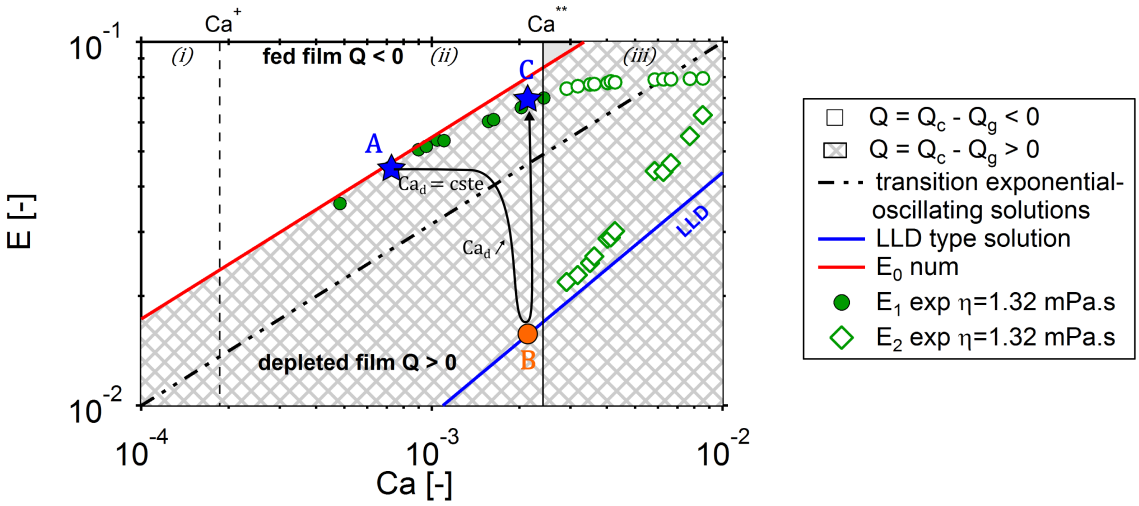

FIGURE 5.17: *Pathway of the experiment from Figure 5.16 represented in the phase diagram $E = e/l_c$ and Ca.*

As in the experimental example provided in Section 5.4.1, we can analyze this experiment on the phase diagram shown in Figure 5.17. State A corresponds to a quasi-stationary thick film solution, where the minimal thickness is selected at a given capillary number. Once the slug velocity has been varied, the capillary number Ca increases along the horizontal arrow, from left to right at constant dewetting capillary number Ca_d (in the example $v_d = 5.2$ cm.s^{-1}) and constant film thickness e_1 with $e_1 = l_c\,(3Ca_d)^{1/2}$.

Along this arrow the dewetting flux Q_g is constant and becomes smaller than Q_c. We go through a domain where no thick film solution is numerically admitted ($Q_g < Q_c < 3Q_g$). Once $Q_c \geq 3Q_g$ there is a sign change in the reduced equation (Equation4.2) leading to exponential solutions. The system jumps in the LLD type solution (point B). This solution is normally not accessible in *regime (ii)* when starting from zero velocity (static

case). Here, because the dewetting flux was initiated at a lower velocity, it is too low right when the slug velocity increases, and the LLD-Bretherton conditions are found. This is why we observe a transient thinner film behind the slug in zone B, similar to the capillary jump of *regime (iii)*.

Once the dewetting triple line reaches the $z-$position of the slug around the transition A−B in Figure 5.16, the dewetting capillary number starts to increase. Consequently, the film thickness e_1 thickens progressively. The liquid flux between the film and the slug increases, making the thickness of the film uniform, and the thinner film disappear. The system is finally in state C corresponding to *regime (ii)*, where $e_1 = l_c\,(3Ca_d)^{1/2}$.

5.5 Conclusion

In conclusion, we have observed a liquid film with a double structure in a tube: a LLD-Bretherton film followed by a thick film. Previous works by Snoeijer *et al.* [2, 76] also present such films on a plate. Both films are flat and present significantly different thicknesses. The junction of the two films corresponds to a rather sharp step named capillary jump.

The formation of this capillary jump, corresponding to the lower limit of *regime (iii)*, is prompted by the saturation in velocity of the dewetting contact line. This value of the dewetting velocity at saturation decreases when increasing the viscosity of the liquid, quite in good agreement with Cox-Voinov. It corresponds to one unique value Ca_d^{sat} of the reduced velocity, and is accounted for by the value of Ca for which the forced wetting transition is predicted by Cox-Voinov relation.

In this *regime (iii)*, the thickness of the first thick film is also saturated at $e_1^{sat} = l_c\sqrt{3Ca_d^{sat}}$ as established in Chapter 4. The second lower film arises from a balance between capillary forces and viscous forces given by the LLD-Bretherton law with a film thickness consistent with a $Ca^{2/3}$ dependency but intermediate between LLD and Bretherton [11, 12, 14]. This regime perfectly reflects the film behavior found in the literature with constant dewetting velocity and two films [2, 76, 5].

Numerically, we are able to account for our experimental results. When the dewetting velocity saturates, the downward flux Q_g saturates as well. This induces a change of sign of the overall flux Q leading to numerical and experimental film profiles of LLD-Bretherton type (exponential solution). The mechanism is confirmed by transient experiments where the formation of the second film is triggered by a well chosen increase of the slug velocity.

Finally, once the capillary number is large enough, the second film e_2 can become thicker than the first film. In the meantime oscillations, located close to the capillary jump, appear in the film thickness.

Chapter 6

Other surface chemistries

6.1 Introduction

In the previous chapters we reported the different flow regimes obtained when varying the velocity of the fluid segment displaced in a PVC tube. At very low velocity (*regime (i)*), the rear meniscus bends due to the motion of the slug. Above a first critical capillary number $Ca^+ = 1.8\ 10^{-4}$, a liquid film is entrained behind the slug (instantaneous wetting transition at $Ca^* = 4\ 10^{-4}$). This film dewets at a velocity v_d which depends on the velocity of the slug v. In *regime (ii)*, the thickness e_1 of the liquid film is given by the dynamics of the triple line so that $e_1 = l_c\sqrt{3Ca_d}$ and corresponds to a thick film solution. Above a second threshold $Ca^{**} = 2.2\ 10^{-3}$, the dewetting velocity of the film saturates and a two film structure is observed. The film is divided into two parts, both having a homogenous thickness, and separated by a sharp step. The upper part is a thick film. The lower part, between the slug and the upper film, has a thickness consistent with the LLD-Bretherton law and varying as $Ca^{2/3}$.

To strengthen our understanding of the problem, this chapter aims at investigating the influence on the film formation of the physico-chemical interactions at the liquid/solid interface. We investigate how the surface chemistry of the tube impacts the dynamic wetting transition. We will in particular characterize the transition velocities (Ca^* and Ca^{**}) and compare the results with our conclusions from the previous chapters.

6.2 PDMS vs PVC tubes

In this section, to vary the nature of the tube, we use commercial PDMS tubes of inner diameter 6.4 mm whose characteristics are given in Section 2.2. These PDMS tubes, which quasi-static contact angle is $\theta_r^0 = 80°$, are more hydrophobic than the PVC tubes ($\theta_r^0 = 60°$) previously used in Chapter 3–5. To strongly vary the liquid viscosity and the physico-chemical interactions at the liquid/solid interface (surface tensions), we now use more concentrated solutions of water-glycerol ($50 - 75$%wt) and low concentration solutions of water-ethanol ($0 - 15$%wt). As already mentioned in Section 2.2.2, the quasi-

static receding contact angle θ_r^0 measured at very low velocity for PVC does not present significant variations with the glycerol or ethanol concentrations in the range investigated and we can assume this is also the case for PDMS.

We use the "large velocity setup" and techniques developed in Chapter 2, and already used in the previous chapters to visualize and measure the velocities of the different interfaces in the two regimes *(ii)* and *(iii)*. Because of the low transparency of the PDMS tubes, we were not able to finely measure the film thickness. Contrary to PVC tubes, we have not investigated the evolution of the dynamic contact angles with Ca for PDMS. The dewetting velocity v_d of the film as a function of the slug velocity v is plotted in Figure 6.1 for solution of 10%wt ethanol in water as an example, along with the results for PVC. Note that the data for PVC are also new results since we have not used water-ethanol solution in the previous chapters.

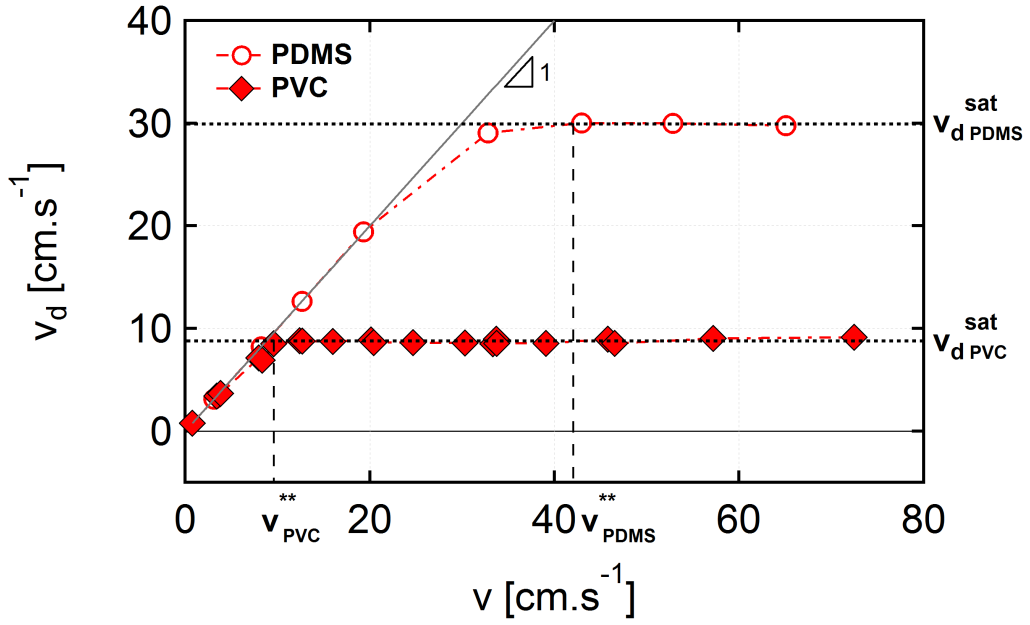

FIGURE 6.1: *Dewetting velocity of the liquid film (or meniscus) end v_d as a function of slug velocity v for a PDMS tube of diameter d_{in} = 6.4 mm (circles) and 10%wt ethanol solution. The data for PVC (diamonds) have been added for comparison. PDMS is more hydrophobic than PVC.*

We observe the same regimes and the same trend, $v_d = f(v)$, for the two materials but the thresholds (v^* and v^{**}) are shifted towards larger velocities for the more hydrophobic surface, *i.e* the PDMS. As seen in Chapter 3, before the dynamic wetting transition $v < v^*$, the dewetting velocity v_d is equal to the slug velocity v: there is no liquid film behind the slug. The threshold velocity v^* is about 9 cm.s^{-1} for PDMS and is larger than for PVC where $v^* \approx 2$ cm.s^{-1} (consistent with previous results for PVC: $Ca^* = 4\ 10^{-4}$ in Chapter 3). Above v^*, v_d increases with v (*regime (ii)* of Chapter 4). Then the dewetting velocity v_d reaches a maximum value v_d^{sat} corresponding to *regime (iii)* detailed

in Chapter 5. We can notice that the value of the saturation for the PDMS $v_d^{sat} = 30$ cm.s^{-1} is three times larger than for PVC ($v_d^{sat} = 9$ cm.s^{-1}) and consequently v^{**}: the two film regime appears for larger velocities for the PDMS because of its larger hydrophobicity.

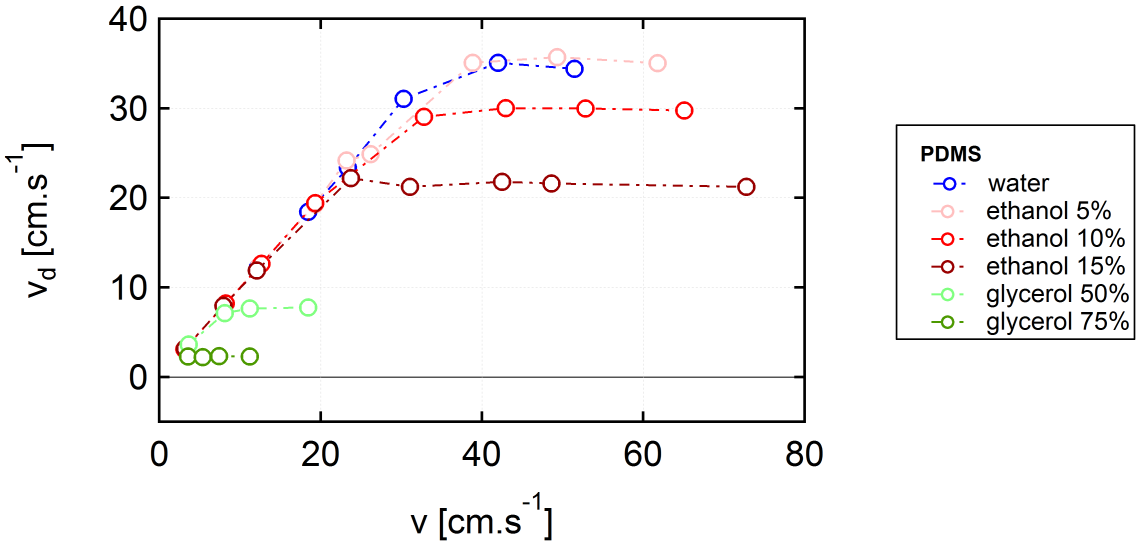

(a)

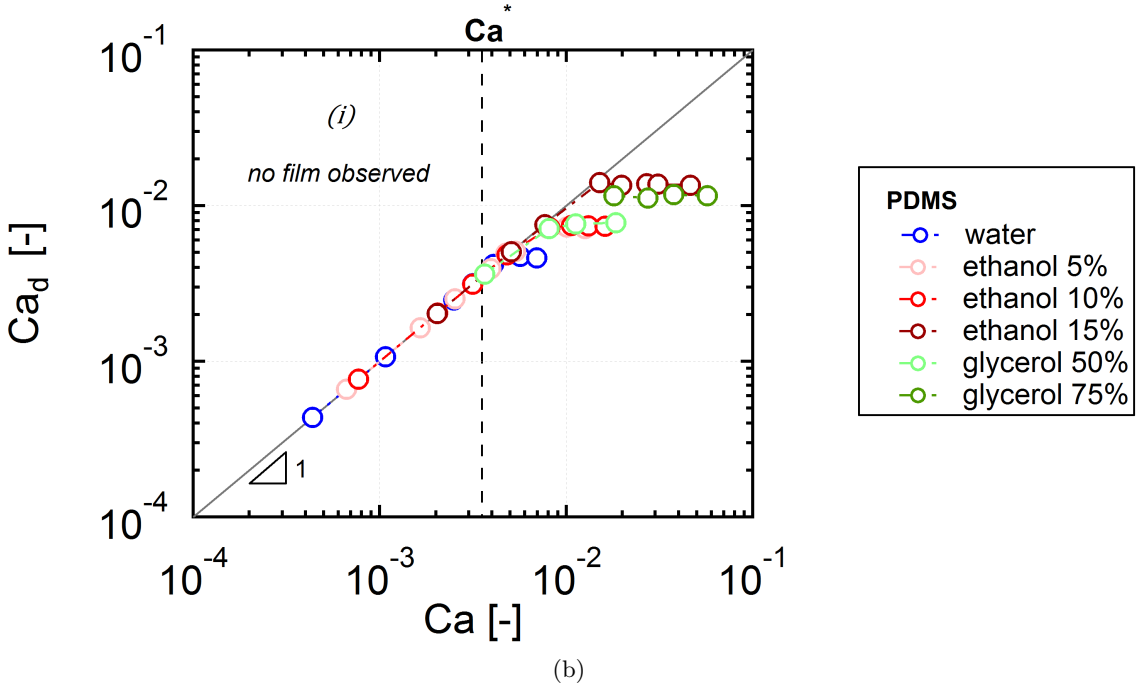

(b)

FIGURE 6.2: *(a) Dewetting velocity of the film end v_d as a function of the flow velocity v, on PDMS tube of diameter $d_{in} = 6.4$ mm for different concentrations of glycerol (green color scale) and ethanol (red color scale). (b) Dewetting capillary number Ca_d versus meniscus capillary number Ca.*

Figure 6.2a gathers the dewetting velocity v_d as a function of the velocity of the slug v using PDMS tubes for all the liquids investigated in this section. Pure water corresponds to blue symbols. As already observed for PVC, the physical properties of the liquid impact the v_d^{sat} value but not the trend $v_d = f(v)$. It impacts also the first threshold velocity v^* but it cannot be observed in Figure 6.2a. An increase of the viscosity η or a decrease of the surface tension γ both induce a decrease of the saturation dewetting velocity v_d^{sat}. Note that the saturation dewetting velocity can be very large, up to 35 cm.s^{-1}. No equivalent dewetting velocity is found in the literature to our knowledge. The larger v_d^{sat}, the larger the range of accessible dewetting velocity, the wider the *regime (ii)* in term of velocity or capillary number. In the literature, dewetting velocities are ten to thousand times lower because high viscosity fluids were used. This is probably why the flow *regime (ii)* has never been experimentally observed and identified in the past.

Interface velocities can be rescaled by the characteristic velocity for each liquid to get the capillary number $Ca = \eta v/\gamma$. The resulting rescaled velocities are reported in Figure 6.2b. The data mainly collapse on a single master curve. We identify the three regimes previously discussed: *regime (i)* without film ($Ca_d = Ca$) for $Ca < Ca^*$ (Chapter 3); *regime (ii)* with a single thick film for $Ca^* < Ca < Ca^{**}$ (Chapter 4); *regime (iii)* with two films and where Ca_d saturates (Chapter 5). The first threshold corresponds to an unique capillary number $Ca^* = 3.4\ 10^{-3}$ which does not depend on the liquid viscosities or the surface tensions. We recover one of the main results of Chapter 3 for a wider range of η and γ. This value is approximately ten times larger for PDMS than for PVC ($Ca^* = 4\ 10^{-4}$). Our experiments suggest that Ca^* only depends on the material thereby strengthening our conclusions of Chapter 3 regarding the importance of additional dissipative effects at the triple line compared to the viscous dissipation. Furthermore, we observe a dispersion of the values of Ca_d^{sat} and consequently on Ca^{**} for the different liquids. Ca^{**} increases when the surface tension decreases and we thus did not plot a threshold regime in Figure 6.2b. These results differ from what we observed previously in Section 4.3.1. Interestingly, then, Ca^{**} is found to depend on the surface tension of the liquid, whereas it was measured in Chapter 5 at a single value. Here, a major difference with the liquid used in Chapter 5 is that the water-glycerol series is likely to have analogous interactions with the PVC walls whatever concentrations, whereas the water-ethanol series is very likely to present strong variations in the interfacial energies with air or PDMS: ethanol is tensio-active and PDMS has a high polarity compared to PVC [95]. Altogether, within the glycerol and ethanol series, the contact θ_e setting Ca^{**} is likely to vary. For pure water, we find $Ca^{**} = 4.6\ 10^{-3}$ which is two times larger than for PVC ($Ca^{**} = 2.2\ 10^{-3}$). The experimental observation of *regime (ii)*, for $Ca^* < Ca < Ca^{**}$, is narrowed in the case of pure water and PDMS. The deviation between Ca_d and Ca when increasing Ca, previously observed for PVC in this *regime (ii)*, is less obvious here for PDMS.

Alternatively, we plot v_d^{sat} as a function of the characteristic velocity of the liquid, $v_{liq} = \gamma/\eta$, for the PDMS tube and different water-glycerol mixtures in Figure 6.3, along with the data of PVC tube from Figure 5.7. The data for the water-ethanol mixtures are

also depicted for both surface chemistries. As already emphasized previously in Chapter 5 for the PVC tube and the water-glycerol mixtures, the Cox-Voinov model with $\theta_e = 38°$ provides an adequate fit to the experimental saturation velocity with v_{liq}. We notice that the results for ethanol deviate from this fit ($\theta_e = 38°$), which is consistent with Young's law and previous comments: we expect a variation of θ_e when varying the surface tension γ and/or the interfacial tension between liquid and substrate.

$$v_c^{Cox} \simeq \frac{{\theta_e}^3}{9 \ln\left(\frac{L}{a}\right)} v_{liq} \tag{6.1}$$

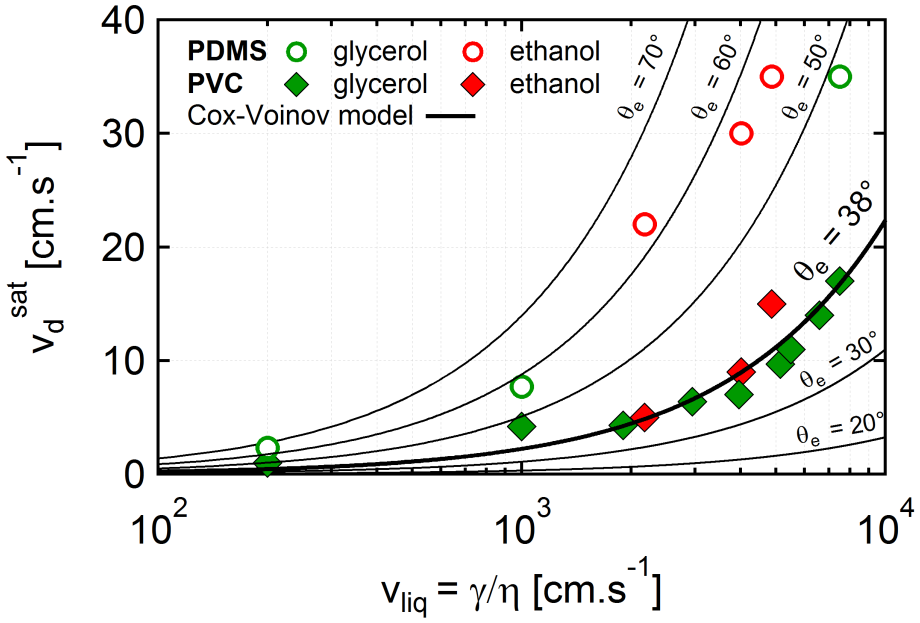

FIGURE 6.3: *Dewetting velocity of the liquid film v_d as a function of the characteristic velocity of the liquid $v_{liq} = \gamma/\eta$ for a PDMS tube of diameter $d_{in} = 6.4$ mm (circles) and different concentrations of glycerol (green symbols) and ethanol (red symbols). The data for PVC and water-glycerol mixtures (green diamonds) have already been presented in Figure 5.7 and have been added for comparison. Black solid line is the analytical prediction given by Equation (6.1) (Cox-Voinov model), taking various values of the equilibrium contact angle θ_e and $L = 200$ μm for the thickness of the film.*

The data for the PDMS tube and the water-glycerol mixtures are also in agreement with the Cox-Voinov model (Equation (6.1)). As seen before, for the PVC tube the appropriate equilibrium contact angle is $\theta_e = 38°$, while this angle becomes $\theta_e = 50°$ for PDMS. This observation is consistent with the fact that the PDMS is more hydrophobic than the PVC. For PDMS the dynamic contact angle could not be measured systematically as a function of Ca due to poor transparency of the material. However, the quasi-static receding contact angles are 60° for PVC and 80° for PDMS. Therefore the difference found

for the plateau angle seems consistent with the difference in quasi-static angles. The fact that there are multiple values of θ_e for water-ethanol mixtures is more obvious for PDMS tube than for PVC. For the lower surface tension, a better fit is obtained when increasing θ_e.

This saturation dewetting velocity increases with θ_e at given v_{liq}. We have seen earlier that once the dewetting velocity at saturation is reached, the shape of the rim is fixed and the thickness of the film is constant. We can assume that this saturation velocity corresponds in fact to the classical maximum dewetting velocity found in the literature and detailed in Section 1.3.1 and 1.3.2. As stated by Redon *et al.* [64], the spontaneous dewetting velocity of a triple line on a horizontal plate is unique for a given liquid/substrate combination and is independent of the film thickness (because the receding contact angle θ_r is supposed to be set at low Ca).

6.3 Large hydrophobicity scale

To test other surface chemistries of the wall and extend further the hydrophobicity scale, we have chemically modified the PDMS tubes by oxidation of the inner tube surface followed by adsorption of hydrophilic polymers (tube A and B). Explanations on the experimental procedure are given in Section 2.2.3. In this part, the liquid is pure water and modified PDMS tubes of inner diameter $d = 3.2$ mm were used in order to be able to carry out surface modification. Note that the influence of the tube diameter has also been investigated (Appendix C) and no qualitative difference is found. To characterize these surfaces in terms of wettability, we measure a quasi-static receding contact angle θ_r^0 by displacing a pure water meniscus at low constant velocity $v = 0.3$ cm.s^{-1} in the tube. As shown previously, the relevant (lower) plateau contact angle θ_e is obtained when fitting the Cox-Voinov law. This can be achieved only for PVC and PDMS because we do not have the data for tube A and B due to lack of time. For PVC, this angle corresponds to the angle measured at the plateau in zone (3) defined in Chapter 3. The evolution of the dynamic contact angle with Ca has not been measured for PDMS. In this section we essentially focus on the threshold values between flow regimes for four tubes of different chemistries:

- modified tube A is a PDMS tube with PEG 2,000,000 chains - $\theta_r^0 = 20°$
- modified tube B is a PDMS tube with PEG 1,000,000 chains - $\theta_r^0 = 40°$
- commercial PVC tube - $\theta_r^0 = 60°$ & $\theta_e = 38°$
- commercial PDMS tube - $\theta_r^0 = 80°$ & $\theta_e = 50°$

For each surface chemistry, we systematically measure the dewetting velocities at saturation and the corresponding capillary number Ca_d^{sat}, which marks the transition between *regime (ii)* and *(iii)*. In Figure 6.4, we plot Ca_d^{sat} (diamonds) as a function of $\theta_r^{0\,3}$ (Section 2.2).

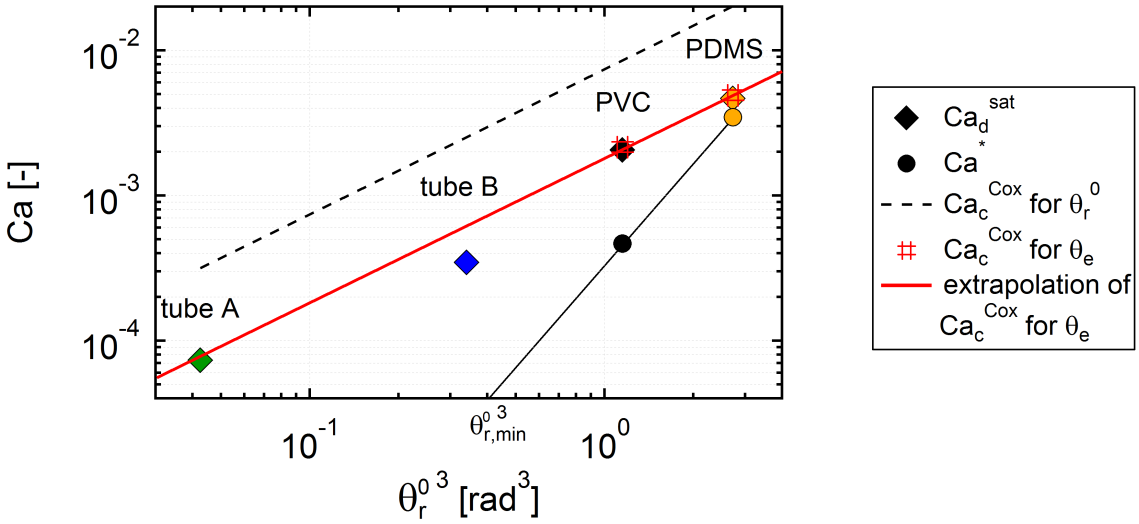

FIGURE 6.4: *Capillary numbers Ca_d^{sat}, Ca^* and Ca_c^{Cox} from the Cox-Voinov model as a function of $\theta_r^{0\,3}$ measured with pure water in four tubes of different surface chemistry ($d = 3.2$ mm). The quasi-static receding contact angle θ_r^0 characterizes the surface chemistry and is given for water menisci displaced at low velocity $v = 0.3$ cm.s^{-1}. The dashed black Cox-Voinov line is calculated using Equation (1.14) when taking θ_r^0 for the static contact angle. The red sharp symbols correspond to the Cox-Voinov model when taking the relevant plateau value θ_e. The red line is an extrapolation of the red sharp symbols considering $\Delta\theta^{Cox} = \theta_r^0 - \theta_e$ constant.*

We observe that the value for the dynamic wetting transition agrees reasonably well with a linear dependence on $\theta_r^{0\,3}$. The more hydrophobic the tube, the larger the capillary number at saturation Ca_d^{sat}. In the same plot, we report as dashed line the threshold capillary number Ca_c^{Cox} obtained either numerically or analytically using the Cox-Voinov model (Equation (1.14)) taking the quasi-static receding contact angle θ_r^0 as suggested in the literature [36, 37]. As already observed for the PVC tube (Section 3.4, the experimental trend is well captured, but the calculated Ca_c^{Cox} significantly overestimates the data. As seen previously in Section 5.3.1), if we calculate Ca_c^{Cox} using θ_e, the Cox-Voinov model accounts fairly well for our experimental values of Ca_d^{sat} (red solid line in Figure 6.4). The equivalent equilibrium contact angle θ_e is the appropriate parameter to describe the saturation velocity of the dewetting contact line. For PDMS and PVC, the value of Ca_c^{Cox} calculated using θ_e (red sharp symbols) corresponds to a shift of $\Delta\theta^{Cox} = \theta_r^0 - \theta_e$ of the predicted value with θ_r^0. An extrapolation of this result to tube A and B accounts fairly well with our experimental Ca_d^{sat} values and may provide an indirect measurement of θ_e.

In Figure 6.4, we also plot the first threshold capillary number Ca^* (circle) at which a liquid film of pure water is entrained (instantaneous dynamic wetting transition between *regime (i)* and *(ii)*). Interestingly, the decrease of Ca^* seems much sharper when decreasing θ_r^0, although this observation is only based on two experimental points. As mentioned

previously, the difference $Ca^{**} - Ca^{*}$, corresponding to the experimental observation of *regime (ii)*, is narrower for PDMS than for PVC. This trend suggests the existence of a minimal value of the contact angle $\theta^{0}_{r,min}$ below which a liquid is always entrained. Indeed, for the more hydrophilic tubes (tube A and B), a liquid film is always observed in the range of velocities investigated ($Ca^{*} \to 0$). We have compared qualitatively the film thicknesses in the hydrophilic tube (tube A) and in the hydrophobic tube (PVC). For a given Ca, the thickness of the film in tube A is much thinner than the film formed in the PVC tube. In addition, for $Ca > Ca^{sat}_{d,PVC}$, the second film in the hydrophobic PVC tube has the same thickness as the single film in the hydrophilic tube A at given velocity. This suggests that the film in the tube A is a LLD-Bretherton film.

6.4 Conclusion

The experimental results obtained with PDMS confirms the phenomenology observed with PVC tubes in the previous Chapters. The more hydrophobic tube exhibits larger values Ca^{*} and Ca^{**} and a lower difference $Ca^{**} - Ca^{*}$. The evolution is roughly consistent with the Cox-Voinov model (Figure 6.4). However, the quasi-static receding contact angle should not be used to predict the threshold value. We suggest that a plot of the dynamic contact angle should be measured, and the reference contact angle involved in the capillary term at the triple line should be extracted from the plateau if any (Chapter 3). The threshold value Ca^{*} does not seem to scale with Cox-Voinov law. The stronger variation suggests a limit contact angle below which a homogeneous LLD-Bretherton film alone is deposited. It would be interesting to gather more data on these surfaces and also to investigate other surface chemistries to establish whether the contact angle is the prime parameter or whether other surface properties such as the polarity of the PDMS surface play a role.

Conclusion and perspectives

We have experimentally and theoretically investigated the flow regimes of low viscosity liquids flowing down a vertical tube under partial wetting condition. We have varied the viscosity as well as the liquid/solid interactions at the triple line. Surprisingly, the cylindrical geometry has been less studied experimentally in the literature compared to the planar geometry. Perhaps because in tubes, the flow visualization is more difficult, but we should emphasized that there is no edge effect. We have built a versatile experimental setup allowing large velocities of the liquid slug within a wide range, with reproducible results, and a high quality of visualization to measure the kinematics of the slug and morphology of the liquid film. An appropriate thickness measurement method has been implemented using light absorption.

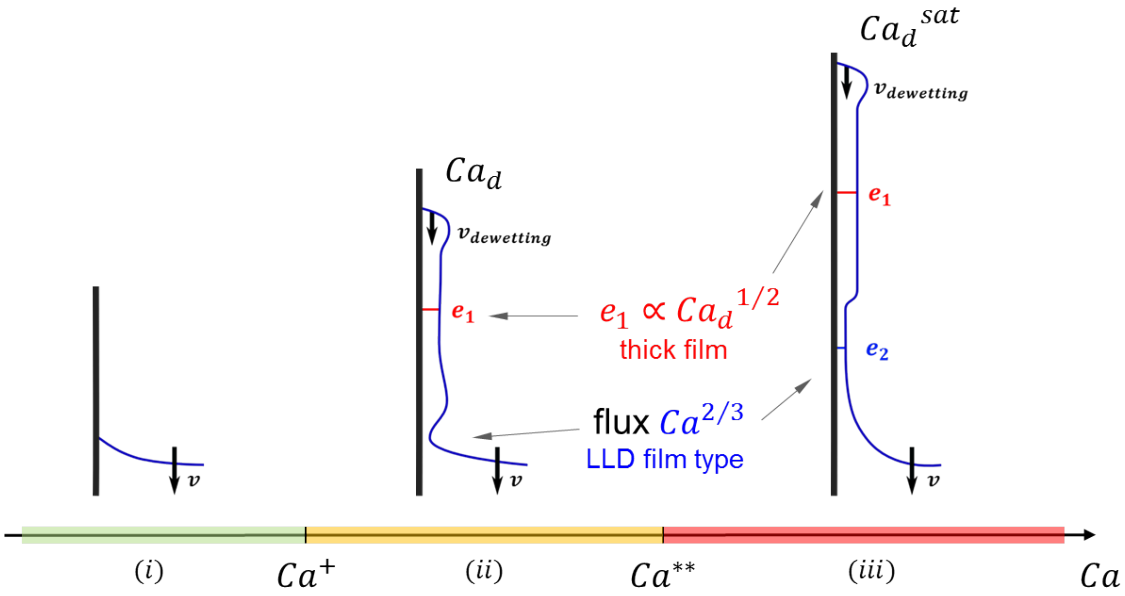

FIGURE 7.1: *Summary of the different flow regimes and film morphologies for varying capillary number.*

We first show that the capillary number Ca is the relevant parameter to account for our observations. When considering dynamic transitions to forced wetting in the classical perspective with a hydrophobic surface, we expect a transition at very large capillary number. For PVC the transition is expected at around $Ca = 3.5\ 10^{-3}$, namely 26 cm.s^{-1}

for pure water. Experimentally, this is not what we observe. A film can be entrained at much lower capillary number $Ca = 1.8\ 10^{-4}$, corresponding to a velocity of 1.4 cm.s^{-1}. A similar effects is found on PDMS as well (Chapter 6). We have shown that there are two reasons for this difference. First because the relevant receding contact angle θ_e is different from the angle of reference taken in quasi-static condition θ_r^0. Second because, even if we corrected the contact angle of reference, the dynamic wetting transition occurs for a velocity lower by one order of magnitude.

The phenomenological behavior observed in our study is reported in Figure 7.1: *(i)* a stationary dynamic meniscus and destabilization of the meniscus (Chapter 3); *(ii)* thick film formation (Chapter 4); *(iii)* coexistence of two films (Chapter 5); and is in agreement with numerical models but the transitions are not at the predicted values of capillary number.

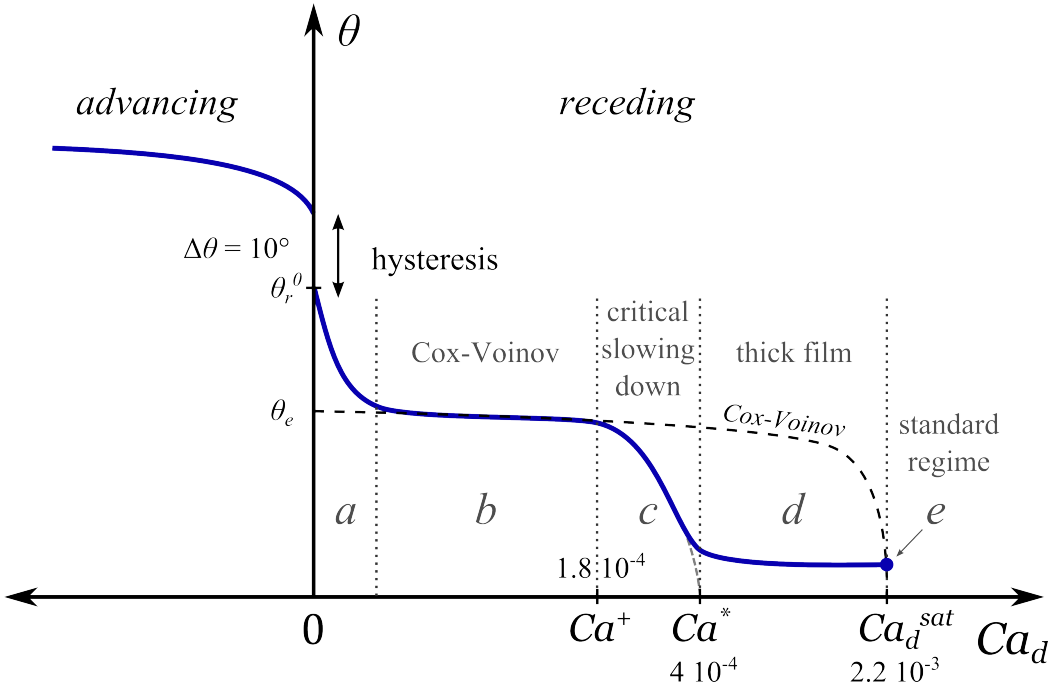

FIGURE 7.2: *Schematic of the evolution of the dynamic contact angle θ as a function of the capillary number based on the triple line velocity Ca_d. Advancing contact lines correspond to negative velocities. Values are given for PVC tubes.*

In *regime (i)* the shape of the meniscus is evolving in time to reach a stationary shape with a finite contact angle. At low Ca, there is a strong dependence of both advancing and receding contact angles with Ca (zone *a* in Figure 7.2). Hydrodynamic models do not account for this feature, this unexpected variation can be attributed to the coupling between surface roughness and pinning of the triple line. For larger Ca (zone *b*), a Cox-Voinov viscous plateau is observed, but it ends prematurely compared to the hydrodynamic predictions. This plateau ends at $Ca^+ = 1.8\ 10^{-4}$ where we find a sharp decrease to about zero over the range Ca^+ and $Ca^* = 4\ 10^{-4}$ (zone *c*). Between these two capillary numbers, Ca^+ and Ca^*, the transition to film formation depends upon

the timescale of the measurement (Figure 3.12). There is a critical slowing down around the transition. All those aspects are included in our numerical simulations. Ca^* defines the instantaneous dynamic wetting transition, corresponding to the transition between *regime (i)* and *(ii)*. In our experimental system the viscous dissipation in the liquid wedge is negligible, instead a friction like dissipation mechanism is found to account qualitatively for both the quasi-static receding contact angle and the critical capillary number Ca^+ at which transition from a meniscus to a film occurs (or Ca^* for instantaneous dynamic transition). This latter value is much smaller than the one found in the literature using classical hydrodynamic models, commonly denoted by Ca_c (but Ca_c^{Cox} in this thesis). In these cases, the transition is defined when the stationary solution of the meniscus ceases to exist ($z_{cl} = \sqrt{2}$) [1]. In our work, Ca^* is one order of magnitude lower than Ca_c^{Cox}. Experimentally the transition is not only shifted but also broadened. This remarkable result is an opportunity for observing in detail the phenomenology around the transition.

Above this critical capillary number, we observe experimentally the existence of thick films on a much larger capillary range $Ca^+ < Ca < Ca^{**}$ (zone d in Figure 7.2). Moreover, in contrast to the literature (Chapter 1), the thickness of the thick film is not unique and depends on the velocity of the triple line: $e_1 = l_c\sqrt{3Ca_d}$. The velocity Ca_d increases with the slug velocity but is slightly smaller. We observe thick films with a variety of thicknesses ranging roughly from 50 to 200 μm. The difference $Ca - Ca_d$ is more and more pronounced until a certain value, where the dewetting velocity saturates at Ca_d^{sat}. The saturation of the triple line velocity was identified at $Ca^{**} = 2.2\ 10^{-3}$ and defines the transition between *regime (ii)* and *(iii)* and is accounted for by the value of Ca for which the forced wetting transition is predicted by Cox-Voinov relation.

In *regime (iii)* a thinner film grows between the previous thick film and the meniscus (zone e). We recover a thickness independent of the velocity $e_1^{sat} = l_c\sqrt{3Ca_d^{sat}}$ of the upper thick film, similarly to some authors Snoeijer *et al.* [2, 3] (experimentally) and Hocking [4], Snoeijer *et al.* [1], Gao *et al.* [5] (numerically). The transition towards two liquid films is associated to the saturation of the downward flux generated by the dewetting and the gravity. This flux becomes smaller than the upward flux of liquid ejected by the slug by viscous forcing, that selects a second thickness: two film thicknesses coexist and are linked by a capillary jump formed at the transition. The lower film corresponds to a Landau-Levich-Derjaguin/Bretherton film, usually observed for complete wetting conditions and has a thickness varying as $Ca^{2/3}$. In *regime (ii)* and *(iii)*, stationary numerical profiles account fairly well for our experimental observations in terms of thickness evolution with Ca, apart from the rim we observe close to the triple line. The existence of *regime (iii)* can be obtained when taking into account the time derivatives. Doing so, we find the different regimes found by Gao *et al.* [5]. This does not predict a velocity-dependent thick film for *regime (ii)*, the thickness of the film is constant, consistent with $e_1 = l_c\sqrt{3Ca^*}$ and not with our experimental result $e_1 = l_c\sqrt{3Ca_d}$. Moreover, the difference between Ca^* and Ca^{**} is much more pronounced experimentally ($\Delta Ca = 1.8\ 10^{-3}$) than numerically ($\Delta Ca = 10^{-4}$).

When the capillary number is large enough, the second film can become thicker than the first film. In the meantime, oscillations located close to the capillary jump appear in the film thickness. A last scenario is occasionally observed where the film destabilizes either in the thin zone or in the oscillating zone. A dry zone nucleates and grows leaving only a rivulet connecting the upper film to the slug or the new film formed below (Figure 7.3). Once the film has completely drained through the rivulet, the rivulet itself is destabilized into droplets (Rayleigh-Plateau instability). These droplets are subjected to evaporation and leave pollutants, generating contamination of the substrate.

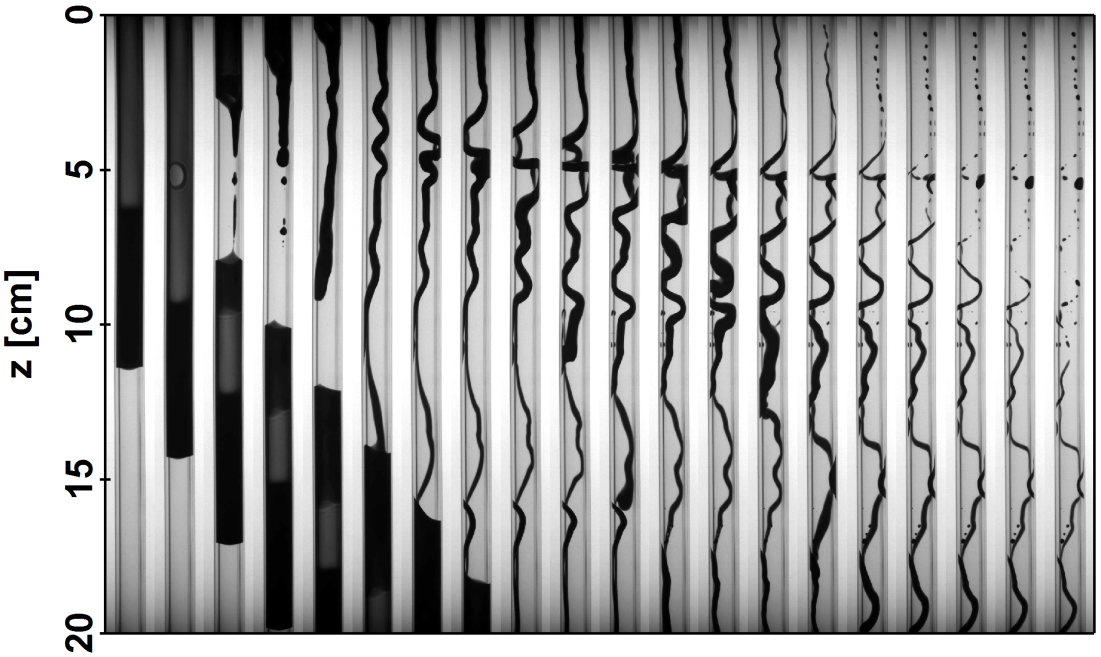

(a)

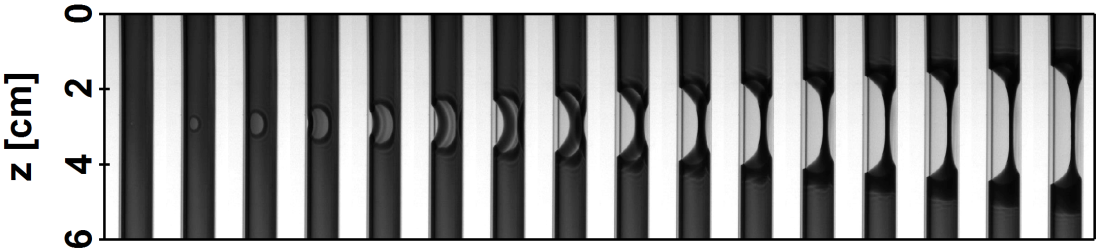

(b)

FIGURE 7.3: *(a) Image sequence obtained for a typical experiment where the liquid film breaks ($\Delta t = 100$ ms). A dry zone nucleates and grows leaving a rivulet which itself destabilized into droplets that remain pinned at the surface. (b) Zoom in on the nucleation zone ($\Delta t = 4$ ms).*

Our work provides fundamental insights on the classical problem of moving contact lines in cylindrical geometry and film deposition on partially wetting substrates. Furthermore, these results found a practical application for tube's manufacturers, like Saint-Gobain, or its customers. Indeed, as explained in the introduction, one crucial point is to reduce the contamination of the tube due to the transferred liquid. This requires first the reduction of the contact time between the liquid and the tube, and second the stabilization of the flow in order to avoid the pinning of droplets. For both aspects, it is preferable to avoid any film deposition and to process the flow in a stable zone: *regime (i)*. We have demonstrated the possibility to tune parameters (liquid and material properties) in order to either prevent or induce liquid film formation. We have a complete view of the problem that may help the manufacturer to advice their customers in term of tube properties for a given liquid (η, γ, processing flow rate via Ca, chemistry of the tube via θ_r).

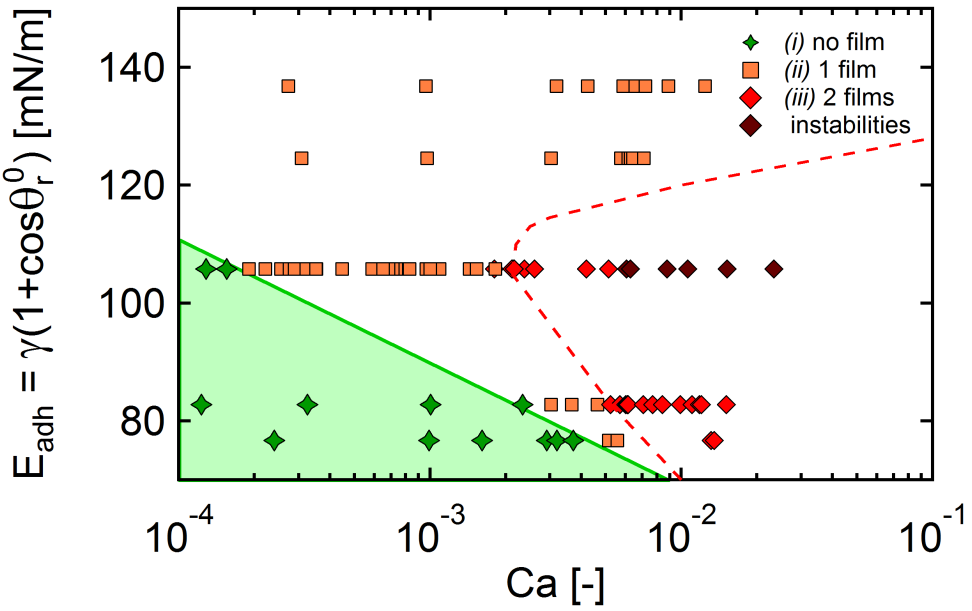

FIGURE 7.4: *Phase diagram for pure water: adhesion energy* $E_{adh} = \gamma\,(1 + \cos\theta_r^0)$ *versus capillary number* Ca*. The green and the red curves correspond to the qualitative limit between regime (i) and (ii), and regime (ii) and (iii) respectively.*

A phase diagram E_{adh} versus Ca was built in Figure 7.4. The adhesion energy E_{adh} accounts for the liquid/solid interactions through the tube chemistry θ_r^0 and through the liquid surface tension γ. Using this phase diagram, the tube chemistry for a given surface tension and a given flow rate can be adjusted to place the system in a stable regime, namely *regime (i)*.

Appendix A

Bretherton calculation

We consider a long bubble moving steadily at constant velocity v in the z direction in a capillary tube of radius R filled with a liquid (Figure A.1).

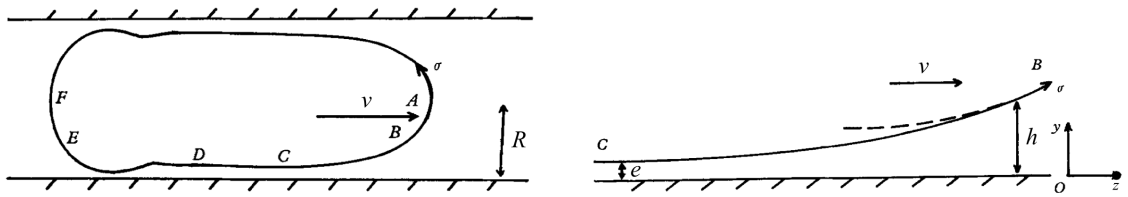

FIGURE A.1: *Bretherton problem: air bubble displaced in a capillary [14].*

A film of thickness e is squeezed between the bubble and the walls away from the bubble ends. The liquid is completely wetting the tube. Invariance in the $x-$direction is assumed and inertial and gravitational effects are neglected. The velocity in the $z-$direction is denoted as $v(z)$, the film thickness $h(z)$ and the pressure in the liquid phase P. Fluid viscosity is η and surface tension γ. Three regions within the bubble can be defined, the first one where a film of constant thickness e is connecting front and rear meniscus (zone $C-D$), the second one where the thickness is varying called the dynamic meniscus (zone $B-C$ of length l) and finally the static meniscus (zone $A-B$). The radius of the tube is supposed smaller than the capillary length $R << l_c = \sqrt{\gamma/\rho g}$ and the film thickness is smaller than the tube radius $e << R$.

A.1 Scaling approach

Pressure in the liquid film and in the liquid reservoir where the capillary tube is fully filled with liquid (bubble ends) can be expressed as:

$$P_{film} = -\frac{\gamma}{R-e} \simeq -\frac{\gamma}{R} \tag{A.1}$$

$$P_{reservoir} = -\frac{2\gamma}{R} \tag{A.2}$$

These two pressures are different, consequently there is a pressure gradient in the dynamic meniscus of length l $(B-C)$ inducing a flow from the film towards the reservoir of liquid at both sides of the bubble. In the opposite direction (-$z-$axis), a viscous stress acting on the length scale e arise from the flow. Therefore Stokes equation scales as:

$$\frac{\eta v}{e^2} \sim \frac{\gamma}{Rl} \tag{A.3}$$

Because e and l are two unknowns, a second equation is required: the pressure continuity between dynamic and static menisci:

$$P_{static} = P_{dynamic} \quad \Leftrightarrow \quad -\frac{2\gamma}{R} \sim -\frac{\gamma e}{l^2} - -\frac{\gamma}{R} \tag{A.4}$$

The last term corresponds to the two curvatures of the dynamic meniscus. Doing so, l can be expressed as:

$$l \sim (eR)^{1/2} \tag{A.5}$$

Finally the Bretherton law without its prefactor is obtained:

$$e \sim R\left(\frac{\eta v}{\gamma}\right)^{2/3} \tag{A.6}$$

This scaling law shows that as the velocity of the meniscus or the tube radius increases, the deposited film becomes thicker.

To obtain the exact expression of the film thickness profile, the Stokes equation has to be written in the lubrication approximation to get the flux in the dynamic meniscus. Matching this flux with the flux in a thin film of constant thickness e, gives a third-order non linear differential equation. Considering the first asymptotic case, in the limit of large film thicknesses (close to bubble ends A and F), we can show that the curvature is constant. After numerical integration, it gives the Bretherton law:

$$\frac{e}{R} \sim 1.34Ca^{2/3} \tag{A.7}$$

The second asymptotic case is the limit where the thickness of the liquid film is constant and equal to e. It exhibits two kind of solutions according to flux direction. The thickness profile will be purely exponential at the bubble front and exponential oscillatory at the bubble rear. The complete calculation of the Bretherton problem is presented in next section.

A.2 Complete calculation

Considering the Stokes equation in the lubrication approximation for the dynamic meniscus, equation of motion can be written as:

$$\eta \partial_{yy} v_z = \partial_z P \tag{A.8}$$

where the pressure is defined by the Laplace equation in the lubrication approximation for small liquid thickness compared to tube radius $h << R$

$$P = \gamma\kappa \simeq -\gamma \left(\partial_{zz} h + \frac{1}{R} \right) \tag{A.9}$$

Therefore, the second derivative of the velocity is:

$$\partial_{yy} v_z = \frac{\gamma}{\eta} \partial_{zzz} h \tag{A.10}$$

Considering a no slip boundary condition at the liquid/solid interface and a stress free boundary condition at the liquid/air interface, in the moving reference frame Equation (A.10) can be integrated into

$$v_z(y) = \frac{\gamma}{\eta} \left(\frac{y^2}{2} - hy \right) \partial_{zzz} h - v \tag{A.11}$$

The resulting flux per unit length is given by

$$q(h) = \int_0^h v_z(y) \mathrm{d}y = -\frac{\gamma}{\eta} \frac{h^3}{3} \partial_{zzz} h - vh \tag{A.12}$$

The flux per unit length in the zone $(C - D)$, where the film thickness is constant and equal to e, is $q(h_\infty = e) = ve$. Writing the flux conservation, a third-order non linear differential equation is obtained:

$$\partial_{zzz} h = -3Ca \frac{h - e}{h^3} \quad \text{with} \quad Ca = \frac{\eta v}{\gamma} \tag{A.13}$$

Defining two dimensionless parameters $H = h/e$ and $\xi = (3Ca)^{1/3} z/e$, the reduced equation can be written as:

$$H''' = -\frac{H - 1}{H^3} \tag{A.14}$$

The first asymptotic case of the previous Equation (A.13), the limit of large film thickness $H \to \infty$ is:

$$H''' \simeq -\frac{1}{H^2} \to 0 \tag{A.15}$$

In this limit, the curvature is constant and asymptotic matching with the static meniscus is possible, the solution is:

$$H(\xi) = \alpha\frac{\xi^2}{2} + \beta\xi + \delta \tag{A.16}$$

Thus,

$$h(z) \simeq \alpha(3Ca)^{2/3}\frac{z^2}{2e} + \beta(3Ca)^{1/3}z + \delta e \tag{A.17}$$

And the curvature in this limit is:

$$\kappa \simeq \partial_{zz}h + \frac{1}{R} \simeq (3Ca)^{2/3}\frac{\alpha}{e} + \frac{1}{R} \tag{A.18}$$

In first approximation, the profile is considered as a spherical cap with a curvature $\kappa \simeq 2/R$

$$\partial_{zz}h^{dynamic} = \partial_{zz}h^{static} \quad \Leftrightarrow \quad (3Ca)^{2/3}\frac{\alpha}{e} + \frac{1}{R} = \frac{2}{R} \tag{A.19}$$

$$\frac{e}{r} \simeq \alpha(3Ca)^{2/3} \tag{A.20}$$

Coefficient α is obtained numerically when $H \to \infty$, $H'' \to 0.643$ (Figure A.2). One obtains finally the Bretherton law

$$\frac{e}{R} \simeq 1.34Ca^{2/3} \tag{A.21}$$

As the velocity of the meniscus or the tube radius increases, the film deposited becomes thicker.

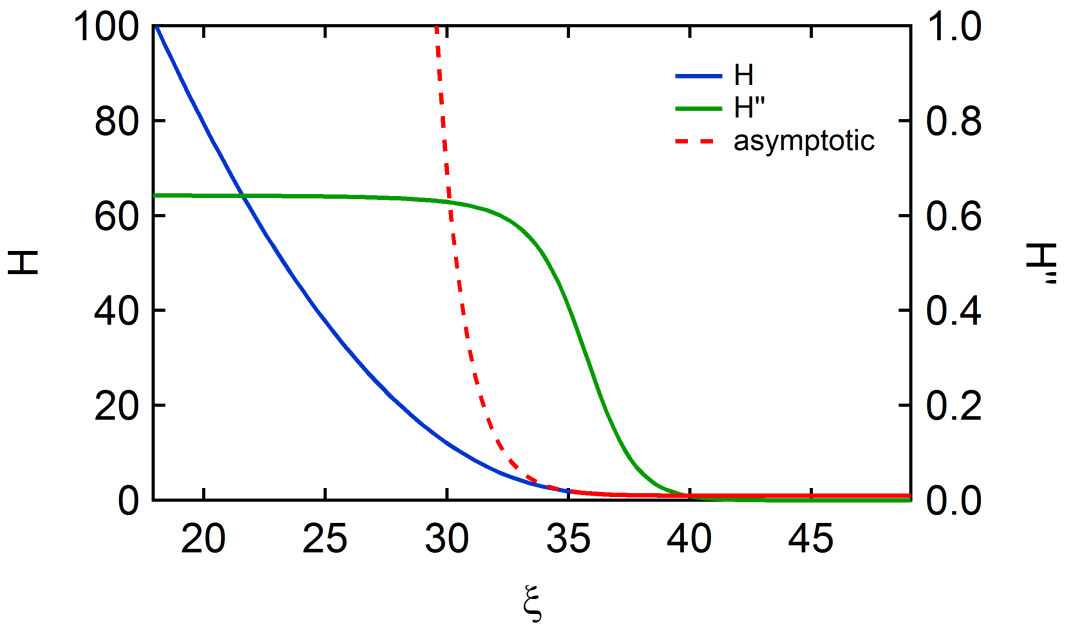

FIGURE A.2: *Numerical integration of the film thickness profile calculated with Equation (A.14). For $H \to \infty$, $H'' \to 0.643$.*

The second asymptotic case, limit where the thickness is constant and equal to e : $h \to e$, reduces to the following equation

$$\partial_{zzz}\Delta h = -\frac{3Ca}{e^3}\Delta h \quad \text{with} \quad \Delta h = h - e \tag{A.22}$$

Equation (A.22) exhibits two kind of solutions according to flux direction (sign of v):

$$h(z) = e^{-\frac{(3Ca)^{1/2}}{e}z} \tag{A.23}$$

$$h(z) = e^{\frac{(3Ca)^{1/2}}{2e}z}\cos\left(\frac{\sqrt{3}}{2}\frac{(3Ca)^{1/3}}{e}z + \phi\right) \tag{A.24}$$

The thickness profile will be purely exponential at the front of the air bubble ($v > 0$, solution A.23) and exponential oscillatory at the rear of the air bubble ($v < 0$, solution A.24).

Appendix B

Comparing meniscus elevation z_{cl} and contact angle θ_r

In this appendix, we propose an alternate method to measure contact angles at the triple line : indirect measurement method. This method uses the "low velocity setup" (Figure 2.6a) to measure the meniscus elevation z_{cl} on the same set of images as illustrated in Figure 3.2. It is the distance between the lower point at the center of the tube and the contact line at the tube surface.

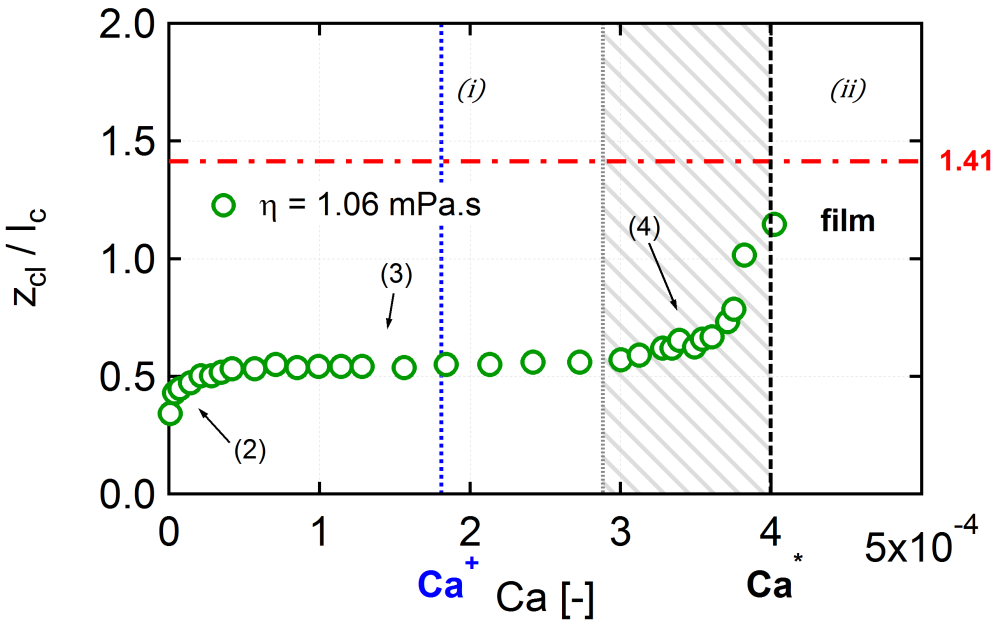

FIGURE B.1: *Contact line elevation z_{cl} normalized by the capillary length l_c as a function of the capillary number Ca for 5%wt glycerol solution ($\eta = 1.06$ mPa.s). The black dashed vertical line indicates our measurement of the dynamic wetting transition (Ca^*). The blue vertical dotted line indicates Ca^+ as defined in Section 3.5. The red dashed-dotted horizontal line at $z_{cl}/l_c = \sqrt{2} = 1.41$ corresponds to the maximal contact elevation for a static meniscus.*

This method assumes that the shape taken by the interface is a static meniscus while the contact line is moving and that there is no effects of the tube curvature (out of the planar curvature). Once the liquid meniscus is moving it takes on an equilibrium shape. We can derive the dynamic contact angle from the vertical extension z_{cl} using :

$$z_{cl} = l_c\sqrt{2\,(1-\sin\theta)} \tag{B.1}$$

This relations is valid for flat surface (Section 2.3.1) and is used here as an approximation because the tube diameter is larger than l_c. From Equation (B.1), we see that the maximum height of the meniscus cannot exceed $l_c\sqrt{2}$, which equals 3.8 mm with water.

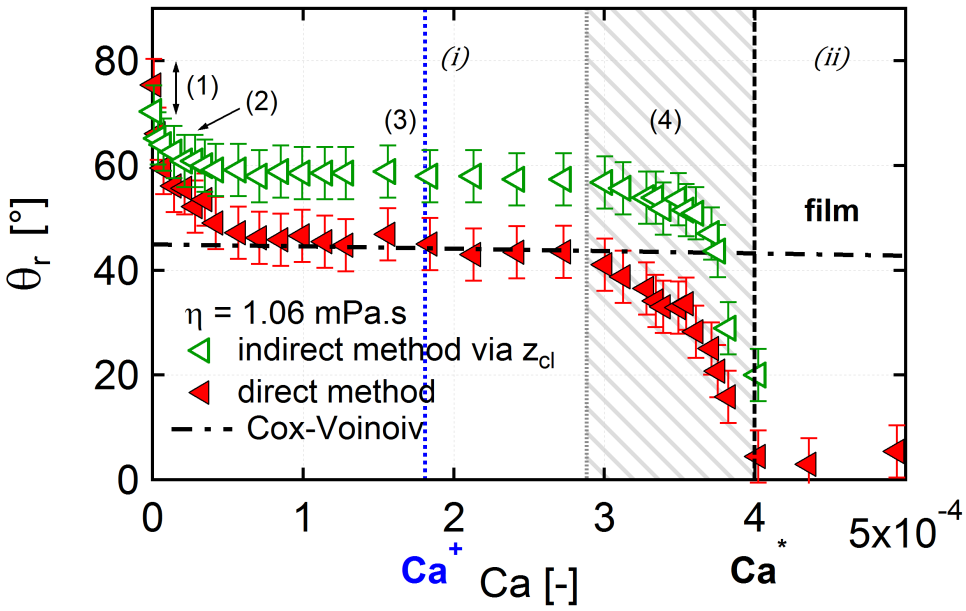

FIGURE B.2: *Converted contact angle calculated from the meniscus extension z_{cl} (blue), and contact angle from the direct measurement (red) as a function of the capillary number Ca for 5%wt glycerol solution ($\eta = 1.06$ mPa.s). The black dashed curve represents the Cox-Voinov prediction. The black dashed vertical line indicates our measurement of the dynamic wetting transition (Ca^*). The blue vertical dotted line indicates Ca^+ as defined in Section 3.5.*

At rest, z_{cl} is null. When the motion is induced, the contact line raises until a certain position where the meniscus takes a stationary shape. Normalized contact elevation z_{cl}/l_c is given as a function of the capillary number of the meniscus Ca in Figure B.1 for 5%wt glycerol solution ($\eta = 1.06$ mPa.s and $l_c = 2.63$ mm). We observe the same different zones as for Chapter 3. Zone (2) where the contact line position increases quite rapidly at very low capillary number. Zone (3) where the contact elevation is constant at about $z_{cl} = 0.5l_c$. And finally, zone (4) where the normalized quantity is increasing quite strongly with the capillary number until film entrainment. Above Ca^*, we could still define z_{cl} but it would correspond to the length of the film and no more to the meniscus elevation. We

have chosen not to depict the length of the film in Figure B.1.

As mentioned earlier, the contact angle θ_r can be obtained out of the contact line elevation z_{cl} using Equation (B.1): the result is plotted in Figure B.2 (green open symbols). Red symbols are contact angles from the direct measurement method, already shown in Figure 3.3b.

We can note that the two methods lead to two similar curves with an offset. This offset is probably due to Equation (B.1) which provides a correspondence between z_{cl} and θ_r adapted for a planar geometry. For a tube, there is no analytical equation, but we can obtain a numerical value. Note that both methods provide the same value of the capillary numbers that separate the four above mentioned zones (zone (1), (2), (3), (4)) and in particular, the instantaneous forced wetting transition at the end of zone (4) for which $Ca^* = 4\ 10^{-4}$ for both methods (and the critical transition $Ca^+ = 1.8\ 10^{-4}$).

Appendix C

Influence of tube diameter

In this appendix we investigate briefly the influence of the tube diameter. We use PVC tubes and we vary the inner diameter d_{in} : 3.2 mm, 4.8 mm, 6.4 mm. Characteristics are given in the Experimental description chapter (Section 2.2). The range of available diameters was limited by the manufacturer. The liquid used is pure water: $\eta = 0.94$ mPa.s and $l_c = 2.66$ mm.

C.1 On the dynamic wetting transition

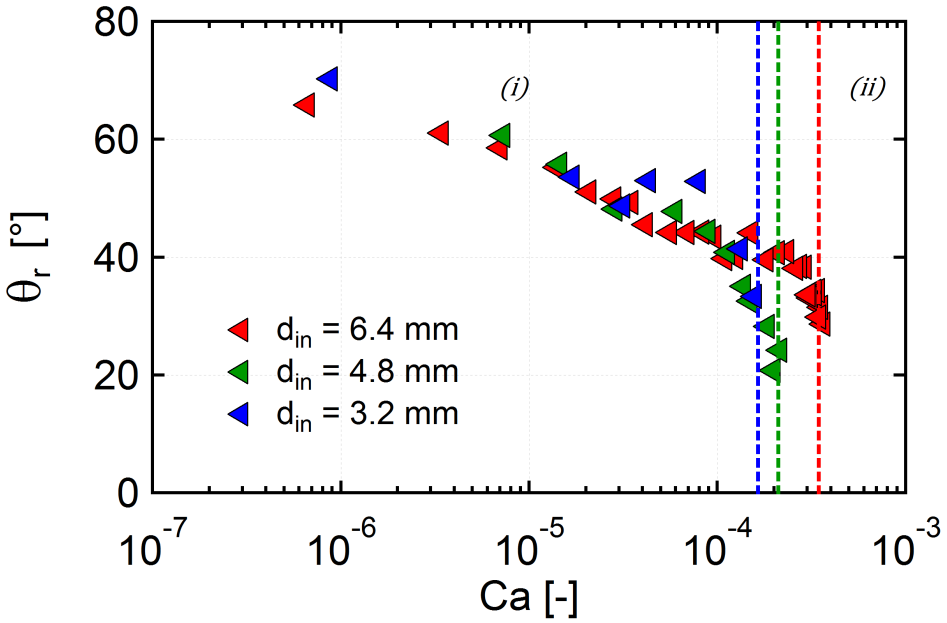

FIGURE C.1: *Receding contact angle from the direct measurement as a function of the capillary number Ca for different tube diameters : 3.2 mm (blue), 4.8 mm (green), 6.4 mm (red). The vertical dashed lines indicate our measurement of the dynamic wetting transition (Ca^*) for each tube diameter.*

In this section we investigate the impact of the tube diameter on the evolution of the

contact angle and the dynamic wetting transition. Here, we measure the capillary number Ca^* at which film deposition develops instantaneously with experimental time accuracy, as defined in Chapter 3. In Chapter 3, we studied the case of a diameter $d_{in} = 6.4\ mm$ and we found a dynamic wetting transition at $Ca^* = 4\ 10^{-4}$.

Along the same path as in Chapter 3, we measure the receding contact angle θ_r as a function of the capillary number of the slug Ca for a series of experiments with various inner diameters and various slug velocities. Figure C.1 gathers the receding contact angles θ_r versus the capillary number of the meniscus Ca for the three tube radii R investigated. We observe that a change in the tube radius R in the range used does not modify the evolution of the receding contact angle with the capillary number. θ_r decreases with Ca, down to the dynamic wetting transition. Nevertheless, we note that the capillary number at the dynamic wetting transition Ca^* depends on the tube diameter. Ca^* increases with the tube diameter.

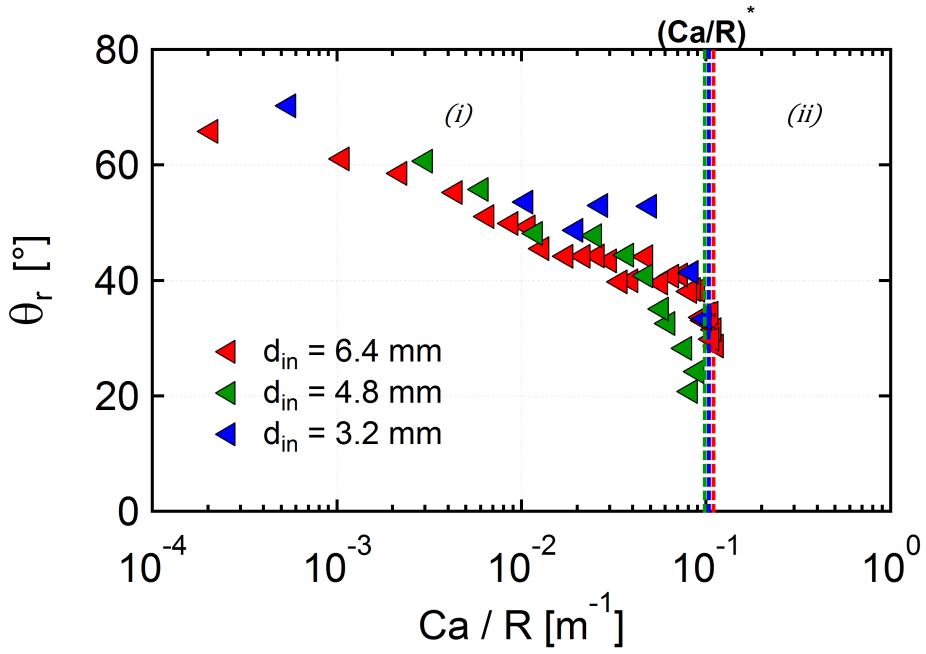

FIGURE C.2: *Receding contact angle for different tube diameters : 3.2 mm (blue), 4.8 mm (green), 6.4 mm (red), as a function of the capillary number normalized by the tube radius Ca/R. The vertical dashed lines indicate the dynamic wetting transition ($(Ca/R)^* = 10^{-1}$) for three tube diameters.*

This experimental observation suggests that there is an effect of the radial curvature. The receding contact angle can be replotted as a function of the capillary number divided by the tube radius Ca/R (Figure C.2). The data collapse on a single curve and provide a critical value $(Ca/R)^* = 10^{-1}$ for the dynamic wetting transition. We have initiated numerical simulations taking into account the full curvature expression (Equation (2.12)), and these preliminary calculations suggest no significant difference when varying the tube diameter. Further investigations have to be carried out. Notably, to be more accurate we

should measure the critical value Ca^+ rather than the threshold Ca^*. Besides, the same phenomenology is observed for all tube diameters.

C.2 On the kinematics

We now report on the flow phenomenology after the dynamic wetting transition, similarly to Chapter 4 and 5. As in the previous section, we use the same tube diameters and pure water. For the case of a diameter $d_{in} = 6.4\ mm$, we found a second transition at $Ca^{**} = 2.2\ 10^{-3}$.

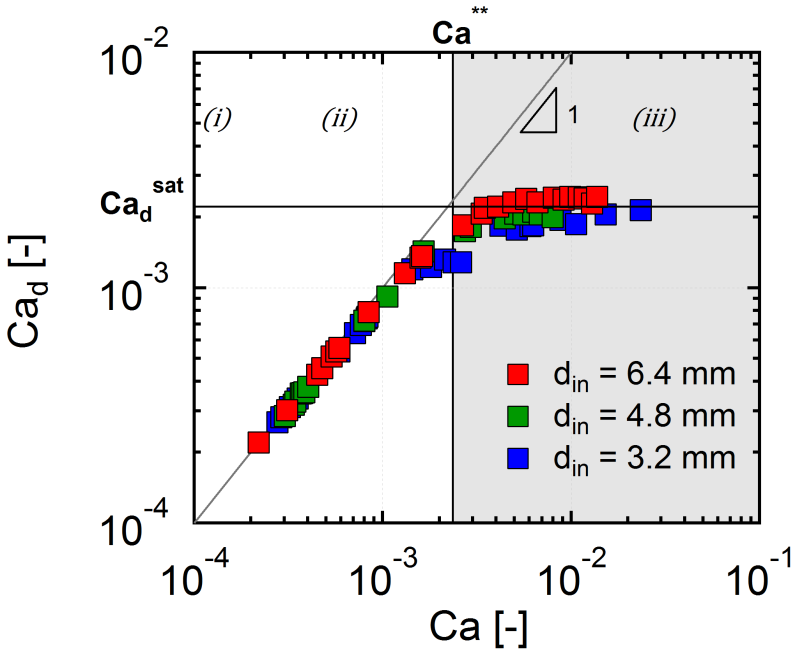

FIGURE C.3: *Dewetting capillary number Ca_d versus slug capillary number Ca for different tube diameters : 3.2 mm (blue), 4.8 mm (green), 6.4 mm (red). The grey zone represents regime (iii).*

In Figure C.3 we report Ca_d as a function of Ca for three tube diameters of interest : 3.2 mm (blue), 4.8 mm (green), 6.4 mm (red). The evolution $Ca_d = f(Ca)$ is unchanged when varying the tube diameter. The three regimes identified for $d_{in} = 6.4\ mm$ are identical for the two others diameters: *regime (i)* without film discussed in Section C.1; *regime (ii)* with a thick film where $Ca_d \simeq 0.8Ca$; *regime (iii)* with two films (grey zone) where the dewetting capillary number saturates at Ca_d^{sat}. The first threshold capillary number Ca^* depends on R (Section C.1) and we thus did not plot a threshold regime in Figure C.3, whereas the Ca^{**} is independent of R. We can conclude that there is no influence of the tube diameter, in the range investigated, on the kinematic evolution and flow morphology.

C.3 On the thickness of the film

Finally we examine the film thickness evolution as a function of the capillary number for the three tube diameters. We plot in Figure C.4 the film thickness e_1 rescaled by the capillary length l_c versus the dewetting capillary number Ca_d for the different diameters.

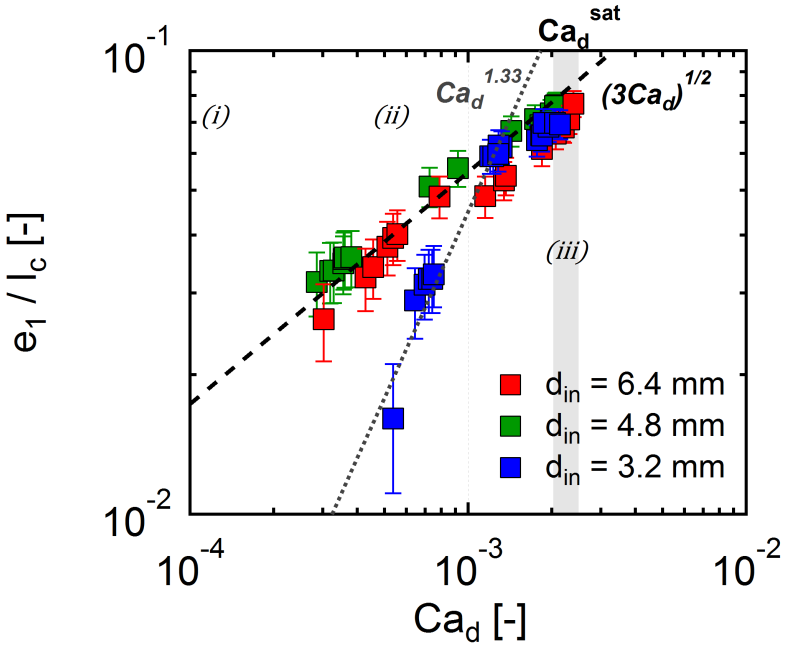

FIGURE C.4: *Average film thickness e_1 normalized by the capillary length l_c as a function of the capillary number of the dewetting film Ca_d for different tube diameters : 3.2 mm (blue), 4.8 mm (green), 6.4 mm (red). Predictive model considering a gravitational drainage at constant film thickness (black dashed line). The grey dotted line in $Ca^{1.33}$ is a fit of the data for the smaller tube.*

We observe that for the diameter $d_{in} = 4.8\ mm$, we recover the same values as for $d_{in} = 6.4\ mm$. The thick film thickness is given by $e_1 = l_c\sqrt{3Ca_d}$. The saturation of the film thickness and of the dewetting capillary number are simultaneous and independent of the tube diameter : $e_1 = e_1^{sat}$ when $Ca_d = Ca_d^{sat}$. The same statements can be attributed to the smaller tube diameter, $d_{in} = 3.2\ mm$, but only for $Ca_d > 10^{-3}$. Below $Ca_d = 10^{-3}$, the film thickness is smaller than expected and increases more sharply with Ca_d. In this capillary number range, the data for the smaller tube can be fitted to a power law and we find $e_1/l_c \propto Ca_d{}^{1.33}$ (grey dotted line). We have no explanation for this unexpected result.

Note that we have also measured the thickness of the second film e_2 in *regime (iii)*, and we have found that there was no dependency of e_2 on the tube diameter in the range investigated.

Bibliography

[1] JH Snoeijer, B Andreotti, G Delon, and M Fermigier. Relaxation of a dewetting contact line. Part 1. A full-scale hydrodynamic calculation. *Journal of Fluid Mechanics*, 579:63–83, 2007. 11, 41, 72, 98, 137

[2] JH Snoeijer, G Delon, M Fermigier, and B Andreotti. Avoided critical behavior in dynamically forced wetting. *Physical review letters*, 96(17):174504, 2006. 11, 42, 43, 96, 98, 99, 102, 103, 105, 115, 125, 137

[3] G Delon, M Fermigier, JH Snoeijer, and B Andreotti. Relaxation of a dewetting contact line. Part 2. Experiments. *Journal of Fluid Mechanics*, 604(55):24, 2008. 11, 42, 105, 137

[4] LM Hocking. Meniscus draw-up and draining. *European Journal of Applied Mathematics*, 12(03):195–208, 2001. 11, 42, 98, 102, 115, 137

[5] P Gao, L Li, J Feng, H Ding, and X Lu. Film deposition and transition on a partially wetting plate in dip coating. *Journal of Fluid Mechanics*, 791:358–383, 2016. 11, 12, 43, 44, 75, 98, 105, 113, 125, 137

[6] KG Kornev, AV Neimark, and AN Rozhkov. Foam in porous media: thermodynamic and hydrodynamic peculiarities. *Advances in colloid and interface science*, 82(1):127–187, 1999. 27

[7] CN Mulligan, RN Yong, and BF Gibbs. Surfactant-enhanced remediation of contaminated soil: a review. *Engineering Geology*, 60(1):371–380, 2001. 27

[8] JB Grotberg. Respiratory fluid mechanics and transport processes. *Annual review of biomedical engineering*, 3(1):421–457, 2001. 27

[9] P Hayoun, J Engmann, S Mowlavi, B Le Reverend, A Burbidge, and M Ramaioli. A model experiment to understand the oral phase of swallowing of Newtonian liquids. *Journal of biomechanics*, 48(14):3922–3928, 2015. 27

[10] P Tabeling. A brief introduction to slippage, droplets and mixing in microfluidic systems. *Lab on a Chip*, 9(17):2428–2436, 2009. 27

[11] LD Landau and BV Levich. Dragging of a Liquid by a Moving Plate. *Acta Physicochim. URSS*, 17:42, 1942. 28, 98, 114, 125

[12] BV Derjaguin. Thickness of liquid layer adhering to walls of vessels on their emptying. *Acta Physicochim URSS*, 20:349, 1943. 28, 31, 98, 102, 114, 125

[13] KJ Ruschak. Coating flows. *Annual Review of Fluid Mechanics*, 17(1):65–89, 1985. 28

[14] FP Bretherton. The motion of long bubbles in tubes. *J. Fluid Mech*, 10(2):166–188, 1961. 29, 30, 93, 114, 125, 141

[15] I Cantat. Liquid meniscus friction on a wet plate: Bubbles, lamellae, and foamsa). *Physics of Fluids (1994-present)*, 25(3):031303, 2013. 29

[16] F Fairbrother and AE Stubbs. 119. Studies in electro-endosmosis. Part VI. The "bubble-tube" method of measurement. *Journal of the Chemical Society (Resumed)*, pages 527–529, 1935. 29

[17] GI Taylor. Deposition of a viscous fluid on the wall of a tube. *Journal of Fluid Mechanics*, 10(02):161–165, 1961. 29, 30, 98

[18] P Aussillous and D Quéré. Quick deposition of a fluid on the wall of a tube. *Physics of Fluids*, 12(10):2367–2371, 2000. 30, 50

[19] M Heil. Finite Reynolds number effects in the Bretherton problem. *Physics of Fluids (1994-present)*, 13(9):2517–2521, 2001. 30

[20] A de Ryck. The effect of weak inertia on the emptying of a tube. *Physics of Fluids*, 14:2102, 2002. 30

[21] Y Han and N Shikazono. Measurement of the liquid film thickness in micro tube slug flow. *International Journal of Heat and Fluid Flow*, 30(5):842–853, 2009. 30

[22] G Callegari, A Calvo, and JP Hulin. Dewetting processes in a cylindrical geometry. *The European Physical Journal E*, 16(3):283–290, 2005. 30, 50

[23] SDR Wilson and AF Jones. The entry of a falling film into a pool and the air-entrainment problem. *Journal of Fluid Mechanics*, 128:219–230, 1983. 31, 32, 98, 103

[24] RA Cook and RH Clark. An analysis of the stagnant band on falling liquid films. *Industrial & Engineering Chemistry Fundamentals*, 12(1):106–114, 1973. 32

[25] EJ Cullen and JF Davidson. Absorption of gases in liquid jets. *Transactions of the Faraday Society*, 53:113–120, 1957. 32

[26] KJ Ruschak. Flow of a falling film into a pool. *AIChE Journal*, 24(4):705–709, 1978. 32

[27] M Maleki, M Reyssat, F Restagno, D Quéré, and C Clanet. Landau–Levich menisci. *Journal of colloid and interface science*, 354(1):359–363, 2011. 32

[28] T Young. An essay on the cohesion of fluids. *Philosophical Transactions of the Royal Society of London*, 95:65–87, 1805. 32

[29] JF Joanny and PG de Gennes. A model for contact angle hysteresis. *The journal of chemical physics*, 81(1):552–562, 1984. 33

[30] PG de Gennes. Wetting: statics and dynamics. *Reviews of modern physics*, 57(3):827, 1985. 33, 37

[31] R Golestanian and E Raphaël. Roughening transition in a moving contact line. *Physical Review E*, 67(3):031603, 2003. 33, 38

[32] R Ablett. An investigation of the angle of contact between paraffin wax and water. *The London, Edinburgh, and Dublin Philosophical Magazine and Journal of Science*, 46(272):244–256, 1923. 34, 73

[33] C Huh and LE Scriven. Hydrodynamic model of steady movement of a solid/liquid/fluid contact line. *Journal of Colloid and Interface Science*, 35(1):85–101, 1971. 34

[34] EB Dussan and SH Davis. On the motion of a fluid-fluid interface along a solid surface. *Journal of Fluid Mechanics*, 65(01):71–95, 1974. 34

[35] VEB Dussan. On the difference between a bounding surface and a material surface. *J Fluid Mech*, 75:609–623, 1976. 34

[36] RG Cox. The dynamics of the spreading of liquids on a solid surface. Part 1. Viscous flow. *Journal of Fluid Mechanics*, 168:169–194, 1986. 34, 35, 36, 41, 133

[37] OV Voinov. Hydrodynamics of wetting. *Fluid Dynamics*, 11(5):714–721, 1976. 34, 35, 36, 41, 133

[38] PG de Gennes. Deposition of langmuir-blodgett layers. *Colloid and Polymer Science*, 264(5):463–465, 1986. 34, 37

[39] PG de Gennes, X Hua, and P Levinson. Dynamics of wetting: local contact angles. *Journal of Fluid Mechanics*, 212:55–63, 1990. 34, 37

[40] J Eggers. Hydrodynamic theory of forced dewetting. *Physical review letters*, 93(9):094502, 2004. 34, 39, 72

[41] TD Blake and JM Haynes. Kinetics of liquidliquid displacement. *Journal of colloid and interface science*, 30(3):421–423, 1969. 34, 38

[42] TD Blake and KJ Ruschak. Wetting: static and dynamic contact lines. In *Liquid film coating*, pages 63–97. Springer, 1997. 34, 39

[43] Y Pomeau. Représentation de la ligne de contact mobile dans les équations de la mécanique des fluides. *Comptes Rendus de l'Académie des Sciences-Series IIB-Mechanics*, 328(5):411–416, 2000. 34

[44] P Petrov and I Petrov. A combined molecular-hydrodynamic approach to wetting kinetics. *Langmuir*, 8(7):1762–1767, 1992. 34, 39

[45] JG Petrov, J Ralston, M Schneemilch, and RA Hayes. Dynamics of partial wetting and dewetting in well-defined systems. *The Journal of Physical Chemistry B*, 107(7):1634–1645, 2003. 34, 39

[46] E Guyon, JP Hulin, and L Petit. *Hydrodynamique physique*. EDP Sciences-CNRS Editions, 2001. 35

[47] BR Duffy and SK Wilson. A third-order differential equation arising in thin-film flows and relevant to Tanner's law. *Applied Mathematics Letters*, 10(3):63–68, 1997. 36

[48] H Hervet and PG de Gennes. Dynamique du mouillage: films précurseurs sur solides «sec». *Comptes-rendus des séances de l'Académie des sciences. Série 2, Mécanique-physique, chimie, sciences de l'univers, sciences de la terre*, 299(9):499–503, 1984. 37

[49] S Glasstone, H Eyring, and KJ Laidler. *The theory of rate processes*. McGraw-Hill, 1941. 38

[50] TD Blake. The physics of moving wetting lines. *Journal of Colloid and Interface Science*, 299(1):1–13, 2006. 38, 40

[51] R Golestanian and E Raphaël. Dissipation in dynamics of a moving contact line. *Physical Review E*, 64(3):031601, 2001. 38

[52] M Maleki, E Reyssat, D Quéré, and R Golestanian. On the landau-levich transition. *Langmuir*, 23(20):10116–10122, 2007. 39

[53] F Brochard-Wyart and PG de Gennes. Dynamics of partial wetting. *Advances in Colloid and Interface Science*, 39(0):1–11, April 1992. 39, 40

[54] MJ De Ruijter, TD Blake, and J De Coninck. Dynamic wetting studied by molecular modeling simulations of droplet spreading. *Langmuir*, 15(22):7836–7847, 1999. 39

[55] H Perrin, R Lhermerout, K Davitt, E Rolley, and B Andreotti. Defects at the Nanoscale Impact Contact Line Motion at all Scales. *Physical review letters*, 116(18):184502, 2016. 39

[56] W Ren and E Weinan. Boundary conditions for the moving contact line problem. *Physics of Fluids (1994-present)*, 19(2):022101, 2007. 39

[57] W Ren, D Hu, and E Weinan. Continuum models for the contact line problem. *Physics of Fluids (1994-present)*, 22(10):102103, 2010. 39, 76

[58] LH Tanner. The spreading of silicone oil drops on horizontal surfaces. *Journal of Physics D: Applied Physics*, 12(9):1473, 1979. 40

[59] R Fetzer and J Ralston. Dynamic dewetting regimes explored. *The Journal of Physical Chemistry C*, 113(20):8888–8894, 2009. 40

[60] K Davitt, MS Pettersen, and E Rolley. Thermally activated wetting dynamics in the presence of surface roughness. *Langmuir*, 29(23):6884–6894, 2013. 40, 73

[61] RL Hoffman. A study of the advancing interface. I. Interface shape in liquid—gas systems. *Journal of Colloid and Interface Science*, 50(2):228–241, 1975. 40

[62] M Fermigier and P Jenffer. An experimental investigation of the dynamic contact angle in liquid-liquid systems. *Journal of colloid and interface science*, 146(1):226–241, 1991. 40

[63] D Quéré. On the minimal velocity of forced spreading in partial wetting. *Comptes Rendus De l'Académie des Sciences Série II*, 313(3):313–318, 1991. 41, 65, 75, 98

[64] C Redon, F Brochard-Wyart, and F Rondelez. Dynamics of dewetting. *Physical review letters*, 66(6):715, 1991. 41, 98, 113, 132

[65] J Eggers. Toward a description of contact line motion at higher capillary numbers. *Physics of Fluids (1994-present)*, 16(9):3491–3494, 2004. 41

[66] J Eggers. Contact line motion for partially wetting fluids. *Physical Review E*, 72(6):061605, 2005. 41

[67] TS Chan, JH Snoeijer, and J Eggers. Theory of the forced wetting transition. *Physics of Fluids (1994-present)*, 24(7):072104, 2012. 41

[68] M Galvagno, D Tseluiko, H Lopez, and U Thiele. Continuous and discontinuous dynamic unbinding transitions in drawn film flow. *Physical review letters*, 112(13):137803, 2014. 41

[69] D Tseluiko, M Galvagno, and U Thiele. Collapsed heteroclinic snaking near a heteroclinic chain in dragged meniscus problems. *The European Physical Journal E*, 37(4):1–17, 2014. 41

[70] TD Blake and KJ Ruschak. A maximum speed of wetting. *Nature*, 282(5738):489–491, November 1979. 42, 65, 75, 105

[71] JG Petrov and RV Sedev. On the existence of a maximum speed of wetting. *Colloids and surfaces*, 13:313–322, 1985. 42, 105, 113

[72] T Podgorski, J-M Flesselles, and L Limat. Corners, cusps, and pearls in running drops. *Physical review letters*, 87(3):036102, 2001. 42, 105

[73] N Le Grand, A Daerr, and L Limat. Shape and motion of drops sliding down an inclined plane. *Journal of Fluid Mechanics*, 541:293–316, 2005. 42, 105

[74] E Rio, A Daerr, B Andreotti, and L Limat. Boundary conditions in the vicinity of a dynamic contact line: experimental investigation of viscous drops sliding down an inclined plane. *Physical review letters*, 94(2):024503, 2005. 42, 105

[75] P Gao, L Li, and XY Lu. Dewetting films with inclined contact lines. *Physical Review E*, 91(2):023008, 2015. 42

[76] JH Snoeijer, J Ziegler, B Andreotti, M Fermigier, and J Eggers. Thick films of viscous fluid coating a plate withdrawn from a liquid reservoir. *Physical review letters*, 100(24):244502, 2008. 42, 92, 96, 102, 103, 113, 125

[77] PG de Gennes, F Brochard-Wyart, and D Quéré. *Capillarity and wetting phenomena: drops, bubbles, pearls, waves*. Springer, 2004. 55

[78] RC Ernst, CH Watkins, and HH Ruwe. The Physical Properties of the Ternary System Ethyl Alcohol–Glycerin–Water. *The Journal of Physical Chemistry*, 40(5):627–635, 1936. 56

[79] Glycerine Producers' Association. *Physical properties of glycerine and its solutions*. Glycerine Producers' Association, 1963. 56

[80] IS Khattab, F Bandarkar, MAA Fakhree, and A Jouyban. Density, viscosity, and surface tension of water+ ethanol mixtures from 293 to 323k. *Korean Journal of Chemical Engineering*, 29(6):812–817, 2012. 56

[81] A Papra, A Bernard, D Juncker, N B Larsen, B Michel, and E Delamarche. Microfluidic networks made of poly (dimethylsiloxane), Si, and Au coated with polyethylene glycol for patterning proteins onto surfaces. *Langmuir*, 17(13):4090–4095, 2001. 58

[82] M Morra, E Occhiello, R Marola, F Garbassi, P Humphrey, and D Johnson. On the aging of oxygen plasma-treated polydimethylsiloxane surfaces. *Journal of Colloid and Interface Science*, 137(1):11–24, 1990. 58

[83] BT Ginn and O Steinbock. Polymer surface modification using microwave-oven-generated plasma. *Langmuir*, 19(19):8117–8118, 2003. 59

[84] K Chaudhury and GM Whitesides. Direct measurement of interfacial interactions between semispherical lenses and flat sheets of poly (dimethylsiloxane) and their chemical derivatives. *Langmuir*, 7(5):1013–1025, 1991. 59

[85] J Kim, MK Chaudhury, and MJ Owen. Hydrophobic recovery of polydimethylsiloxane elastomer exposed to partial electrical discharge. *Journal of Colloid and Interface Science*, 226(2):231–236, 2000. 59

[86] J Kim, MK Chaudhury, MJ Owen, and T Orbeck. The mechanisms of hydrophobic recovery of polydimethylsiloxane elastomers exposed to partial electrical discharges. *Journal of Colloid and Interface Science*, 244(1):200–207, 2001. 59

[87] J Kim, MK Chaudhury, and MJ Owen. Modeling hydrophobic recovery of electrically discharged polydimethylsiloxane elastomers. *Journal of colloid and interface science*, 293(2):364–375, 2006. 59

[88] GK Batchelor. *An introduction to fluid dynamics*, volume 515. Cambridge University Press, 1967. 63

[89] AL Bertozzi, A Münch, X Fanton, and AM Cazabat. Contact line stability and "undercompressive shocks" in driven thin film flow. *Physical review letters*, 81(23):5169, 1998. 63

[90] RV Sedev and JG Petrov. The critical condition for transition from steady wetting to film entrainment. *Colloids and surfaces*, 53(1):147–156, 1991. 65

[91] TD Blake. Dynamic contact angles and wetting kinetics. *Wettability*, 49:251–309, 1993. 73

[92] JH Snoeijer and B Andreotti. Moving contact lines: Scales, regimes, and dynamical transitions. *Annual review of fluid mechanics*, 45:269–292, 2013. 75, 113

[93] SDR Wilson. The drag-out problem in film coating theory. *Journal of Engineering Mathematics*, 16(3):209–221, 1982. 98, 102, 103

[94] R Buckingham, M Shearer, and A Bertozzi. Thin film traveling waves and the Navier slip condition. *SIAM Journal on Applied Mathematics*, 63(2):722–744, 2003. 103

[95] S Mettu and MK Chaudhury. Stochastic relaxation of the contact line of a water drop on a solid substrate subjected to white noise vibration: roles of hysteresis. *Langmuir*, 26(11):8131–8140, 2010. 130

Partial wetting of thin liquid films in polymer tubes

Abstract Polymer tubes, made of PDMS or PVC, are versatile, low cost, hydrophobic materials. They are heavily used in industry for transferring more or less complex fluids such as drinkable water, emulsions (*e.g* milk), suspensions (*e.g* coffee), or solution of active molecules (*e.g* pharmaceutics). Most of these applications involve repeated, intermittent flow of liquids which can lead to unwanted contamination. This study aims at better understanding the mechanisms of contamination for intermittent flow. We experimentally and theoretically investigate the flow regimes of low viscosity liquid slugs flowing down a vertical tube under partial wetting condition. Two processes are in competition: because of the large slug velocity, a liquid film tends to be created at the back of the slug whereas because of the partial wetting condition, the liquid film dewets. We investigate how this competition controls film deposition in hydrophobic tubes. We show that above the threshold velocity for dynamic wetting which is much lower than predicted by Cox-Voinov, a previously unknown regime is found where we observe a velocity dependent thick film well before the classical Landau-Levich-Derjaguin regime.

Keywords: Contact angle, Dynamic wetting, Hydrophobicity, Liquid film, Polymer tube, Surface modification

---

Mouillage partiel de films liquides dans des tubes polymères

Résumé Les tubes polymères, de PDMS ou de PVC, sont des matériaux hydrophobes polyvalents et peu couteux. Ils sont très largement utilisés dans l'industrie pour transférer des fluides plus ou moins complexes tels que de l'eau potable, des émulsions (*e.g* lait), des suspensions (*e.g* café), ou encore des solutions de molécules actives (*e.g* médicament). La plupart de ces applications mettent en jeux des écoulements intermittents répétés de liquide qui peuvent contaminer le matériau. Cette étude a pour but de mieux comprendre comment ces écoulements de fluides complexes entraînent la contamination des tubes. Nous étudions expérimentalement et théoriquement les régimes d'un segment de liquide de faible viscosité s'écoulant dans un tube en conditions de mouillage partiel. Deux processus sont en compétition : à cause de la vitesse élevée du segment de liquide, un film de liquide se forme à l'arrière du segment, alors qu'à cause de des conditions de mouillage partiel le film de liquide démouille. Nous montrons qu'au-delà de la limite en vitesse correspondant à la transition de mouillage dynamique qui est bien inférieure à la prédiction de Cox-Voinov, un régime précédemment inconnu avec un film épais, dont l'épaisseur dépend de la vitesse, est obtenu bien avant la formation classique d'un film de Landau-Levich-Derjaguin. Nos simulations numériques sont en partie en accord avec nos observations.

Mots-clefs: Angle de contact, Mouillage dynamique, Hydrophobicité, Film liquide, Tube polymère, Modification de surface